

Proceedings of
**International Conference on
Advanced Materials and
Manufacturing Technologies**

(AMMT)

December 18th-20th, 2014

Sponsored by



University Grants Commission
(UGC) New Delhi

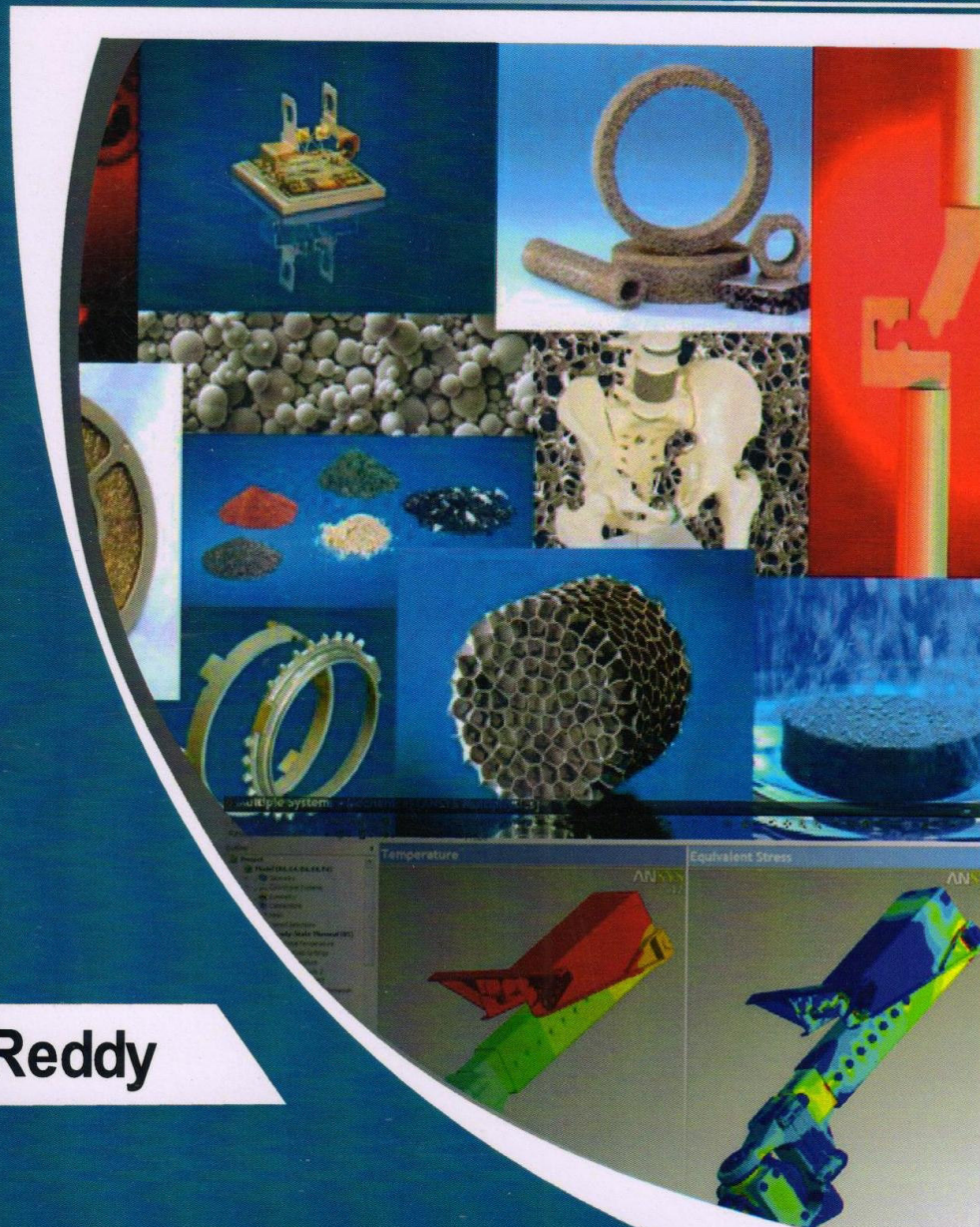


TEQIP-II

JNTUH College of
Engineering Hyderabad

Editor

Dr. A. Chennakesava Reddy



Chief Patron

Smt. Shailaja Ramayar, Vice Chancellor, JNTUH, Hyderabad, Telangana, India

Patron

Dr. T. Kishen Kumar Reddy, Rector, JNTUH

Chairman

Dr. N.V.Ramana Rao, Registrar, JNTUH

Vice- Chairman

Dr. N. Yadaiah, I/C Principal, JNTUH CEH

Convener

Dr. B. Anjaneya Prasad, HOD, Mechanical Engg.,

Organizing Secretary

Dr. A. Chennakesava Reddy, Professor, Mechanical Engg.

Organising Coordinators

Dr. E. Ramjee, Professor, Mechanical Engg.

Dr. G. Krishna Mohana Rao, Professor, Mechanical Engg.

Technical Coordinators

Dr. M. Indira Rani, Professor, Mechanical Engg.

Dr. M. Vidya Sagar, Associate Professor, Mechanical Engg.

Dr. P. Bharamara, Associate Professor, Mechanical Engg.

Mr. P. Prasanna, Asst. Professor, Mechanical Engg.

Advisory Committee:

Dr. A.V. Sita Rama Raju, Director, Admissions, JNTUH

Dr. K. Vijaya Kumar Reddy, Director, DAP, JNTUH

Dr. K. Eshwara Prasad, Director, Examinations, JNTUH

Dr. M. Manzoor Hussain, Principal, JNTUH CES

Dr. M. T. Naik, Professor, JNTUH

Dr. P. Madhusudhan Reddy, Scientist – G, DMRL, Hyderabad

Dr. A.C.S.Kumar, Principal, Hi-Tech College of Engg. & Tech.

Prof. P. Nageswara Rao, Univeristy of Northen Iowa, USA

Dr. Saeid Nahavandi, Deakin University, Victoria, Australia

Prof. Mats Walter, Blekinge Institute of Technology, Sweden

Technical Committee:

Mr. V. U. B Reddy, Deputy Director, CITD, Hyderabad

Dr. P. Laxminarayana, OU, Hyderabad

Dr. G. Chandramohan Reddy, Principal, MGIT, Hyderabad

Dr. P.Ravindar Reddy, HOD, Mechanical, CBIT, Hyderabad

Dr. G. Poshal, Principal, Institute of Aeronautical Engg.

Dr. M. Ashok Kumar, Sai Sudhir of Engg. & Tech.

Dr. P. Ravi Kumar, Professor of Mech. Engg., NIT-Warangal

Dr. N. Venkat Reddy, Professor of Mech. Engg., IITH

Dr. K. Sreenivasa Reddy, Professor of Mech. Engg., IIT – Madras

Dr. Sujayath Khan, Principal Director, CITD, Balanagar, Hyderabad

Dr. A.V.S.S.K.S. Gupta, Professor of Mechanical Engineering, JNTUH, Hyderabad

**PROCEEDINGS OF INTERNATIONAL CONFERENCE
ON
ADVANCED MATERIALS AND MANUFACTURING
TECHNOLOGIES
(AMMT)**

DECEMBER 18-20, 2014

SPONSORED BY



UNIVERSITY GRANTS COMMISSION (UGC) – NEW DELHI



TEQIP-II, JNTUH COLLEGE OF ENGINEERING HYDERABAD

EDITOR

Dr. A. CHENNAKEASVA REDDY

Professor of Mechanical Engineering
JNTUH College of Engineering
Kukatpally; Hyderabad

**INTERNATIONAL CONFERENCE ON ADVANCED
MATERIALS AND MANUFACTURING TECHNOLOGIES
(AMMT)**

All rights are reserved. No part of this publication which is material protected by this copyright notice may not be reproduced or transmitted or utilized or stored in any form or by any means now known or hereinafter invented, electronic, digital or mechanical, including photocopying, scanning, recording or by any information storage or retrieval system, without prior written permission from Paramount Publishing House.

Information contained in this book has been published by Paramount Publishing House, Hyderabad and has been obtained by its Author(s) from sources believed to be reliable and are correct to the best of their knowledge. However, the Publisher is not liable for any errors, omissions or damages arising out of use of this information and specifically disclaim any implied warranties or merchantability or fitness for any particular use. The authors are solely responsible for the contents published in the paper.

International Conference on Advanced Materials and Manufacturing Technologies (AMMT)

First Edition - 2014

Copyright © **Dr. A. Chennakesava Reddy**

ISBN : 978-93-82163-46-6

Price : ₹ 675.00

Paramount Publishing House

3-5-1105, 2nd Floor, PVR Estates, Behind Hero Honda Showroom, Narayanaguda, Hyderabad-500 029.

Phone: 040-64554822.

Sales Offices :

Hyderabad

3-5-1105, 2nd Floor, PVR Estates, Behind Hero Honda Showroom, Narayanaguda, Hyderabad-500 029.

Phone: 040-64554822.

Visakhapatnam

43-18-19/1, Krupa Residency, Venkatarjuna Nagar, Dondaparthi, Visakhapatnam - 530 016. Andhra Pradesh. Phone: 9490708474.

New Delhi

C/14, SDIDC Work Centre Jhilmil Colony, New Delhi-100095. Phone: 011-22162365.

paramountpublishers@gmail.com | alluriasr2005@yahoo.com

Published by Krishna Prasad Alluri for Paramount Publishing House and printed by him at Sai Thirumala Printers.

PREFACE

Rapid technological developments in the materials and the manufacturing methods are essential for the new class of industrial and domestic products, which are quite different from their current designs.

This international conference provides the platform for active interaction to Industrialist, Engineers, Scientists, the policy makers, Academicians to discuss the activities, researches and developments in depth about the advanced trends in the design and manufacturing technologies of industrial and domestic products. The awareness about possible use of the advanced materials and manufacturing technologies will certainly help to deliver high quality and cheaper products to the society and the world.

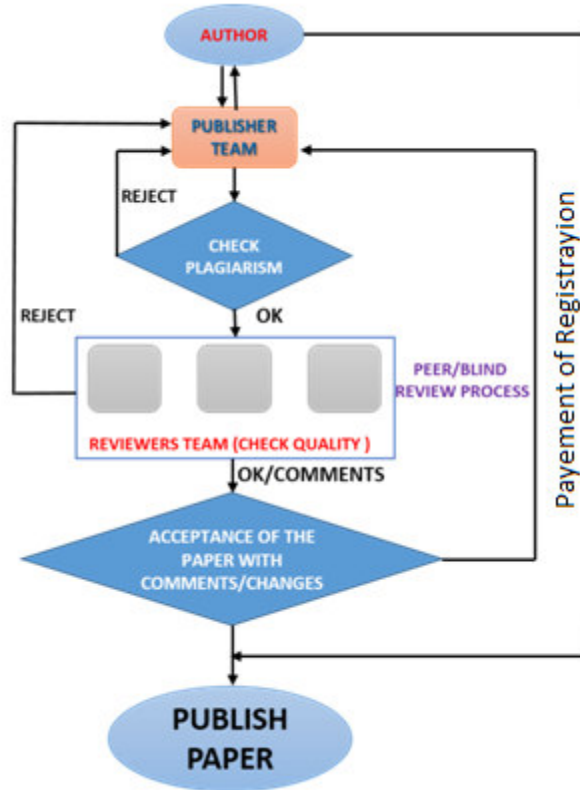
CONFERENCE STRUCTURE

- Advanced (high and low temperature) alloys
- Composites and Smart materials
- Advanced heat treatment techniques
- Advanced manufacturing technologies & simulation
- Static and dynamic durability and stability
- Thermal aspects of manufacturing processes
- CAD/CAM/CAE/FMS
- Material testing and characterization
- Fracture modeling & analysis
- Computer aided process planning
- Quality control policies & methods
- Group technology
- Fuzzy logic/Neural Networks/Genetic algorithms
- Micro/Nano Manufacturing
- Robotics
- Collaborative manufacturing
- Reverse engineering
- Rapid prototyping
- Cellular manufacturing
- CNC / DNC / ACS
- Concurrent engineering
- Six sigma
- Nesting of manufacturing industries for single goal
- Nonfluids in manufacturing applications

The statistics of the papers received and accepted to this conference are given below:

1. Number of abstracts received : 132
2. Number of abstracts accepted : 90
3. Number of full papers received : 64

4. Number of full papers accepted to present in the conference : 44
5. Number of full papers accepted to print in the proceedings : 32



The accepting the papers are based on the criteria mention in the flow chart above:

1. Percentage plagiarism not exceeding 24% in total and 3% for each source. This is the first stage of filtering to move to second stage.
2. Remarks of two subject experts and proof reader. The two subject experts review the paper in terms of technical quality. The proof reader check format of the paper. This is the second stage of filtering papers.
3. Incorporation of remarks and comments in the paper. The publishing committee checks the incorporation of remarks and comments suggested by the experts after obtaining them from authors. The acceptance of the paper is based on complete discussion of the contents therein.
4. Payment of registration and additional page charges.
5. Remarks of the Organizing Secretary based on cooperation extended by the authors.

The conference proceedings are brought in two categories, namely:

1. Abstract Proceedings of International Conference on Advanced Materials and Manufacturing Technologies (AMMT), and
2. Full Length Paper Proceedings of International Conference on Advanced Materials and Manufacturing Technologies

The conference is held on six sessions. Each session is chaired by two subject experts (one is external and another is internal).

Dr. A. CHENNAKESAVA REDDY

B.E., M.E (mech)., M.Tech (CAD/CAM)., Ph.D (mech)., Ph.D (CAD/CAM).
M.ISTE., M.ISME., M.IIPE., M.IIF., M.IIW., M.IE., C.Engg.

Professor & Chairman (BOS), Mechanical Engineering
Organizing Secretary, AMMT



ACKNOWLEDGEMENTS

The organizing secretary, International Conference on Advanced materials and Manufacturing Technologies (AMMT) thanks by name the following:

1. University Grants Commission (UGC), New Delhi for the financial assistance.
2. TEQIP – II, JNTUH College of Engineering, Hyderabad for financial assistance
3. Vice-Chancellor, Rector, and Registrar of JNT University Hyderabad for their approval to organize this event in JNTUH.
4. Principal, and Vice-Principal of JNTUH College of Engineering, Hyderabad for their permission to organize this event.
5. HOD, Department of Mechanical Engineering, JNTUH CEH for his encouragement to organize this event.
6. The Delegates and Participants for their participation and presentation of papers in this event.
7. The Subject Experts who accepted to review the papers
8. The Publisher to structure the printing format and editing the papers in the printing format.
9. The judges of the various sessions of this conference.
10. The Organizing Committee Members for their support to make this program a grand success.
11. All teaching and non-teaching staff of Department of Mechanical Engineering, JNTUH CEH for their support to happen this event.
12. All the research scholars working under me.
13. Press and Media for their advertisement.
14. Finally all those people who directly and indirectly helped this event to make grant success.

Dr. A. Chennakesava Reddy
Organizing Secretary

MESSAGES



JAWAHARLAL NEHRU TECHNOLOGICAL UNIVERSITY HYDERABAD

Kukatpally

Hyderabad – 500 085

Telangana (India)

Phone: 040-23156109 (O)

Fax: 040-23156112

Email: vcjntu@jntuh.ac.in

Website: www.jntuh.ac.in

**Smt. Shailaja Ramaiyer, IAS,
Incharge Vice-Chancellor**

I congratulate the organizing committee for conducting an International Conference on Advanced Materials and Manufacturing Technologies (AMMT) which has the aim of promoting the growth and development of engineered materials for next generation by identifying and providing cutting-edge solutions in materials science, manufacturing technologies, and new product development. This conference can be an effective interface between the global scientific community and customer's needs. More advanced, high-end manufacturing will require a stronger focus on innovation—particularly in processes, markets, products, services, delivery and business and management models. More manufacturers are likely to be engaged in research and development (R&D), design, production of prototypes, and the small-scale manufacture of complex, high value added goods. Success in this new environment will require new and higher level skills, particularly science, technology, engineering and mathematics skills. Raising skill levels, including by employing a larger proportion of university graduates, will be critical to success; as will stronger collaboration between manufacturers and universities to ensure the supply of skilled graduates and drive innovation through research.

I wish all participants to discuss the need of new materials and technology to raise the standards of society in general and enhancement of research needs to the developing country like India during conference.

VICE-CHANCELLOR I/C



JAWAHARLAL NEHRU TECHNOLOGICAL UNIVERSITY HYDERABAD

Dr. T. Kishen Kumar Reddy, Ph.D., FIE
Professor of Mechanical Engg. &
RECTOR

Kukatpally
Hyderabad – 500 085
Telangana (India)
Phone: +91-040-32422256 (O)
Fax: +91-040-23158665
Email: reddykishen@jntuh.ac.in
Website: www.jntuh.ac.in



I am happy to note that the Department of Mechanical Engineering, JNTUH CEH is going to organize an International Conference on **“Advanced Materials and Manufacturing Technologies” (AMMT)** during 18-20 December, 2014.

This conference will provide a platform for students, R&D scientists, Industry Experts, and users etc., to interact and share their experiences and enrich themselves and provide a facilitative mechanism for solving problems.

E xtend my warm greetings to the participants of the International Conference (AMMT).

I congratulate the faculty, staff members of the Department of Mechanical Engineering, JNTU h CEH for their efforts in conducting this event.

T. Kishen Kumar Reddy
T. KISHEN KUMAR REDDY



JAWAHARLAL NEHRU TECHNOLOGICAL UNIVERSITY HYDERABAD

Dr. N.V. Ramana Rao
B.E., M.Tech., PGDCS, Ph.D(UK), Post Doc. (UK)
Professor of Civil Engg. &
RECTOR

Kukatpally
Hyderabad – 500 085
Telangana (India)
Phone: +91-040-32422253 (O)
Fax: +91-040-23158665
Email: rao.nvr@jnru.ac.in
Website: www.jntuh.ac.in



I congratulate the organizing committee for conducting an International Conference on Advanced Materials and Manufacturing Technologies (AMMT) which has an objective of materials research, technologies as well as applied, plays a central role in the development of more efficient and cost effective applications for industrial growth. The growing threat posed by competitors in China and other Asian Countries offering low prices has compelled us to undertake an urgent review of new production system. The first is “flexibility to address change”. Because of the short life cycles of computers, obile phones and other electronic equipment, we cannot survive without constantly developing new products. The second motto is “more competitive products for the global market”. The third motto is ‘comfort of the society’.

Of equal importance is an understanding of both advanced manufacturing technologies and the latest computer based design procedures , essential for product commercialization from the concept phase. Technological, economic and environmental pressures will ensure that the demand for materials experts will increase in the future. I wish that participants will address new materials and manufacturing methodologies to make developed India instead of developing India.

I appreciate the efforts made by the students, staff, volunteers and organizing committee members in organizing this three day International Conference.


Prof. N.V. RAMANA RAO



JNTUH COLLEGE OF ENGINEERING HYDERABAD (autonomous)

Dr. N. Yadaiah, Ph.D.
Professor of Electrical & Electronics Engg. &
PRINCIPAL

Kukatpally
Hyderabad – 500 085
Telangana (India)
Phone: +91-40-23057787
Fax: +91-40-23057787
E-mail: principal.ceh@intuh.ac.in
Website: www.intuhceh.ac.in



It gives me immense pleasure to welcome you to the International Conference on Advanced Materials and Manufacturing Technologies (AMMT), being hosted by Department of Mechanical Engineering, JNTUH College of Engineering Hyderabad. I wish this International Conference to be one of the most referred conferences.

The main objective of the conference is to create a platform for academicians, scientists, industry practicing engineers to share their experiences, expertise and developments in Advanced Materials and Manufacturing Technologies.

I hope this conference will unfold new panorama in the sphere of new technologies in the field of engineering. I hope the participants would find these three days technically stimulating and professionally rewarding.

I wish all the success for the event.

Best Wishes

PRINCIPAL



JNTUH COLLEGE OF ENGINEERING HYDERABAD (autonomous)

Dr. S. Chandralingam, Ph.D.
Professor of Physics &
VICE - PRINCIPAL

Kukatpally
Hyderabad – 500 085
Telangana (India)
Phone: +91-40-2315814
Fax: +91-40-23119102
E-mail: vp.ceh@jntuh.ac.in
Website: www.intuhceh.ac.in



I am delighted to learn that the Department of Mechanical Engineering, JNTUH setting its focus on manufacturing process by organizing the International Conference on **Advanced Materials and Manufacturing Technologies (AMMT)** during 18-20 December, 2014 in JNTUH CEH, Hyderabad campus which covers all aspects of processing, fabrication, structure/property evaluation and applications of advanced materials.

It gives me immense pleasure to welcome all delegates to this International Conference. The conference, I trust, shall provide an excellent platform to researchers for in-depth deliberations on the theme, but will also serve as an eye-opener to teacher, students and researchers in their respective area of specialization. I hope the participants would find these three-days technically stimulating and professionally rewarding.

I take the opportunity of conveying my felicitations to the organizers of the conference for arranging such a significant conference and crave for the success of the conference and I wish this conference to be one of the most referred conferences.

My best wishes once again for the success of AMMT conference.

Dr. S. CHANDRALINGAM
Vice-Principal



JNTUH COLLEGE OF ENGINEERING HYDERABAD (autonomous)

Dr. B. Anjaneya Prasad, Ph.D.
Professor of Mechanical Engg. &
HOD

Kukatpally
Hyderabad – 500 085
Telangana (India)
Phone: +91-9441124725
Fax: +91-40-23119102
E-mail: baprasadjntu@jntuh.ac.in
Website: www.intuhceh.ac.in



Research is becoming increasingly focused on producing advanced materials with targeted properties, from novel high temperature superconductors to newly-developed polymer nanocomposites. Such materials have new or improved structural or functional properties and have applications across a wide range of sectors, including telecommunications, electronics, pharmaceuticals, aerospace, automotive, security and medicine. In addition, nanomaterials are intended to improve the performance of existing production technologies, and to give new functionalities to products.

The developments in advanced materials are invariably connected to the advanced characterization of the materials as well as developing manufacturing technologies for producing them, by engaging industry's interest. The development of manufacturing technologies should be in line with sustainable growth. This calls for wide surveys to be conducted among stake holders which will eventually lead to the enhancement of living standards.

I am sure the “International Conference on Advanced Materials and Manufacturing Technologies” being organized by the Department of Mechanical Engineering will provide one such platform for interaction among academia and industry personnel and give a direction to the young research scholars for initiating research in this field.



CENTRAL INSTITUTE OF TOOL DESIGN HYDERABAD
(A Government of India Society Ministry of MSME)
Balanagar, HYDERABAD - 500 037, INDIA
Tel.No : 91-40-2377 2748, 2749, 6178
Fax : 91-40-23772658

Sri. Sujayath Khan, M.S.
Principal Director



It is indeed great pleasure to note that Department of Mechanical Engineering, Jawaharlal Nehru Technological University, Hyderabad is conducting seminar on Advanced Material and Manufacturing Technology, during 18-20th December 2014. Currently manufacturing technology has been undergoing phenomenon transformation with advent of concepts such as 3D printing, obtaining near “Net Shape Components”, aiming at conservation of material and energy. Environmental concerns have been greatly influencing use of Materials and Manufacturing Technology.

Besides, these efforts have been intensified at national level to enhance manufacturing contribution to GDP.

I am sure that outcome of this seminar will be very useful to industry as well. I congratulate organizers and participants and wish the success of this conference.



JAWAHARLAL NEHRU TECHNOLOGICAL UNIVERSITY KAKINADA

Dr. G. Ranga Janardhana, Ph.D.
Professor of Mechanical Engg. &
Director, Institute of Science & Technology

Kakinada – 500 085
Andhra Pradesh (India)
Phone: 0884-2300913
E-mail: director.ist@jntuk.edu.in
Website: www.jntuk.edu.in



I am happy to learn that Three Day International Conference on Advanced Materials and Manufacturing Technologies (AMMT-2014) is being organized by the Department of Mechanical Engineering, JNTUH College of Engineering, Hyderabad. I welcome all the delegates from various parts of the Country and the Globe. I am sure the practical experience, technical ideas, analytical results and innovations from delegates shared during the conference would be valuable for both the institutions and industries.

The International Conference on Advanced Materials and Manufacturing Technologies (AMMT-2014) brings the researchers, manufacturers, academicians and students on to a single platform and plays vital role to bridge the gap between pure research and the more practical activities of manufacturing systems. It therefore provides an outstanding forum for the people from various parts of the world inviting the international standard papers covering applications-based research topics spanning the entire manufacturing spectrum. Today, Composite & Nano Technologies, offers the most comprehensive line of strengthening products and development of newer materials in the world for fortifying and protecting the parts against corrosion, erosion, and minimising environmental damage. I am sure that the accepted papers will be of high standard of excellence and meet the requirements to demonstrate the manufacturing applications.

I extend my best wishes to all the members of organizing committee to achieve a grand success in organising AMMT-2014.



**UNIVERSITY COLLEGE OF ENGINEERING
OSMANIA UNIVERSITY**

Dr. P. Laxminarayana, Ph.D.
Professor of Mechanical Engg. &

Hyderabad – 500 007
Telangana (India)
Phone: +91- 40-27097346
E-mail: plax@osmania.ac.in



It is a very great pleasure for me to know that the University College of Engineering, JNT University, Hyderabad, for organizing **International Conference on Advanced Materials & Manufacturing Technologies (AMMT)** during **18-20th Dec, 2014**. I am glad that we can have this multinational Conference in Telangana State, India.

This conference provides an opportunity for transmission of knowledge based on latest research in the field of Material Science and Manufacturing Technology. I hope that this Conference will make visible in concentrated form the great challenge and stimulus in Advanced Materials and rapidly advancing new technologies.

I convey my best wishes to Organizing Secretary, AMMT and all the staff of University College of Engineering, JNT University, Hyderabad for organizing this conference.

Wishing you all a very fruitful and rewarding conference

(Prof. P. Laxminarayana)



NATIONAL INSTITUTE OF TECHNOLOGY WARANGAL

Dr. P. Ravi Kumar Puli, Ph.D.
Professor of Mechanical Engg.

Warangal – 506 004
Telangana (India)
Phone: 0870-246-2333
E-mail ravikumar.puli@gmail.com



Welcome to the International conference on advanced materials and manufacturing technologies (AMMT) being held in JNTUH COLLEGE OF ENGINEERING Jawaharlal Nehru Technological University Hyderabad from December 18-20, 2014. This type of International Conference held annually and this conference provides rapid technological developments in the materials and manufacturing methods and this event covers all the aspects of advanced trends in the design and manufacturing technologies of industrial and domestic products. The awareness about possible use of the advanced materials and manufacturing technologies will certainly help to deliver high quality and cheaper products to the society and the world. This year this International Conference on advanced materials and manufacturing technologies (AMMT) held in Hyderabad got more than 200 papers will be presented from different countries. All of the submissions were rigorously checked by plagiarism software and the maximum limit to accept the paper is 24% as per UGC norms. The activities of the college are basically supported by the budgetary allocation from the University funds. The Organizing and Program Committees have worked hard to produce a first class technical conference and a pleasing, enjoyable social event.

On behalf of the Organizing and Program committees I welcome you all to the International conference on advanced materials and manufacturing technologies (AMMT) being held in JNTUH COLLEGE OF ENGINEERING Jawaharlal Nehru Technological University Hyderabad and hope that you enjoy the presentations and the trends in design and manufacturing technologies of industrial and domestic products.



CHAITANYA BHARATHI INSTITUTE OF TECHNOLOGY
(UGC AUTONOMOUS)

Dr P.Ravinder Reddy, Ph.D.
Professor of Mechanical Engg. &
HOD & Dean (R&D)

Hyderabad – 506 075
Telangana (India)
Phone: +91-9391033002
E-mail: reddy.prr@gmail.com



I am glad that the department of mechanical engineering is organizing an International conference on advanced materials and manufacturing technologies (AMMT) during 18th -19th December 2014 in Hyderabad in the state of Telangana, India

Materials and Manufacturing is an important activity of human civilization. It is very crucial for improving the economy of our country and achieving sustainable development. At present share of manufacturing sector to Gross Domestic Product (GDP) of India is just about 15%. This has to be increased tremendously for making India an economic super power. India is rich in natural resources and manpower. Science, technology and management can tap the potential available with us and strengthen the manufacturing sector. Concentrated efforts should be made for carrying out quality research in improving the manufacturing processes and systems and development of new materials. The outcome of research should not be confined to research laboratories and effort must be put so that manufacturing organizations can benefit from the new developments in manufacturing research. At the same time, the manufacturing education should also be given due importance, in order to attract the young talented persons in this area and equip them with the knowledge, information and wisdom suitable for industry.

I hope that the deliberations in the conference will help researchers from academia and industry and the conference will provide a platform for initiating collaborative research projects. The outcomes of the conference definite benefit to the new state of Telangana. I believe the onference will surely prove conducive to all in equal length.

I wish the conference all success and I convey hearty compliments to all concerned for their untiring efforts to make it a grand event.

(Dr P.Ravinder Reddy)



MAHATMA GANDHI INSTITUTE OF TECHNOLOGY

Dr G. Chandra Mohan Reddy, Ph.D.
Professor of Mechanical Engg. &
Principal
Past Hon Secretary &
Member- State Centre Committee IEIAPSC

Hyderabad – 506 075
Telangana (India)
Phone: 040 - 24193057
Fax: 040 - 24193067
E-mail: principal@mgit.ac.in



The continuous developments in Materials and Manufacturing Technologies lead us to where we are today. The contribution of materials for human civilization is immense and it had its effect in every sphere of life, be it Aerospace industry, Defence, Naval, Electronic Industry and one can not name any product without Materials and Technologies associated with its development. It is important that we discuss the latest developments in these fields continually and the AMMT – 2014 provides the correct forum.

The Three Day International Conference on Advanced Materials and Manufacturing Technologies (AMMT-2014) envisaged by the Department of Mechanical Engineering, JNTUH College of Engineering, Hyderabad will definitely see the delegates from various parts of the Country and abroad actively participating and sharing the experience, ideas, innovations, research results during the conference and it would be valuable for everyone and the country in particular at this crucial juncture. The AMMT 2014 provides an opportunity to the researchers from Industry and Academia and students and brings them on to a single platform and plays an important role to bridge the gap between theory and practice in the activities of manufacturing for the people from various parts of the world by inviting standard papers on application oriented manufacturing related to theme and sub themes as per the Brochure. I am confident that the presentation and discussion on some of the papers will provide solutions to our local manufacturing related problems also.

I convey my best wishes to the members of organizing committee for their efforts to make this event a grand success and I also wish the participants a great learning during AMMT-2014.

CONTENTS

Paper Title and Authors	Paper No.
ROLE OF ALLOYING ELEMENTS ON MECHANICAL PROPERTIES, RESIDUAL STRESSES & CORROSION BEHAVIOUR OF AISI 430 FERRITIC STAINLESS STEEL GTA WELDS G. Mallaiah, P. Ravinder Reddy, A. Kumar	1
AN EXPERIMENTAL STUDY ON AMORPHOUS Fe _{73.5} Cu ₁ Nb ₃ Si _{16.5} B ₆ and Fe _{68.8} Cu _{0.5} Nb _{2.6} Si _{18.6} B _{9.5} ALLOYS M.D.V. Srilalitha, B. Bhanu Prasad and A.R. Subrahmanyam	13
STUDY OF WELDING ECONOMY AND IMPROVE PRODUCTIVITY OF (2205) DUPLEX STAINLESS STEEL MATERIAL A.Balaram Naik, A.Chennakesava Reddy	19
STUDY ON MECHANICAL BEHAVIOUR OF PHENOLIC BASED COMPOSITES WITH AND WITHOUT ZIRCONIUM FILLER R. Ramanarayanan, C. Hari Venkateswara Rao A. Panindra	34
TENSILE AND FRACTURE BEHAVIOR OF 6061 Al-Si Cp METAL MATRIX COMPOSITES T. Prasad · A. Chennakesava Reddy · S. Jushkumar	39
EFFECT OF MATRIX COMPOSITION ON MECHANICAL PROPERTIES IN CARBON FIBRE REINFORCED COMPOSITES K. Srinivasa Vadayar, G. Madhuri, L.S. Mahajan, V.V. Bhanu Prasad	47
EFFECT OF GLASS FILLER MATERIAL ON MECHANICAL PROPERTIES OF GLASS/EPOXY (RT CURE) COMPOSITES R.Ramnarayanan, C.Venkateshwar Reddy	53
METALLURGICAL CHARACTERISTICS OF FRACTURE BEHAVIOUR IN Al/SiC METAL MATRIX COMPOSITE Essa Zitoun and A.Chennakesava Reddy	61
FRACTURE BEHAVIOR OF ALUMINA PARTICLES REINFORCED WITH DIFFERENT MATRIX ALUMINIUM ALLOYS G. Satish Babu and A. Chennakesava Reddy	71
EXPERIMENTAL ANALYSIS OF Z-PINNED CARBON FIBER COMPOSITES J.Dhanraj Pamar, B.Balu Naik and Md.Kashfuddoja	80
MECHANICAL PROPERTIES OF NATURAL COMPOSITE MATERIALS Akula Komuraiah , DR.N.Shyam Kumar and B.Durga Prasad	91
TENSILE AND FLEXURAL STRENGTH OF GLASS FIBER EPOXY COMPOSITES S.Pichi Reddy, P.V.Chandra Sekhar Rao, A.Chennakesava Reddy, G.Parneswari	98
EXPERIMENTAL STUDY OF MECHANICAL PROPERTIES OF 5083 ALUMINIUM ALLOY USING GAS TUNGSTEN ARC WELDING B.V.R. Ravikumar and M. Srivatsva	104
MICRO-HARDNESS AND MECHANICAL PROPERTIES OF 5052 ALUMINIUM ALLOY WELDMENTS USING PULSED AND NON-PULSED CURRENT GAS TUNGSTEN ARC WELDING A.Raveendra, B.V.R. Ravi kumar	113
WELDABILITY OF FRICTION WELDING USING H30 ALUMINUM WITH BS970 MILD STEEL V. PRASANNA	123
EFFECT OF TOOL SHOULDER DIAMETER TO PIN DIAMETER (D/D) RATIO ON MECHANICAL PROPERTIES OF FRICTION STIR PURE ALUMINUM WELDMENTS S. Rajendra Prasad · A. Kumar , Ch. Sridhar Reddy	131
EXPERIMENTAL INVESTIGATION ON ROUNDNESS ERROR IN DRILLING OF GFR/PC THERMOPLASTIC MATRIX COMPOSITES USING BOX-BEHNKEN DESIGN (BBD) T. Srinivasan · K. Palanikumar and K. Rajagopal	138
SELECTION OF OPTIMAL PROCESS PARAMETERS IN WIRE-ELECTRICAL DISCHARGE TURNING WHILE MACHINING TI-6AL-4V ALLOY Naresh Baki, A. Chennakesava Reddy and T.Babu Rao	149
OPTIMIZATION OF MOLD COOLING TIME IN THE INJECTION MOLDING PROCESS	160

L.Sivakumar, Bhramara Panitapu	
THERMO-MECHANICAL PROPERTIES OF SILICONNITRATE POLYMERIC COMPOSITES FOR FUSED DEPOSITION MODELING S.Sreenivasulu, A chennakeshava Reddy	168
INFLUENCE OF HEAT TREATMENT ON MECHANICAL BEHAVIOR OF ALUMINIUM-7075/SILCON CARBIDE COMPOSITES MANUFACTURED BY SQUEEZE CASTING PROCESS P. Laxminarayana and A. Chennakesava Reddy	184
MECHANICAL DESIGN OF TRAILER SYSTEM FOR NON CONVENTIONAL POWER DEVICES B. Sandhya Rani, P.H.V.Sesha Talpa Sai, Y. Vijay Kumar, C.Udayakiran	196
DESIGN OF CAM-FOLLOWER MECHANISMS USING RATIONAL B-SPLINES N. Sateesh, C.S.P. Rao, K. Prashanth Reddy, R. Raman Goud	204
HONEYCOMB MECHANICS AND AGENERIC APPROACH FOR ITS MODELING AND ANALYSES Suvir Kumar, Dr MSY Sivaprasad, Dr Manzoor Hussain and Praveen Garg	214
MESH INDEPENDENCE AND CONVERGENCE TEST IN THE OIL FILM CHARACTERISTICS OF A TILTING PAD THRUST BEARING D.V.Srikanth, K.K.Chaturvedi and A.Chenna Keshav Reddy	225
FINITE VOLUME ANALYSIS OF TWO-STAGE FORGING PROCESS FOR ALUMINIUM 7075 ALLOY M. Vidya Sagar and A. Chennakesava Reddy	231
GEOMETRICAL AND MATERIAL OPTIMIZATION OF ALLOY WHEEL FOR FOUR WHEELER M.Indira Rani, Racha Venu	242
MODIFICATION OF GATING SYSTEM FOR PROPER MOULD FILLING OF BRACKET CASTING USING PROCAST G. Devendar, K. Shiva Kumar, and A. Chennakesava Reddy	252
INFLUENCE OF PARAMETERS AND OPTIMIZATION OF EDM PERFORMANCE MEASURES ON MDN 300 STEEL USING PCA-TAGUCHI BASED METHOD P. Raghu Ram Reddy, P. Prasanna, G. Shravan, K. Raju	257
DIFFERENCE BETWEEN DENAVIT - HARTENBERG (D-H) CLASSICAL AND MODIFIED CONVENTIONS FOR FORWARD KINEMATICS OF ROBOTS WITH CASE STUDY A. Chennakesava Reddy	271
AWJM PROCESS OPTIMIZATION USING PRINCIPAL COMPONENT ANALYSIS (PCA) B. SATYANARAYANA, G. SRIKAR	292
MODELING THE DYNAMIC BEHAVIOR OF MR FLUID DAMPER FOR STRUCTURAL VIBRATION MITIGATION G. Sailaja, N. Seetharamaiah, M. Janardhana	304

ROLE OF ALLOYING ELEMENTS ON MECHANICAL PROPERTIES, RESIDUAL STRESSES & CORROSION BEHAVIOUR OF AISI 430 FERRITIC STAINLESS STEEL GTA WELDS

G. Mallaiah^a, P. Ravinder Reddy^b, A. Kumar^c

^a Department of Mechanical Engineering, KITS, Huzurabad-50546, T.S., India.

^b Department of Mechanical Engineering, CBIT, Hyderabad -500075, T.S., India.

^c Department of Mechanical Engineering, NIT, Warangal -506004, T. S., India.

Abstract: The influence of grain refining elements such as copper (Cu), titanium (Ti) and aluminium (Al) on mechanical properties of AISI 430 ferritic stainless steel welds through gas tungsten arc welding process was studied. Copper (in foil form), titanium and aluminium powders of -100 μ m mesh (99% purity level) were added in the range from 1g to 3g between the butt joint of ferritic stainless steel. The effect of post weld annealing at 830 °C, 30 min holding followed by a water quenching on microstructure and mechanical properties of ferritic stainless steel welds was studied. Residual stresses and corrosion behavior of ferritic stainless steel welds was also studied. The coupled field finite element analysis is carried out to get the residual stresses by coupling thermal analysis to the static analysis. From this investigation, it is observed that the joints made by the addition of 2g Ti (0.7 wt %) in post-weld annealed condition led to improved strength. There is a marginal improvement in the ductility and pitting corrosion resistance of ferritic stainless steel welds by the addition of 2g Cu (0.18 wt %) in post-weld annealed condition. The observed mechanical properties have been correlated with microstructure and corrosion behavior of ferritic stainless steel weldments. A correlation is also made between the estimated finite elemental solutions with experimental residual stresses.

Key words: ferritic stainless steel, gas tungsten arc welding, mechanical properties, residual stresses, corrosion.

Address all correspondence to: gmallaiiah_kits@yahoo.co.in

1. INTRODUCTION

Ferritic stainless steel (FSS) in the absence of nickel provides moderate corrosion resistance at lower cost. The higher chromium grades offer good resistance to oxidation at high temperature [1]. Ferritic stainless steels are commonly used in automobile exhaust systems [2], furnace parts and combustion chambers because of their excellent resistance to stress corrosion cracking, good toughness, ductility and weldability compared with austenitic stainless steels [3]. For many of these applications welding is a major route adopted for fabrication of

components made by these alloys. Gas Tungsten Arc Welding (GTAW) is generally used for fabrication of ferritic stainless steel components because it produces a very high quality welds. Ferritic stainless steels exhibit the problem of grain coarsening in the weld zone and heat affected zone of fusion welds and consequent low toughness and ductility [4]. This is due to the absence of phase transformation during which grain refinement could occur. The problem of grain coarsening in the weld zone of ferritic stainless steel welds is addressed by limiting heat input by employing low heat input welding processes [5-8]. Studies have been conducted to grain refine ferritic stainless steel welds by electromagnetic stirring [9] by employing alternate current gas tungsten arc welding process [10-12]. Grain refining elements such as aluminium and titanium are added to transform the columnar grains in the centre of the weld to equiaxed microstructure in Gas Tungsten Arc (GTA) welds. This has been reported to result in elimination of weld centre line cracking and also improve the toughness of welds. The transition from columnar to equiaxed grains is reported to be due to fine precipitates of carbonitrides aiding heterogeneous nucleation. It has also been suggested that nitrogen in the shielding gas can refine the weld metal grain size by the formation of nitride [13]. From the reported work it is observed that the grain refinement in the weld zone of ferritic stainless steel joints by the addition of copper (Cu) , titanium (Ti) and aluminium (Al) with specified weight percentage has, so far, not been studied. The objective of the present study is to investigate the influence of Cu, Ti and Al addition on mechanical properties, residual stresses and corrosion behaviour of AISI 430 ferritic stainless steel welds.

Table 1: Chemical composition of base and filler materials (wt %)

Material	C	Mn	Si	P	S	Ni	Cr	Fe
Base material (AISI 430 FSS)	0.044	0.246	0.296	0.023	0.002	0.164	17.00	Bal.
Filler material (ER 430)	0.044	0.246	0.296	0.023	0.002	0.164	17.00	Bal.

2. EXPERIMENTAL PROCEDURE

The rolled plates of 5mm thick AISI 430 FSS were cut into the required dimension. The chemical composition and mechanical properties of the base material were presented in tables 1 and 2 respectively. GTA welding was carried out using a TIG AC/DC 3500W welding machine. A single V butt-joint configuration shown in figure 1 was selected to fabricate the joints. The base metal plates were wire brushed and degreased using acetone and preheated to 100 °C. A filler material conforming to the composition given in Table 1 is used. Copper (in foil form) was added between the butt joint of FSS after the root weld. Titanium and aluminium powders of -100µm mesh (99% purity level) were added to the molten pool in the range from 1g to 3g through hopper and a fine pipe by the controlled way using the motor mechanism over a length of 300 mm of the FSS joints. Weld joint is

completed in three passes. The welding parameters are given in table 3. The effect of post weld annealing at 830 °C, 30 min holding followed by a water quenching on microstructure and mechanical properties of ferritic stainless steel welds was studied [14].

Table 2: Mechanical properties of base material

Material	Ultimate Tensile Strength (MPa)	Yield Strength (MPa)	Elongation (%)	Impact toughness (J)	Microhardness (HV)
AISI 430 ferritic stainless steel	424	318	13	22	220

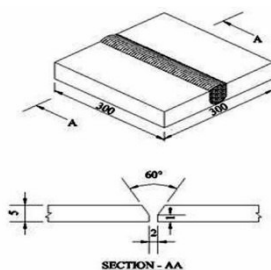


Figure 1: Schematic sketch of the weld joint (all dimensions in ‘mm’)

Table 3: Gas tungsten arc welding parameters

Parameter	Value
Welding current (Amps)	120
Welding speed (mm/min)	50
Electrode polarity	DCSP
Arc voltage (V)	10-13
Arc gap (mm)	2
Filler wire diameter (mm)	1.6
Electrode	2% Thoriated tungsten
Number of passes	3
Shielding gas (Argon), flow rate (L/min)	10
Purging gas(Argon) flow rate (L/ min)	5
Preheat temperature (°C)	100

2.1. Mechanical Testing

Microhardness tests were carried out using a Vickers digital microhardness tester in transverse direction of the weld joint. A load of 300g was applied for duration of 10 s. The specimens for tensile testing were taken in transverse to the weld direction and machined to ASTM E8 standards [15] by Wire cut Electrical Discharge Machining (WEDM).

The configuration of the tensile test specimen adopted is given in figure 2. The tensile test was conducted with the help of computer controlled universal testing machine (Model: Autograph, Make: Shimatzu) at a cross head speed of 0.5mm/min. Specimens for impact testing were taken in transverse to the weld direction and machined according to ASTM (sub size) standards [15]. The impact test was conducted at room temperature using a pendulum type charpy impact testing machine.

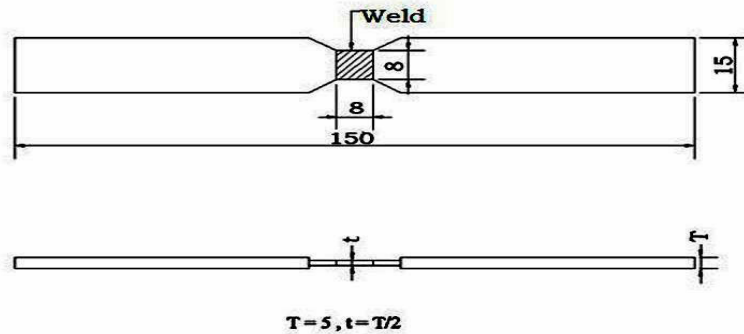


Figure 2: Configuration of tensile test specimen (all dimensions in 'mm')

2.2. Metallography

In order to observe the microstructure under the optical microscope, specimens were cut from the weld joints and then prepared according to the standard procedures, and etched using aquaregia (1 part HNO_3 , 3 parts HCL). Microstructures of welds in as-welded and post-weld annealed conditions were studied and recorded. Scanning electron microscope (SEM) was used for energy dispersive X-ray (EDX) analysis. Electron probe microanalysis (EPMA) is carried out to measure the chemical composition of base material (AISI 430 FSS), filler material (ER 430) and all weld metals.

2.3. Residual Stress Measurement

Residual stress measurements were performed on ferritic stainless steel weld specimens by computerized X-ray diffractometer using $\sin^2 \psi$ technique with $CrK\alpha$ radiation.

2.4. Corrosion Testing

The base metal and weld joints were tested for pitting corrosion in an electrolyte of 0.5M H_2SO_4 + 0.5M HCL. The electrochemical measurements were made using a potentiometer. Steady state potential was recorded 10 minutes after immersion of the sample into the electrolyte and the potential was raised anodically using scanning potentiostat at a scan rate of 2mV /s.

2.5. Finite Element Simulation of Weldments

In fusion welding a weldment is locally heated by the welding heat source. Due to non-uniform temperature distribution during the thermal cycle, incompatible strains lead to thermal stresses. These incompatible strains due to dimensional changes associated with

solidification of the weld metal, metallurgical transformations and plastic deformation are the sources of residual stresses and distortion. The finite element analysis (FEA) was carried out to evaluate the residual stress distribution in the AISI 430 ferritic stainless steel weld joints. The general purpose FEA Package ANSYS was used for both the thermal and stress analysis performed sequentially.

3. RESULTS AND DISCUSSION

The mechanical properties, residual stresses, pitting corrosion and corresponding microstructures of AISI 430 FSS weldments are discussed.

Table 4: Mechanical properties of ferritic stainless steel weldments in as-weld and post-weld annealed conditions

Joint condition	UTS (MPa)		YS (MPa)		% EL		Impact toughness (J)		Microhardness at the weld center (HV)	
	As-weld	Post-weld	As-weld	Post-weld	As-weld	Post-weld	As-weld	Post-weld	As-weld	Post-weld
1g Cu (0.1 wt %) addition	400	435	295	356	3.3	16	4	10	230	200
2g Cu (0.18 wt %) addition	417	455	312	366	6.0	17.5	6	18	250	225
3g Cu (0.25 wt%) addition	460	462	345	371	3.0	15	4	14	265	235
1g Ti (0.3 wt %) addition	419	421	335	340	2.7	8	4	4	210	225
2g Ti (0.7 wt %) addition	424	484	356	365	4.6	15	4	6	245	255
3g Ti (0.9 wt %) addition	414	415	330	334	2.5	10	3	4	232	240
1g Al (1.7 wt %) addition	455	467	346	355	3.6	12	2	4	200	215
2g Al (2.4 wt %) addition	468	478	357	385	6.0	14	4	6	230	240
3g Al (6.2 wt %) addition	440	450	328	346	2.7	8	4	4	210	220
Filler material (ER 430) addition without Cu Ti & Al	385	393	325	330	2.3	7.8	3	4	195	200

3.1. Mechanical Properties

Mechanical properties of all the weld joints in as-welded and post-weld annealed conditions were evaluated and the results are presented in table 4. From the results it is observed that by the addition of Ti to the weld pool up to 2g (0.7wt %), the strength and ductility of the FSS weldments increases due to the formation of precipitates such as titanium carbides (TiC) and titanium carbonitrides [Ti(C,N)] during welding. Whereas by increasing Ti content beyond 2g (0.7wt %), the tensile properties are deteriorated due to the strong detrimental effect of ferrite promotion compared to the beneficial effect of precipitation

In the post-weld annealed condition, the weldments made by the addition of 2g Ti (0.7 wt %) exhibit higher tensile strength compared to all other conditions. This is due to the fine grained microstructure and also formation of precipitates. The addition of Cu between the butt joint up to 3g (0.25wt %) resulted in increased ultimate tensile strength (UTS) , yield strength (YS) and hardness with marginal decrease in ductility, this can be attributed to precipitation strengthening by copper precipitates. In the post-weld annealed condition, the weldments made by the addition of 2g Cu (0.18wt %) possesses slightly superior ductility compared to all other conditions. This can be attributed to the equiaxed morphology of fusion zone grains in the FSS welds. There is a marginal improvement in the hardness of FSS weldments with 3g Cu (0.25wt %) addition in post-weld annealed condition. This is due to precipitation hardening effect of copper [16]. The addition of Al to the weld pool up to 2g (2.4wt %), the strength and ductility of the FSS weldments increases due to the formation of precipitates such as aluminium carbides (Al_4C_3) and aluminium oxides (Al_2O_3) during welding. Whereas by increasing Al content beyond 2g (2.4wt %), the tensile properties are deteriorated due to the strong detrimental effect of ferrite promotion compared to the beneficial effect of precipitation. In the post-weld annealed condition, the weldments made by the addition of 2g Al (2.4 wt %) exhibit higher tensile strength compared to 1g Al (1.7wt %) and 3g Al (6.2 wt %) addition. This is due to the fine grained microstructure and also formation of precipitates.

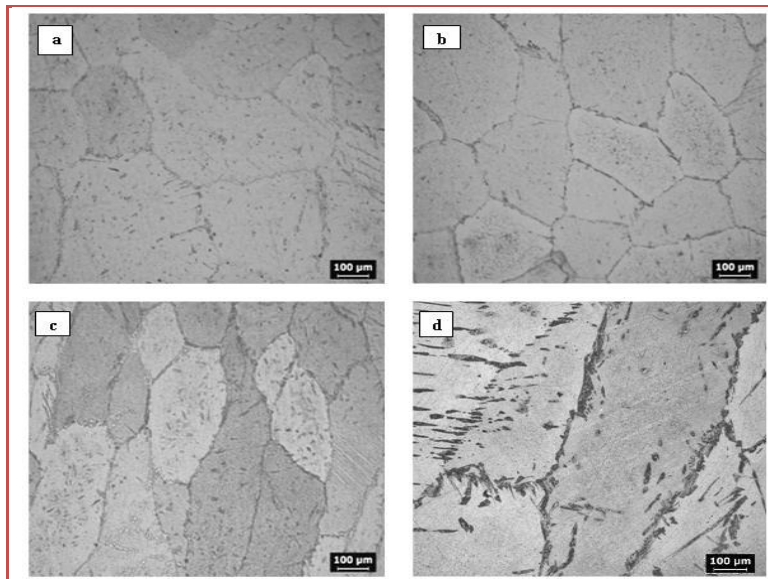


Figure 3: Microstructure of weld region of ferritic stainless steel welds in as-welded condition: (a) 1g Cu (0.1wt %) addition (b) 2g Cu (0.18 wt %) addition (c) 3g Cu (0.25 wt %) addition (d) Filler material(ER 430) addition without Cu.

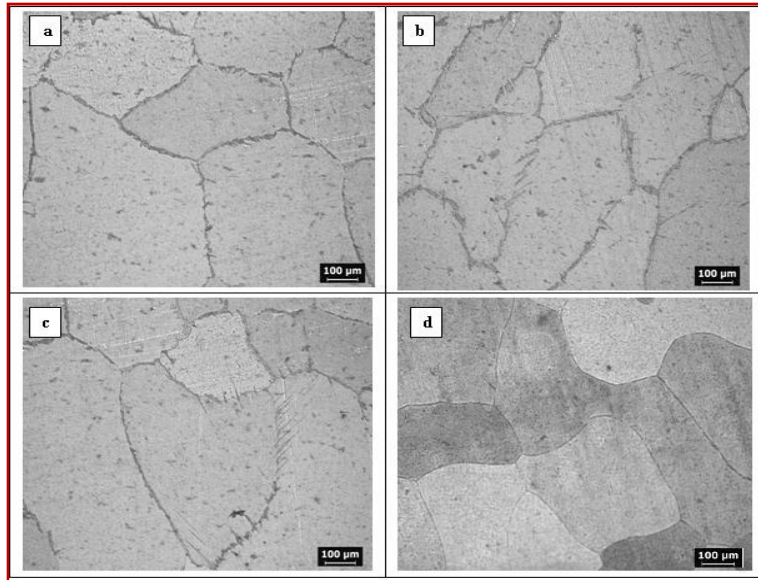


Figure 4: Microstructure of weld region of ferritic stainless steel welds in post-weld annealed condition: (a) 1g Cu (0.1wt %) addition (b) 2g Cu (0.18wt %) addition (c) 3g Cu (0.25 wt %) addition (d) Filler material (ER 430) addition without Cu

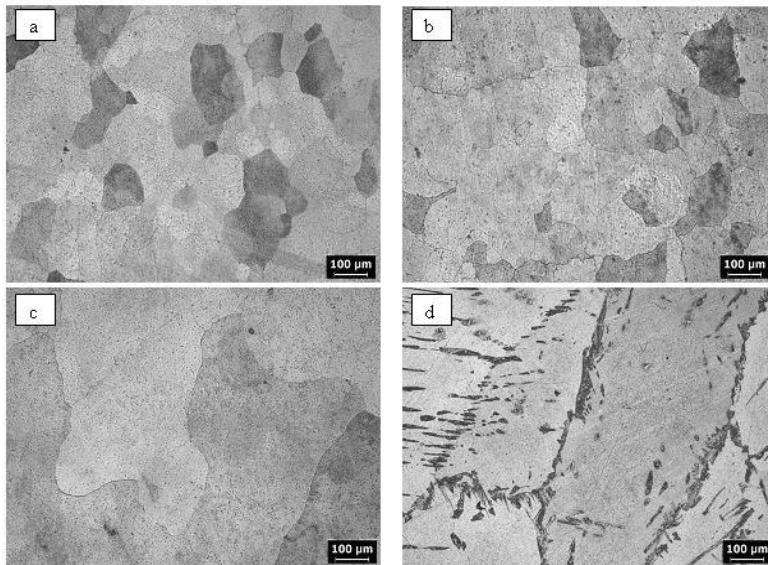


Figure 5: Microstructure of weld region of ferritic stainless steel welds in as-welded condition: (a) 1g Ti (0.3wt %) addition (b) 2g Ti (0.7wt %) addition (c) 3g Ti (0.9 wt %) addition (d) Filler material (ER 430) addition without Ti

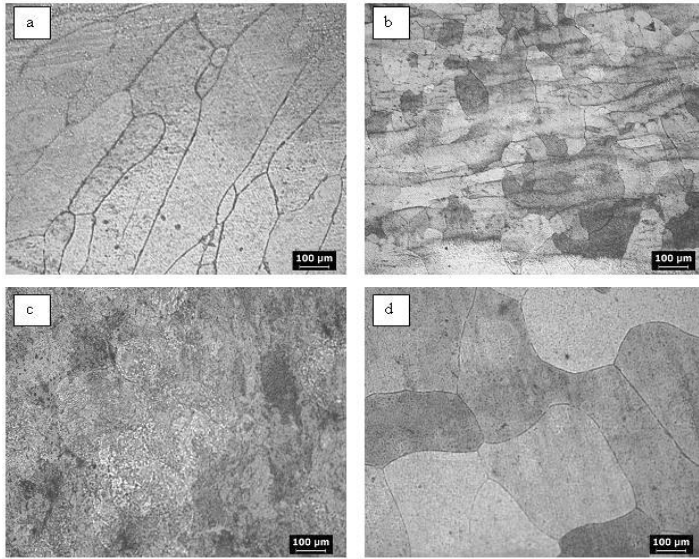


Figure 6: Microstructure of weld region of ferritic stainless steel welds in post-weld annealed condition: (a) 1g Ti (0.3wt %) addition (b) 2g Ti (0.7wt %) addition (c) 3g Ti (0.9 wt %) addition (d) Filler material (ER 430) addition without Ti

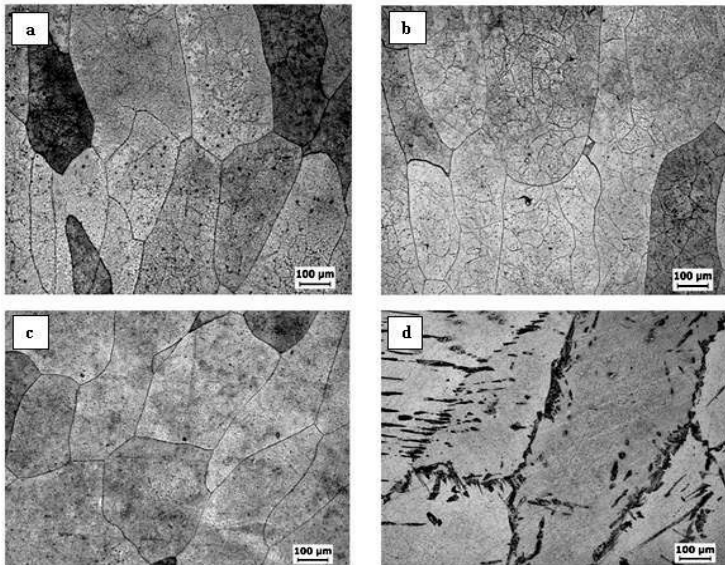


Figure 7: Microstructure of weld region of ferritic stainless steel welds in as-welded condition: (a) 1g Al (1.7wt %) addition (b) 2g Al (2.4wt %) addition (c) 3g Al (6.2 wt %) addition (d) Filler material (ER 430) addition without Al

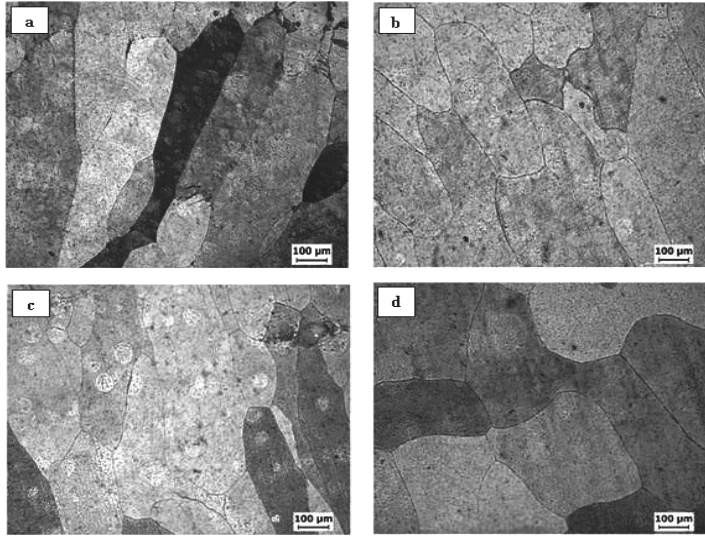


Figure 8: Microstructure of weld region of ferritic stainless steel welds in post-weld annealed condition: (a) 1g Al (1.7wt %) addition (b) 2g Al (2.4wt %) addition (c) 3g Al (6.2 wt %) addition (d) Filler material (ER 430) addition without Al

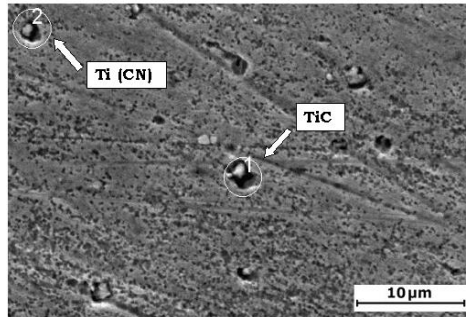


Figure 9: SEM micrograph of precipitates in the fusion zone of FSS welds made by 2g Ti (0.7wt %) addition.

3.2 Microstructure Studies

Microstructures of all the joints made by the addition of Cu, Ti, and Al and without the addition of Cu, Ti & Al were examined at the weld region of FSS welds in as-welded and post-weld annealed conditions and presented in figures 3 to 8 respectively. It is observed that the joints fabricated by the addition of 2g Ti (0.7 wt %), 2g Al (2.4wt %) and 3g Cu (0.25 wt %) resulted in fine equiaxed grains compared to the joints made with 1g Ti (0.3wt %), 3g Ti (0.9wt %), 1g Al (1.7wt %), 3g Al (6.2 wt%) , 1g Cu (0.1wt %), 2g Cu (0.18wt %) and filler material addition without Ti, Al and Cu. This is attributed to the formation of fine precipitates such as TiC, Ti(C,N), Al₄C₃, Al₂O₃ and copper precipitates respectively, which are effective in promoting equiaxed grains and to refine the grain size in the fusion zone.

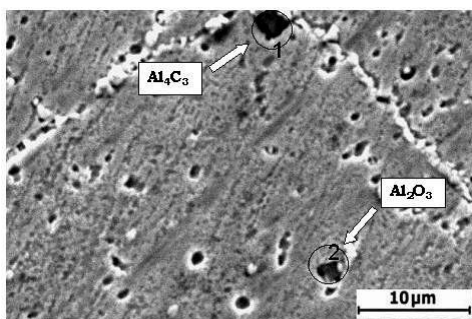


Figure 10: SEM micrograph of precipitates in the fusion zone of FSS welds made by 2g Al (2.4wt %) addition.

The distribution of precipitates in the fusion zone of weldments made by 2g Ti (0.7 wt %) addition was observed using SEM (figure 9) which are believed to be responsible for the grain refinement. The distribution of precipitates (Al_4C_3 , Al_2O_3) in the fusion zone of weldments made by 2g Al (2.4 wt %) addition was observed using SEM (figure10) which are believed to be responsible for the grain refinement.

3.3. Residual Stresses

The X-ray diffraction method is used to measure the residual stresses in the ferritic stainless steel welds. Fusion zone residual stresses of FSS welds in as-welded condition are presented in Table 5. From the results it is observed that the FSS welds made by the addition of 2g Cu (0.18 wt %) exhibit lower value of residual stresses. This can be attributed to the lower yield strength value (312 MPa) of welds, which can be leads to lower value of residual stresses.

Table 5: Residual stresses in the fusion zone of FSS welds

Joint condition (As-welded)	Residual stresses (MPa)	
	Experimental approach	ANSYS (FEA Software)
2g Cu (0.18 wt %) addition	45 ± 10	49
2g Ti (0.7 wt %) addition	100 ± 20	115
2g Al (2.4wt %) addition	80 ± 10	82

3.4. Pitting Corrosion Studies

The pitting potential (E_{pit}) was used as a measure of resistance to pitting. E_{pit} values of base material and FSS welds made by the addition of 2g Ti (0.7wt %), 2g Cu (0.18wt %), 2g Al (2.4wt %) and filler material (ER 430) addition without Cu, Ti & Al in as-weld and post-weld annealed conditions are presented in Table 6.

From the results it is observed that the joints fabricated by the addition of 2g Ti (0.7wt %) in post-weld annealed condition exhibit higher pitting corrosion resistance. Enhanced pitting corrosion resistance corresponding to post-weld annealed condition could be due to the dissolution or refinement of carbide or carbonitride particles and the presence of higher content of retained austenite.

Table 6: Pitting potentials, E_{pit} (mV) of FSS welds and base material

Joint condition		E_{pit} (mV)
2g Ti (0.7 wt %) addition	As-welded	380
	Post-weld annealed	390
2g Cu (0.18 wt %) addition	As-welded	250
	Post-weld annealed	370
2g Al (2.4wt %) addition	As-welded	190
	Post-weld annealed	260
Filler material (ER 430) addition without Cu , Ti &Al	As-welded	203
	Post-weld annealed	230
Base material (AISI 430 FSS)	----	215

4. CONCLUSIONS

The influence of Cu , Ti and Al addition in the range from 1g Cu (0.1wt %) to 3g Cu (0.25 wt %), 1g Ti (0.3 wt%) to 3g Ti (0.9 wt%) , 1g Al (1.7 wt%) to 3g Al (6.2 wt%) and filler material (ER 430) addition without Cu , Ti &Al on mechanical properties, residual stresses and corrosion behaviour of AISI 430 ferritic stainless steel welds were analyzed in detail and the following conclusions are derived.

1. The ferritic stainless steel joints fabricated by the addition of 2g Ti (0.7 wt %) in post-weld annealed condition resulted in better tensile properties (ultimate tensile strength, yield strength and elongation %) compared to all other joints. This is due to the fine grain microstructure and also formation of precipitates such as TiC and Ti (C,N) which are believed to be responsible for grain refinement in the weld zone.
2. There is a marginal improvement in the ductility of ferritic stainless steel weldments by the addition of 2g Cu (0.18 wt %) in post-weld annealed condition compared to all other joints and base metal. This is attributed to the formation of fine dimples in the weld zone of the ferritic stainless steel joints.
3. The FSS welds made by the addition of 3g Cu (0.25wt %) in as-weld condition resulted in increased hardness. This could be due to the precipitation hardening effect of copper.

4. The FSS welds made by the addition of 2g Cu (0.18wt %) in as-weld condition exhibit lower value of residual stresses. This could be due to the lower yield strength of weldments.
5. Post-weld annealed FSS welds made by the addition of 2g Ti (0.7 wt %) showed relatively better pitting corrosion resistance. This is due to the dissolution or refinement of carbide or carbonitride particles and the presence of higher content of retained austenite.

5. ACKNOWLEDGEMENTS

The authors would like to thank the authorities of Defence Metallurgical Research Laboratory (DMRL), Hyderabad, India and NIT, Warangal for providing the facilities to carry out this research work.

REFERENCES

1. E.Folkhard, *Welding metallurgy of stainless steel*, Springer Verlag, New York, 1984: pp.172-178.
2. D.Kotecti, *Welding stainless steel, Advanced Materials and Processes*, 1999: 5, pp. 41-43.
3. N.Fujita, K.Ohmura, and A.Yamamoto, Changes of microstructures and high temperature properties during high temperature service of Niobium added ferritic stainless steels, *Material Science and Engineering*, 2003: 351A(1-2), pp.272-281.
4. F.B.Pickering, *The metallurgical evolution of stainless steels*, *International Metals Reviews*, 1976: p.1.
5. G.Madhusudhan Reddy, and T.Mohandas, *Welding aspects of ferritic stainless steels*, *Indian Welding Journal*, 1974: 27 (2), p.7.
6. K.E.Dorsch, *Weldability of a new ferritic stainless steel*, *Welding Journal*, 1971: 50 (9), p. 408s.
7. D.H.Kah, and D.W.Dickinson, *Weldability of Ferritic Stainless Steels*, *Welding Journal*, 1981: 60, p. 135.
8. W.S.Brando, *Avoiding Problems when welding AISI 430 Ferritic Stainless Steel*, *Weld International*, 1992: 6, p. 713.
9. J.C.Villafuerte, and H.W.Kerr, *Electromagnetic stirring and grain refinement in stainless steel GTA welds*, *Welding Journal*, 1990: 69(1), pp.1-13.
10. J.C.Villafuerte, E.Pardo, and H.W.Kerr, *The effect of alloy composition and welding conditions on columnar-equiaxed transitions in ferritic stainless steel gas tungsten arc welds*, *Metallurgy Transactions*, 1990: 21A, pp. 2009 -2019.
11. G.Madhusudhan Reddy, and T.Mohandas, *Effect of frequency of pulsing in gas tungsten arc welding on the microstructure and mechanical properties of ferritic stainless steel welds*, *Symposium on Joining of Materials*, WRI, Tiruchirapalli. 1996: p.105.
12. G.Madhusudhan Reddy, T.Mohandas, *Explorive studies on grain refinement of ferritic stainless steel welds*, *Journal of Material Science Letters*, 2001: 20, p. 721.
13. H.H.Uhlig, *Corrosion and corrosion control*. 2nd. ed. Wiley, New York, p. 1971.
14. B.Pollard, *Ductility of ferritic stainless steel weld metal*, *Welding Journal Supplement*, 1972: 51(4), pp. 222s - 230s.
15. *American Society for Testing of Materials, Annual Book of ASTM Standards*. Philadelphia, PA, 2004.
16. T.Mohandas, G.Madhusudhan Reddy, and MD Naveed, *A comparative evaluation of gas tungsten and shielded metal arc welds of a ferritic stainless steel*, *Journal of Materials Processing Technology*, 1999: 94, pp.133-140.

AN EXPERIMENTAL STUDY ON AMORPHOUS $\text{Fe}_{73.5}\text{Cu}_1\text{Nb}_3\text{Si}_{16.5}\text{B}_6$ and $\text{Fe}_{68.8}\text{Cu}_{0.5}\text{Nb}_{2.6}\text{Si}_{18.6}\text{B}_{9.5}$ ALLOYS

M.D.V. Srilalitha, B. Bhanu Prasad and A.R. Subrahmanyam
M.V.S.R. Engineering College, Nadargul, Hyderabad.

Abstract: The crystallization of amorphous $\text{Fe}_{73.5}\text{Cu}_1\text{Nb}_3\text{Si}_{16.5}\text{B}_6$ and $\text{Fe}_{68.8}\text{Cu}_{0.5}\text{Nb}_{2.6}\text{Si}_{18.6}\text{B}_{9.5}$ alloys have been studied by DSC, XRD, SEM and EDS. DSC of the samples showed two peaks indicating two step crystallization. XRD on the annealed samples showed a single peak showing the presence of a primary crystalline phase $\alpha\text{-Fe}$. The sharpness of the peak increases and grain size increases with increasing annealing temperature. Scanning Electron Microscope (SEM) and Electron Dispersive Spectroscopy (EDS) showed the structure of a completely crystallized sample. The comparative studies reveal that the primary phases change from $\alpha\text{-Fe(Si)}$ to $\text{Fe}_3\text{Si (DO}_3\text{)}$ on increasing the Si content.

Keywords: crystallization, amorphous alloy, annealing temperature, scanning electron microscopy, X-ray diffraction, differential scanning calorimetry

Address all correspondence to: bbpproofphys56@gmail.com

1. INTRODUCTION

Nanocrystalline alloys exhibiting superior soft magnetic behavior with the composition known as FINEMET. They have attracted much interest because of their excellent soft magnetic properties. These properties include very high saturation magnetization ($\sim 1.3\text{T}$), low coercivity H_c ($\sim 0.5\text{Am}^{-1}$), low saturation magnetostriction ($\sim 2 \times 10^{-6}$) and high effective permeability μ ($\sim 10^5$). Fe-based Nanocrystalline alloys are used in several commercial applications including power devices, power electronics, telecommunications, information handling and magnetic sensors. They are also indispensable in many applications in magnetic parts and devices such as inductors, low and high energy frequency transformers, motors, generators and sensors [1,2]. Recently, downsizing and energy saving have been required for electrical machinery and apparatus from an environmental stand point. Accordingly the demand of high B_s of the conventional Fe-based nanocrystalline alloys is at most 1.7 T, because they contain non magnetic elements, from 2 to 7 atomic % of Nb. The substitution of Cu for Fe plays an important role for nanocrystalline structure and excellent soft magnetic properties. In the present work, the crystallization of amorphous $\text{Fe}_{73.5}\text{Cu}_1\text{Nb}_3\text{Si}_{16.5}\text{B}_6$ and $\text{Fe}_{68.8}\text{Cu}_{0.5}\text{Nb}_{2.6}\text{Si}_{18.6}\text{B}_{9.5}$ alloys is discussed using DSC, XRD, SEM, EDS. A comparison is made with the results of other published papers.

2. MATERIALS AND METHODS

Amorphous ribbons of $\text{Fe}_{73.5}\text{Cu}_1\text{Nb}_3\text{Si}_{16.5}\text{B}_6$ and $\text{Fe}_{68.8}\text{Cu}_{0.5}\text{Nb}_{2.6}\text{Si}_{18.6}\text{B}_{9.5}$ alloys, having thickness of about $30\mu\text{m}$ and width of about 5mm produced by single roller melt spinning were procured from our other group of Researchers. Samples of size $7\text{mm} \times 7\text{mm}$ were cut and heat treated at 100°C , 200°C , 400°C , 569°C and 709°C for one hour. The thermal behavior of the alloy was investigated by high temperature differential scanning calorimetry (DSC) conducted at a heating rate of $20^\circ\text{C}/\text{min}$. XRD patterns of the as-cast and heat-treated samples were taken for the identification of crystalline phases. SEM micrographs were taken for as-cast and heated samples at various resolutions. EDS studies were also done to verify the composition of the materials for as-cast and heated samples.

3. RESULTS AND DISCUSSION

To investigate the thermal behavior of amorphous $\text{Fe}_{68.8}\text{Cu}_{0.5}\text{Nb}_{2.6}\text{Si}_{18.6}\text{B}_{9.5}$ alloy, high temperature DSC was conducted at a heating rate of $20^\circ\text{C}/\text{min}$ and the plot is given in the Figure 1.

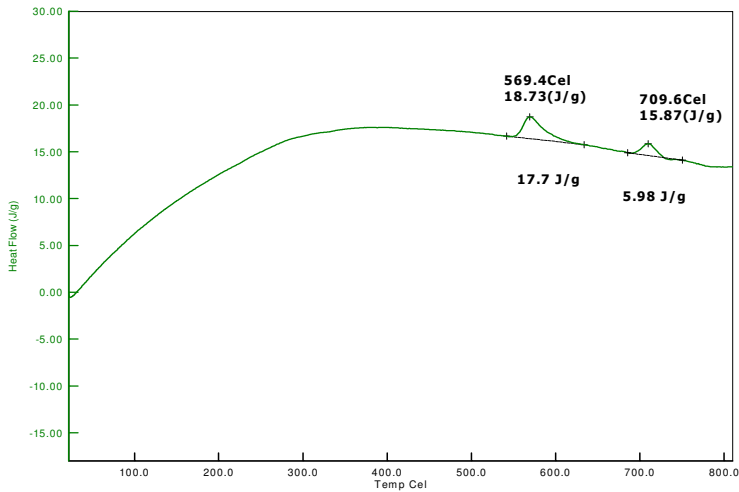


Figure 1: DSC curve of $\text{Fe}_{68.8}\text{Cu}_{0.5}\text{Nb}_{2.6}\text{Si}_{18.6}\text{B}_{9.5}$ alloy at a heating rate of $20^\circ\text{C}/\text{min}$.

Figure 1 shows two peaks, first peak at 569.4°C (842.4 K) and second peak at 709.6°C (982.6 K). Thus, it reveals that the alloy undergoes two stage crystallization reactions at 569.4°C and 709°C . This gives wide temperature interval of 140.2°C between two crystallization stages.

Observation of two step crystallization is more common in metallic glasses contained more than three elements than in those containing less components. The first peak in the present case arises due to (1). Structural relaxation occurring with a broad range of relaxation times due to a variety of atomic rearrangements and (2). Formation of

intermediate metastable phases. The second peak arises due to crystallization as in glass which is a defined nucleation and growth reaction. Broadening also occurs due to kinetic reasons as the kinetics involving structural processes slows down due to the disappearance of free volume during relaxation processes. Samples were heat treated at various temperatures for one hour to investigate the crystallization process. Thus, Figure 2 shows XRD patterns for the as received and heat treated samples. The XRD pattern of as-cast alloy shown in Figure 2 reveals the amorphous nature of the sample. The XRD pattern of the sample annealed at 200°C and 400°C for one hour indicates slightly a different behaviour but still can be attributed with no major changes in the amorphous nature. It refers that the crystallization has been not yet started at those temperatures. Sample heat-treated at 569°C reveals a peak in the XRD pattern indicating the primary crystallization. We also analysed that the phases obtained at 569°C are α -Fe and Fe₃Si. The formation of Fe₃Si phase during annealing is attributed to the presence of Nb clusters that act as nucleation sites due to strong attractive interaction between Si and Nb atoms. The sample heat-treated at 709°C shows a sharp peak (Figure 2), almost in the same position observed for the sample heat-treated at 569°C. The increase in the intensity of the peak and decrease in the broadening indicates enhancement in the density and size of Fe₃Si phase. The crystallite size of Fe₃Si particles was estimated by X-ray peak using Scherrer equation.

Thus,

$$D = \frac{0.94\lambda}{\cos\theta FWHM} \quad (1)$$

Where λ is the wavelength, θ is the glancing angle and FWHM is the Full-width at half maximum of reflection.

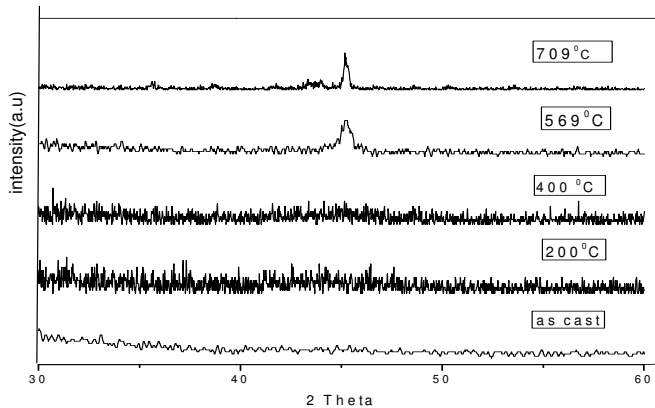


Figure 2: X-Ray diffraction pattern (XRD) of the as received and heat treated samples.

The crystallite size of the annealed sample at 560°C is about 18 nm. And the crystallite size of the annealed sample at 709°C is about 43

nm. Hence, the sharpness of the peak increased and grain size is also increased with increasing annealing temperature. A Scanning Electron Microscopy (SEM) of the sample was taken at room temperature before and after heating and at different resolutions where Figure 3 and Figure 4 show patterns for a particular resolution. Figure 3 shows the amorphous structure of the as cast sample whereas Figure 4 shows the pattern of the crystallized sample. As a supportive work, Electron Dispersive Spectroscopy (EDS) patterns for the as-cast and crystallized sample are recorded and are shown in Figure 5(a) & Figure 5(b) and Figure 6(a) & Figure 6(b), respectively. Before heating, the sample is amorphous as shown by the SEM photo of Figure 3 and EDS photo of Figure 5(a). For the sample which is heated to 1000°C and cooled, the SEM photo shown in Fig 4 and EDS photo shown in Fig 6(a) indicate the crystallization of the sample. Figure 5(b) shows the EDS spectrum of as received (before heating) sample. Fig 6(b) shows the EDS spectrum of the crystallized (heated to 1000°C and cooled) sample showing additional peaks representing the crystalline phases.

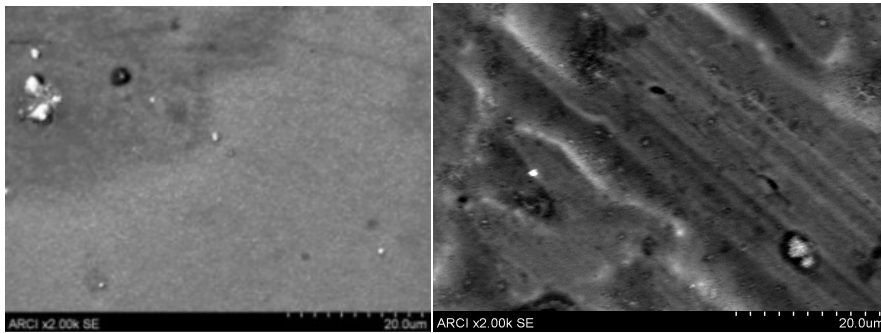


Figure 3: SEM photo before heating Figure 4: SEM photo after heating

Evidence for new crystalline phases formed during early stages of crystallization of amorphous FeCuNbSiB alloys is also reported [3]. It is observed that the size of the α -Fe(Si) solid solution increases with the annealing temperature and the recrystallization behavior depends on the Si and B contents [4].

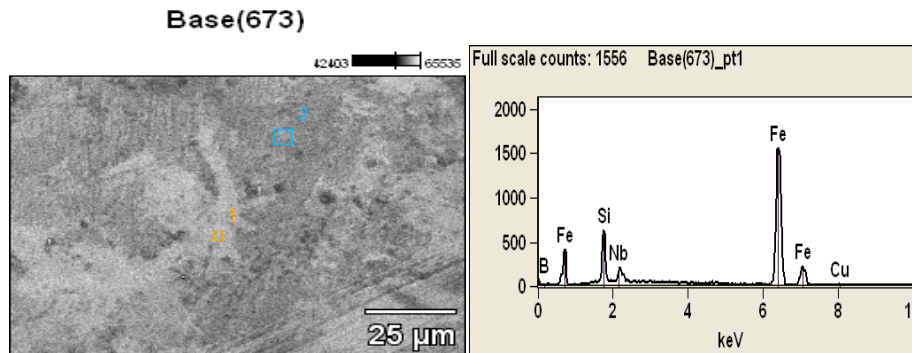


Figure 5: EDS (a) photo before heating (b) spectrum before heating

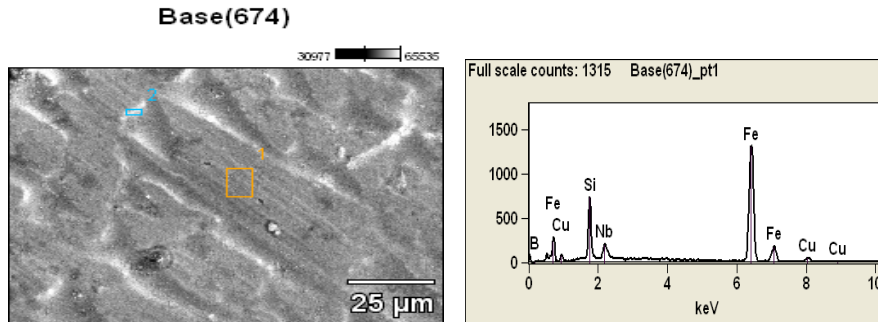


Figure 6: EDS (a) photo after heating (b) spectrum after heating

It is reported that XRD spectra of the as spun ribbons of $\text{Fe}_{77.3}\text{Cu}_{0.8}\text{Nb}_{3.3}\text{Si}_{11.2}\text{B}_{7.2}$ (FIN-1), $\text{Fe}_{73.2}\text{Cu}_{0.9}\text{Nb}_{2.7}\text{Si}_{13.7}\text{B}_{9.5}$ (FIN-2) and $\text{Fe}_{68.8}\text{Cu}_{0.5}\text{Nb}_{2.6}\text{Si}_{18.6}\text{B}_{9.5}$ (FIN-3) alloys revealed a diffused intensity pattern, characteristic of amorphous phase. DSC thermograms of the melt spun FIN-1, FIN-2 and FIN-3 alloys, at a heating rate of 20 K/min make it clear that the temperature of onset of crystallization (T_x) for FIN-1 alloy is around 515°C (788 K) whereas FIN-2 and FIN-3 crystallize at a higher temperature of around 544°C (817 K). XRD patterns of FIN-1 and FIN-2 samples heat treated at 570°C (843 K) for 60 min. It is interesting to note that heat treated samples of FIN-1 show the evolution of $\alpha\text{-Fe}(\text{Si})$ phase (bcc) whereas the primary phase for FIN-2 sample is indexed to ordered Fe_3Si phase (DO_3). The featureless contrast in microstructure and diffused rings in SAD pattern confirms the presence of amorphous phase in the as quenched samples. One observes very fine clusters of size less than 3 nm; these can be frozen in nuclei during rapid solidification. Typical TEM micrograph (bright field) of the sample heat treated at 525°C (798 K). The ring pattern in SAD (inset) corresponds to Fe_3Si phase. By increasing the heat treatment temperature the fraction of nanocrystalline grains increases at the expense of amorphous phase. No amorphous phase is left in the sample heat treated at 600°C (873 K). The results indicate that on annealing, $\alpha\text{-Fe}(\text{Si})$ nanocrystalline phase is formed in FIN-1 alloy (11% Si) whereas ordered $\text{DO}_3\text{-Fe}_3\text{Si}$ phase is observed in the other alloys. [4]. The soft magnetic properties of FINEMET alloys are significantly improved due to the particles of nanocrystalline $\alpha\text{-Fe}(\text{Si})$ dispersed in a residual amorphous material. In these alloys Copper(Cu) promotes the nucleation of the bcc grains, while Niobium(Nb) hinders their growth and at the same time inhibits the formation of boride compounds. It was proposed that Cu clustering occurs prior to the onset of primary crystallization reaction, which enhances the nucleation rate of $\alpha\text{-Fe}$ grains, and Nb helps to restrict crystallization as it hinders the grain growth due to its higher thermal stability. Simultaneously, Cu and Nb produces two stage crystallization in the alloy after annealing. The temperature interval between the crystallization stages become very wide and nanocrystalline structure

appears during the first stage of crystallization. As a result a single phase of α -Fe responsible for good soft magnetic properties, exists in a much wider range of temperature. It is reported that without Nb addition, the refinement of α -Fe(Si) due to the Cu addition in as-cast ribbons is limited. It also suggests that Nb addition plays a role in reducing the grain size of α -Fe(Si) in the as-cast ribbons. It has been found that the grain sizes of α -Fe(Si) are about 10–12 nm for Fe_{73.5}Cu₁Nb₃Si_{13.5}B₉ ribbons annealed at 550°C for 1 h) which are even smaller than those for Fe_{77.5-x}Cu_xNb₃Si_{13.5}B₉ as-cast ribbons [5].

4. CONCLUSIONS

Two peaks were observed in DSC at a heating rate of 20°C/min, indicating two step crystallization in the sample. From XRD data, the as-cast sample has the characteristic of amorphous nature and a single peak observed in annealed samples at higher temperatures, may indicating the presence of a crystalline phase α -Fe. It is also observed that as the annealing temperature increases the width of the crystallization peak decreases and becomes narrow. It is also observed that the grain size increases with increase in annealing temperature. SEM and EDS photos confirmed the complete crystallization of the heated samples. Also, the primary crystallization of amorphous Fe–Si–B–Nb–Cu alloy yields α -Fe(Si) phase at a Si content of 11–12 at% and Fe₃Si phase at higher Si contents.

5. ACKNOWLEDGEMENTS

The Authors would like to thank Dr. Akhtar and Dr. Mujumdar for providing the samples. The authors would also like to thank the Management, Principal and Head of Sciences & Humanities of M.V.S.R. Engineering College for continuous encouragement and support in completing the work.

6. REFERENCES

1. W. Lu, L. Yang, B. Yan, W. Huang, B. Lu, Nanocrystalline Fe₈₄Nb₇B₉ alloys prepared by mechanical alloying and ultra high-pressure consolidation, *Journal of alloys and compounds*, 2006: 413, pp. 85-89.
2. J.J Sunol, A. Gonzalez, J. Saurina, L.I. Escoda, P. Bruna, Thermal and Structural characterization of Fe-Nb-B alloys prepared by mechanical alloying, *Material Science and Engineering* 2004: A 375-377, pp. 874-880.
3. G.A. Basheed, S. Sarkar and S.N. Kaul, Evidence for new crystalline phases formed during early stages of crystallization of amorphous FeCuNbSiB alloys, *Journal of Physics: Condensed Matter*, 2006: 18, pp. 6607-6620.
4. B. Majumdar and D. Akhtar, Structure and coersovity of nanocrystalline Fe-Si-B-Nb-Cu alloys, *Bulletin of Materials Science*, 2005: 28, pp. 395-399.
5. B. Hernando, P. Gorria, M.L. Sanchez, V.M. Prida and
6. G.V. Kurlyyandskaya, *Encyclopedia of Nanoscience and Nanotechnology*, Edited by H.S. Nalwa, 2003, Volume X, pp.1-19.

STUDY OF WELDING ECONOMY AND IMPROVE PRODUCTIVITY OF (2205) DUPLEX STAINLESS STEEL MATERIAL

^aA. Balaram Naik and A.Chennakesava Reddy^b

^aAssistant Professor, Mechanical Engineering Department, JNTUH College of Engineering Hyderabad, Telangana, India,

^bProfessor, Mechanical Engineering Department, JNTUH College of Engineering Hyderabad, Telangana.

Abstract: Welding input parameters and skill of welder plays a very important role in determining the quality of a weld joint. Duplex stainless steels (DSS) are two-phase alloys consisting of approximately equal proportions of 50 % ferrite (δ) and 50% austenite (γ) phases. The welding DSS is more often referred to as a skill based activity when compared to scientific activity and it is an interdisciplinary subject with convergence of different stream of basic science like physics and chemistry in addition to engineering subjects like mechanical, electrical, metallurgy and chemical. This study deals with economy of welding on DSS material, which helps the industries to reduced input cost and improve profits. To improve the productivity and quality of weld, the welding process should follow the best terminologies. It also depends upon the usage of essential welding parameters like, electrode diameter, wire diameter, current, voltage, shield gas, arc time, polarity, penetration, deposition rate and their effect on weld metal. This paper presents a comprehensive literature of optimum methods in the area of welding. This review was classified according to the major process parameters for different welding processes on Duplex Stainless Steel. Additionally few tips will enlighten the ways to improve the productivity and quality of weld.

Keywords: duplex stainless steel, welding economy, productivity.

Address all correspondence to: ballujntuh@gmail.com

1. INTRODUCTION

Duplex stainless steels are characterized by well controlled ferrite/austenite microstructure and are well known for their excellent corrosion resistance and higher strength compared with common austenitic stainless steels. The problems related to duplex stainless steels (DSS) are mostly associated with the heat-affected zone (HAZ) and not with the weld metal. The HAZ problems are not hot cracking but loss of corrosion resistance and toughness. The welding characteristics of duplex stainless steels are much more sensitive to minor variations in chemistry or processing than austenitic stainless steels. No amount of procedure is effectively qualified if the material is not thoroughly clean before welding. Duplex stainless steel is a common structural

material in the oil and gas industries, and has special application in chemical, wastewater and marine engineering fields as well. The phase balance of the weld metal is critical to maintain the original chemical and physical properties of duplex stainless steel. The welding techniques that control the ferrite and austenite content of the weld metal are very important, according to Tsann-Shyi Chern [1]. The knowledge, the capabilities, the attitude, the focus on objectives, the effectiveness, the dedication, the togetherness or team work and the application of their minds towards attaining the goals of the organization decides the effective utilization of resources which results in business excellence. An organization can earn more profit only when it can keep the cost lesser than the market price. In the competitive environment the companies are in a fix to accept the price offered by the market. The buyer's market exposes the organizations to intense competition. When, it is happening in the opened up economy, the competition becomes more severe as it comes from all corners of the globe, especially from the advanced countries. Hence, the focus should be on productivity rather than mere production. This has been reported in AWS CWS manual [2]. The advantages of productivity are not only restricted to the boundaries of the organization but also extended to the development of the whole nation. Improved productivity of DSS material leads to the improved quality, price reduction, more revenue and standard of living.

By Omya Hassan [3] in comparison to austenitic stainless steels, precipitation of sigma phase in 2205 Duplex stainless steels (DSS) occurs, within the ferrite phase at shorter time, at higher temperatures and with large volume fractions. Table 1 shows the chemical composition of DSS (2205) material.

Table 1: Chemical composition of 2205 duplex stainless steel (DSS)

Element	C	Si	Mn	Ni	Mo	Cr	P	S	Cu	N
2205 DSS (wt %)	0.03	0.36	1.77	5.70	2.258	22.05	0.018	0.015	0.2	0.14

2. WELDING PRODUCTIVITY

Welding is the most widely used material joining process being used in many fabrication industries. Ongoing developments in the field of Duplex stainless steel (DSS) material joining, particularly in welding, the widely used process in manufacturing industries are Shield Metal Arc Welding, Submerged Arc Welding, Tungsten Inert Gas Welding and Metal Inert Gas welding techniques. The development of newer materials and newer applications for exiting materials make the manufacturing industries to change from the traditional methods of production. The cost of DSS welding is especially important when the cost itself is large or when represent a significant proportion of the total cost of a project on contract or when expressed on an annual basis. The following are the operation to be considered to improve productivity for DSS Material:

1. Preparation of DSS material for welding like marking, shearing, cutting, edge preparation, machining, gas cutting.
2. Setting up the components for DSS welding like jigs, fixtures, positioners, manipulators, clamps, cleaning the fusion areas by grinding.
3. Actual welding i.e., dressing the welds, chipping, grinding, machining after welding DSS.
4. Inspection of the welds, Visual, destructive and non-destructive testing.

Table 2: Comparison of welding cost with other costs

S.No.	Type of process	Cost % for processes
1	Preparation	10%
2	Assembly	05%
3	Preheating	05%
4	Welding	59%
5	Dressing	05%
6	PWHT	10%
7	Inspection	05%

Table 2 show the comparison of welding cost with other costs for duplex stainless steel materials.

West Germany and Britain National Productivity Council, 38, Golf Links, New Delhi [4] have reported that the welding is the core operation of the fabrication, then productivity of any fabrication shop is directly affected by the productivity of welding operation. Minimizing the waste component in all the resources involved in welding, which are detailed as follows:

1. Man: The welding supervisor, the designer, the welding engineer, the NDE (Non Destructive Equipment) inspector to a large extent and people from other departments of the organization who deal with welding.
2. Machine: power source, NDE system, clamping, accessories are forming part of this segment.
3. Materials: Base metal, filler metal, The NDE consumables.
4. Methods: The specification, procedure and practices are coming under the methods domain.
5. Money: The cost and outcome of automation, the investments, the working capital.

There are many welding practices like Shielded Metal Arc Welding, Semi automatic and automatic submerged Arc welding, Semi automatic GMAW, GTAW, Electro slag welding etc...But among all these practices the Shielded Metal Arc Welding (SMAW) is one of the most widely employed. The Objectives for effective utilization of the resources:

1. Avoiding over size welds.
2. Rejections and scraps.

3. Minimizing weld time, work effect, motion and delay.

The Objective will affect the following characteristics of DSS weld process:

1. Operation factor, Arc time, Non arc time.
2. Deposition rate, Requirement of welding consumables, fixturing.
3. Mechanization and automation.
4. Improved welding system.
5. Recording and feedback.

Easwaran et.al [5] has proposed a hot wire Gas Tungsten Arc Welding process is the best way to improve the productivity. Lower deposition is one of the limitations of conventional GTAW process. Development of suitable power source for main arc, hot wire power source, wire feeder, torch for hot wire GTAW and most importantly, avoidance of arc deflection due to hot wire has been the focus area of research in GTAW. With increasing application for newer breed of creep strength enhanced ferrite steels and Ni-base alloys for high temperature application, the technology offers the best solution for tube , pipe joints and also in the case of dissimilar weld joints. Shielded gas mixture such as 80 % Argon + 20 % CO₂ is commonly used for GMA welding of carbon and low alloy steels. However, the shielding gases used for Duplex stainless steels differ from those used in GMAW of unalloyed steels as they contain less active gases, such as oxygen and carbon dioxide [6, 7]. After welding stainless steels with particular low carbon contents, the weld metal should not exceed 0.03% of carbon. Special gas mixture will be used to weld DSS Materials for improvement in productivity and quality of weld metal.

2.1 Terminologies

The following are the terminologies and techniques associated for improving Duplex Stainless Steel welding productivity:

1. Weld Metal Volume
2. Deposition rate and Efficiency.
3. Filler metal Consumption.
4. Total Labour time, arc time, Non arc time.
5. Operation factor.
6. Arc time per weldment.

In Welding Engineers Hand Book [8] it was published that the weld metal volume is the amount of filler metal consumed in making welds. The area of cross section of the edge preparation when multiplied by the length would give the volume for which the weld metal has to be deposited.

Deposition Weight: This indicates the weight of weld metal deposited in the intended groove or location for effecting the joint.

Deposited Weight = Specific density of weld metal (ρ) x Deposited weld metal Volume. (1)

From the weld metal weight other welding details like total arcing time, total labour time, filler metal consumption can be arrived.

Deposition rate: The deposition rate is the weight of the weld metal deposited per unit time (gms/min). It depends on the type of the electrode, size of electrode and the current used. The deposition efficiency for various types of processes has show in the table: 3.

Deposition Rate = The amount of filler metal wire/ electrode deposit in one hour. (2)

Deposition Efficiency:

$$\eta = \frac{\text{Weighth of weld Metal Deposited}}{\text{Weight of filler Material Used}} \times 100 \quad (3)$$

Table 3: Deposition Efficiency for various Processes

Deposition Efficiency: η for various Processes		
1	SMAW	55.55%
2	GMAW (wire)	90.97%
3	GMAW (Coated wire)	80.90%
4	SAW	97%

Filler Metal Consumption: It is the weight of filler material required to make the given size of the weld.

Total Labour Time = Total Non-Arc Time + Total Arc Time (4)

$$\text{Total Arc Time} = \frac{\text{Weighth of weld metal deposited}}{\text{Deposition Rate}} \quad (5)$$

Total Non-Arc Time: It is the time for which the welder is not able to do arcing. The following are the unproductive timing has to be reduced.

1. Loading and unloading parts
2. Time between each passes.
3. Alignment and initial equipment setup.
4. Cleaning during welding.
5. Grinding interpass and final.
6. Inspection.
7. Heat treatment when required.

$$\text{Operating Factor} = \frac{\text{Total Arc Time}}{\text{Total Arc Time} + \text{Tatal Non Arc Time}} \quad (6)$$

Every effect should be made to increase the Operation Factor, because it reduces the waste component in time. The welders performance determines the appearance and the quality of the weld. Work should be

planned and positioned to minimize physical strain and ensure maximum comfort and safety. It may be the economy which is to provide the welder with a helper who can set up jobs for him. Every operation the welder has to perform, apart from that the actual welding reduces the arc time, and it naturally reduces the operation factor. It is not unusual for a welder to spend 50 % of his time in setting up a job. If he is provided with a helper and an additional jig, his production is doubled and at the same time the cost is reduced simultaneously.

Time standards for manual arc welding [9] have reported that the Arc time per weldment is the amount of time the welding arc is maintained while making a specific length of weld. Developments in welding technology and automation help the industries to improve its productivity and economy. Recent developments in design and operation have put to lot of challenges in front of welding engineers which has led to many innovations such as introducing of new terminology or variants of processes, new techniques, mechanization and several others. The equipment used while welding a high thickness welds, adoption of narrow gap Submerged Arc Welding technique provides great advantage in terms of reduction in welding consumables and cycle time. Dileep Kulkarni et al [10] have presented the use of industrial robotic welding in heavy industry for mass production e.g. automobile sector. However, robotic welding can be applied in ship building as well as in pressure vessel manufacture. Apart from panel welding applications at shipyard, robotic welding is been used for overlaying critical components of pressure vessels

2.2 Avoiding Over Size DSS Welds

The over sized welds leads to more arc time, increased filler material addition, more heat input, more power consumption and affects the productivity as well as quality of the DSS weld by increasing the residual stress in the weldment. The increased weld size will result in more reinforcement which becomes a point for stress concentration and may lead to failure of the DSS joint [11, 12]. The following factor s will be responsible for over sized welds:

1. The fit up of the job, if it is done with mismatches, large root gap will require more deposition and result in over sized welds.
2. The welder deposits welds large than the size required by the design specifications (as indicated in the drawing), by following improper welding parameters.
3. The designer fails to specify the weld sizes based on current load and service conditions for the material being used.

2.3 Avoiding or Minimizing Rework, Rejects and Scraps

The major problems that are faced by the welding engineer not only affects the arcing time but also the non arcing time, offset the production plan, increase the cycle time and also affects the quality of the products. The following are the essential welding variables for duplex stainless steel.

1. Amperage or Wire Feed Speed
2. Arc Voltage
3. Travel speed
4. Electrode Extension.
5. Transverse Gun Angle.
6. Travel Angle.
7. Electrode Position.
8. Polarity (Inductance in the case of GMAW).

Arc voltage and Wire Feed Speed are the two variables which must always be in balance. From weld quality standpoint, an arc voltage that supports given amperage is need to avoid welding defects such as undercut and cold lap. Travel speed is determined by the weld size and the parameters like voltage and current. If the speed is very slow, weld joint will be over sized or it will have rollover resulting in cold lap. If the travel speed is too fast, the weld will be undersized and defective.

Electrode Extension is also known as contact tube to work distance. This applies to arc-welding processes with continuous wire feed and refers to the portion of the contact tube-to—work-distance between the end of contact tip and welding arc. Long extension results in reduction in temperature of base metal and reduces penetration to an unacceptable level or cause lack of fusion. In too short electrode extension excessive heat for the wire feed speed will go into base metal and result in excessive melting and even burn through the base metal. Transverse Gun Angle is an angle with the work piece in a plane perpendicular to the direction of travel and this is know as transverse gun angle. It helps the welder to control the bead shape, fillet weld leg size and weld bead. Improper transverse angle control lead to defective weld condition requires rework. Travel angle is the angle formed by the wire with the work piece in a plane parallel to the direction of travel. Table 4 indicates the effects push and pull angles.

Table 4: Effect of Drag / Push Angles

Feature	Push	Drag
Travel speed	Very fast	Very slow
Spatter	More	Less
Penetration	Slightly less	Slightly more
Bead Shape	Flatter	More Convex

Reports of the welding studies by BHEL [13] has presented that the welder should have control over electrode position to prevent roll-over, undercut, slag entrapment, incomplete fusion and incomplete penetration. Direct current Electrode Negative Polarity and Direct current Electrode Positive polarity are used for Direct Current (DC) welding. The change in polarity will have affect in melting, deposition rate, arc starting, arc blow sensitivity as well as penetration. The following factors could be affecting the goal of avoiding or minimizing reworks, rejects and scraps.

1. Lack of Workmanship standards and training.
2. Lack of proper shop surveillance by welders and supervisor.
3. Lack of understanding by welder and supervisors of the essential welding variables and their effects on weld quality.

2.4 Minimizing Arc Time per Weldment

To achieve the maximum deposition rate, correct ratio of wire, feed rate the amperage and arc time per weldment should be maintained. By reducing the arc time per weldment, more length of weld can be made in the available arc time. The Following tables indicate the typical benefits of using the higher range of amperage and voltage for enhanced deposition rate. Tables 5 and 6 indicate the typical benefits of using the higher range of amperage and voltage for enhanced deposition rate.

Table 5: Low hydrogen, iron power electrodes (E 7018)

Electrode Diameter	Amperage	Voltage	Deposition Rate (Kg/hr)
2.5 mm	70-110	20-30	0.60-0.80
3.15 mm	110-140	20-30	1.05-1.23
4 mm	140-200	20-30	1.25-1.95
5 mm	200-300	20-30	2.18-2.54

Table 6: Spray transfer mode 98 % ar + 20 % co₂(ER 70 SX).

Wire Diameter	Amperage	Wire Feed Per mint	Voltage	Deposition Rate in Kg/hr.
0.8 mm	180-230 A	10 m-14 m	25-27	2.87-3.63
1.2 mm	260-340 A	8 m-13 m	25-30	3.63-5.90
1.6 mm	290-400 A	4 m- 7m	26-36	4.00-6.36

Kuang-Hung and Tseng [14] have investigated that to improve high quality welds and stable weld arc, the activated TIG process requires large diameter electrodes to support a given level of the weld current. TIG welding with SiO₂ and MoO₃ fluxes achieves an increase in weld depth and a decrease in bead width, respectively. The activated TIG welding can increase the arc voltage, the amount of heat input per unit length in a weld is also increased, and therefore the delta-ferrite content in weld metal will be increased. The addition of oxide flux does not significantly affect the hardness of type 316L stainless steel activated TIG weld metal.

2.5 Minimizing Work Efforts

Using of welding fixtures, which will help the welder to hold the job firmly and guide him to carry out the work with ease. Welding position decides the easiness of deposition of weld metal. A deposition which is made in down hand position will have better quality, bead shape and requires lesser effort from the welder. The same if it is carried out in overhead position it will affect not only the deposition rate, but also the

quality, work effort, etc...The size of molten weld pool dictates the current that can be used for position welding [15]. Thus, while the maximum current which can be used in down hand welding position is limited generally only by the material and its thickness, the maximum current usable for positional welding is severely limited by the effect of gravity on the molten pool. An authoritative welding hand book says that if the welding costs are taken as 100 % in the down hand position, they rise to 165 % in the horizontal to 294% in the overhead position.

Sun and Kuo [16] have presented a dual-torch arc welding technique (plasma torch followed by a Gas Tungsten Arc torch) to improve productivity of Duplex stainless steel. It was found that by using dual-torch technique, undercut produced by keyhole plasma welding can be abated by the GTA arc remelting, thus produce a better weld profile. The corrosion rate increase with increasing torch pitch and or decreasing GTA arc remelting current. By adjusting the torch pitch, modification of weld microstructure may be realized. The present study demonstrated the potential of using dual torch technique to overcome undercut problem in keyhole plasma welds and to improve weldability and productivity of duplex stainless steel.

2.6 Minimizing Motion and Delays

Focusing on eliminating the unnecessary activities, excess motion, repeated movements, delay/waiting time etc...will enable better work centre planning and control. The use of jigs and fixtures or positioners enables the job to be done in down hand position welding. In addition, down hand welding with the use of manipulators or positioners calls for less skill on the part of the operator. It is also less fatiguing. Welding Hand Book-Published by the AWS [17] have presented that the Jig and Fixture also helps in minimizing distortion and the consequent rework. Working towards achieving the above simple objectives will results in enhanced productivity without making any change in the welding process, equipment, consumables, etc...But with little modification in the welding practices and by training of welders the required quality can be achieved.

2.7 Waste and Waste Reduction

In any ideal system the output is equal to input, but in actual conditions, $\text{Output} = \text{Input} - \text{Waste}$. It will be clear that to match the output to the input; the waste component should be reduced. Therefore to improve the productivity, one should look in to the waste component, which affects the output. A focused approach on waste minimization or elimination will result in improved output and or reduced input. Both ways, it will help us to enhance the productivity.

3. IMPROVING WELD PRODUCTIVITY

Young et al. [18] has presented that the α/γ ratio in the Duplex Stainless Steel fusion zone was drastically increased after laser welding .Preheating before welding DSS or changing the plasma-assisted gas

from He to N₂, especially for later, could raise the γ content of the fusion zone. Impact toughness of the fusion zone increased with rising γ content. Meanwhile, the effect of N addition during laser welding also improves the welds ability to resist impact fracture. The Notched Tensile Test of the specimen in air increases with increasing content in the DSS fusion zone. As a whole, all the specimens were susceptible to gaseous hydrogen embrittlement but to different degree. Hydrogen embrittlement susceptibility is more obvious for the specimens containing a greater amount of α phase. The following illustration will be more helpful to understand the way to improve the productivity.

3.1 Weld Design

The designer should design the joint so that the minimum amount of weld metal is being deposited. An Unnecessary increase in the fillet size from 6 mm to 8 mm can cause a consequent increase in the labour costs. The joint can be kept as few as possible by using standard rolled sections. Weld design is based upon this principal of minimum weld metal that the joints of higher thickness are designed as 'K' welds, 'j' welds, etc. Design the weld sizes depending upon the load the weld metal is to carry. There may be many parts in the machines that are lightly loaded or not loaded at all and it may be wasteful to deposit full strength welds on these parts. Tables 7 and 8 show the weld metal cost for different types of electrodes.

Table 7: weld metal cost for different types of electrodes-a typical comparison

S.No	Electrode Type	Metal Recovery Rate	Price for 1000 (Rs)	No for 1000 pieces Kg	Cost of weld metal (Rs/kg)
1	General purpose Rutile	90	1112	35.3	31.50
2	Low Hydrogen Iron Power	115	1774	45.0	39.42
3	Rutile Iron power	140	2033	54.9	37.03
4	Rutle Iron power	210	2909	82.3	35.35
All electrodes are 4 mm diameter and 450 mm long stub thrown away is 50 mm.					

3.2 Selection of Right Type of Electrode

The welding Institute, Cambridge [19] has reported that The ratio of the weight of deposited metal to the net weight of the electrodes consumed is known as Metal Recovery (MR). To achieve maximum welding productivity or in other words to reduce welding costs. It is not sufficient to judge the economics of an electrode merely from the price list. The Iron Powder Electrodes having higher Deposition Efficiency should be used. These electrodes contain an appreciable quality of

metal power in the coating, such that the resulting deposit is more than that of the weights of the core wire melted.

Table 8: weld metal cost for different types of electrodes-a typical comparison

S.No	Electrode	Melting time per electrode Mins	Matl.cost of weld metal Rs/Kg	Labour cost of weld metal Rs/Kg	Total cost of weld Metal Rs/Kg
1	General purpose Rutile	1.90	31.50	8.24	39.74
2	Low Hydrogen Iron Power	1.70	39.42	5.80	45.22
3	Rutile Iron Power	1.85	37.03	5.16	42.19
4	Rutile Iron Power	2.15	35.35	4.20	39.55

The labour cost per Kg of weld metal are calculated from the melting time per electrode, arc time required to deposit 1 Kg of metal, weld time factor of arc time factor LOC's as Rs.4/hour and the arc time factor as 2.4, the costs for the four electrodes have been related and given in the column number 5 of above table. The total cost of weld metal is given in the last column.

Arc Time Factor (or) Weld Time Factor is defined as the ratio of Arc Time to total Welding time. The fact that items number 4, which is the most expensive electrode in the price list, works out most economical may seem astonishing. There are further advantages in using such high deposition efficiency electrodes. Suppose a fabricating shop employs 100 welders each of whom consumes 100 pieces of item number 1 in an 8 hour shift. This means that 353 Kgs of weld metal is deposited in a shift to maintain the production schedule. If the shop changes over to item number 3, only 64 welders would be required to give this output. If it changes over to 4, only 43 welders need be employed. Fewer welders means fewer welding machines, reduced maintenance cost, saving in floor space, fewer welding accessories and a smaller electric load ect. Table 9 show the type of electrode compositions for welding duplex stainless steel material.

3.3 Largest Size of Electrode to Be Used

The diameter of the electrode used has a great bearing, on productivity. The time of fusion of the electrode or the arcing time depends very much on this. Table 10 gives, at rated currents, the deposition rates of the coated electrodes of different diameter.

Table 11 shows that how much time is gained or lost by using large or smaller diameter electrodes. The figure along the diagonal read 1.00.All the figure above the diagonal are more than 1, and all the figure below

the diagonal is less than 1. From 4th column and 4th row, we find the value to be 1.00. The values above this are 1.32, 2.07, 2.22 respectively. This means that instead of 4.00 mm diameter electrode, if we use diameter 3.25 electrode, the time will increase by 32 %. If a 2.5 mm electrode is used instead of 4.00 mm electrode, the time will increase by 107 %. Instead of using 4.00 mm electrode if we use 5.00 mm electrode, the time will be only 71.4% or saving of nearly 30%. A further advantage resulting from changing over to large diameter electrodes from the lower diameter electrode is the reduction in number of times required for changing the electrodes. By reducing the number of change, we can reduce the number of starts or stop and related issues as well as control the total heat input to the weld.

Table 9: Filler metal composition for duplex stainless steel (DSS)

Classification	C	Mn	Si	Cr	Ni	Mo	N	S	P	Cu	N	Al
E 2209-17	0.03	0.8	0.9	22.5	9	3.2	0.15					
E 308L-16	0.03	0.8	0.9	19.8	10.2							
Filler Metal	0.022	1.35	0.28	17	11.52	2.10						0.014
ER 2209	0.009	1.57	0.39	22.25	8.55	3.29		0.001	0.008	0.10	0.10	
ER2594	0.03	0.73		25.9	9.2	4.2	0.22	0.002	0.001	0.54		
AWS E 316L	0.020	1.80	0.07	18.70	11.7	2.70						
ER 2209 Duplex	0.030	1.50	0.90	23	9.50	3.0						
ER 2209 GRD 5.9	0.13	1.75	0.41	22.7	8.7	3.2	0.17	0.002	0.015			
Tech 2209	0.02	1.65	0.52	22.4	8.9	3.3	0.16					
ER 312 AWS A 5.9.	0.11	1.60	0.40	29	9.25	0.15		0.013	0.013			

The balance is Fe

Table 10: Rate of deposition of electrode in different diameters

S.No	Diameter Of Electrode(mm)	Rate of Deposition gm / Average Minute.
1	2.00	11.4
2	2.50	12.2
3	3.25	19.2
4	4.00	25.3
5	5.00	35.5
6	6.30	51.5

Table 11: Arc time and diameter of electrodes

Diameter of the Electrode(mm)	Increase /Decrease in Arcing time with respect to diameter of electrodes)					
	2.00	2.50	3.25	4.00	5.0	6.30
2.00	1.00	1.07	1.69	2.22	3.12	4.50
2.50	0.935	1.00	1.58	2.07	2.92	4.23
3.25	0.590	0.632	1.00	1.32	1.65	1.85
4.00	.0450	0.483	0.756	1.00	1.40	2.04
5.00	0.320	0.342	0.540	0.714	1.00	1.45
6.30	0.22	0.238	0.973	0.490	0.63	1.00

Riad Badji et al. [20] have presented an experimental work that the TIG welding of 2205 duplex stainless using ER 2209 filler metal of 2.5 mm

diameter, interpass temperature 120°C, 15 Voltage, 115 Amperage resulted in a significant variation in the ferrite-austenite balance in the HAZ and fusion zone compared to the base metal. An increase in annealing temperature cause change in the toughness and tensile properties has been observed as a consequence of precipitation phenomena or an increase of ferrite content. The optimal combination of mechanical properties was obtained when precipitation of sigma and the γ -to- δ ferrite transformation are suppressed, i.e., at 1050°C. Table 12 show the number of changes per kg of deposit for a rutile electrode.

Table 12: electrode diameter and electrode changes for making 1 kg of weld [21].

Electrode Size dia (mm)	Electrode Length	No.of Electrode changes per kg.of deposited weld metal
3.15	450	36
4.00	450	24
5.00	450	14
6.30	450	11

Ravichandran et al. [22] have presented that the addition of iron power in electrode coatings can be anything from a few percent up to more than 60 %.In some metal cored wires, iron power can account for up to 80 % of the core material. For coated high efficiency electrodes such as the rutile AWS E 7024,the basic AWS E 7028 and the acidic AWS E 7027,all characterized by the large amount of iron powder in the coating, range of coarse high apparent density powders are used. Among various types of electrodes specified in AWS 5.1 the coated iron power content may vary as show in table 13.

Table 13: type of electrodes specified in AWS 5.1 with the coating iron powder content

AWS 5.1 CLASSIFICATION	MAIN COATING CONSTITUENT	TYPICAL COATING IRON POWER CONTENT, WT %.
E 6010	CELLULOSE	10
E 7014	RUTILE	20-30
E 7024	RUTILE	30-60
E 7018	BASIS COATING	30
E 7028	BASIC COATING	30-60

3.4 Deep Penetration Electrode

The productivity of a deep penetration electrode is derived from the fact that a butt joint can be made in plates upto 12 mm thickness with square edges by depositing one pass on each side. The need for edge preparation is eliminated. Square edges ensure easy and accurate fit-up and root gap. Very little weld metal is required for fill the gap since a large proportion of the welded joint is made-up of the fused parent metal. Also back gauging operation is dispensed with. The type of electrode used in India has an extremely heavy coating which consists mainly of Rutile Iron Power and cellulose. It is made 350 mm long. It can carry very high current: 3.15 mm diameter-170 amp, 4.00 mm

diameter 225 amp, 5.00 mm diameter-300 amp. The penetrating arc lifts-up all the slag inclusions and gives a smooth weld metal with complete fusion.

4. CONCLUSION

The objectives briefed here as well as the typical tips will enlighten the ways to improve productivity. But, one has to remember that productivity is linked to the mind and attitude of people concerned.

1. Achieving the above goals could be accelerated by having a motivated team. A motivated team can make the difference and achieve the results. Therefore, creating a motivated team is the first step towards the journey for enhanced productivity.
2. This paper shows clearly that productivity and quality of DSS weld increase by selecting a right type of electrode and the best type of welding technique with optimal input parameter.
3. The rate of DSS weld metal deposition increase by maintaining optimal arc time and increasing the diameter of electrode. Deep penetration and narrow bead width occurs by connecting Direct Current Electrode Negative (DCEN) Straight polarity, constant current, constant melting rate.
4. The productivity, Economy and quality of weld metal mainly depends upon the skill and commitment of the welders of manual welding techniques.

REFERENCES

1. T.S.Chern, K.H.Tseng, and H.L.Tsai, Study of the characteristics of duplex stainless steel activated tungsten inert gas welds, *Journal of Materials and Design*, Elsevier, 2011: 32, pp:255-263.
2. J.R.Barckhoff and Kenneth, American Welding Society- Certified Welding Supervisor manual for Quality and Productivity Improvement, 2005: pp. 68-70.
3. O.H. Ibrahim, I.S.Ibrahim and T.A.F. Khalifa, Effect of Aging on the Toughness of Austenitic and Duplex Stainless steel Weldments, *Science Direct, Journal of Material Science and Technology*, Elsevier, 2010: 26(9), pp.810-816.
4. G.Narain, *Welding Industry in U.S.A., West Germany and Britain* National Productivity Council, Issue 34 report, 2010: 38, Golf Links, New Delhi.
5. R.Easwaran, A.Raja, G.Ravinchandran, and G.Buvashekarana, *Welding Research in India: Present Status and Future Directions*, Indian Welding Journal, Welding Research Institute, Bharat Heavy Electrical Limited-Tiruchirappalli-620014, India, 1014: pp.18-23.
6. A. Chennakesava Reddy, Studies on the effects of oxidation and its repression in MAG welding process, *International Journal of Advanced Research in Engineering and Technology*, 2012: 03 (01), pp. 48-54.
7. A. Chennakesava Reddy, K. Gokul, P.Mahesh, G.S.Reddy, C.R. Suresh, Effect of shielding gases on the performance of weld bead in MIG welding, 13th National convention of Mechanical Engineers, Conference on Modern Trends in Manufacturing Technology, New Delhi, 6-7th November, 1997, pp. 273-279
8. H. I. Lewenz, *Electric Arc Welding Practice: Hand Book for Welding Engineers and Welders*, Crosby Lock wood & sons Publisher, 2007: pp.78-80.
9. J.S.Colton, *Time standards for Manual Arc Welding*, ME 6222: Manufacturing Processes and System, Georgia Institute of Technology, 2009.

- 10..D. Kulkarni and K.Iyer, Welding in Heavy Industries-An Indian Perspective, Indian Welding Journal. Larsen & Toubro, Powai, Mumbai-400072, India, 2014: pp.14-20.
- 11.Report by J.A.Dates, D.B.Thraporevala Sons and Corporation private Limited,Bombay, 2013.
12. A. Chennakesava Reddy, K Ravaivarma, E. Thirupathi Reddy, A study on the effects of joint and edge preparation to produce cost reduction and distortion free welds, National Welding Seminar, IIT Madras, 07-09 **January2002**, pp. 51-55.
13. Annual Reports of the welding studies done in Boiler plant unit of Bharat Heavy Electricals Limited, Tiruchy, Tamilnadu, India, 2012-2013.
14. Kuang-Hung Tseng, Chih-Yu Hsu, Performance of activated TIG process in austenitic stainless steel welds, Journal of Materials Processing Technology, 2011: 211, pp.503-512.
15. A. Chennakesava Reddy, Fluidity and weld bead characteristics of Al-Si-Cu alloy prepared by MIG welding, International Journal of Manufacturing Science and Engineering, 2010: 01(02), pp. 55-59.
16. Z.Sun, M.Kuo, I.Annergren, and D.Pan, Effect of dual torch technique on duplex stainless steel welds, Journal of Materials Science and Engineering, 2003: 356 A, pp.274-282.
17. R.L.O'Brien, Welding Hand Book-Published by the American Welding Society, 1998: pp.120-125.
18. M.C.Young, S.L.I.Chan, L.W.Tsay, and C.S.Shin, Hydrogen-enhanced cracking of 2205 Duplex Stainless Steel welds, Journal of Materials Chemistry and Physics, ELSEVIER, 2005: 91, pp.21-27.
19. Welding Engineering-Welding Inspection and Training manual, 2013, Published by Welding Research Institute's, Bharat Heavy Electricals Limited, Tiruchirappalli, India, pp.239-242.
20. R.Badji, M.Bouabdallah and B. Bacroix, Phase transformation and mechanical behavior in annealed 2205 duplex stainless steel welds materials characterization, Journal of Material Science and Technology, ELSEVIER, 2008: 59, pp.447-453.
21. P.P.Mc Mohan, The price of welding-Welding and Metal Fabrication, Book of ASTM Standards, 990: 01, pp.140-146.
22. C.P.Ravichandran, A.Raja and T.S.Sekar, The Role of Iron Power Additions in Shielded Metal Arc Welding Electrode Coatings, Journal of the Welding Research Institute, 2012, 33 (4), pp.30-35.

STUDY ON MECHANICAL BEHAVIOUR OF PHENOLIC BASED COMPOSITES WITH AND WITHOUT ZIRCONIUM FILLER

**R. Ramanarayanan^a, C. Hari Venkateswara Rao^b,
A. Panindra^c**

^aACC, Advanced Systems Laboratory, DRDO, Hyderabad -58.

^b SSQAG, ASL, DRDO, Hyderabad-500 058.

^cManipal Institute of Technology, Jaipur

Abstract: Particulate fillers are of considerable interest, not only from an economic viewpoint, but as modifiers especially the physical / mechanical properties of the polymer. A notable advance in the polymer industry has been the use of fiber and particulate fillers as reinforcements in polymer matrix. Over the last few decades, the considerable attention has been devoted towards zirconium filled polymer composites due to its many advantages. These include mainly the improved mechanical and thermal performance. Although there are several reports in the literature which discuss the mechanical behavior of zirconium/polymer composites, however, very limited work has been done on effect of zirconium fillers on mechanical behavior carbon fiber based polymer composites. Against this background, the present research work has been undertaken, with an objective to explore the potential utilization of zirconium filler as a reinforcing material in carbon/phenolic composites and to investigate its effect on the mechanical behavior of the resulting composites. The test laminates were prepared by hand layup process and cured in the autoclave. Four types of test laminates with /without filler were made. Test samples were prepared as per ASTM standards. Results of study showed that the carbon/phenolic composites with zirconium filler exhibited better properties than the carbon/phenolic composites without zirconium filler.

Keywords: carbon, phenolic, autoclave, mechanical properties, hand lay-up technique, zirconium filler.

Address all correspondence to: rrn030857@gmail.com

1. INTRODUCTION

Composites are the pioneers for the future generation in aero space applications. The aerospace or missiles structures are require high strength, light weight and withstand the high temperatures. Phenolic based composites are widely used for thermosetting resins having the better mechanical properties [1].

Phenolic resins are polycondensation products of phenols and aldehydes, in particular phenol and formaldehyde. PAN carbon fabric reinforced phenolic (C-Ph) composites are widely used as thermal protection systems for aerospace applications due to the low thermal conductivity of the rayon based carbon fabric and the high char yielding properties of the phenolic matrix [2].

Many research groups attempted to reduce the weight saving for the aerospace systems. This paper deals with study on mechanical behavior of Phenolic based composites with zirconium filler added and without zirconium filler added [4]. This type of comparative study is not explored so far by any research group. This study aimed to (a) develop a phenolic based composite with zirconium filler and without zirconium filler (b) To study whether enhanced the physical properties and mechanical properties without filler (L₀), 5% filler zirconium added to phenolic composite (L₁), 10% filler zirconium added to phenolic composite (L₂) and 15% filler zirconium added to phenolic composite (L₃). The total comparative study will be explained subsequently.

2. MATERIALS AND METHODS

The following raw materials are used for experimental work:

1. PAN based carbon fabric
2. Phenolic Resin
3. Zirconium powder as a filler

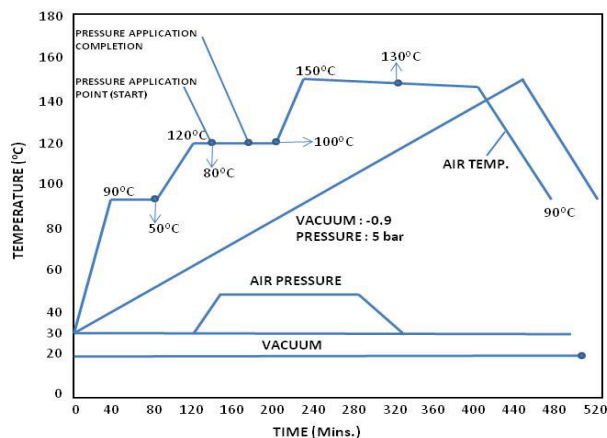


Figure 1: Curing cycle of carbon-phenolic laminates

Four types of test laminates are prepared by hand layup process by using the above said raw materials without zirconium filler and with zirconium filler added as 5%, 10% and 15% to the Phenolic composite. The hand layup composite laminate is prepared by using the mould box. The mould surface is cleaned with solvents such as acetone and release agent like wax or petroleum jelly is applied for easy removal of laminate from the mould. The rayon based carbon fabric cut into required size and laid on the flat surface of the mould with phenolic

resin. The resin is squeezed evenly on the surface by roller and compressed thoroughly with roller. The reinforcing laminates are stacked one above the other to the required thickness of the laminate. The laminates are subject to cured in autoclave by a cycle of temperature Vs time under vacuum and pressure [3]. The graphical representation of cured cycle is shown in figure 1.

Test samples are prepared as per ASTM standard [3]. Specimen subject to as per ASTM D792 standard describes the determination of the specific gravity / relative density. Some more specimen subject to as per ASTM D 2584 standard describe the determination of the ignition loss of cured reinforced resins i.e. resin content and ensured remaining portion is fiber content.

To evaluate the mechanical properties as per ASTM D 2344 determine the short beam strength of high modulus fiber reinforced composite material i.e. inter laminar shear stress (ILSS) at room temperature. ILSS is usually limiting design characteristics because conventional manufacturing techniques do not reveal reinforcing fibers oriented in the thickness direction to sustain load [2]. As per ASTM D 790 standard the flexural properties of laminate are determined by 3-point bend test. Six specimens were tested and average value is considered for flexural strength and the test specimens were examined through visual inspection for failure of fiber and matrix. Finally as per ASTM D 3039 determines the in plane tensile properties of the laminate at room temperature by using INSTRON universal testing machine (UTM), model No.1185 with load cell capacity of 100 KN made by UK. The specimen was loaded between two adjustable grips of UTM [5]. Each test was repeated three times and the average value was taken to calculate the tensile strength of the laminate.

3. RESULTS

The comparative study has been carried out between physical properties and mechanical properties. Physical properties like density, resin content and fiber content were measured. Mechanical properties like inter laminate shear stress (ILSS), flexural strength and tensile strength were measured. The physical properties are achieved by using the above said test samples are given Table 1. The mechanical properties are achieved by using the above said test samples are given Table 2.

Table 1: Physical properties

Sl. No	Test sample	Density	Resin Content	Fiber Content
1	L ₀	1.3640	30.90	69.10
2	L ₁	1.5146	32.51	67.49
3	L ₂	1.6041	35.06	64.94
4	L ₃	1.5529	28.11	71.89

Table 2: Mechanical properties

Sl. No	Test sample	ILSS (MPa)	Flexural Strength (MPa)	Tensile Strength (MPa)
1	L ₀	19.21	330.16	305.49
2	L ₁	25.99	417.18	387.23
3	L ₂	25.81	425.64	421.91
4	L ₃	25.07	405.80	342.62

4. DISCUSSION

In the present research work phenolic composite filled with zirconium filler with varying volume fraction by weight (%) were prepared. Fabrication of reinforcement laminates samples are prepared by hand layup process using mould at room temperature. Several important considerations can be drawn based up on the test results obtained from the experimental test.

The study of results revealed that the phenolic composite with zirconium filler have the better physical (figure 2) as well as mechanical properties (figure 3) as compared with without zirconium filler added to phenolic composite. The test results exhibits the 10% of zirconium filler added to the phenolic composites are enhance the ILSS, flexural strength, tensile strength properties and physical properties like Density and Resin content as compared with other samples.

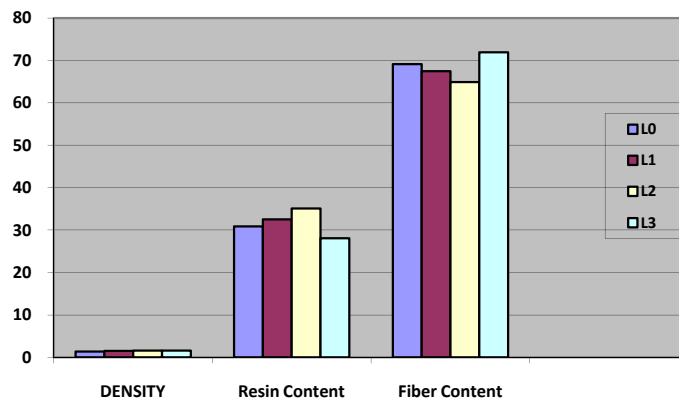


Figure 2: Graphical representations of physical properties

The test results reveals that the reinforcement composite laminate filled by (10% volume) of zirconium filler exhibited maximum tensile strength (421.91 MPa) compared with other filled composite laminates this may be due to good particle dispersion and strong polymer/filler interface adhesion for effective stress transfer. Increase in adhesion of filler materials leads to decrease in tensile strength this may be due to more filler distribution and filler metal dominated in the materials.

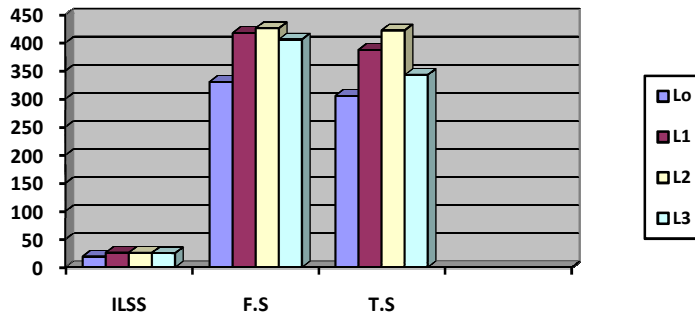


Figure 3: Graphical representations of mechanical properties

The flexural strength results indicated that composite laminates filled with by (10% volume) of zirconium filler exhibited maximum flexural strength (425.64 MPa) compared with other filled composite laminate this may be due to good compatibility between filler and matrix. However, test results shows that increase in addition of filler reduces flexural strength this may be due to that the further increase in filler content as increased brittleness thus failed to withstand bonding load of higher magnitude. The ILSS test results indicates that composites filled by (5% volume) of zirconium filler exhibited Inter Laminar Shear Strength (25.99 MPa). This is due to good bonding between layer to layer.

5. CONCLUSION

The Results of study showed that the carbon / phenolic composites with zirconium filler exhibited better properties than the carbon / phenolic composites without zirconium filler. However, 10% zirconium filler laminates are exhibits the better mechanical properties than others. Further increase in filler content has detrimental effect due to improper bonding between the matrix and filler interface and increased embrittlement of the composites. On basis of these results, there is scope for study to analyse the same combination of materials for high temperature (thermal) applications.

6. REFERENCES

1. P.K.Mallick, Fiber Reinforced Composites: Materials, Manufacturing and Design, Marcel Dekker Inc., New York, 1993: pp1-30.
2. M. Balasubramaniam, Composite Materials and Processing, CRC Press, 2013: pp 97-166.
3. K. C. Krishan, Composite Materials and Engineering, CRC Press 2012, pp 7-103.
4. Scott Bader, Crystic Composite Hand Book, 1997: pp 9-20.
5. Debroah DC Chung, Composite Materials Science and Applications, CRC Press, 2010: pp 47-93, 277-331.

TENSILE AND FRACTURE BEHAVIOR OF 6061 Al-Si Cp METAL MATRIX COMPOSITES

**T. Prasad^a and A. Chennakesava Reddy^b and S.
Jushkumar^c**

^aAssociate professor in Department of Mechanical Engineering,
Anurag Group of Institutions, Hyderabad

^bProfessor in Department of Mechanical Engineering
Jawaharlal Nehru Technological University, Kukatpally, Hyderabad-085

^cAssistant professor in Department of Mechanical Engineering,
Anurag Group of Institutions, Hyderabad

Abstract: In this paper, fabrication of aluminum MMC by bottom pouring in mushy state with secondary roller processing has been presented. The mechanical properties of 6061 aluminum alloy discontinuously – reinforced with fine particulates of SiCp is discussed. The influences of weight fraction of SiCp reinforcement on tensile strength and fracture toughness have been evaluated. Also crack path morphology has been studied to determine micro-mechanisms of failure and the influence of microstructure on crack growth characteristics.

Keywords: aluminum MMC, bottom pouring, secondary processing, fracture toughness.

Address all correspondence to: tatapudi.prasad@gmail.com Phone No: 9989177045

1. INTRODUCTION

The unique tailorability of the composite materials for the specific requirements makes these materials more popular in a variety of applications such as aerospace, automotive (pistons, cylinder liners, bearings), and structural components, resulting in savings of material and energy [1-7]. In this paper, 6061 Al/SiCp MMCs were produced by bottom pouring followed by secondary hot rolling. The aim of the present study is to investigate and the tensile and fracture behavior of 6061Al/SiCp metal matrix composites.

2. EXPERIMENTAL PROCEDURE

Aluminum alloy Al6061 with composition (weight percent) Mg - 0.9, Si- 0.68, Cu-0.20, Mn- 0.10, Cr- 0.10 and Al- remainder was used as the matrix material. The reinforcement is silicon carbide particles of sizes 5.5 μ m, 12.2 μ m and 18.12 μ m in 5%, 10% and 15% by weight.

Stir casting was employed to manufacture composites [8, 9]. The preheated SiC particulates at temperature 800^oC were added to the

liquid metal. The mixture was stirred using graphite stirrer at 400 rpm to get uniform slurry. A stirring time of 15 min was allowed to enhance the wetting of particulates by the liquid metal. The temperature of the slurry was sufficiently raised above the melting range of the matrix alloy before pouring the composite melt into preheated cast iron die. The as-cast composite billets were hot rolled for 20 % reduction at 400°C for 1 hour [10-15]. The hot rolling details of metal matrix composite (Al 6061 + SiCp) are shown in Table 1. Round tensile specimens with the gauge diameter 4.5 ± 0.1 mm and gauge length of 17.5 mm as per BS-18, as shown in Figure 1 were used for tensile testing.

Table 1: Hot rolling details of MMC

Matrix + SiCp(wt%)	Size of SiCp (µm)	Thickness (mm) (In 15 Passes)		Percentage Reduction %
		Before rolling	After rolling	
6061 + 5% SiCp	18.15	21	16	23
6061 + 10% SiCp	18.15	24.5	20.5	16
6061 + 15% SiCp	18.15	20	16.5	18
6061 + 0% SiCp	--	20.5	16	22

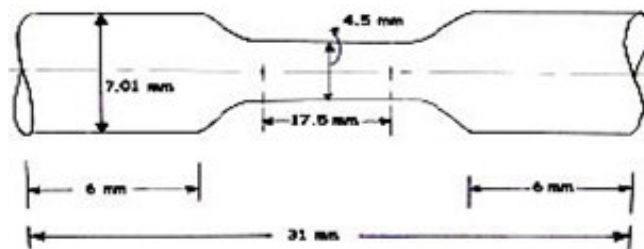


Figure 1: Tensile Specimen

3. RESULTS AND DISCUSSION

The tensile properties and fracture behavior of Al6061/SiCp metal matrix composites are discussed.

3.1 Microstructure

The optical micrograph of Al6061 alloy and composites with 5%, 10% and 15% SiC particles in rolling direction are shown below in figure 2. It is observed that the SiC particles are uniformly distributed in the composites. EDAX of 6061-alloy (Figure 3) shows that there is a loss of Mg and Si content during manufacturing metal matrix composites.

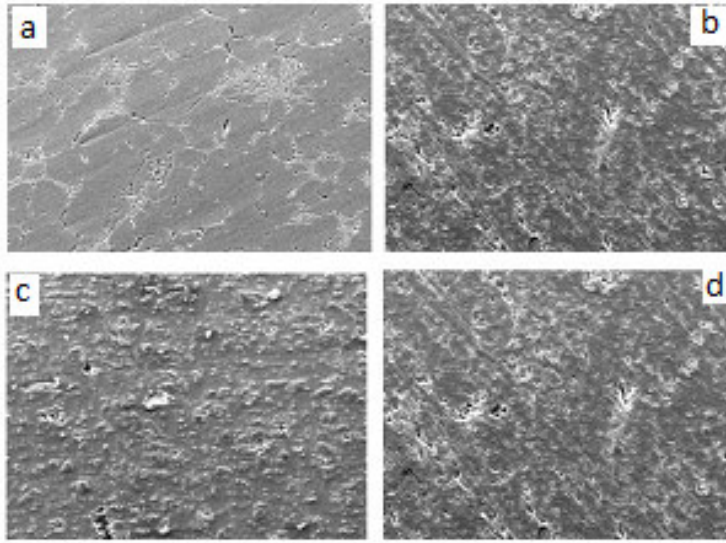


Figure 2: Optical micrographs (x200) (a) Al 6061 (b) Al6061/SiCp (5% wt) (c) Al6061/SiCp (10% wt) (d) Al6061/SiCp (15% wt)

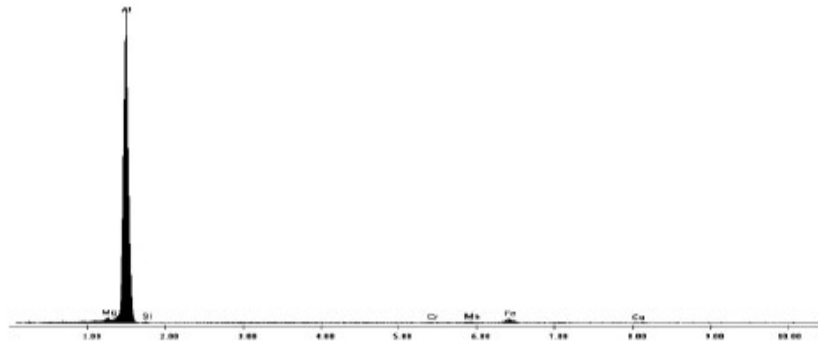


Figure 3: EDAX of AA 6061 alloy showing the loss of Mg and Si Content during stirring process.

3.2 Fracture Toughness Testing

Plane strain fracture toughness (K_{IC}) tests were conducted on BiSS 50 KN servo hydraulic universal testing machine (UTM) using CTS as per ASTM E-1820. The conditional fracture toughness was calculated using following equation.

$$K_Q = \left[\frac{P_Q}{B \cdot W^{3/2}} \right] f \left[\frac{a}{b} \right] \quad (1)$$

where, K_Q = Conditional Fracture Toughness
 B = Thickness of the specimen
 W = Width of the specimen

3.3 Tensile Testing

The tensile properties such as 0.2% yield strength, ultimate tensile strength, and percentage elongation have been evaluated for Al 6061 base alloy (T6), composites are shown in table 2.

Table 2: Mechanical properties of different composites

Condition (Rolled)	%Elongation	0.2% YS (Mpa)	UTS (Mpa)
AA6061 (T6)	22	289.91	328.5
AA6061 (Annealed) + 0% wt. SiCp	35	56.12	
AA 6061 + 5% wt. SiCp (18 μ m)	1.8	52.1	52.8
AA 6061 + 10% wt. SiCp (18 μ m)	1.2	40	40.5
AA 6061 + 15% wt. SiCp (18 μ m)	0.4	50	53.4

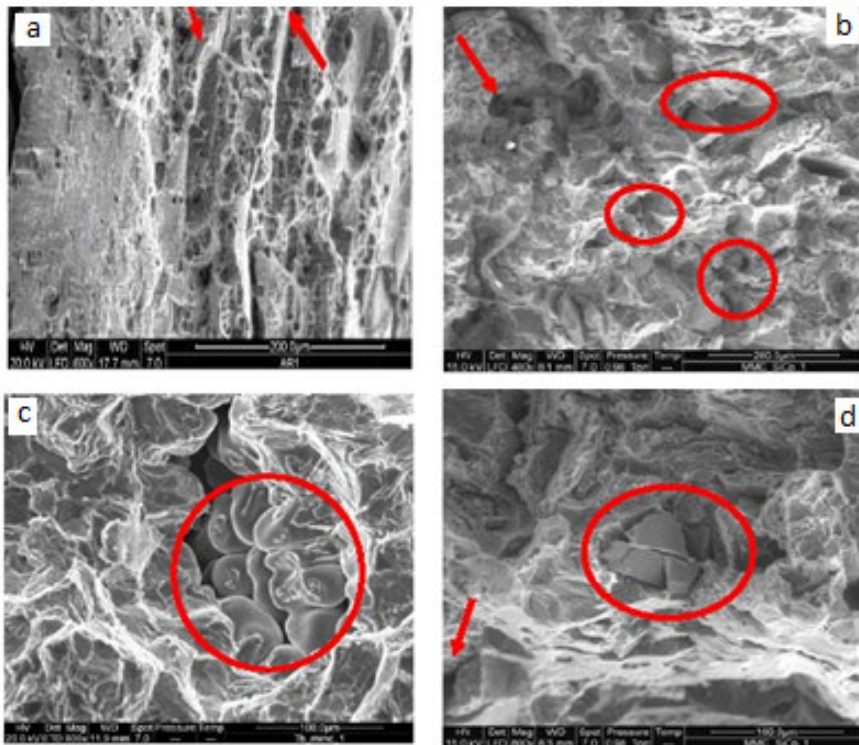


Figure 4: Tensile fractograph of (a) Al 6061 matrix alloy (b) Al 6061/15% SiCp (c) Al 6061/10% SiCp (d) Al 6061/15% SiCp

3.4 Fractographic Analyses and Discussion

The fracture surfaces of Al 6061 unreinforced alloy and Al 6061/SiCp MMCs that failed during fracture toughness tests and tensile tests were investigated for identifying the micro mechanisms of failure. Figure 4a reveals very few dimples and cracks in Al 6061 matrix alloy. The nature of fracture is ductile. Fractograph shown in figure 4b of Al 6061/5% SiCp reveals dimples, less in number and shallower when compared to matrix alloy. In Al 6061/10% SiCp composite (figure 4c), the mode of fracture is mainly interface debonding and particle fraction [5]. In Al 6061/15% SiCp composite (figure 4d), the fraction of dimples decreases with increasing SiC content resulting reduced plastic strain. Particle matrix interface decohesion along with some tear ridges is observed in the matrix region.

Hot rolling of MMC causes coarse dendritic cell structure displaying shrinkage cavities. These cavities are formed due to SiC particles. This type of failure is a brittle failure. The presence of tear ridges in AL 6061/SiCp MMC indicates that there is a constraints on the plastic flow of matrix imposed by SiC particles due to which the matrix in the interparticle regions undergoes extensive localized plastic strain [6]. The fractured particles as well as interface decohesion [7] can induce voids in the matrix which may result in lower fracture toughness and tensile properties in 15% SiCp MMC.

3.5 Validation of Uniaxial Tensile Test using ANSYS

Material model validation consists of modeling the same uni-axial tensile test from which the stress-strain data points have been recorded. The tensile test conditions were validated using ANSYS software [15]. The tensile specimen was meshed with plane 42 elements as shown in figure 5. The maximum displacement of Al 6061 matrix alloy is 1.694 mm as shown in figure 6.

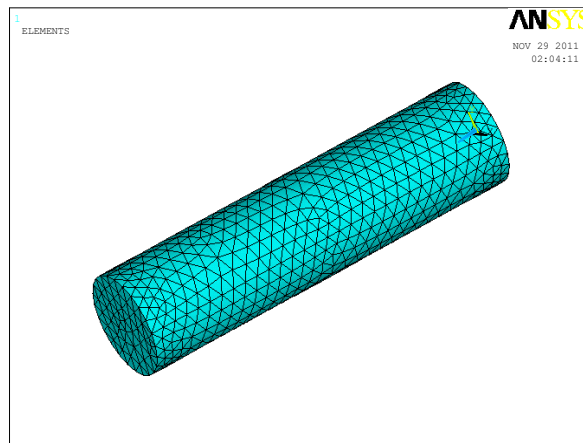


Figure 5: Meshing tensile specimen

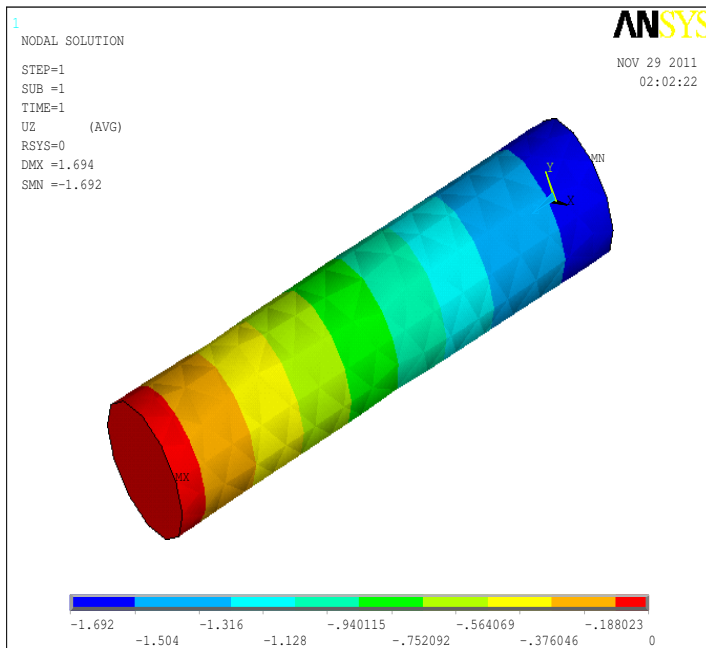


Figure 6: Displacement of Al 6061 matrix alloy

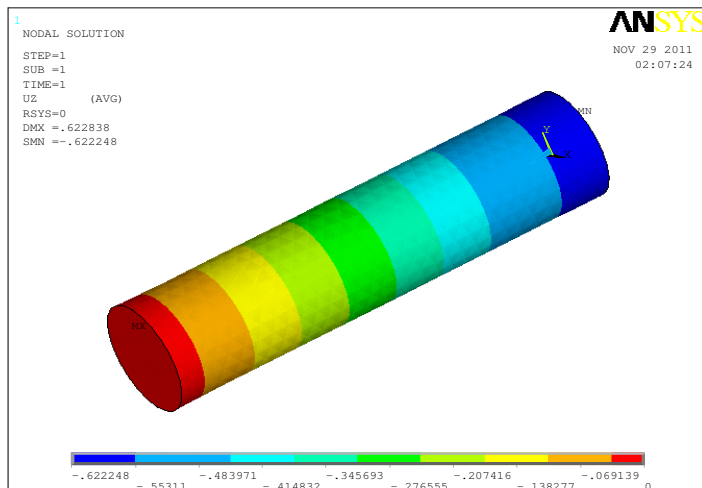


Figure 7: Displacement of Al 6061/5% SiCp composite

The maximum displacement of Al 6061/5% SiCp composite is 0.622 mm as shown in figure 7. The maximum displacement of Al 6061/5% SiCp composite is 0.240 mm as shown in figure 8. The maximum displacement of Al 6061/5% SiCp composite is 0.186 mm as shown in figure 9.

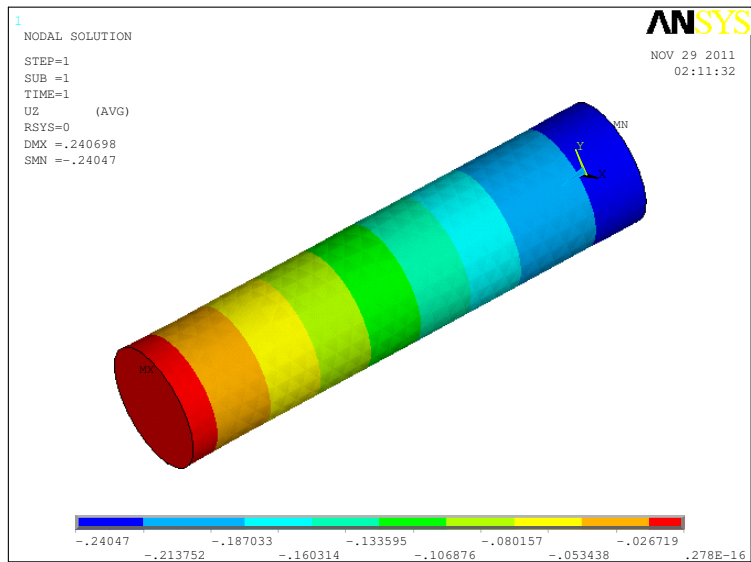


Figure 8: Displacement of Al 6061/10% SiCp composite

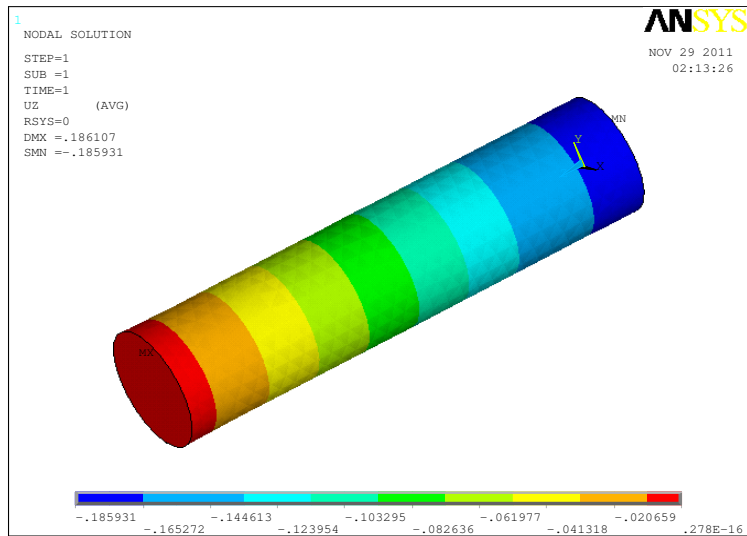


Figure 9: Displacement of Al 6061/15% SiCp composite

7. CONCLUSIONS

The mechanical properties of metal matrix composites after hot rolling were not significantly improved due to the presence of shrinkage cavities and particle cracking. It has been observed that there is a loss of Mg content during stirring of MMC fabrication and hence decreases in mechanical properties. The brittle fracture is observed in Al 6061/SiCp composites.

REFERENCES

1. A. Chennakesava Reddy, B. Kotiveerachari, Effect of matrix microstructure and reinforcement fracture on the properties of tempered SiC/Al-alloy composites, National conference on advances in materials and their processing, Bagalkot, 28-29th November 2003: pp.121-124.
2. A. Chennakesava Reddy, Experimental evaluation of elastic lattice strains in the discontinuously SiC reinforced Al-alloy composites, National Conference on Emerging Trends in Mechanical Engineering, Nagapur, 05-06th February 2004: VC-12.
3. A. Chennakesava Reddy, Mechanical properties and fracture behavior of 6061/SiC_p Metal Matrix Composites Fabricated by Low Pressure Die Casting Process, Journal of Manufacturing Technology Research, 2009:1(¾), pp.273-286.
4. A. Chennakesava Reddy, B. Kotiveerachari, Effect of aging condition on structure and the properties of Al-alloy / SiC composite, International Journal of Engineering and Technology, 2010: 02(6), pp.462-465.
5. A. Chennakesava Reddy, Tensile properties and fracture behavior of 6063/SiC_p metal matrix composites fabricated by investment casting process, International Journal of Mechanical Engineering and Materials Sciences, 2010:3(1), pp.73-78.
6. A. Chennakesava Reddy, Essa Zitoun, Matrix al-alloys for silicon carbide particle reinforced metal matrix composites, Indian journal of Science and Technology, 2010: 3(12), pp.1184-1187.
7. A. Chennakesava Reddy, Influence of strain rate and temperature on superplastic behavior of sinter forged Al6061/SiC metal matrix composites, International Journal of Engineering Research & Technology, 2011: 4(2), pp.189-198.
8. A. Chennakesava Reddy, Tensile fracture behavior of 7072/SiC_p metal matrix composites fabricated by gravity die casting process, Materials Technology: Advanced Performance Materials, 2011:26(5), pp.257-262.
9. A. Chennakesava Reddy, Evaluation of mechanical behavior of Al-alloy/SiC metal matrix composites with respect to their constituents using Taguchi techniques, i-manager's Journal of Mechanical Engineering, 2011:1(2), pp.31-41.
10. A. Chennakesava Reddy, B. Kotiveerachari, Influence of microstructural changes caused by ageing on wear behavior of Al6061/SiC composites, Journal of Metallurgy & Materials Science, 2011:53(1 0), pp.31-39.
11. A. Chennakesava Reddy, Fracture behavior of brittle matrix and alumina trihydrate particulate composites, Indian Journal of Engineering & Materials Sciences, 2002:9(5), pp.365-368.
12. B.Ramana, A. Chennakesava Reddy, and S. Somi Reddy, Fracture analysis of mg-alloy metal matrix composites, National Conference on Computer Applications in mechanical Engineering, Anantapur, 21st December 2005, pp.57-61.
13. A. Chennakesava Reddy, and Essa Zitoun, Matrix al-alloys for alumina particle reinforced metal matrix composites, *Indian Foundry Journal*, 2009:55(1), pp.12-16.
14. A. Chennakesava Reddy, and Essa Zitoun, Tensile behavior Of 6063/Al₂O₃ particulate metal matrix composites fabricated by investment casting process, International Journal of Applied Engineering Research, 2010:1(3), pp.542-552.
15. Chennakesava R. Alavala, Fundamental and Applications of Finite Element Methods, Prentice hall of India, New Delhi, 2008.

EFFECT OF MATRIX COMPOSITION ON MECHANICAL PROPERTIES IN CARBON FIBRE REINFORCED COMPOSITES

**K. Srinivasa Vadayar^a, G. Madhuri^b, L.S. Mahajan^b,
V.V. Bhanu Prasad^b**

^aAssistant Professor, Department of Metallurgical Engineering, JNTUH College of Engineering, Hyderabad-85.

^bStudents, Department of Metallurgical Engineering, JNTUH College of Engineering, Hyderabad-85.

^cScientist -G, Ceramics & Composites Group, DMRL, Hyderabad-58

Abstract: Carbon fibre reinforced with silicon carbide ceramic matrix composites are not easily machined due to their high hardness and stiffness. In the present work carbon composites were fabricated using two different matrix materials. One is carbon fibre reinforced with phenol formaldehyde resin and acetone in the ratios of 75:25, 25:75 respectively. Another one is carbon fibre reinforced with urea solution. The resin impregnated samples are kept in the muffle furnace at 150°C for 4 hours. Microstructural analysis was carried out. The strength of the composites were evaluated by the 3-point bend test (flexural test). The test revealed that the composite with resin: acetone ratio of 75:25 exhibited high flexural strength followed by carbon fibre reinforced in urea solution and the lowest strength was exhibited by a composite having resin: acetone ratio of 25:75.

Key words: Carbon fibre; Phenol formaldehyde resin; Urea solution; 3-point bend test.

Address all correspondence to: ksvadayar@gmail.com, +91-9640101069

1. INTRODUCTION

Composite materials are macroscopic combination of two or more materials with significantly different physical or chemical properties and which remain separate and distinct within the finished structure. The major and continuous phase forms the matrix while the additives act as the reinforcements, both being separated by an interface [1]. The composites are used not only for their structural properties, but also for electrical, thermal, tribological and environmental applications. The need of composite materials arises from the fact that no one-material-fits-all solution in the engineering world [2]. In the sense that a single material generally doesn't possess all the properties that the application demands for, therefore two or more materials are combined in order to achieve the combination of properties required. Since the structure and properties are related, the composite characteristics can be changed to tailor the properties required for the application. Composites cannot be made from constituents with divergent linear expansion characteristics. Choice of fabrication method depends on matrix properties and the effect of matrix on properties of reinforcements and vice-versa. One of

the prime considerations in the selection and fabrication of composites is that the constituents should be chemically inert and non-reactive [3]. Composite materials are commonly classified into Polymer Matrix Composites (PMCs), Metal Matrix Composites (MMCs) and Ceramic Matrix Composites (CMCs) based on the nature of the matrix material present in the composites. In another system of classification of composite materials into fibre reinforced composites, laminar composites and particulate composites based on the reinforcement form. Fibre reinforced composites can be further divided into those containing discontinuous or continuous fibres [4].

Carbon is very light element with density equal to 2.268g/cm³. Carbon can exist in variety of crystalline forms. The allotropes of carbon are graphite, diamond and Buckminster Fullerene (C₆₀ or C₇₀). Carbon in the graphitic form is highly anisotropic; with a theoretical Young's modulus is 1000 GPa, while that along the c-axis is equal to about 35GPa. The raw material for carbon fibre is organic precursor fibre. The commonly used precursor fibre is poly acrylonitrile (PAN). Other precursor fibres include rayon and the ones obtained from pitches, polyvinyl alcohol, polyamides and phenolics. The carbon fiber is a material consisting of thin, strong crystalline filaments of carbon, used as a strengthening material, especially in resins and ceramics. It is alternatively known as Graphite fibre [5-7]. The properties of carbon fibres are given below:

- High stiffness
- High tensile strength
- Low in weight
- High chemical resistance
- High temperature resistance up to 2200°C
- Low thermal expansion

The applications of carbon fibres: Every day, a new application is found for carbon fiber. What started out forty years ago as a highly exotic material is now a part of our everyday lives? These thin filaments, a tenth the thickness of a human hair, are now available in a wide range of useful forms. The fibers are bundled, woven and shaped into tubes and sheets (up to ½” thick) for construction purposes, supplied as cloth for molding, or just regular thread for filament winding.

The primary objective of the present investigation is synthesis of carbon fibre reinforced phenolic resin matrix composites and Urea matrix composites and to study the effect of matrix composition on mechanical properties of these carbon fibre reinforced composites.

2. EXPERIMENTAL WORK

The present study involves synthesis and characterization of carbon fibre reinforced composites. These composites are light in weight and finds applications in automobile and aerospace applications.

2.1 Preparation of Composites

Carbon fibre woven cloth (figure 1a) is taken and glue is applied along the cutting lines and dried prior to cutting which prevents in spreading of edges during cutting. The cloth is cut it into ten pieces of 230 X 250 mm size and stacked one above other. This whole assembly is placed on a metallic frame and their position is maintained using holding pins. With the help of a needle and a carbon fiber which is soaked in water, these 10 pieces bound or stitched into a single preform. The preform cut into four equal parts for further processing.

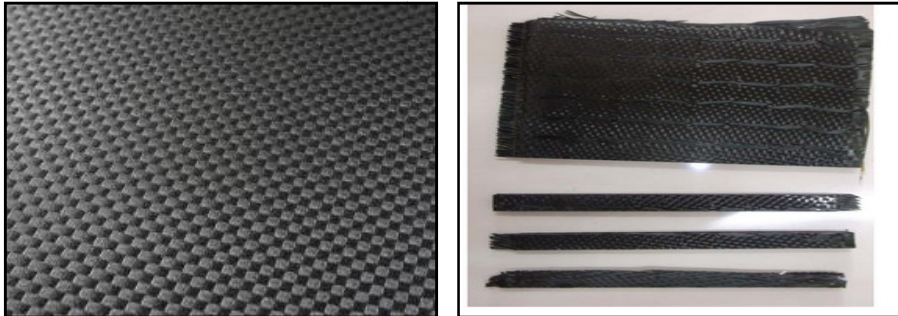


Figure 1: (a) Carbon fiber before impregnation, (b) Carbon fiber after impregnation

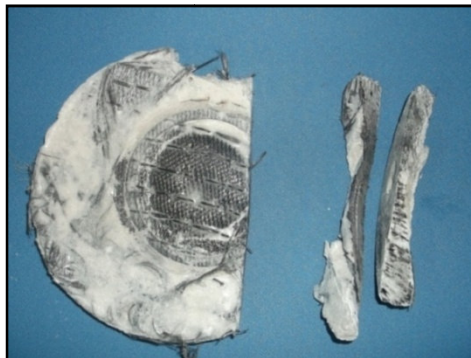


Figure 2: Urea impregnated carbon fiber composite

The preform is placed in a solution consisting of a mixture of phenolic formaldehyde resin and acetone in 75:25 respectively for one hour (figure 1b). Aluminum foil is used to cover the assembly and pressed to remove the excess solution. The impregnated piece is heated at 140°C for four hours in a muffle furnace. The sample is allowed to cool in the furnace itself. The above procedure is repeated for a solution consisting of a mixture of phenolic formaldehyde resin and acetone in 25:75 respectively. For Urea impregnated Carbon fibers (figure 2) first the Urea is taken in a glass bowl and melted at 150°C. To this boiling solution the preform is introduced and soaked for one hour. All the above samples after cooling to room temperature were cut into 11mm wide for further characterization.

2.2 Characterization Techniques

The structure of the composites reveals important properties like distribution of reinforcement phases, presence of interface, strength properties etc.

2.2.1 Metallography

Metallographic studies were conducted on the composites using Leica optical microscope. The samples for metallographic examination were prepared using standard procedures of cutting, mounting, polishing and observation under microscope. The microstructures were recorded using image analyzer software at various surface areas/locations.

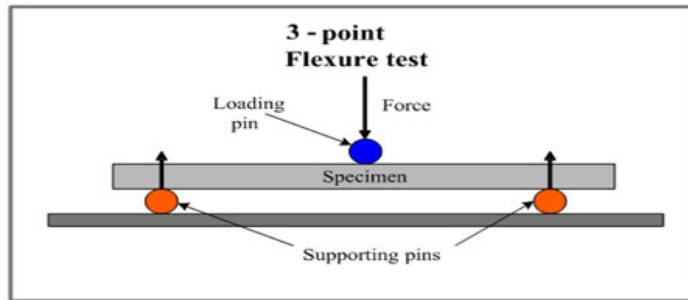


Figure 3: Schematic of three point bend test

2.2.2 Three-Point Bend Test

The strength properties of a material are evaluated by tensile test / bend test /compression test etc. In the bend test a specimen with rectangular or flat cross-section is placed on two parallel supporting rollers. The loading force is applied in the middle by means of a loading roller. The supporting and loading rollers are mounted in a way, allowing their free rotation about axis parallel to the pin axis and axis parallel to the specimen axis. This configuration provides uniform loading of the specimen and prevents friction between the specimen and the supporting pins. In this test, the highest stress is reached on the mid point of the span of the sample where, in general failure occurs. Flexural strength (σ) at the point of failure is calculated by using the formula:

$$\sigma = \frac{3LF}{(2bd^2)} \quad (1)$$

where, L is span length, F is total force applied to the specimen by loading roller, b is specimen width and d is specimen thickness. Schematic of loading configuration of the samples in three point bend test is shown in figure 3. Readings reported were the average of three measurements made.

3. RESULTS AND DISCUSSION

Based on the structure obtained and the strength properties under compression the results are analysed followed by discussion.

3.1 Microstructure

Figure 4a shows the microstructure of composite (C_f - Phenolic resin-75:25 dilution) at 200X. The microstructure reveals the clear presence of individual carbon fibres with in the continuous phenol formaldehyde matrix. Figure 4b reveals the microstructure of composites C_f reinforced urea matrix at a magnification of 200X. In this case also there is the presence of the individual carbon fibres into the continuous Urea matrix with no interfacial reactions.

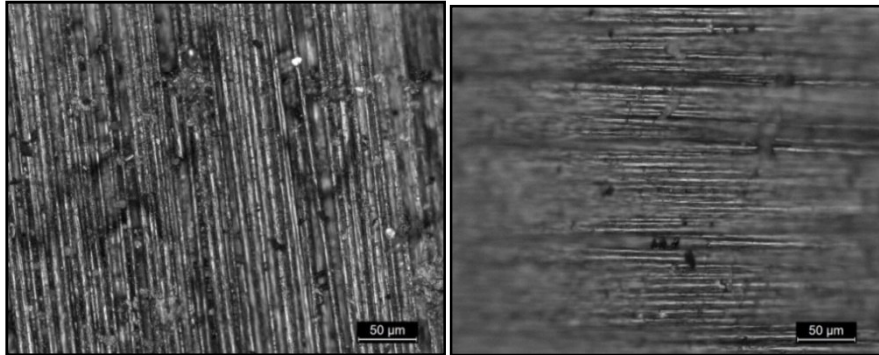


Figure 4: Optical Micrographs of (a) Composite (C_f -Phenol formaldehyde) (b) Composite (C_f -Urea).

3.2 Three- Point Bend Test

From the above table 1 it is observed that composite- resin: acetone (75:25) gives the maximum stress of 151 MPa under a maximum load of 256 KN. The composite having resin: Acetone 50:50 exhibited a lower strength value of 33 MPa. This may be due to less amount of resin in the resin acetone mixture. Composite-U exhibited a strength value of 46MPa which is higher than above composite.

Table 1: The strength values of the composites

Sample	Maximum load (KN)	Maximum stress (MPa)
Resin: acetone (75:25)	256	151
Resin: acetone (50:50)	82	33
Urea	252	46

4. CONCLUSIONS

The following conclusions can be drawn out from the present study:

1. Carbon fiber reinforced composites with phenolic resin as matrix were prepared by solution impregnation technique using different dilutions of resin and acetone (75:25, and 25:75) followed by curing at 150°C for 4 hours.
2. Carbon fiber reinforced composites with Urea as matrix were prepared by melt impregnation technique using molten urea at 150°C followed by solidification of urea matrix.

3. The micrographs of both the composites showed the embedded system of resin and urea matrix around the carbon fiber reinforcements without any interfacial reaction.
4. From the three point bend test results, it is observed that there is an increase in bend strength values of carbon fiber reinforced phenolic resin composites (from 33 MPa to 151 MPa) with increased resin concentration (resin : acetone) from 25:75 to 75:25. Carbon fiber reinforced Urea matrix composite is exhibited a strength value of also (45 MPa) under three point bend test.

5.

5. ACKNOWLEDGEMENTS

The authors are thankful to Director, DMRL, Kanchanbagh, Hyderabad for giving permission to carry out this work in the laboratory and for extending full cooperation throughout the work.

REFERENCES

1. K.K.Chawla, Composite Materials, Springer-Verlag publications, New York, 2012: pp. 4-5.
2. A.K. Bhargava, Engineering Materials, PHI publications, New Delhi, 2010: pp. 224-225.
3. S.C. Tjong, and Z. Y. Ma, Microstructural and mechanical characteristics of *in situ* metal matrix composites, Materials Science and Engineering: R, 2000: 29, pp. 49-113.
4. S.Ranganath, A Review on Particulate-Reinforced Titanium Matrix Composites, Journal of Material Science, 1997: 32, pp. 1-16.
5. A. S. Singha and Vijaya Kumar Thakur, Mechanical properties of natural fiber reinforced polymer composites, Bulletin of Material Science, 2008: 31(5), pp. 791-799.
6. R. Selzer - K. Friedrich, Mechanical properties and failure behaviour of carbon fibre-reinforced polymer composites under the influence of moisture, Composites Part A: Applied Science and Manufacturing, 1997: 28(6), pp. 595-604.
7. A. Chennakesava Reddy, Analysis of the Relationship Between the Interface Structure and the Strength of Carbon-Aluminum Composites, NATCON-ME, Bangalore, 13-14th March 2004, pp.61-62.

EFFECT OF GLASS FILLER MATERIAL ON MECHANICAL PROPERTIES OF GLASS/EPOXY (RT CURE) COMPOSITES

R.Ramnarayanan^a and C.Venkateshwar Reddy^b

^aAdvanced systems laboratory (DRDO) Hyderabad

^bMatrusri engineering college Hyderabad.

Abstract: Polymer matrix composites are emerging as promising materials in many engineering applications, the present research has been under taken with an idea to explore the potential utilization of glass filler as filler material in polymer composites and to investigate its effect on the mechanical behavior of resulting composites. The glass /epoxy composites with varied volume fraction of glass filler were prepared by hand lap techniques. The physical properties and mechanical properties viz. tensile behavior, flexural behavior and shear behavior are studied. The objective is to study the influence of glass filler in mechanical characteristics of glass/ epoxy (RT cure) composites. The effect of glass filler on the properties on these composites was studied. The test specimens are prepared as per ASTM standards to conduct tensile, flexural and shear test. Results of this study showed that the glass/ epoxy composite with glass filler material exhibited better mechanical properties than unfilled glass/epoxy composites.

Keywords: Composite materials; RT Cure (Room Temperature cure); Mechanical properties; Hand lay-up technique; Glass filler, Epoxy resin.

Address all correspondence to: rrn030857@gmail.com

1. INTRODUCTION

over the past few decades polymer matrix composites are widely used for different applications in aerospace, structures, spaceship structures, structural engineering, automobile, and chemical industries. The high performance continuous fiber (glass fiber) reinforced polymer composites gives high strength high stiffness and resistance to corrosion etc to the composite material.

In this study E-glass fiber reinforcements are used in composite material due to its best mechanical properties glass fiber as been a major reinforcement for the FRP (fiber reinforced plastics) industry [1]. Among the thermosetting polymers epoxy resins are most widely used to aerospace field for high performance applications. Epoxy resins posses' characteristics such as high strength, low creep, good adhesion to the most of the substrate materials, low shrinkage during curing and low viscosity due to these reasons epoxy resins are specifically used as matrix material. Mechanical and physical properties of glass fiber reinforced composites depending on the properties of ingredients used

in material. Specific (glass) filler or additives are added to enhance and modify the properties of composite material [2].

In this regard the present investigation has been concentrated on mechanical properties such as tensile behavior, flexural and shear behavior of glass/epoxy (RT cure) composite with glass as filler material.

2. EXPERIMENTATION PROCEDURE

This includes selection of materials, fabrication of laminates, specimen preparation and testing of specimens for mechanical properties.

2.1 Material

The polymer laminates prepared in the present research work are plane wave bi-woven E-glass fiber with epoxy resin (LY 556 and HY 951) as adhesive with 0/90 fiber orientation the adhesive made from a mixer of LY 556 resin and HY 951 hardener in proportions of 10:1 by weight. Each layer of cloth is measuring 0.28 to 0.33 mm thick.

Table 1: Details of material/samples (laminates) prepared

Reinforcement Fiber	Matrix Resin	Filler	Filler Volume %	Specimen Code
E-Glass	Epoxy (RTcure)	Glass Filler	0	L ₀
E-Glass	Epoxy (RTcure)	Glass Filler	5	L ₁
E-Glass	Epoxy (RTcure)	Glass Filler	10	L ₂
E-Glass	Epoxy (RTcure)	Glass Filler	15	L ₃

Filler materials play an important role for improvement of performance of composite. Different types of filler materials natural or synthetic both organic and inorganic are available like Alumina (Al₂O₃), silica (SiO₂), silicon carbide (SiC), titania (TiO₂) and glass filler (Glass micro spheres). In this study glass filler is selected and used as filler with RTcure epoxy resin system with weight percentage of 0%, 5%, 10% and 15% with glass fiber reinforced composites to study the importance in mechanical properties of the composites [3]. The details of material samples (Laminates) prepared are given in table 1.

2.2 Fabrication of Laminate

The hand layup process is adopted in this study for the fabrication of composite laminates. A mould is used for this hand layup process; the mould is a flat surface with top and bottom plate. The mould surface is cleaned with solution such as acetone and release agent like wax or petroleum jelly is applied to easy removal of laminate from the mould. The reinforcing material weave bi-woven glass fiber cut into required size and laid on the flat surface of the mould. The resin LY556 and hardener HY 951 mixed in the proportion with glass filler material

varied fiber volume fraction spread evenly on the reinforcing fibers [4]. The resin is squeezed evenly on the surface by roller and compress thoroughly with roller. The reinforcing fibers are stacked one above the other to the required thickness of the laminate. After attaining required thickness the laminate has been compressed in mould at room temperature (RT cure) for about 24 hours after the curing process completed. The laminate is removed from the mould and cut into required size of specimen as per ASTM standard and subjected to various tests.

2.3 Specimen Preparation

The prepared laminated composite material were taken from the mould that was cured at ambient conditions for a period of about 24 hours and the specimens size 250mm x 250mm x 4mm are prepared from the laminated composite for different mechanical tests. The test specimens are cut to evaluate the mechanical properties (tensile behavior, flexural behavior, shear behavior) according to ASTM standards [5]. Tensile test has been conducted as per ASTM D638, flexural test as per ASTM D790 and inter laminar shear strength has been conducted as per ASTM D2344.

2.4 Mechanical Property Testing

Three sample specimens with varied filler material and without filler material. Tensile behavior, flexural behavior and shear behavior tests were carried out using universal testing machine and Torsion testing machine.

2.4.1 Tensile Test

The tensile behavior of prepared samples were determined at room temperature using universal testing machine in accordance with ASTM D 3039 test specimens having dimensions of length 250mm width of 25mm and thickness of 4.0mm. The specimen was loaded between two adjustable grips of a 60KN computerized universal testing machine (UTM) with an electronic extensometer. Each test was repeated three times and the average value was taken to calculate the tensile strength and tensile modulus of the composite.

2.4.2 Flexural Test

Flexural strength is determined by 3-point bend test in accordance with ASTM D 790. The test specimens of dimensions 130mm x 25 mm x 4.0 mm were used for test. Three point bending test were performed in a servo controlled UTM machine having load cell capacity of 5kN. Six specimens were tested and average value is considered for flexural strength the test specimens were examined through visual inspection for failure of fiber and matrix. Flexural strength is calculated by the following equation.

$$\sigma_f = \frac{3PL}{2bh^2} \quad (1)$$

where,

σ_f = stress in the outer fibers at mid point (MPa)
 P = Applied load at a given point on the load deflection curve (N)
 L = Support span mm
 b = Width of the beam tested mm
 h = Depth of beam tested mm

2.4.3 Inter laminar shear test

The inter laminar shear strength prepared samples were determined at room temperature their ILSS is usually limiting design characteristics because conventional manufacturing techniques do not produce reinforcing fibers oriented in the thickness direction to sustain load. Inter laminar shear properties are important data required for the analysis of polymer composite structure in this investigation 3-point bend test ASTM D2344 specified laminates was studied.

3. RESULTS AND DISCUSSIONS

The physical properties like fiber content resin content and density of the sample laminates prepared were evaluated and physical properties obtained after the test were tabulated in table 2. The physical properties test results shows that optimum fiber volume fraction(38.83% resin, 61.17% resin) and maximum density of 1.7247 is obtained in the composite filled by (10% volume) of glass fiber.

The tensile strength, flexural strength and inter laminar shear strength (ILSS) for different combination of filler with glass/epoxy (RT cure) composites are presented in table 3 - 5 and their variations shown in figure. 1 - 6.

Table 2: Details of physical properties of samples

Specimen Code	Filler Volume Fraction %		Density
	Resin	Filler	
L ₀	28.64	71.36	1.6032
L ₁	34.00	66.00	1.6786
L ₂	38.83	61.17	1.7247
L ₃	29.50	70.50	1.7083

3.1 Tensile Strength

The tensile strength of the composite materials depend upon the strength and modulus of fibers, the strength and chemical stability of the matrix, the fiber matrix interaction and fiber length.

From obtained results it is observed that the composite filled by (10% volume) of glass filler exhibited maximum ultimate tensile strength (281.31 MPa), when compared with other filler composites, but lower than the unfilled composites. This may be due to good particle dispersion and strong polymer/filler interface adhesion for effective

stress transfer but further increase in filler content (up to 15% volume). The tensile strength is found to be less this due to more filler material distribution in the material.

Table 3: Tensile strength, tensile modulus and % elongation at failure.

Composite Materials	Tensile Strength (MPa)	Tensile Modulus (GPa)	% Elongation At Failure
L0	317.7	24.61	1.31
L1	263.06	13.03	2.03
L2	281.31	13.50	2.08
L3	262.42	12.30	2.13

From the test results it is observed that unfilled and filled glass/epoxy with 5 %, 10% and 15% of volume fraction of glass filler as shown in the figures (figure-1, figure-2, and figure-3). The tensile strength and tensile modulus glass/epoxy composite filled with glass filler decreases with

Glass filler content compared with unfilled glass/epoxy (RT cure) composite. The % elongation at failure increases with glass filler content of 5% and decreases with 10% again increasing with addition of 15% glass filler.

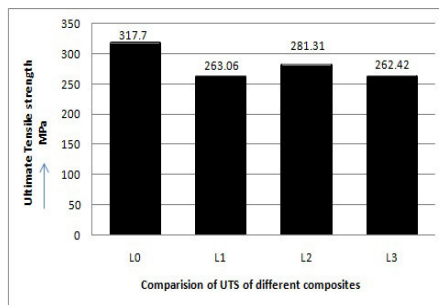


Figure 1: Tensile strength MPa

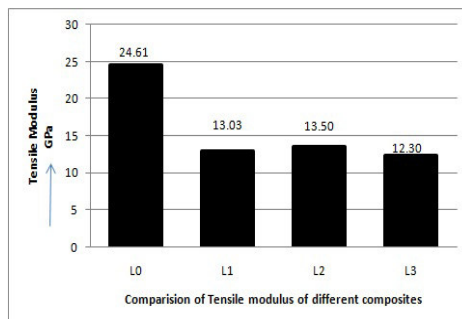


Figure 2: Tensile modulus GPa

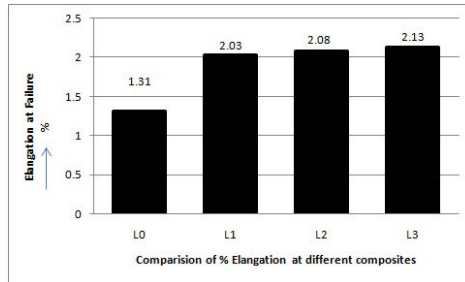


Figure 3: % Elongation at failure

3.2 Flexural Strength

Comparisons of the flexural strength of composite materials are shown in figure 4. They indicated that composites filled by (10% volume) exhibited maximum flexural strength(270.85MPa) the reduction of flexural strength is observed with increase in addition of filler this may be due to fillers disturb matrix continuity and reduction in bonding strength between filler matrix and fiber.

Table 4: shows Flexural strength and Flexural modulus.

Composite Materials	Flexural Strength (MPa)	Flexural Modulus (GPa)
L0	236.92	21.51
L1	237.34	20.12
L2	270.85	23.34
L3	265.70	21.42

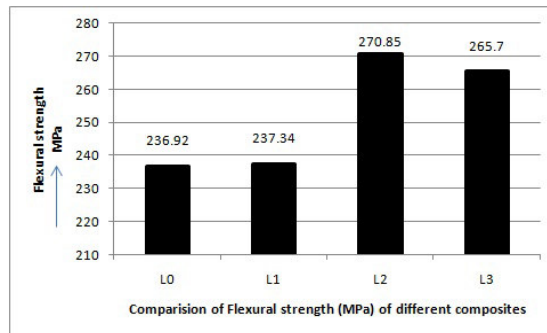


Figure 4: Flexural strength

The comparison of flexural test (3-point bend test) results obtained from unfilled glass/epoxy composites and filled with 5%, 10% and 15% volume fraction glass filler as shown in figure 4 and 5. The results shows that the flexural strength glass epoxy with glass filler increasing till 10% of glass filler further increases with 15% of glass filler content lead to decrease in its flexural strength and modulus. This is due the fact that increase filler content has increased its brittleness thus fails to with stand bending load.

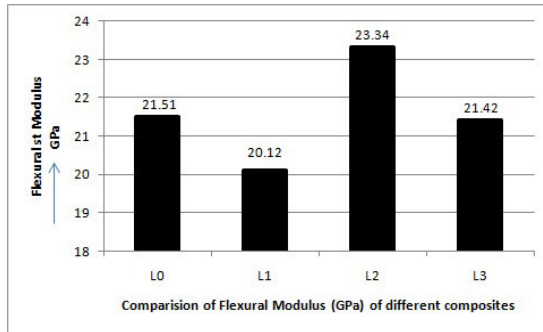


Figure 5: Flexural modulus

3.3 Inter Laminar Shear Strength (ILSS)

ILSS test results shows that composites filled by (10% volume) exhibited maximum ILSS. The reduction of ILSS is observed with increase in addition of filler. This may be due to increase in filler interlayer bonding between layers is reduced.

Table-5: shows inter laminar shear strength

Composite material	ILSS (MPa)
L0	21.20
L1	23.81
L2	24.71
L3	24.52

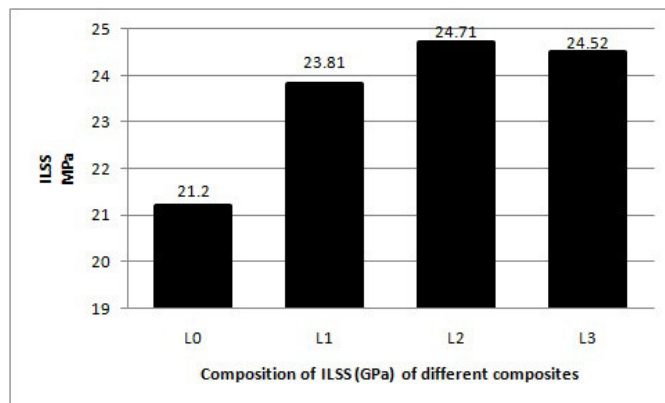


Figure 6: ILSS in MPa

From the test results it is observed that unfilled glass/epoxy and filled with 5%, 10% and 15% volume fraction of glass filler as shown figure 6. The inter laminar shear strength of glass/epoxy composite filled with

glass filler increases with varied fiber volume fraction. This indicates that with addition of filler increases the ILSS is also increases.

4. CONCLUSIONS

In the present research work E-glass/Epoxy based composites filled with glass filler with varying volume fraction by weight (%) were prepared. Fabrication of laminates (Samples) was done at room temperature by hand layup process using mould. Based up on the test results obtained from the tests several important considerations can be drawn.

From the obtained results composites filled by (10% volume) of glass filler exhibited maximum tensile strength (281.31 MPa). When compared with other filled composites this may be due to good particle dispersion and strong polymer/filler interface adhesion for effective stress transfer. Increase in adhesion of filler materials leads to decrease in tensile strength this may be due to more filler distribution and filler metal dominated in the materials. The flexural strength results indicated that composites filled by (10% volume) of glass filler exhibited maximum flexural strength (270.85 MPa). When compared with other filled composites this is due to good compatibility between filler and matrix. However test results shows that increase in addition of filler reduces flexural strength this may be due to that the further increase in filler content as increased brittleness thus failed to withstand bonding load of higher magnitude. The ILSS test results indicates that composites filled by (10% volume) of glass filler exhibited inter laminar shear strength (24.71 MPa). This is due to good bonding between layer to layer.

The obtained results reveal that in E-glass/epoxy (RTcure) composites glass filler filled by (10% volume) has proved to be beneficial. Further increase in filler content as detrimental effect due to improper bonding between the matrix and filler interface and increased embrittlement of the composites.

REFERENCES

1. P.K.Mallick, Fiber-reinforced composites: materials, manufacturing, and design, CRC press, 1993: pp.51-114.
2. H.S.Kartz and J.V.Milewski, Hand Book of Fillers for plastics, Van Nostrand Renhold, N.Y, 1987: pp.243-268.
3. G.Lubin, Hand Book of Composites Van Nostrand, N.Y, 1982: Chapter 2, pp.12-36.
4. H.Lee and K.Neville, Hand Book of Epoxy Resin, Mc Graw Hill, 1967: pp.291-306.
5. H.S.Kartz and J.V.Milewski, Hand Book of Fillers and Reinforcements, Van Nostrand Renhold, 1978: pp.351-360.
6. B. Kotiverachari, A. Chennakesava Reddy, Interfacial effect on the fracture mechanism in GFRP composites, CEMILAC Conference, Ministry of Defence, India, 20-21st August 1999, B85-87.

METALLURGICAL CHARACTERISTICS OF FRACTURE BEHAVIOUR IN Al/SiC METAL MATRIX COMPOSITE

Essa Zitoun ^a and A.Chennakesava Reddy ^b

^a Research Scholar, Department of Mechanical Engineering, OU College of Engineering, Hyderabad

^b Professor of Mechanical Engineering Department, JNTUH College of Engineering, Hyderabad

Abstract: Aluminium based metal matrix composite reinforced with particles of SiC exhibit higher strength and stiffness, in addition to isotropic behavior at a lower density, when compared to the unreinforced material. The aim of this paper is to study the damage and fracture processes of particle reinforced metal matrix composites caused by tensile loading. This paper through the use of SEM fracture analysis shows that the main fracture mechanism is based on void nucleation, and the test result shows that the strength increased with the increase in volume fraction (Vf) and decrease particle size (Ps).

Keywords: silica, fracture, metal matrix composite,

Address all correspondence to: essajessus@yahoo.com

1. INTRODUCTION

Metal-matrix composites (MMCs) are engineered combinations of two or more materials (one of which is a metal). MMCs consist of continuous or discontinuous fibres, whiskers, or particles as reinforcement. MMCs provide significantly enhanced properties over conventional monolithic materials, such as higher strength, stiffness, and weight savings [1, 2]. While continuous fibres reinforcement provides the most effective strengthening (in a given direction), particle reinforced materials are more attractive due to their cost-effectiveness, isotropic properties, and their ability to be processed using similar technology used for monolithic materials. The mechanical properties of aluminum alloys reinforced with ceramic particulates are known to be influenced by the particle size and the volume fraction [1-21]. It is also generally found that 0.2% proof stress and tensile strength tend to increase and toughness and ductility decrease with increasing volume fraction of particulate or decreasing particles. Some investigations have indicated that commercial particulates generally have a size ranging from a few micrometers to several hundred micrometers. The fracture mechanism of composites is controlled by the ability to form cavities and voids around particles in the matrix, which in turn depends on the particle size of the particles. For optimum strength, the second-phase dispersion strengthened particles must be fine and inter particulate spacing small.

In the present work, we attempted to fabricate aluminum 6061 matrix composites with different volume fractions and different particles. The aim has been to study the effect of volume fraction and reinforcement particle size on the tensile properties and fracture behavior of the composites.

2. EXPERIMENTAL PROCEDURE AND MATERIALS

For the present investigation, aluminum alloy 6061 was reinforced with 12%, 16% and 20% (V_f) of SiC particles with average particle diameter (10, 20 and 30 μm). Table 1 shows the composition of the matrix Al-6061. Al-6061 alloy was melted in an oil-fired furnace. The melting losses of alloy constituents were taken into account while preparing the charge. The charge was fluxed with coverall to prevent dressing. Figure 1 shows Al-6061 alloy ingots. The composites were prepared by stir casting process. The preheated reinforcement particles were added to the liquid melt. The molten alloy and reinforcement particles were thoroughly stirred using a mixer to make the melt homogenous as shown in figure 2.

Table 1: Chemical composition of alloys

Al	Composition determined spectrographically, %								
	Al	Si	Fe	Cu	Ti	Mg	Mn	Zn	Cr
6061	97.6	0.68	0.61	0.02	0.053	0.92	0.044	0.072	0.005



Figure 1: Aluminum 6061 alloy ingots

The samples were machined to get dog-bone specimen for tensile test. The computer-interfaced UTM (Universal Testing Machine) was used for the tensile test. The specimens were loaded hydraulically. The loads at which the specimen has reached the yield point and broken were noted down.

Metallographic samples from 12%, 16% and 20% (V_f) SiC reinforced composites were cut with a low speed diamond-blade wheel. They were wet ground on 320, 400 and 600 grit SiC abrasive paper using water as

lubricant, followed by polishing on diamond slurry (1 μ m), followed by cleaning in deionized water. The specimens were coated with electrically-conductive metal (gold) which would ground the specimen to the stub and drain off electrons. The specimens were coated with gold by Vacuum Evaporator Toshiba in IICT. Fracture behavior was analyzed using scanning electron microscope (SEM) of Hitachi S-3000N in Indian Institute of Chemical Technology (IICT).

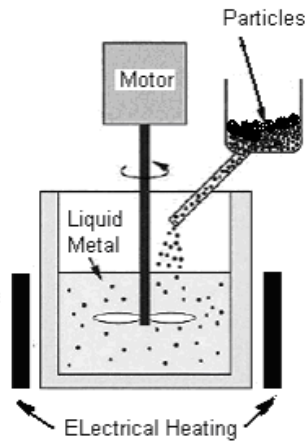


Figure 2: Charge preparation in the stir casting process

3. RESULT AND DISCUSSION

The tested tensile specimens are shown in figure 3. Three samples were tested for each trial. The average values of yield strength, ultimate tensile strength.



Figure 3: Tested tensile Al/SiC Composite specimens

3.1 Effect of Volume Fraction on Mechanical Properties

Figure 4-5 shows the influence of volume fraction on the ultimate tensile strength (σ_u) and yield strength (Y_s) of Al-SiC composites respectively. As expected, the σ_u and Y_s values were substantially influenced by the addition of SiC particles. Experimental results show an increase in σ_u and Y_s with an increase in reinforcement.

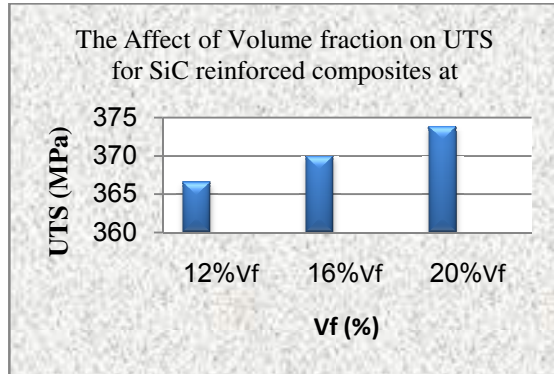


Figure 4: Influence of volume fraction on the ultimate tensile strength of Al/SiC composite

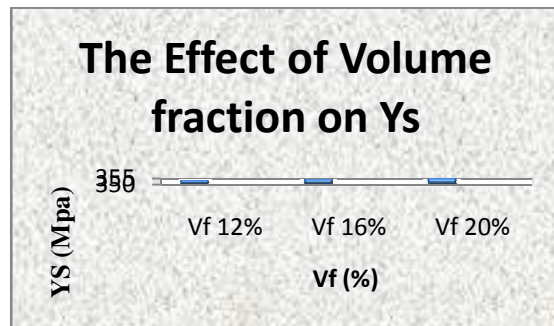


Figure 5: Influence of volume fraction on the yield strength of Al/SiC composite

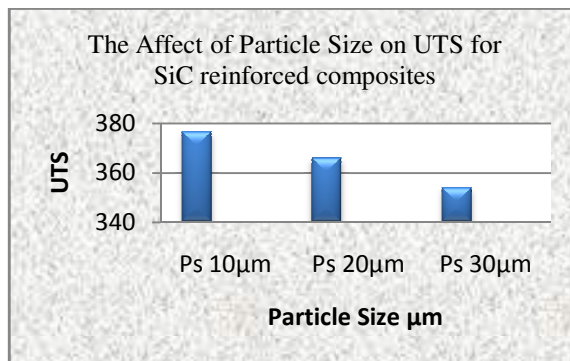


Figure 6: Influence of particle size on the ultimate tensile strength of Al/SiC composite

3.2 Effect of Particle Size on the Mechanical Properties

The effect of the particle size on σ_u and Y_s can be noticed in the figure 6-7. The ultimate tensile strength σ_u and yield strength Y_s have been influenced by particle size, decrease the particle size increase σ_u and Y_s because increase in dislocation density depends upon size of the

reinforcement. As the particle size increase for constant volume fraction, the inter-particle spacing increase and the dislocation due to the coefficient of thermal expansion mismatch decrease [5].

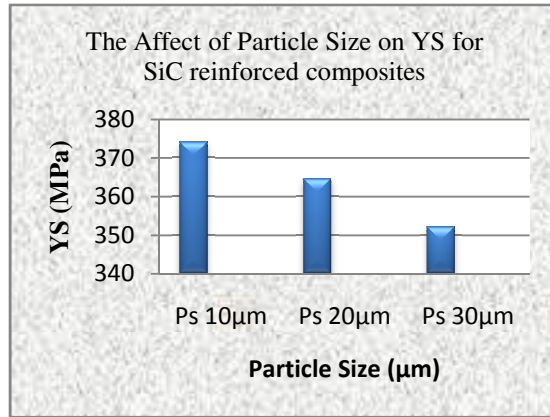


figure 7: Influence of particle size on the yield strength of Al/SiC composite

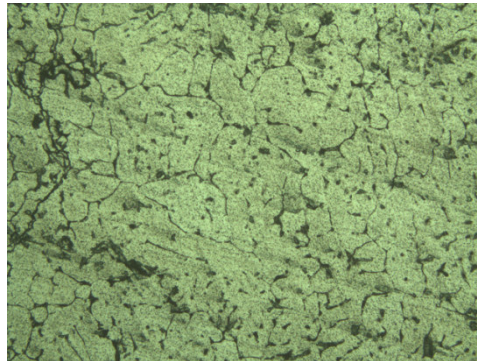


Figure 8: Microstructure of Al 6061/SiC metal matrix composite,12% V_f , 200X.

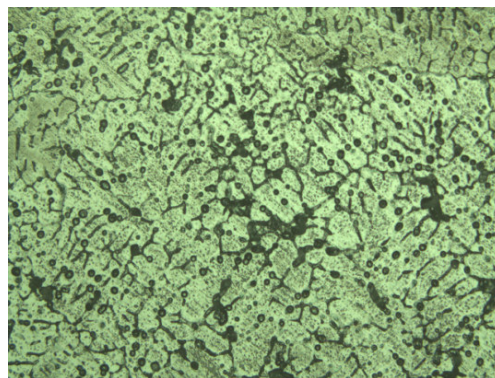


Figure 9: Microstructure of Al 6061/SiC metal matrix composite,16% V_f 200X

3.3 Microstructure

The various intermetallics can be revealed in the microstructures shown in figure 8-10. Figures also show the distribution of the SiC particles in the composites. Microstructure of 6061/SiC metal matrix composite of 12% V_f shown in figure 8 reveals near uniform distribution and shaped, few clustering and agglomeration. There is less of agglomeration of aluminum oxide in 6061 aluminum matrix. While in the figure 9 shows higher degree of agglomeration and clustering. Figure 10 shows irregularly shaped agglomeration and these are dispersed randomly through the metal matrix. If compare these figures we can observe that the degree of clustering and agglomeration increases if volume fraction increased. An agglomeration site consisted of a few large SiC particulates intermingled with the smaller, uniform and more regularly shaped particles. It may be concluded that as a result of particles agglomeration, the inter-particle distance hindered uniform matrix infiltration by the particles and as a result porosity may be elevated in these regions.

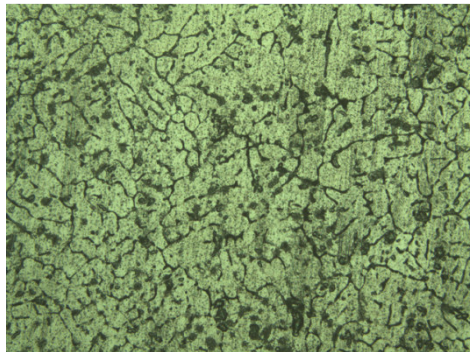


Figure 10: Microstructure of Al 6061/SiC metal matrix composite, 20% V_f 200X



Figure 11: SEM tensile fracture surface of the 12% V_f Al/SiC composite

3.4 Fracture Behaviour

The influence of SiC particles clustering and the micro structural effects on ductility and fracture properties of the composites are analyzed by examining SEM fracture surface of the tested specimens. Two factors appear to control the ductility of these composites: distribution of the

SiC particles and deformation characteristics of the metal matrix [6]. While the figure 11 shows ductile fracture for the Al 6061/SiC, 12% V_f composite, with no extensive diameter contraction. Figure 12 shows the SEM of the same composite revealing medium size dimples with tear ridges, and most of the particles are firmly embedded in the matrix.

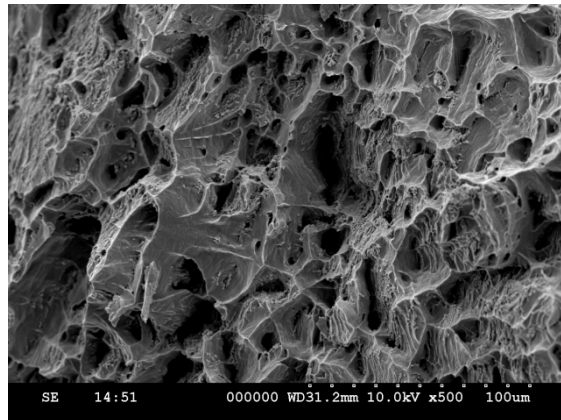


Figure 12: SEM tensile fracture surface of the 12% V_f Al/SiC composite

Figure 13 shows that the fracture is intermediate between the ductile and brittle fracture. The dimples in the figure 14 for Al 6061/SiC, 16% V_f are same to that in figure 12 but greater percentage matrix-particle decohesion than previously was observed for the 12% SiC composite.



Figure 13: SEM tensile fracture surface of the 16% V_f Al/SiC composite

Figure 15 shows the fracture surface of the Al 6061/SiC 20% V_f , the fracture surface appears to be flat and normal to stress axis on macroscopic scale. The fracture surface appears to contain many macrovoids (figure 16) in the matrix. With much different from those observed for smaller volume fraction. The matrix-particle decohesion was also observed but more extensively than those observed for 12% and 16% volume fraction composites. The brittle fracture of these composites indicates that void growth and coalescence occurred rapidly.

Voids nucleation, growth, and coalescence contributed to final fracture in the matrix.

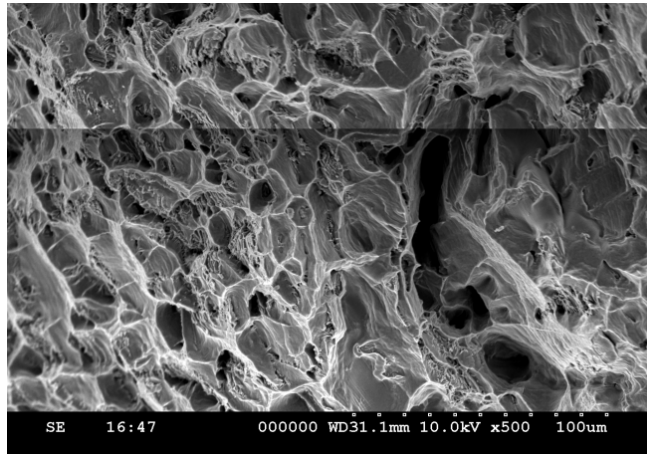


Figure 14: SEM of fracture surface of 16% V_f Al 6061/SiC composite



Figure15: SEM tensile fracture surface of the 20% V_f Al/SiC composite

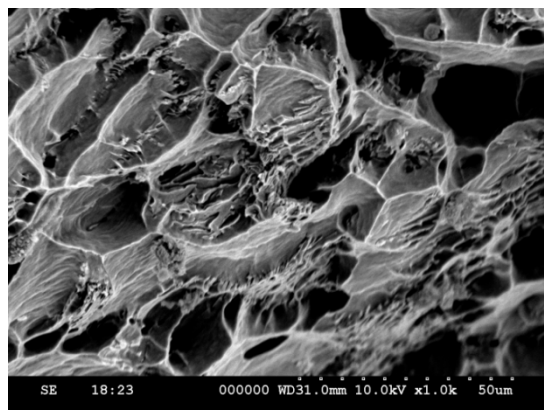


Figure 16: SEM of fracture surface of 20% V_f Al 6061/SiC composite

4. CONCLUSION

The geometrical constraints imposed on deformation cause by the presence of the hard and brittle SiC particles in the soft and ductile Al 6061 metal matrix. It is required a high value of stress to initiate plastic deformation in the matrix. This result in increase σ_u and Y_s for the composites and it is increase with increase of volume fraction and decrease the particle size. The degree of clustering and agglomeration in Al-6061/SiC increases and the ductility decreases with increase the reinforcement.

5. ACKNOWLEDGMENT

The authors acknowledge with thanks, ICCR Indian Council for Culture Relation, Tapasya Casting Private Limited – Hyderabad, Jyothi Laboratories – Hyderabad, Indian Institute of Chemical Technology – Hyderabad for technical help and Hyderabad Engineering Laboratories.

REFERENCES

1. B. Kotiveerachari, A. Chennakesava Reddy, Interfacial effect on the fracture mechanism in GFRP composites, CEMILAC Conference, Ministry of Defence, India, 20-21st August, 1999: B85-87.
2. A. Chennakesava Reddy, Fracture behavior of brittle matrix and alumina trihydrate particulate composites, Indian Journal of Engineering & Materials Sciences, 2002:5, pp.365-368.
3. A. Chennakesava Reddy, B. Kotiveerachari, Effect of matrix microstructure and reinforcement fracture on the properties of tempered SiC/Al-alloy composites, National conference on advances in materials and their processing, Bagalkot, 28-29th November 2003, pp.121-124.
4. A. Chennakesava Reddy, Finite element analysis of elastic-plastic and tensile damage response in carbon-carbon composites under vehicular crush conditions, National Conference on Emerging Trends in Mechanical Engineering, Nagpur, 05-06th February, 2004: IIA-6.
5. A. Chennakesava Reddy, Experimental evaluation of elastic lattice strains in the discontinuously SiC reinforced Al-alloy composites, National Conference on Emerging Trends in Mechanical Engineering, Nagapur, 05-06th February 2004: VC-12.
6. A. Chennakesava Reddy, Analysis of the relationship between the interface structure and the strength of carbon-aluminum composites, NATCON-ME, Bangalore, 13-14th March 2004, pp.61-62.
7. B. Ramana, A. Chennakesava Reddy, S. Somi Reddy, Fracture analysis of mg-alloy metal matrix composites, National Conference on Computer Applications in mechanical Engineering, Anantapur, 21st December 2005, pp.57-61.
8. A. Chennakesava Reddy, Strength and fracture mechanisms in carbon-carbon composites, International symposium on Advanced Materials and Processing, Bagalkot, 29-30, October 2007, pp.138-145.
9. A. Chennakesava Reddy, Mechanical properties and fracture behavior of 6061/SiCp Metal Matrix Composites Fabricated by Low Pressure Die Casting Process, Journal of Manufacturing Technology Research, 2009:1, pp.273-286.
10. A. Chennakesava Reddy, Essa Zitoun, Matrix al-alloys for alumina particle reinforced metal matrix composites, Indian Foundry Journal, 2009:55(1), pp.12.

10. A. Chennakesava Reddy, B. Kotiveerachari , Effect of aging condition on structure and the properties of Al-alloy / SiC composite, International Journal of Engineering and Technology, 2010:2(6), pp.462-465.
11. A. Chennakesava Reddy, Tensile properties and fracture behavior of 6063/SiC_p metal matrix composites fabricated by investment casting process, International Journal of Mechanical Engineering and Materials Sciences, 2010:3(1), pp.73-78.
12. A. Chennakesava Reddy, M. Vidya Sagar, Two-dimensional theoretical modeling of anisotropic wear in carbon/epoxy FRP composites: comparison with experimental data, International Journal of Theoretical and Applied Mechanics, 2010:6(1), pp.47-57.
13. A. Chennakesava Reddy, Essa Zitoun, Tensile behavior Of 6063/Al₂O₃ particulate metal matrix composites fabricated by investment casting process, International Journal of Applied Engineering Research, 2010:1(3), pp.542-552.
14. A. Chennakesava Reddy , Essa Zitoun , Matrix al-alloys for silicon carbide particle reinforced metal matrix composites, Indian journal of Science and Technology, 2010:3(12), pp.1184-1187.
15. A. Chennakesava Reddy, Essa Zitoun, Tensile properties and fracture behavior of 6061/Al₂O₃ metal matrix composites fabricated by low pressure die casting process, International Journal of Materials Sciences, 2011:6(2), pp.147.
15. A. Chennakesava Reddy, Influence of strain rate and temperature on superplastic behavior of sinter forged Al6061/SiC metal matrix composites, International Journal of Engineering Research & Technology, 2011:4(2), pp.189.
16. A. Chennakesava Reddy, Strengthening mechanisms and fracture behavior of 7072Al/Al₂O₃ metal matrix composites, International Journal of Engineering Science and Technology, 2011:3(7), pp.6090-6100.
17. A. Chennakesava Reddy, Evaluation of mechanical behavior of Al-alloy/Al₂O₃ metal matrix composites with respect to their constituents using Taguchi , International Journal of Emerging Technologies and Applications in Engineering Technology and Sciences, 2011:4(2), pp.26-30.
18. A. Chennakesava Reddy, Tensile fracture behavior of 7072/SiC_p metal matrix composites fabricated by gravity die casting process, Materials Technology: Advanced Performance Materials, 2011:26(5), pp.257-262.
19. A. Chennakesava Reddy , Evaluation of mechanical behavior of Al-alloy/SiC metal matrix composites with respect to their constituents using Taguchi techniques, i-manager's Journal of Mechanical Engineering, 2011:1(2), pp.31.
20. A. Chennakesava Reddy, B. Kotiveerachari, Influence of microstructural changes caused by ageing on wear behavior of Al6061/SiC composites, Journal of Metallurgy & Materials Science, 2011:53(1), pp.31-39.
21. S. Sreenivasulu, A. Chennakesava Reddy, Mechanical Properties Evaluation of Bamboo Fiber Reinforced Composite , International Journal of Engineering Research, 2014:3(1), pp.187-194.

FRACTURE BEHAVIOR OF ALUMINA PARTICLES REINFORCED WITH DIFFERENT MATRIX ALUMINIUM ALLOYS

G. Satish Babu and A. Chennakesava Reddy

Professor, Department of Mechanical Engineering, JNTUH College of Engineering, Hyderabad

Abstract: Al/Al₂O₃ metal matrix composites exhibits lower ductility than the matrix alloy. The ductility decreases with increasing amount of reinforcement in Al/Al₂O₃ metal matrix composites. The larger ceramic particle size is detrimental to composite strength. The decrease in the particle size increases the ultimate tensile strength. The fracture surfaces of fractured Al/Al₂O₃ MMC specimens reveal dimple morphology. The tensile fracture behavior of Al/ Al₂O₃ metal matrix composites is observed to be ductile in nature.

Keywords: alumina, metal matrix composites, low pressure die casting process, fracture.

Address all correspondence to:

1. INTRODUCTION

Metal matrix composites usually consist of a continuous phase called the matrix and discontinuous phase in the form of fibers, whiskers or particles called the reinforcement. The addition of ceramic particles into light alloys would guarantee exceptionally high specific elastic modulus, strength-to-weight ratio, fatigue strength, wear resistance [1]. These important characteristics have made the reinforced aluminium alloy based metal matrix composites an attractive and viable nominee for automobile and aerospace applications [1-21].

2. THE MOTIVATION AND OBJECTIVES

The need for satisfying high fuel-economy goals in the automobile and ground transportation industries is a major challenge. The metal matrix composites based on lightweight alloys will play a significant role. Classes of MMCs which have grown in stature to emerge and attract attention are both the magnesium and aluminium alloy metal matrices discontinuously reinforced with silicon carbide and Al₂O₃ particulates. While few studies have focused on establishing an understanding of the influence of particulate reinforcements on matrix microstructure and concurrent fracture behavior for particulate reinforced metal matrix composites is limited and there does a critical need to examine and understand this aspect of mechanical consideration.

The main objectives of this work are to characterize fracture behavior of Al/Al₂O₃ metal matrix composites. In this research work, the effect of

type of aluminum alloy matrix and type of reinforcement materials, and volume fraction and particle size of the reinforcement on the mechanical behavior have been evaluated. The fracture mechanisms in Al/Al₂O₃ metal matrix composites have also been characterized. The schematic representation of the current research work is shown in figure 1.

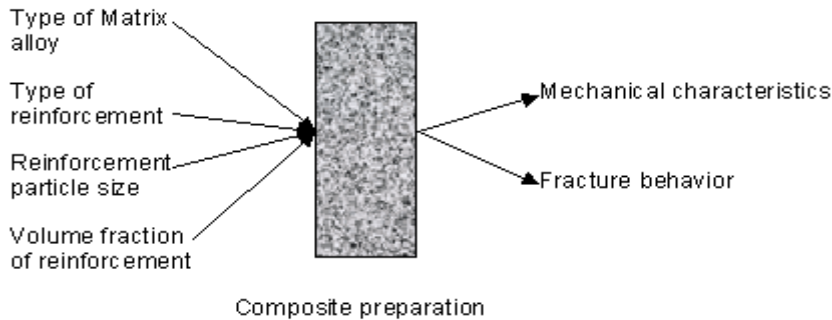


Figure 1: Schematic representation of the current research work

3. EXPERIMENTAL PROCEDURE

Al/Al₂O₃ metal matrix composites were prepared by low pressure die casting process. Several test samples of these composites were prepared with reinforcement content of 12, 16 and 20% volume fraction, different type of aluminum matrix Al6061, Al6063 and Al7072, and different particle sizes (such as 10, 20 and 30 μm) of Al₂O₃ reinforcements.

The mechanical behavior of the metal matrix composites was evaluated in terms of ultimate tensile strength, and ductility (in terms of tensile elongation). The microstructural examination of the test samples was carried out to reveal and study the distribution of reinforcement particles, grain structure, the matrix-particle interfaces, and the formation of intermetallics in the metal matrix composites. The fractured surfaces of the tested specimens under tensile loading were examined using scanning electron microscope (SEM). The dimensions of tensile specimens are shown in figure 2.

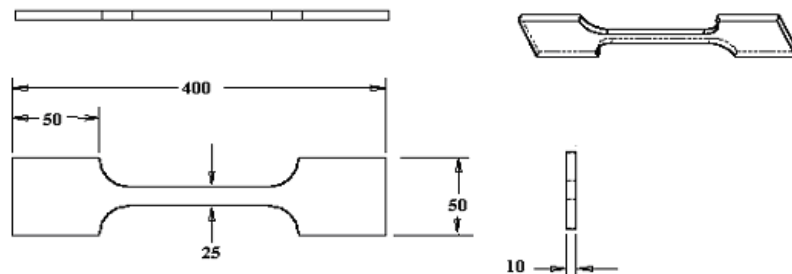


Figure 2: Tensile specimen, all dimensions are in mm

4. RESULTS AND DISCUSSION

The effects of matrix microstructure and reinforcement (in terms of % volume fraction and particle size) are focused on the properties of

alumina (Al_2O_3) and SiC reinforced Al-alloy composites. Type of fracture occurred in these composites is also addressed. Suitability of manufacturing automobile components is also presented.

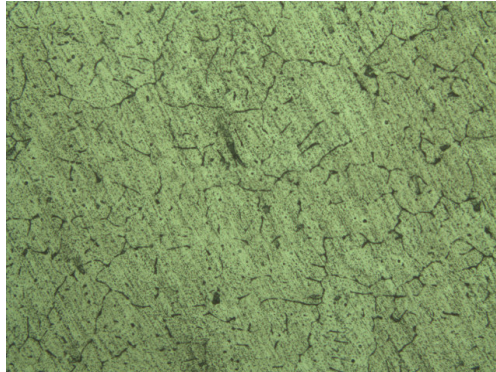


Figure 3: Microstructure of MMC (Al 6061 matrix, 12% Al_2O_3 , 10 μm particle size), 200X

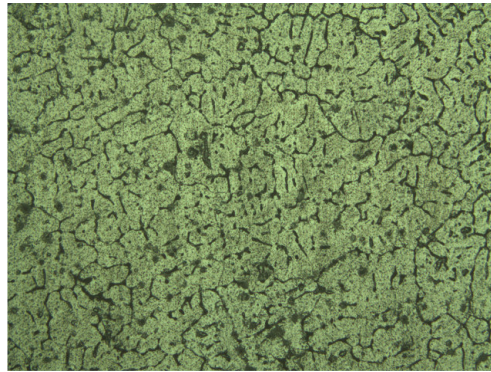


Figure 4: Microstructure of MMC (Al 6063 matrix, 20% Al_2O_3 , 10 μm particle size), 200X

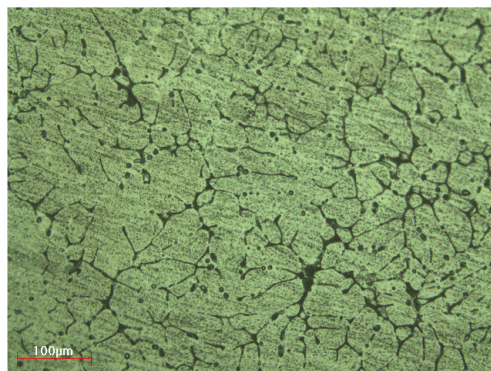


Figure 5: Microstructure of MMC (Al 7072 matrix, 16% Al_2O_3 , 10 μm particle size), 200X

4.1 Undeformed Microstructures of Al-alloy/ Al₂O₃ composites

The various intermetallics can be revealed in the microstructures shown in figures 3-5. In the as-cast condition, Al is present both in solid solution with the matrix and precipitated as Al₁₂Mg₁₇ phase that is present at and along the grain boundaries. A non-uniform distribution of Al₂O₃ particulates through the Al-alloy metal-matrix with evidence of clustering, or agglomeration is observed. MgO and MgAl₂O₄ are also seen along the grain boundaries. The phases Al₂Cu, Mg₂Si, Al₅Cu₂Mg₈Si₆ and Al₄CuMg₅Si₄ are also observed in the microstructures.

4.2 Effect of % Volume Fraction on Mechanical Properties

Figure 6 illustrates the influence of % volume fraction of Al₂O₃ (reinforcement) on the ultimate tensile strength of Al-Al₂O₃ metal matrix composites. The graphs indicate that the ultimate tensile strength increases with increase in % volume fraction of reinforcement in the composite. With increasing volume fraction, more load is transferred to the reinforcement which results in a higher ultimate tensile strength.

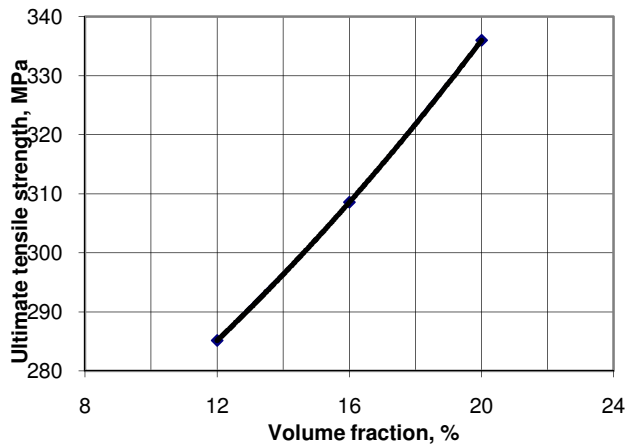


Figure 6: Influence of volume fraction on the ultimate tensile strength of Al/Al₂O₃ composite

The effect of volume fraction on the ductility of the composites is shown in figure 7. The decrease in ductility can be attributed to the earlier onset of void nucleation with increasing amount of reinforcement. The high stress concentration at the tip of the cracked particles can also contribute to a decrease in the ductility (tensile elongation) in the composite.

4.3 Effect of particle size of reinforcement on the mechanical properties

Figure 8 illustrates the effect of particle size on the ultimate tensile strength. The decrease in the particle size increases the ultimate tensile strength. This is because, the small particle size means a lower inter-particle spacing so that nucleated voids in the matrix are unable to coalesce as easily. Also, the larger ceramic particle size is detrimental to

composite strength. This is on account of the strength distribution of a ceramic particulates population obeys weibull statistics. The agglomeration could contribute a reinforcing effect in the aluminium matrix. The inhomogeneous distribution of reinforcement reduces the effective amount of particulates for strengthening.

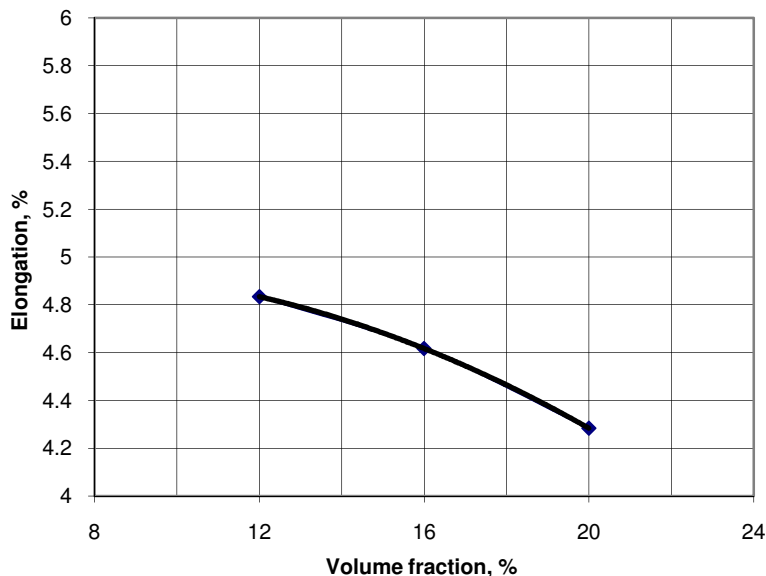


Figure 7: Influence of volume fraction on the ductility of Al/ Al₂O₃ composite

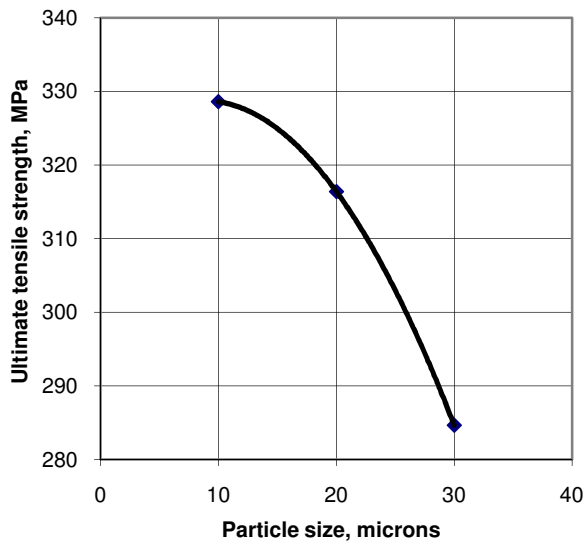


Figure 8: Influence of particle size on the ultimate tensile strength of Al/ Al₂O₃ composite

There is an increase in the ductility with a decrease in the particle size of the reinforcement (figure 9). At relatively large particle sizes, a significant amount of particle cracking takes place during tensile testing

of the composites. Cracked particles do not carry any load effectively and can be effectively thought of as voids, so the ductility is decreased.

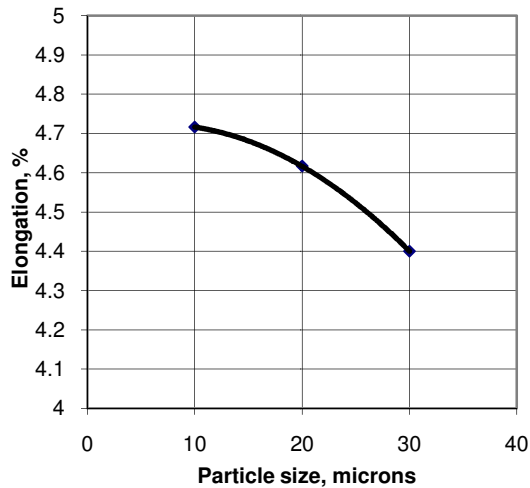


Figure 9: Influence of particle size on the ductility of Al/ Al₂O₃ composite

4.4 FRACTURE MECHANISM IN Al/Al₂O₃ COMPOSITES

Study of the fracture surface of fractured MMC specimens by scanning electron microscope (SEM) reveals dimple morphology (figures 10-12). In fact, it is very difficult to detect any major change in dimple morphology in different samples because both in size and distribution of the dimples in the dimple-dominated areas are mainly governed by the size and distribution of the reinforcing particles. In addition, there is a minor fraction of fracture surface that is dominated by smaller dimples (figures 10 and 12) that is mainly distributed at the boundaries between the larger dimples, probably due to ductile rupture of the matrix. Occurrence of the dimple morphology certainly leads to the conclusion that these types of materials fail mainly via a void nucleation and growth mechanism.

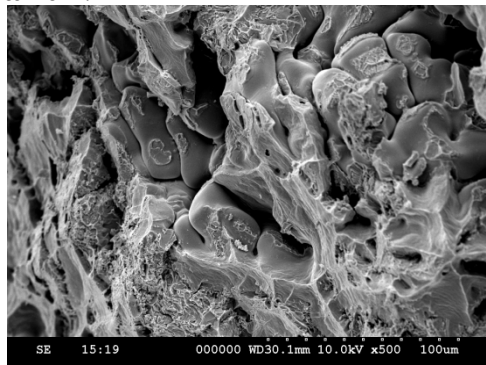


Figure 10: SEM of fracture surface of Al₂O₃/Al6061 composite (V=20% and P =30μm); 1000X

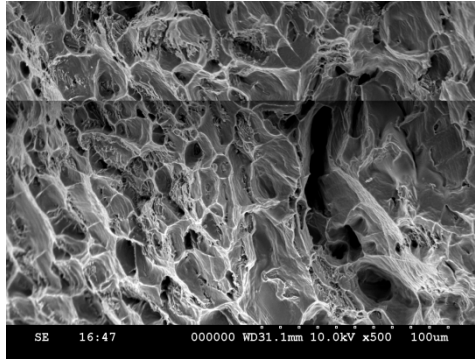


Figure 11: SEM of fracture surface of Al₂O₃/Al6063 composite (V=20% and P=10 μ m); 1000X

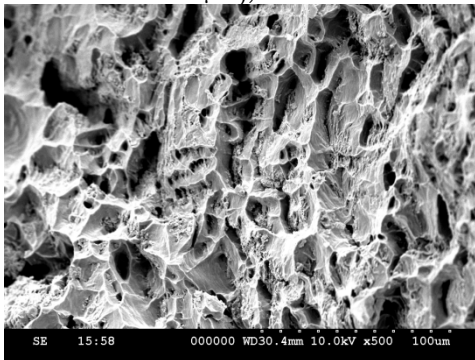


Figure 12: SEM of fracture surface of Al₂O₃/Al7072 composite (V = 6% and P =10 μ m); 1000X

5. CONCLUSIONS

The major conclusions drawn from the current research work are as follows:

1. The ductility of Al/Al₂O₃ metal matrix composites is much lower than that of un-reinforced Al-alloy.
2. The ultimate tensile of Al/Al₂O₃ metal matrix composites is only marginally higher than yield strength indicating that the work hardening rate past yielding is low.
3. In the as-cast condition, Al is present both in solid solution with the matrix and precipitated as Al₁₂Mg₁₇ phase along the grain boundaries. MgO and MgAl₂O₃ are also formed along the grain boundaries.
4. The ductility decreases with increasing amount of reinforcement in Al/Al₂O₃ metal matrix composites.
5. The decrease in the particle size increases the yield strength, ultimate tensile strength, bending force, hardness, and ductility (tensile elongation). The larger ceramic particle size is detrimental to composite strength.
6. Al₂O₃ particles aggregated to form coarse clusters in the matrix. The degree of agglomeration increases with the particulate volume fraction in the case Al 6063 and Al 7072 matrix alloys.

7. The tensile fracture behavior of Al/ Al₂O₃ metal matrix composites is observed to be ductile in nature.
8. The fracture surfaces of fractured Al/Al₂O₃ MMC specimens reveal dimple morphology. There is an occurrence of interface or near interface debonding in the Al/Al₂O₃ composites.

REFERENCES

1. B. Kotiveerachari, A. Chennakesava Reddy, Interfacial effect on the fracture mechanism in GFRP composites, CEMILAC Conference, Ministry of Defence, India, 20-21st August, 1999: B85-87.
2. A. Chennakesava Reddy, Fracture behavior of brittle matrix and alumina trihydrate particulate composites, Indian Journal of Engineering & Materials Sciences, 2002:5, pp.365-368.
3. A. Chennakesava Reddy, B. Kotiveerachari, Effect of matrix microstructure and reinforcement fracture on the properties of tempered SiC/Al-alloy composites, National conference on advances in materials and their processing, Bagalkot, 28-29th November 2003, pp.121-124.
4. A. Chennakesava Reddy, Finite element analysis of elastic-plastic and tensile damage response in carbon-carbon composites under vehicular crush conditions, National Conference on Emerging Trends in Mechanical Engineering, Nagpur, 05-06th February, 2004: IIA-6.
5. A. Chennakesava Reddy, Experimental evaluation of elastic lattice strains in the discontinuously SiC reinforced Al-alloy composites, National Conference on Emerging Trends in Mechanical Engineering, Nagapur, 05-06th February 2004: VC-12.
6. A. Chennakesava Reddy, Analysis of the relationship between the interface structure and the strength of carbon-aluminum composites, NATCON-ME, Bangalore, 13-14th March 2004, pp.61-62.
7. B. Ramana, A. Chennakesava Reddy, S. Somi Reddy, Fracture analysis of mg-alloy metal matrix composites, National Conference on Computer Applications in mechanical Engineering, Anantapur, 21st December 2005, pp.57-61.
8. A. Chennakesava Reddy, Strength and fracture mechanisms in carbon-carbon composites, International symposium on Advanced Materials and Processing, Bagalkot, 29-30, October 2007, pp.138-145.
9. A. Chennakesava Reddy, Mechanical properties and fracture behavior of 6061/SiCp Metal Matrix Composites Fabricated by Low Pressure Die Casting Process, Journal of Manufacturing Technology Research, 2009:1, pp.273-286.
10. A. Chennakesava Reddy, Essa Zitoun, Matrix al-alloys for alumina particle reinforced metal matrix composites, Indian Foundry Journal, 2009:55(1), pp.12.
10. A. Chennakesava Reddy, B. Kotiveerachari, Effect of aging condition on structure and the properties of Al-alloy / SiC composite, International Journal of Engineering and Technology, 2010:2(6), pp.462-465.
11. A. Chennakesava Reddy, Tensile properties and fracture behavior of 6063/SiCP metal matrix composites fabricated by investment casting process, International Journal of Mechanical Engineering and Materials Sciences, 2010:3(1), pp.73-78.
12. A. Chennakesava Reddy, M. Vidya Sagar, Two-dimensional theoretical modeling of anisotropic wear in carbon/epoxy FRP composites: comparison with experimental data, International Journal of Theoretical and Applied Mechanics, 2010:6(1), pp.47-57.
13. A. Chennakesava Reddy, Essa Zitoun, Tensile behavior Of 6063/Al₂O₃ particulate metal matrix composites fabricated by investment casting process, International Journal of Applied Engineering Research, 2010:1(3), pp.542-552.

14. A. Chennakesava Reddy , Essa Zitoun , Matrix al-alloys for silicon carbide particle reinforced metal matrix composites, *Indian journal of Science and Technology*, 2010:3(12), pp.1184-1187.
15. A. Chennakesava Reddy, Essa Zitoun, Tensile properties and fracture behavior of 6061/Al₂O₃ metal matrix composites fabricated by low pressure die casting process, *International Journal of Materials Sciences*, 2011:6(2), pp.147.
15. A. Chennakesava Reddy, Influence of strain rate and temperature on superplastic behavior of sinter forged Al6061/SiC metal matrix composites, *International Journal of Engineering Research & Technology*, 2011:4(2), pp.189.
16. A. Chennakesava Reddy, Strengthening mechanisms and fracture behavior of 7072Al/Al₂O₃ metal matrix composites, *International Journal of Engineering Science and Technology*, 2011:3(7), pp.6090-6100.
17. A. Chennakesava Reddy, Evaluation of mechanical behavior of Al-alloy/Al₂O₃ metal matrix composites with respect to their constituents using Taguchi , *International Journal of Emerging Technologies and Applications in Engineering Technology and Sciences*, 2011:4(2), pp.26-30.
18. A. Chennakesava Reddy, Tensile fracture behavior of 7072/SiCp metal matrix composites fabricated by gravity die casting process, *Materials Technology: Advanced Performance Materials*, 2011:26(5), pp.257-262.
19. A. Chennakesava Reddy , Evaluation of mechanical behavior of Al-alloy/SiC metal matrix composites with respect to their constituents using Taguchi techniques, *i-manager's Journal of Mechanical Engineering*, 2011:1(2), pp.31.
20. A. Chennakesava Reddy, B. Kotiveerachari, Influence of microstructural changes caused by ageing on wear behavior of Al6061/SiC composites, *Journal of Metallurgy & Materials Science*, 2011:53(1), pp.31-39.
21. S. Sreenivasulu, A. Chennakesava Reddy, Mechanical Properties Evaluation of Bamboo Fiber Reinforced Composite , *International Journal of Engineering Research*, 2014:3(1), pp.187-194.

EXPERIMENTAL ANALYSIS OF Z-PINNED CARBON FIBER COMPOSITES

J.Dhanraj Pamar ^a B.Balu Naik ^b and
Md.Kashfuddoja ^c

Senior Assistant Professor^a, M.J. College of Engineering & Technology,
Hyderabad

Principal^b, JNTU College of Engineering, Hyderabad, Manthani
Research Scholar^c, Indian Institute of Technology, Hyderabad

Abstract: Finite element model for predicting delamination resistance of z-pin reinforced composites laminates. End notched flexure specimen is simulated using a cohesive zone model. The main difference of this approach to the cohesive zone models is that the individual bridging force exerted by z-pin is governed by a specific traction-separation law derived from a unit-cell model of single pin failure process, which is independent of the fracture toughness of the unreinforced laminate. Therefore, two separate traction-separation laws are employed; one represents unreinforced laminate properties and the other for the enhanced delamination toughness owing to the pin bridging action. This approach can account for the so-called large scale bridging effect and avoid using concentrated pin forces in numerical models, thus removing the mesh-size dependency and permitting more accurate and reliable computational solutions.

Keywords: Delamination, Fracture, Finite element Method, Multiscale modeling, Z-pins.

1. INTRODUCTION

Failure characteristics and z-pin delamination suppression mechanism are well understood and developed in this paper. Z-pin bridging effect has been modelled by either averaging the bridging forces over the entire reinforced area, nonlinear springs exerting concentrated traction force at the pin location. Usually the bridging force is not constant during crack growth due to the pin's local effect; therefore enhanced fracture toughness is not best represented by averaging the traction forces. On the other hand, using concentrated forces in numerical models can cause stress singularities, consequently the solution can be mesh dependent. To overcome these difficulties, cohesive zone models (CZM) have been used recently for modelling adhesive failure or delamination in both pinned and unpinned laminates. However, there is still the need for more robust and efficient analysis models for design purpose. Models are also needed for recently developed structures reinforced by larger diameter rods. A novel approach based on the cohesive fracture model is presented for predicting the mode I delamination suppression in z-pinned laminates. It is different from the current methods in the open literature that use either an average value

of enhanced toughness or CZM for unpinned area only. Rather, two separate cohesive laws are employed to represent the delamination toughness of the unpinned and pinned areas, respectively. Due to the pin's nonlinear behavior under the mode II load and deformation mode switch from bending dominant to axial tension, single pin pullout model presented in this paper is different from that of the model I. Pin bridging law is determined analytically using the classic beam theory that is subsequently implemented into a macro scale model of the End Notched Flexure (ENF) geometry.

2. MODELLING STRATEGY

The model is presented in Figure 1. Fracture mechanics theory on strain energy balance in z-pinned laminates can be found. The idea is to use two traction-separation laws (TSL) representing the unpinned laminate and pinned locations respectively. The unpinned TSL is governed by the intrinsic toughness of the laminate, whereas the pin bridging force offers much enhanced toughness in pin locations. A multi-scale model has been developed. Firstly, the pin bridging force is evaluated by an analytical unit-cell model of single-pin accounting for two failure modes: pin rupture or pullout. The resultant bridging law is then implemented in a macro-scale structural model. This modelling approach has the advantage of accounting for the local enhancement effect due to z-pins, avoiding either averaging the pin forces over the whole reinforcement area or using concentrated pin forces. The large scale bridging effect is better represented.

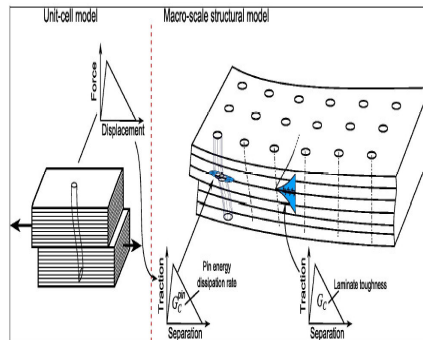


Figure 1: Multiscale modeling

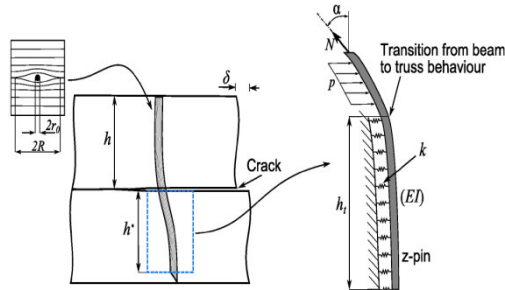


Figure 2: Single pin pull out model

3. SINGLE-PIN PULLOUT MODEL

It comprises a laminate with a centre delamination and a z-pin. Assuming the pin's chamfer end is negligible; the specimen is symmetric with respect to the central plane and is loaded anti symmetrically. Therefore only one half of the pin is modelled. Considering that pin pullout is more likely to occur at the part with the chamfer, pin insertion depth in the model is reduced by the chamfer size. All afore mentioned three phases are modelled. During the elastic response the pin is assumed to react as a beam supported by an elastic spring foundation. Stiffness of the spring foundation is estimated by the elastic properties of the nearby laminate using the dimension of the resin rich zone around the pin. Since the resin rich pocket extends in the fibre direction and the laminate properties in the cross-fibre direction are dominated also by the resin, material properties close to the pin are assumed to be homogeneous and isotropic, and equal to the transverse stiffness of the surrounding laminate. During the elastic deformation phase pin's lateral displacement u can be expressed by following differential equation:

$$EI \frac{\partial^2 u}{\partial z^4} + ku = 0 \quad (1)$$

where EI is the pin's bending rigidity, k the elastic constant of the spring foundation mimicking the stress distribution in the laminate acting on the pin, which is calculated by:

$$k = \frac{\prod E_{lam}}{2 \ln\left(\frac{R}{r_o}\right)} \quad (2)$$

where r_o and R are radius of the pin and resin rich zone, which is usually 4-6 times of the pin radius (in this model $R = 5r_o$). Let δ be the applied shear displacement between the two laminate parts and set the following boundary conditions:

$$u(h) = \frac{\delta}{2}, \quad u''(h) = 0, \quad u''(0) = 0, \quad u'''(0) = 0 \quad (3)$$

During the pin ploughing phase laminate is assumed to react as a perfectly plastic material; the lateral force exerted on the pin is therefore constant and independent of the displacement. The force per unit length (p) represents the resistance of the laminate being punched by a blunt notch. Following differential equation describes the pin's lateral displacement in the ploughing zone.

$$N \frac{\partial^2 u}{\partial z^2} + \frac{\partial^2 N}{\partial z} \frac{\partial u}{\partial z} = p \quad (4)$$

where N is the axial stress on the pin and p the lateral reaction force per unit length acting on the laminate. Z-pin displacement in the transverse direction depends on the distribution of the axial stress in the pin. The friction resistance is the physical mechanism by which pin carries axial

load. Following differential equation, derived from the force balance in the pin axial direction, describes pin's axial stress distributed along the axis:

$$\frac{\partial N}{\partial z} = \mu(\sigma_{o+k|u|}) \quad (5)$$

$$\frac{\partial N}{\partial z} = \mu p$$

where μ is the Coulomb friction coefficient between pin and laminate, σ_0 the compressive residual stress arising from the curing process and h_t the length of transition between the elastic and plastic behaviour. Note that h_t is not constant during the simulation. The transition is assumed to occur when the pin starts having large lateral displacements, thus when the shear strength (S_u) is exceeded the pin will split into several ligaments. Initial stress σ_0 is estimated by the following equation.

$$\sigma_0 = \frac{\Delta T(\alpha_{lam} - \alpha_{pin})E_{lam}E_{pin}}{E_{lam} + E_{pin}} \quad (6)$$

where temperature difference $\Delta T=150^\circ\text{C}$, coefficients of thermal expansion of the pin and laminate are $\alpha_{pin} = 0$ and $\alpha_{lam} = 2.4 \times 10^{-5} \text{ K}^{-1}$. The mathematical problem is solved using the boundary condition of the axial stress:

$$N(L) = F \sin \alpha \quad (7)$$

The extent of ploughing depends on the applied load magnitude (it is larger if the load increases); the maximum bridging force is estimated by considering two critic conditions that lead two failure modes:

- (1) axial stress exceeds the friction resistance resulting in the pin being pulled out;
- (2) axial stress overcomes z-pin tensile strength causing the pin rupture failure.

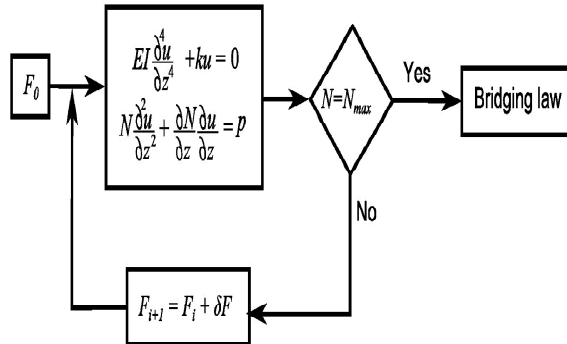


Figure3: Single pin bridging force

Force and shear displacement relationship of different configurations shown in figure 4(a) & (b). (1) an initial linear elastic response before

force reaches 20 N, after which point the pin is subjected to larger deformation and ploughing into the laminate. During the ploughing phase despite the curve becomes more compliant it continuously increases to a maximum value. At this peak force one of the two failures occur: pin abrupt rupture resulting in sudden drop of the reaction force, or pin is gradually pulled out manifesting a linear decrease of the bridging force. When the pin is completely pullout, the displacement equals to the pin embed length. Another failure mode is abrupt pin rupture manifesting a sudden force drop. Following observations can be made: (1) both laminate thickness and pin diameter influence the pin pullout behaviour; the load carrying capability is higher for larger pin diameter and thicker laminates; (2) pin rupture is more likely to occur for smaller diameter pins or pins inserted in thicker laminates; (3) initial stiffness and maximum elastic force are higher for bigger pins.

Figure.5 shows the experimental graph between bridging force vs. displacement. In the test pin were not placed exactly perpendicular to the laminate plane; there was a small deviation to the intended insertion angle. This is characteristic of the technology currently used; therefore, more realistic traction-separation law should be an average of all the possible bridging forces coming from different insertion angles within the range. Two parameters have been used to calibrate the model: the friction coefficient μ and the laminate punch strength p , which is defined. The first parameter controls the occurrence of pin pullout; the higher the friction coefficient, the longer the pullout is delayed and the higher the ultimate bridging force. The second changes the curvature of the upward curve representing the pin's nonlinear response. Higher punch strength results in less surrounding material being affected by pin ploughing; thus stiffer response of the pin. Calibrated model parameters by the test data are given in Table 1.

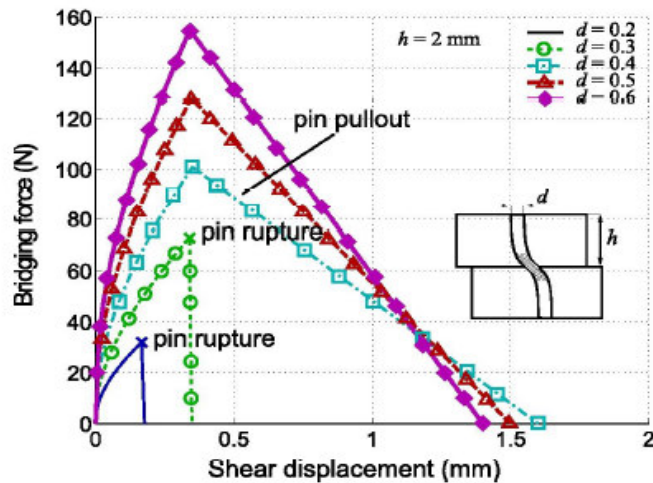


Figure 4: (a) variable pin diameter

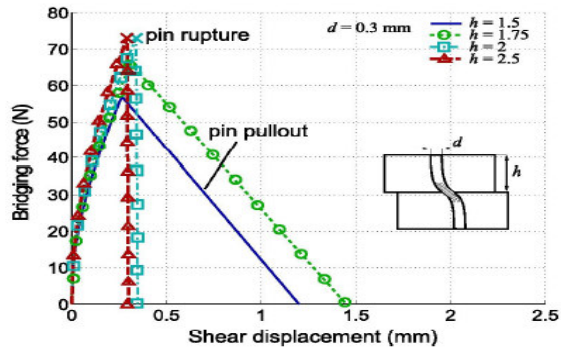


Figure 4: (b) variable laminate

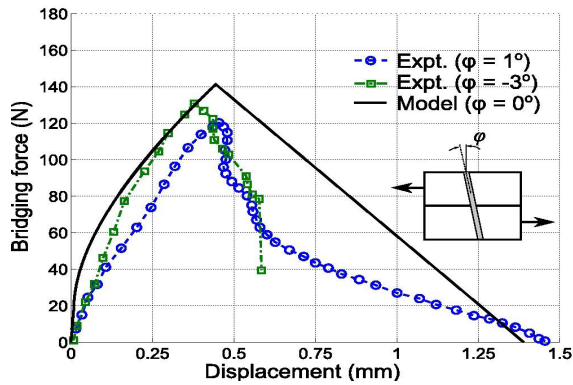


Figure 5: Single pull experimental

Table 1: Mechanical properties used in the unit-cell model.

Z-pin Young's Modulus E_{pin} (GPa)	Laminate Young's Modulus E_{lam} (GPa)	Friction Coefficient $S_{pin} \mu$	Pin axial Strength S_{pin} (MPa)	Pin shear strength S_u (MPa)	Laminate punch strength p (N/mm)
120	11	0.77	1200	100	700

Table 2: Mechanical properties of IMS/924

E_1	E_2	E_3	G_{12}	G_{13}	G_{23}	ν_{12}	ν_{13}	ν_{23}
138	11	11	4.4	4.4	3.92	0.34	0.34	0.4

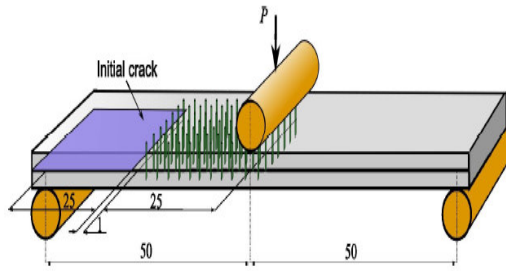


Figure 6: Pinned and unpinned ENF specimen.

4. END NOTCHED FLEXURE MODEL

Pinned and unpinned ENF specimens shown in Figure 6 made of 24 ply unidirectional prepreg IMS/924 resulting in 3 mm nominal thickness. Laminate mechanical properties are listed in Table 2. An initial crack of 25 mm was made by inserting a thin polyamide film in the mid-plane of each specimen. Z-pins were made of pultruded T300/BMI. Reinforced area was designed 5 mm from the initial crack tip extending for 25 mm length covering the entire specimen width. Only half of a pin row and surrounding laminate are modelled by exploiting the pin periodical arrangement. For numerical stability cohesive element size is one fifth of the adjacent shell element. Therefore, this 2D shell element model has one layer of shell elements for each half of the ENF. The bridging force vs. crack opening displacement relation shown in Figure 5 is nonlinear in the curve's rising part. In order to implement this bridging law into a macro-scale FE model. A traction-separation law in terms of the pin stress is deduced from the bridging force shown in Figure 5 & 7; it is expressed as: where u is the shear displacement, $T(u)$ the bridging stress in the pin and $P(u)$ the bridging force.

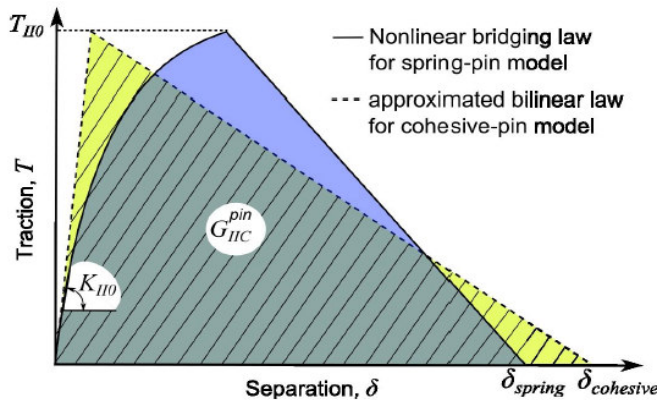


Figure 7: Bridging law spring pin model

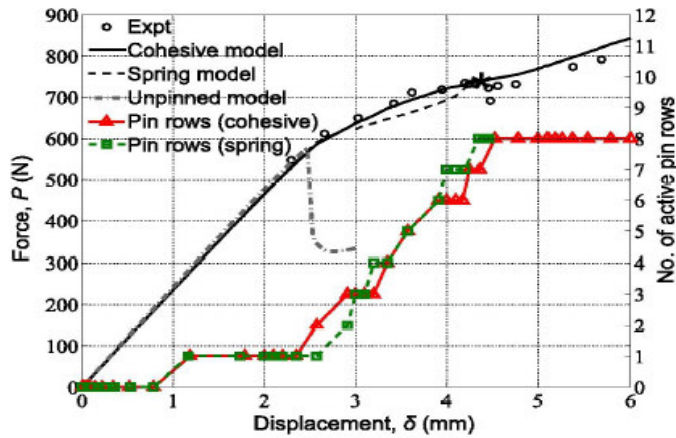


Figure 8: (a) Force Vs Displacement ($d=0.51$)

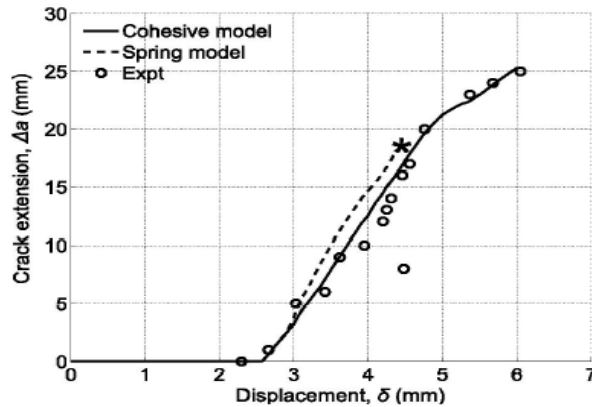


Figure 8:(b) Crack Vs Displacement ($d=0.51$)

Force vs. displacement of three z-pin configurations are shown in Figures. 8(a) & 9(a). Both the cohesive-pin and spring-pin models predict similar force-displacement responses. Cohesive-pin model predicts a slightly higher force and shorter crack extension when the crack size is small (< 4 mm), and two models get closer for larger crack lengths. Difference between the two predictions always remains within 5%, demonstrating that the simplified bilinear bridging law works well. For the 2% pin density cases, the spring-pin model had some difficulty to converge, as the simulation stopped at about 4 mm of applied displacement (marked by asterisk symbol in Figures.8 (b) & 9(b)). On the contrast the cohesive-pin model always reached the end of simulation due to the more robust formulation. For the lower pin density ($A_p = 0.5\%$), spring-pin model ran through. Due to the convergence difficulties the number of incremental steps is much larger for the spring-pin model than that of the cohesive-pin model; consequently, the computing time for the spring-pin model is about four times higher.

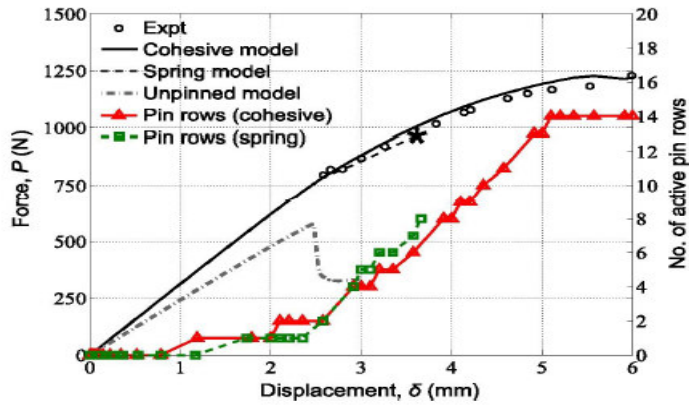


Figure 9: (a) Force Vs Displacement ($d=0.28$)

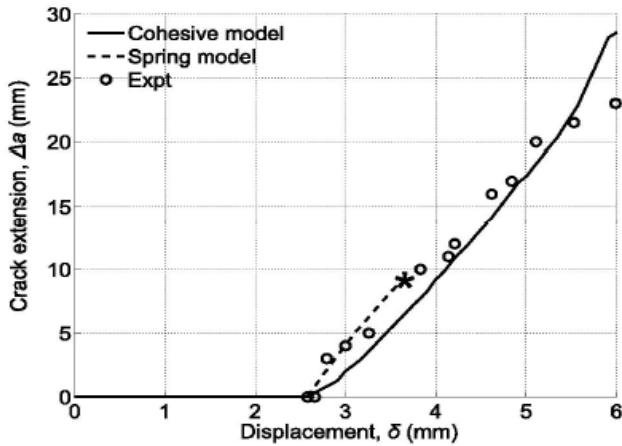


Figure 9: (b) Crack Vs Displacement ($d=0.28$)

The pin bridging effect starts as soon as delaminating crack passes the first pin row. Crack tip is shielded from shear stress as pins bridge the crack wake; hence the applied load recovers from the initial drop and increases to a maximum. Number of active pin rows is presented in figure 10 (a) indicated on the right-hand y -axis. In all three cases the number of active pin rows increases continuously and does not reach a saturate value; it increases up to the total number of pin rows inserted in the laminate. Specimen's final failure occurs due to the laminate crushing failure under bending. This result is in agreement with the constant rising resistance curve (R -curve), where it reports that mode-II fracture toughness of z-pinned laminates constantly increases with the increasing crack length. The absence of a plateau in the R -curve indicates that the number of active pins in the crack wake is still increasing just before the final failure. Edging effect, which is defined as the length of the crack wake where the pins are active.

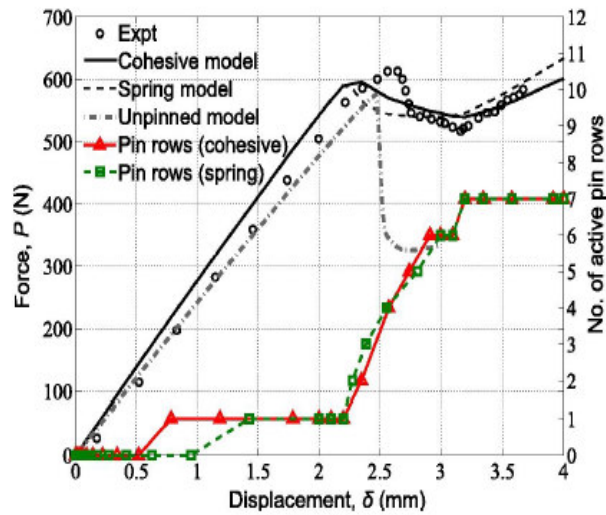


Figure 10: (a) Force Vs Displacement ($d=0.51$)

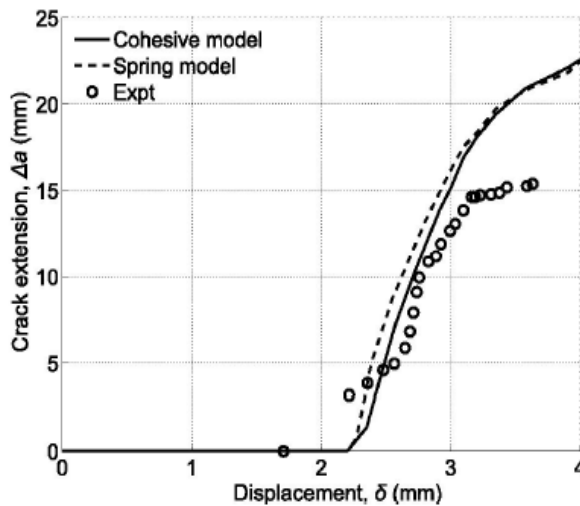


Figure 10:(b) Crack Vs Displacement ($d=0.51$)

Crack length vs. applied displacement is plotted in Figures.9 (b) & 10(b). It is worth noting that in the experiment crack lengths were measured by visual observation; therefore, the comparison of test with models is more for the trend rather than being quantitative. The agreement between the simulation and experiment is reasonably good, particularly for the 2% pin density cases and the 0.5% case when crack is below 15 mm, with percentage error less than 20%. Larger discrepancy is noted for longer cracks (> 15 mm) when it is close to specimen's final failure. Cohesive-pin model predicts slightly shorter

crack length due to employing the simplified bilinear traction-separation law; the pins have stiffer response than the pins model by the springs. However, apart from the initial difference in crack growth length, two models converge in all model cases due to the equivalence in the critical strain energy release rates described by the two bridging laws.

5. CONCLUSION

The main conclusion of this paper is z-pin bridging action can be modelled by nonlinear springs as well as cohesive elements. Bridging laws governing these pin models can be deduced from either single-pin specimen tests or unit-cell models and these pin models can be implemented into a commercial FEM for structural models. The second contribution is the development of a unit-cell model of single-pin pullout model load condition. It can be used for predicting the bridging effect of different pin parameters.

REFERENCES

1. D.D.R.Cartie, M.Troulis, and I.K.Partridge,. Delamination of Z-pinned carbon fibre reinforced Laminates. *Compos Sci Technol* 2006: 66, pp. 855-861.
2. T.M. Koh, S. Feih, A.P.Mouritz, Experimental determination of the structural properties and strengthening mechanisms of z-pinned composite T-joints, *Composite Structures*, 2011: 93, pp. 2269-2276.
3. D.D.R.Cartie, B.N. Cox, and N.a.Fleck, Mechanisms of crack bridging by composite and metallic rods, *Composites Part A* 2004: 35, pp. 1325-1336.
4. K.L.Rugg, B.N.Cox, K.E.Ward, and G.O.Sherrick, Damage mechanisms for angled through-thickness rod reinforcement in carbon-epoxy laminates. *Composites Part A* 1999: 29, pp. 1603-1613.
5. R.M.Jones, *Mechanics of Composites materials*. New York: McGraw-Hill, 1975: pp-34-86.
6. W.H.Michael, *Analysis of Fiber Reinforced Composites Materials*. New York: McGraw-Hill, 1977: pp-213-220.
7. B. Kotiveerachari, A. Chennakesava Reddy, Interfacial effect on the fracture mechanism in GFRP composites, CEMILAC Conference, Ministry of Defence, India, 20-21st August, 1999:B85-87.
8. A. Chennakesava Reddy, Strength and fracture mechanisms in carbon-carbon composites, International symposium on Advanced Materials and Processing, Bagalkot, 29-30 , October 2007, pp.138-145.

MECHANICAL PROPERTIES OF NATURAL COMPOSITE MATERIALS

Akula Komuraiah ^{a *}, N.Shyam Kumar ^b B.Durga Prasad ^c

a. Research scholar JNTU Anantapur, Andhra Pradesh- India ,

b. Principal WITS Warangal Andhra Pradesh India

c. Prof, JNTU Anantapur Andhra Pradesh – India

Abstract: The conventional composite materials make the environment polluted. The pollution makes the soil unfertile, the plants cannot grow in the polluted soils. The soil and water pollution by the plastic based composites is also dangerous for the human living. These conventional plastic based composites should be replaced by natural composites. To fabricate the natural composites resins like PLA, Urea formaldehyde, starch resins and the fibers like cotton, jute , hemp are used. These natural composites have comparable properties with the conventional composites. In this paper, the mechanical properties of hemp fiber reinforced composite materials are found. The mechanical properties like tensile test, three point bending test, fracture toughness, impact strengths are found. These properties are compared with the engineering materials and a conclusion is made to find the application of these natural composites. The natural composites widely used in household interior decorations, automotive interiors. One of the outstanding advantages of the natural composites is that they are easily and safely disposable. Plaster of paris will also be widely used as a resin to make natural composites, this will pollute to some extent but the pollution is not as bad as made by the plastic composites.

Keywords: natural composites, mechanical characterization, plaster of paris, fracture toughness, tensile strength, impact strength.

Address all correspondence to: akulako@gmail.com

1. INTRODUCTION

The natural composites are gaining importance because of their low impact on polluting the atmosphere. A lot of research is going on to make a material with suitable mechanical properties with easily degradable materials. The composite materials should be such that, when they are no longer in use, they should be easily disposable. For complete analysis of the composites they should be characterized.

The advantage of using bio-resources is that, they are multifunctional, their flexibility in characteristics, biodegradability and wide distribution all over the world [1]. The tensile properties of natural fiber reinforce polymers (both thermoplastics and thermo sets) are mainly influenced by the interfacial adhesion between the matrix and the fibers [2]. The natural fiber like coir has significant applications in composites like the conventional fiber like glass, the natural fiber composites have

advantages to use them in automobiles for door panels roof panels[3]. The information of voids in the composites can be found by ultrasonic testing [4]. In hybrid composite made of natural and synthetic fiber reinforced composite, its young's modulus increases with increase in natural fiber content [5] .By 2010 about 40,000 composite products are in use for an array of applications in diverse sector of industry all over the world. The longitudinal elastic modulus increases with the fiber volume fraction in the composite [6] Natural fibers are gaining the interest of scientists and engineers in packaging, low cost housing and other general applications [7]. The natural composites have many applications as structural materials, they have ease of fabrication, low cost and superior mechanical properties compared to polymer resins[8]. The mechanical properties of PLA/Flax composites are 50% better than polypropylene / flax composites[9].Paper pulp is basically a composite made out of recyclable waste paper, consisting wood fibers in a matrix of lignin and hemi celluloses, it is environmental friendly material [10].

2. PROPERTIES USED TO CHARECTERIZ NATURAL COMPOSITES

Three types of natural composites are prepared with POP plaster of paris resin with glass fiber, hemp fiber and jute fiber reinforcements. The tensile strength, flexural strength, compression and Impact tests are conducted to characterize them.

3. MATERIALS AND METHODS

The POP is taken from a building material supplier and the fibers are taken from the agricultural market in our local area.

3.1 Preparation of Composite Laminate

In this experiment the POP resin with glass, hemp and jute fiber laminates are prepared. The composite preparation is done with the hand molding process. On a glass plate the PVA polyvinyl acetate is applied for ease release the fabricated composite from the glass. By keeping a Teflon sheet also the composite laminate can be fabricated. Some resin is applied and evenly distributed by brushing entire glass plate. Some cotton fibers are laid uniformly on the resin, they are gently pressed with a roller. Then some more resin is applied on these fibers and rolled smoothly. This process is repeated till a required thickness is obtained. The rolling with a smooth rubber roller should be done sufficiently to avoid formation of voids in the composite laminate. Then another glass plate is kept on this material gently. This is allowed to dry for 3 to 5 days. This dry makes the composite to cure in the atmosphere. Then the glasses are removed to get the composite laminates. Now the composite laminate is prepared.

4. RESULTS

The Mechanical tests are conducted as per the standards given by ASTM. The samples are cut in the required geometries by manual cutting with the chisels and the files. To get curved shapes the half round files are used. The V groove is obtained by the triangular files.

The experimental results are mentioned in Table 2. The tests procedures are also explained in the work done by G. Bhanu Kiran et al [11].

4.1 Tensile Properties

The tensile properties of the composites are examined in terms of tensile modulus, ultimate tensile strength, and percentage of elongation. The POP -Hemp composite laminate have highest ultimate strength.

Table1: showing standard dimensions

S.N	Test , test standards, dimensions	Samples
1	Tensile Test ASTM D 638 type III	
2	Compression test ASTM D 695 end loading	
3	Flexural testing ASTM D 790	
5	Impact ASTM D 256	

4.2 Flexural Properties

Flexural strength is the ability of the material to withstand bending forces applied perpendicular to its longitudinal axis. ASTM D90

standards three point bending test ,the flexural test is conducted on UTM .

$$\text{Flexural strength} = \frac{3 P L}{2 b d^2}$$

Where P = load, L = length, b = width, d = thickness

Out of the Glass, Hemp, Jute composites the POP – Hemp is having highest Flexural strength.

4.3 Compression Test

The compression test is conducted as per ASTM D 695 on a UTM. The POP – Glass is having highest Compression strength. The glass has good rigidity and strength. This is the reason for the good compression strength of the laminate.

4.4 Impact Test

Impact test is conducted as per ASTM D 256, it is carried out on Charpy type of impact test machines FIT 300 EN. The impact strengths in the experiments are showing lesser values than the literature. Some researchers do the experiments without notch, with notch lesser values obtained. Curing of the POP composites is also an important factor. If the composites are cured in an oven the values can be improved. The results of the tests are tabulated in table 2.

Table 2: Showing different characteristic properties of the composite laminates.

S.N	Composite material	Ultimate Tensile strength N/mm ²	Flexural strength N/mm ²	Compression strength N/mm ²	Impact Strength in J
1	POP - Glass	112	82	280	1
2	POP-Hemp	143	97	260	3
3	POP -Jute	135	89	245	2

5. DISCUSSION

The tensile strengths are in the order of the POP – Hemp, POP Jute and the POP Glass. It shows that, there exists a strong bond between the fiber and the POP in the POP- Hemp. The SEM images shows that the surface is more course (rough) in the Hemp, where as the glass is smooth surface. The smooth surface of fiber may have less interface bonding with the resin. The rough surface is having a strong bond. S.Y. Fu et al [12] gave the fiber interface constant as $\epsilon_c = C (l m r_f^2 / V_f)^2$, where n is a constant taken as 0.3, r f radius of fiber , V f volume fraction of fiber. ϵ_c failure strain of the composites. It is found that composites with more C is having the more tensile strength. The C values are given in table 3.

Table 3 : The Fiber- Matrix interface constants

S.N	Composite	Strain in mm	Mean length of fiber lm	radius of fiber in mm r_f	Volume fraction V_f	n	Fiber-matrix interface constant C	
1	POP Glass	-	0.057	115	0.018	0.6	0.3	0.02643
2	POP Hemp	-	0.078	115	0.025	0.6	0.33	0.03653
3	POP Jute	-	0.068	115	0.02	0.6	0.33	0.03007

The interface between the fiber and the resin is an important factor to determine the properties of the composites. The compressive strength of Glass fiber composite is more, this may be due to the fact that, the glass fiber is more rigid than the hemp and jute fibers. The strain of the single fibers as mentioned by the work done by Mei-po Ho et al [13] are comparable with this results. The glass fibers fails at less strain , then followed by jute and hemp . The strength of composite depends on the strength of the fiber. The strength of composites is also depends on the fiber morphology of the fiber tissues. The fiber geometry is influenced by the way, that they are obtained from processing methods[14].The mechanical properties Tensile strength, compression strength flexural strength properties obtained in this work has good agreement with the work done by Olusegun David Samuel [15], but the Impact strength values are less . V. C. Li and D.K. Mishra[16] , Found that the fibers will induce competing process of modulus improvement, which influences the compressive strength of the composites. The results in this work also agreeing this statement. The compressive strength is more when compared with tensile strength.

6. CONCLUSIONS

For the structural material interior design, the glass fibers can be replaced by the natural fibers like hemp, jute. The natural composites have considerable properties when compared to the conventional composites. The POP – Hemp ,POP –Jute composites have suitable properties for interior design applications. Like the epoxy based plastic composites they do not pollute the environment. The natural composites are promising materials for the safe and clean environment. There is lot o scope for the natural composites for applications in rail way coach interiors, automotive interiors, house hold decorative interiors. The experimental results show that the Tensile strength, Flexural strength, compression strength and impact strengths are suitable for decorative and interior applications.

7. ACKNOWLEDGEMENT

We would like to thank Raghavendra Spectra Metallurgical laboratories – Hyderabad, India for supporting this work.

ABBREVIATION: ASTM - American Society for Testing and Materials, POP – Plaster of Paris , UTM – Universal testing machine, SEM – Scannin electron microscope

REFERENCES

1. Navdeep Malhotra, Khalid Sheikh and Dr. Sona Rani “ A review on mechanical characterization of natural fiber reinforced polymer composites “Journal of Engineering Research and Studies , 2012 , E-ISSN0976-7916
2. H Ku, H Wang, N Pattara chaiyakoop and M Trada “A review on the tensile properties of natural fibre reinforced polymer composites ” 2014, Composites Part B: Engineering, 42 (4). 2011, pp. 856-873. ISSN 1359-8368 <http://eprints.usq.edu.au/18884>
3. Fariba sheikhjaberi Marjan Shayegan, Reza Bagheri, “Mechanical properties evaluation of recycled natural fiber matreinforced polypropylene” ISPST-2007 ,8th international seminar on polymer science and technology, Tehran, Iran
4. K.Oskaman *Skrifvars, M.; Selin, J-F* ” Natural fibers as reinforcement in polylactic acid (PLA) composites” Elsevier, composites science and technology 63(2003)1317-1324
5. S.P.Gurav A Bereznitski, A Heidweiller, P.V Kandachar“ Mechanical properties of paper-pulp packaging” composites science and technology 63(2003)1325-1334, Elsevier,
6. Catherine Potel Thierry Chotard, Jean-François de Belleval and Malk Benzeggagh “ Characterization of composite materials by ultrasonic methods: modelization and application to impact damage” Elsevier, composites part B 29B, 1998 -159-169
7. Vemu Varaprasad “ Textile and flexural properties of glass fiber reinforced polyester hybrid composites” international journal of materials and biomaterials applications 2011, 1(1): 14-16
8. Piyush P.Gohil and Shaik A.A. “Experimental investigation and micro mechanics assessment for Longitudinal elastic modulus in unidirectional cotton-polyester composites” international journal of engineering and technology vol; 2 (2) 2010, 111-118.
9. Bharath K.N., Swamy R.P., Mohan Kumar G.C “Experimental studies on biodegradable and swelling characteristics of natural fibers composites “International Journal of Agriculture Sciences, ISSN: 0975-3710, Volume 2, Issue 1, 2010, pp-01-04
10. Maries Idicula “ Thermo physical properties of natural fiber reinforced polyester composites” Elsevier, composites science and technology 66(2006)2719-2725
11. G. Bhanu Kiran, K. N. S. Suman, N. Mohan Rao, R. Uma Maheswara Rao “ A study on the influence of hot press forming process parameters on mechanical properties of green composites using Taguchi experimental design ”International Journal of

- Engineering, Science and Technology Vol. 3, No. 4, 2011, pp. 253-263
12. S.Y. Fu , B.Luake , E .Mader , C.Y.Yue and X.Hue “ Tensile properties of shortfiber and short cotton fiber reinforced polypropylene composites ” Composites A : applied science and manufacturing , 2000, 1117-1125, Elsevier
 13. Mei-po Ho , Hao Wang,,Joong Hee lee, Chun Kit Ho , Kin –tak Lau, Jinsong Leng and David Hui “ Critical factors on manufacturing processes of natural fibre composites “ Composites: Part B 43 2012, 3549–3562 ,
 14. Paul A Fowler, J Mark Hughes and Robert M Elias ” Review Biocomposites: technology, environmental credentials and market forces ” Journal of the Science of Food and Agriculture 2006, 86:1781–1789
 15. Olusegun David Samuel, Stephen Agbo, Timothy Adesoye Adekanker “Assessing Mechanical Properties of Natural Fibre Reinforced Composites for Engineering Applications ”, Journal of Minerals and Materials Characterization and Engineering, 2012, 11, 780-784
 16. V.C. Li and D.K. Mishra “ Micromechanics of fiber effect on theuniaxial compressive strength of cementitious composites “ Fiberreinforced cement and concrete ,1992 , 400-415, ISBN 0419 18130x

TENSILE AND FLEXURAL STRENGTH OF GLASS FIBER EPOXY COMPOSITES

S.Pichi Reddy^{1*}, P.V.Chandra Sekhar Rao¹, A.Chennakesava Reddy², G.Parmeswari¹

1. Department of Mechanical Engineering, L.B.Reddy College of Engineering, Mylavaram, Andhra Pradesh-521230
2. Department of Mechanical Engineering, JNTUH College of Engineering, JNTUH, Hyderabad-500085

Abstract: Glass fiber reinforced epoxy composites are most widely used as composite materials. The demand for light weight composite materials has led to the development of fly ash based composite materials. In the present work, the effect of fly ash content on tensile strength and flexural strength of 10wt% glass fiber epoxy composites is studied. The fly ash content is varied from 0 to 10grams in steps of 2grams. The composite with 6grams fly ash exhibited better tensile strength when compared to the other composites. Similarly the composite with 4grams fly ash exhibited better flexural strength.

Keywords: epoxy composites, fly ash, tensile strength, flexural strength.

Address all correspondence to: seelamspr@gmail.com

1. INTRODUCTION

Glass fiber reinforced epoxy composites results in an attractive combination of physical and mechanical properties which cannot be obtained by monolithic materials [1, 2]. These are widely used due to ease of availability of glass fibers and economic processing techniques adopted for production of components. Developments are still under way to tailor their properties for extreme loading conditions. One way to improve the strength of the FRP composites is to add various filler materials. These filler materials act as additional reinforcing components and enhance their mechanical properties. The properties of these composites depend on the type and size of the filler material used [3, 4]. Addition of silicon carbide, alumina, and titanium carbide improves hardness, strength and wear resistance of the composites [5, 6]. Graphite particles improved erosive wear resistance of glass fiber epoxy composites [7]. Interest in reinforcing fly ash to FRP composites is mainly due to low density, low coefficient of thermal expansion and high strength obtained in these composites. The addition of fly ash and mica particles to the polyetheretherketone (PEEK) composites increased the tensile strength, tensile modulus and flexural modulus [8]. The addition of fly ash to epoxy resin composites increased the compressive strength [9]. The addition of fly ash as filler material in glass vinyl ester composite increased its wear resistance [10]. The impact strength of the epoxy laminated bamboo composite increased with addition of

cenospher as a filler material [11]. The addition of coal ash to glass fiber polymer matrix composites improved their mechanical strength [12]. In the present work an attempt is made to study the effect of fly ash as a filler material in epoxy glass fiber reinforced composites.

2. EXPERIMENTATION

The following section highlights the materials used, fabrication and testing of composites.

2.1 Materials

The matrix material used for fabrication of the composites is Epoxy resin (L12 grade) and corresponding hardener (K-6) is used. E-glass fiber is used as the reinforcing material and the fly ash collected from NTPPS-Vijayawada, is used as the filler material.

2.2 Fabrication and Testing of Composites

Hand lay-up technique is adopted for fabrication of the composites. The mould used is shown in figure 1. Releasing agent is applied in the mould and a cut ply of glass fiber is placed in the mould. The resin mixed with the fly ash is poured into the mould and allowed to dry for two hours. The dried sample is removed from the mould and cut into the shape of standard specimens. The specimen used for tensile test is shown in figure 2 and the specimen used for 3-point bend test is shown in figure 3. The designation of the specimens is shown in Table 1. Electronic tensometer is used for determining the tensile and flexural strength of the composites.



Figure 1: Mould for preparation of composite specimen



Figure 2: Tensile test specimen



Figure 3: Three point bend test specimen

Table 1: Designation of the Specimen.

S.No	Specimen Designation	Glass fiber (grams)	Resin (grams)	Fly ash (grams)
1	C1	5	50	0
2	C2	5	48	2
3	C3	5	46	4
4	C4	5	44	6
5	C5	5	42	8
6	C6	5	40	10

3. RESULTS AND DISCUSSIONS

From the fabricated composites, the test specimens are prepared as per ASTM standards and are tested to evaluate their tensile and flexural strength. The results obtained by conducting these tests are given below.

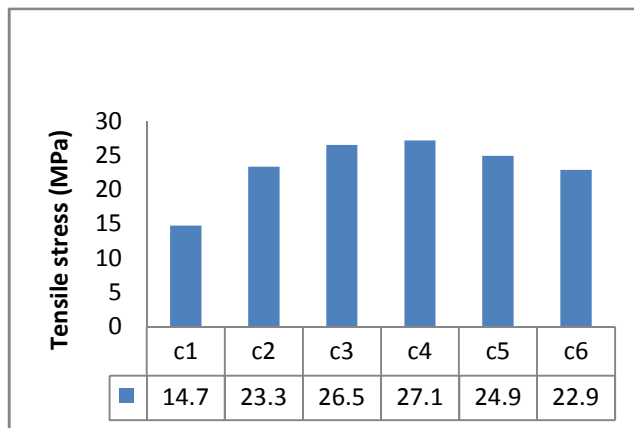


Figure 4: Tensile strength of composites

3.1 Tensile Strength

The effect of fly ash content on the tensile strength of the composite is shown in figure 4. It is observed that the tensile strength varies from

14.7727MPa to 27.179MPa. The tensile strength increases with the increase in fly ash upto 6grmas and thereafter it decreases. The increase in tensile strength with the increase in fly ash can be attributed to the good interfacial bonding between the fly ash and the matrix. As the fly ash content is further increased the composite transforms into brittle and hence the tensile strength decreases.

3.2 Tensile Modulus of Elasticity

Figure 5 shows the effect of fly ash on the tensile modulus of elasticity for various composites. The tensile modulus of elasticity varies from 946.067MPa to 2548.428MPa and the maximum is obtained for specimen with fly ash content equal to 8grams.

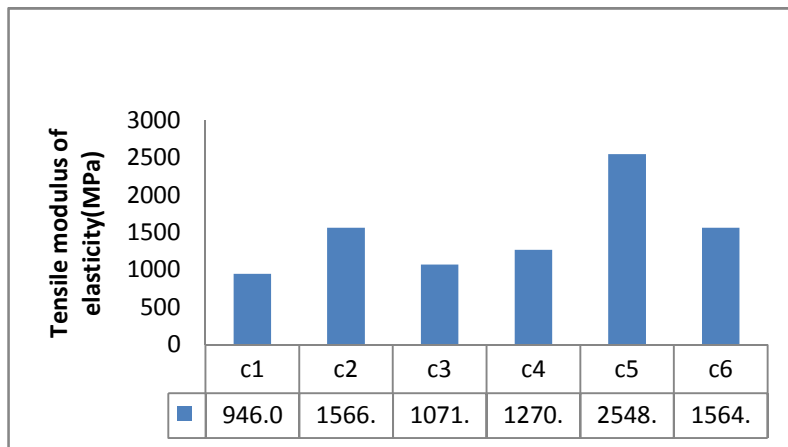


Figure 5: Tensile modulus of composites

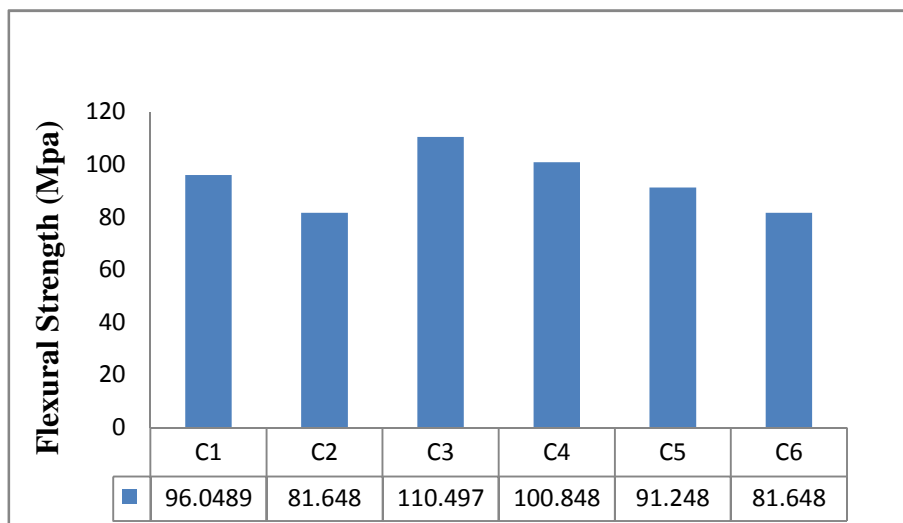


Figure 6: Flexural strength of composites

3.3 Flexural Strength

The flexural strength of the composite is determined from 3-point bend test. The flexural strength for various composites is shown in figure 6. The flexural strength of the composites varies from 81.648MPa to 110.497MPa and the maximum value is obtained for composite with 4grams of fly ash. The flexural strength decreases, reaches a maximum value and again decreases with the addition of fly ash in the epoxy matrix.

4. CONCLUSIONS

The experimental investigation on tensile and flexural behaviour of fly ash reinforced glass fiber epoxy composites with different weight percent of fly ash have been carried out. The conclusions drawn from the present work are.

1. The tensile strength of the composites varied from 14.7727MPa to 27.1790MPa and the maximum is obtained for composite with 6grams fly ash.
2. The maximum tensile modulus of elasticity is obtained for the composite with 8grams fly ash.
3. The flexural strength of the composite varies from 81.648MPa to 110.497MPa. The maximum flexural strength is obtained for the composite with 4grams fly ash.

REFERENCES

1. B. Kotiveerachari, A. Chennakesava Reddy, Interfacial effect on the fracture mechanism in GFRP composites, CEMILAC Conference, Ministry of Defence, India, 20-21st August 1999:, B85-87.
2. A. Chennakesava Reddy, M. Vidya Sagar, Two-dimensional theoretical modeling of anisotropic wear in carbon/epoxy FRP composites: comparison with experimental data, International Journal of Theoretical and Applied Mechanics, 2010:6(1), pp.47-57.
3. R.Sateesh Raja, K.Manisekar, and V.Manikandan, Effect of fly ash filler size on mechanical properties of polymer matrix composites, International Journal of Mining, Metallurgy and Mechanical Engineering, 2013: (1-1),pp.34-37.
4. K.Devendra, and T.Rangaswamy, Strength characterization of E-glass fiber reinforced epoxy composites with filler materials, Journal of Minerals, Material Characterization and Engineering, 2013:(1),pp.353-357.
5. Amar Patnaik and S.S Mahapatra, Study on mechanical and erosion wear behavior of hybrid composites using taguchi experimental design, Journal of Materials and Design, 2009:(30),pp.2791-2801.
6. S.Chauhan, A.Kumar, A.Patnaik, A.Satapathy and I.Singh, Mechanical and wear characterization of GF reinforced vinyl ester resin composites with different comonomers, Journal of Reinforced Plastic Composites, 2009: (28), pp. 2675-2684.
7. T. Basava and A.N.Harirao, Development of graphite particles filled epoxy resin composite material and its erosive wear behavior, Interantional Journal on Manufacturing and Material Science, 2011 :(1-2), pp. 28-30.
8. M. Rahail Parvaiz, Smita Mohanty, Sanjay K. Nayak and P. A. Mahanwar, Polyetheretherketone (PEEK) composites reinforced with fly ash and mica,

- Journal of Minerals Materials Characterization and Engineering, 2010: (9-1), pp.25-41.
9. Manoj Singla , Vikas Chawla, Mechanical properties of epoxy resin – fly ash composite, Journal of Minerals Materials Characterization and Engineering, 2010: (9-3), pp.199-210.
 10. S.R. Chauhan, Anoop Kumar , I. Singh , and Prashant Kumar, Effect of fly ash content on friction and dry sliding wear behavior of glass fiber reinforced polymer composites - A taguchi approach, Journal of Minerals Materials Characterization and Engineering, 2010: (9-4), pp.365-387.
 11. Hemalata Jena, Mihir Ku. Pandit, and Arun Ku. Pradhan, Study the impact property of laminated bamboo-fibre composite filled with cenosphere, International Journal of Environmental Science and Development, 2012: (3-5), pp.456-459.
 12. K. Naresh Kumar, M. Prasanth Kumar, V. Krishna, and D. Srinivasa Rao, Experimental investigation on mechanical properties of coal ash reinforced glass fiber polymer matrix composites, International Journal of Emerging Technology and Advanced Engineering, 2013: (3-8), pp. 250-258.

EXPERIMENTAL STUDY OF MECHANICAL PROPERTIES OF 5083 ALUMINIUM ALLOY USING GAS TUNGSTEN ARC WELDING

B.V.R. Ravikumar^a and M. Srivatsva^b

Professor, Department of Mechanical Engineering

^aVNR Vignana jyothi Institute of Engineering & Technology
Bachupally, Nizampet(SO),Kukatpally,Hyderabad-500090, India.

^bM.Tech Student, VNRVJIET,Bachupally, Hyderabad-500090

Abstract: Aluminum alloy 5083 [AA 5083] is commonly used in the manufacturing of pressure vessels, marine vessels, armored vehicles, aircraft cryogenics, drilling rigs, structures and even in missile components etc. This alloy is considered as a one of the best weldable aluminum alloys and exhibits a slight reduction of the strength of the heat affected zone [HAZ], comparatively to the most of other aluminum alloys. This decline in the strength has to be considered critically in the design stage and it can be considered as a major drawback in applications especially where a better weight to strength ratio required. aluminum alloy 5083 contains Mg-Mn-Cr, in the tempered condition, it is strong and retain good formability due to excellent ductility. AA5083 has high resistance to corrosion and used in marine applications. In this research, AA 5083 welds are made with gas tungsten arc welding (GTAW) using AA 5356 filler wires with non-pulsed current and pulsed current at different pulse frequencies like 2 pulses/sec, 4 pulses/sec and 6 pulses/sec using precision TIG 375 welding machine. This report to investigates the weld quality through non destructive testing (NDT) to study the porosity and surface cracks and also the mechanical properties like ultimate tensile strength (UTS), 0.2% yield strength (YS) and % of elongation using GTAW with non-pulsed current and pulsed current at different pulse frequencies were studied and also to find the weld joint efficiency of the weldments.

Keywords: gas tungsten arc welding, non-destructive testing), heat affected zone, ultimate tensile strength.

Address all correspondence to: ravirajmani1970@gmail.com

1. INTRODUCTION

Welding is one of the most used methods for joining aluminum and its alloys. Tungsten inert gas (TIG) process and gas metal arc welding (GMAW) are the welding processes which are used the most, but there are some problems associated with this welding process like porosity, lack of fusion, incomplete penetration [1] and cracks. Gas metal arc welding offers the advantage of high deposition rate and high welding

speed besides deeper penetration because of high heat input. However, excessive heat input imposes the problems such as melt and distortion specially in welding of thin aluminum sheets [2]. Therefore, to produce high quality weldments, TIG welding process is preferred over gas metal arc welding.

Al-Mg alloys are extensively used in defence and aerospace applications. Tungsten inert gas (TIG) welding is an arc welding process that produces coalescence of metals by heating them with an arc between a consumable electrode and the base metal. TIG welding process [3] is generally used for welding of Al-Mg alloys. The initial strength of the non-heat treatable aluminum alloys depends primarily upon the hardening effect of alloying elements such as silicon, iron, manganese and magnesium [4]. These elements increase the strength either as dispersed phase or by solid solution strengthening. The welding of non-heat treatable aluminum alloys typically have distinct effects when the heat input is increased, the width of the heat affected zone (HAZ) is increased and the minimum reduction in the mechanical properties are observed. Alloys 5XXX series with more than 3.0% magnesium are not recommended for elevated temperatures above 150°F because of their potential for sensitization and subject susceptibility to stress corrosion cracking [5]. The minimum HAZ strength approximates to that of the annealed parent metal regardless of the starting temperature. During welding, vaporization of alloying elements like magnesium can occur and this vaporization loss of any alloying elements can influence the mechanical properties of the welded joints by affecting the chemistry of the weld pool. The gas tungsten arc welding (GTAW) and gas metal arc welding (GMAW) processes are very often used for welding of these alloys. However, gas tungsten arc welding (GTAW) process is generally preferred because it produces a very high quality welds. Distortion is the major problem in welding of thin sections. However, the distortion is controlled in pulsed and magnetic arc oscillation GTAW process. Metallurgical advantages of pulsed and magnetic arc oscillation welds that are frequently reported in the literature includes grain refinement in the fusion zone, reduced width of HAZ, less distortion, control of segregation, reduced hot cracking sensitivity and reduced residual stresses[6].

2. EXPERIMENTAL WORK

The sheets of 2mm thickness Aluminium alloy 5083 (chemical Compositions and mechanical properties are shown in (table 1 and 2) have been cut into required size (150 x 300 mm) by shearing machine. These sheets are cleaned by pickling operation to remove dirt, grease and other foreign materials. The Aluminium sheets are placed on welding table and the initial joint configuration is obtained by securing plates in position using mechanical clamps where the welding process is carried out. In this research study the welding process was performed on AA5083 sheets using filler wire AA 5356 and its chemical compositions are shown in table 3. The weld parameters are shown in table 4 and 5. The equipment used for this study is Lincoln Electrical Precision TIG 375 GTAW machine is shown in figure 1.

The equipment consists of mainly of power supply source, a welding torch, connecting torch, cables and hoses for gas and water supplies. GTAW was conducted with 2.4 mm diameter 2% zirconated tungsten electrode. Argon gas of having 99.99% purity was used for shielding and backing gas during the welding process. In this study, TIG welding process was carried out with three different welding currents i.e., constant current, pulsed current at 2 pulses/sec, 4 pulses/sec and 6 pulses/sec respectively. After the welding process, the NDT carried out on the weldments (figure 2), the ASTM Standards, Section VIII, Division 2 for radiography (figure 3) and ASTM E-1417 for liquid penetrant tests were conducted on AA5083 weldments to find porosity and cracks . The parameters used for NDT are given in table 6.

Table 1: Chemical Composition of the 5083 aluminum alloy (% wt)

Element	Mg	Mn	Fe	Si	Zn	Cr	Ti	Cu	Al
%Wt	4.5	0.7	0.4	0.4	0.25	0.15	0.15	0.1	93.0

Table 2: Mechanical properties of 5083 aluminum alloy

Material	UTS (MPa)	0.2% Y.S (MPa)	Elongation (%)
AA 5083	300	145	15

Table 3: Chemical composition of 5356 and 4043 filler wire (% wt)

Filler wire	Si	Fe	Cu	Mn	Mg	Cr	Zn	Ti	Be	Others
AA 5356	0.25	0.40	0.10	0.05-0.20	4.5-5.5	0.05-0.20	0.10	0.06-0.20	0.0003	0.15

Table 4: Welding parameters for non-pulsed current welding

Material thickness(mm)	Filler wire dia.(mm)	Current	I (amp)	V (volts)	Arc travel speed (cm/min)
2.0	2.4	AC	75	12.5	3.15

Table 5: Welding parameters for pulsed current welding

Material thickness (mm)	Filler wire dia (mm)	Current	Pulse/sec (Hz)	I (amp)		V (volts)	Arc travel speed (cm/min)
				Ip	Ib		
2.0	2.4	AC	2	26	10	13.3	3.0
2.0	2.4	AC	4	31	10	12.3	3.0
2.0	2.4	AC	6	36	11	12.7	3.0



Figure1: Precision TIG 375-TIG welding machine

Table 6: Liquid penetrant test parameters

	5083 aluminum alloy
Penetrant used	The oriental chemical works
Cleaner used	The oriental chemical works
Developer used	The oriental chemical works
Dwell time	10 min
Method	Solvent removable white light method

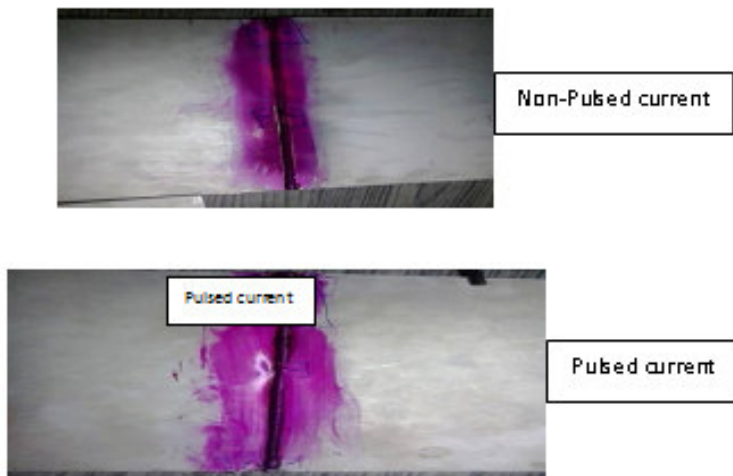


Figure 2: Weldments of 5083 aluminum alloy.

To investigate the mechanical properties of the weldments, as per ASTM E 8 standard the tensile specimens (figure 4) were prepared on HMT CNC wire cut EDM. The finished specimens were tested to find the ultimate tensile strength (UTS) and %elongation using 40 ton Universal Testing Machine (figure 5).

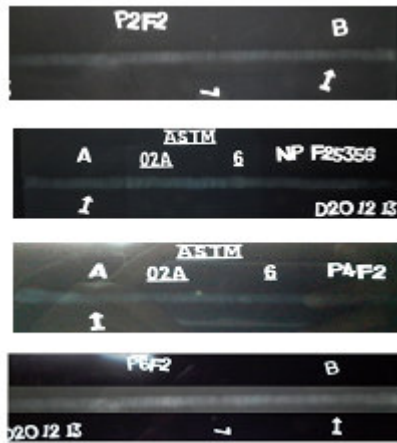


Figure3: Radiography images

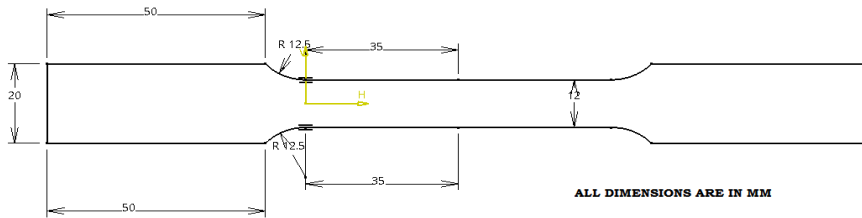


Figure 4: Tensile test specimen



Figure 5: UTM machine

3. RESULTS AND DISCUSSION

The AA 5083 is an Aluminum alloy that relies solely upon cold work and solid solution strengthening for its strength properties.

In this research, we studied the following weld characteristics of the 5083 aluminum alloy sheets welded with constant current and pulsed current using gas tungsten arc welding (GTAW) process.

3.1 Effect of Current on Porosity and Cracks

The effect of pulsed current on the porosity observed during radiography is presented in table 7. Porosity has been measured in present study. No porosity was observed at 2Hz frequency. Two pores with 0.6 mm size were observed with 6Hz frequency. The results show that pores size increases with the increase of frequency. This may be due to more vibration in weld torch and improper cleaning and supply of gases. The aluminum alloy 5083 contains porosity within the acceptable limits. According to the ASTM E-1417, the liquid penetrant (LP) test was conducted on these weldments. The experimental results show that no cracks were observed in the weldments of this alloy in both filler wires with non-pulsed current and pulsed current welding.

Table 7: NDT Results for 5356 filler wire

Radiography test – To investigate the porosity of the weldments			
Sl.No	Method of welding		Observation
1	Non – pulsed welding		No defect observed on welded area
2	Pulsed welding	2 Pulses/sec	No defect observed on welded area
3		6 Pulses/sec	No defect observed on welded area
LP Test – To investigate the surface cracks of the weldments			
4	Non –pulsed welding		No defect observed on welded area
5	Pulsed welding	2 Pulses/sec	No defect observed on welded area
6		6 Pulses/sec	No defect observed on welded area

3.2 Tensile Test

For tensile testing of the weldments, two samples each filler wires are made and tested using taken at all currents. For results which ever sample has produced better strength is taken in to account. The effect of frequency on the tensile strength (2Hz, 4Hz, 6Hz & NP) was shown in table 8. The finished test specimens were tested using the universal testing machine of 40 ton capacity. In this testing we found that all the weld specimens were failed at base metal area. It was observed that the pulsed current weldments produce more strength than the base metal and non-pulsed current weldments. The experimental results shows that , the welding made at low pulse current AA5083 weldments produce the higher value of UTS compared to other welding currents.

The effect of current 1% of elongation values of AA 5083 alloy compared with the help of graph. It is observed that the maximum value is produced at 2 pulse current. The effect of current on strength and % elongation is shown in figures 6 and 7.

Table 8: Tensile Test Table

Method of welding		Ultimate Tensile Strength (MPa)	0.2% proof stress (MPa)	% of elongation	
Non -pulsed welding		Sample 1	296.326	151.447	15.140
		Sample 2	277.821	145.443	10.480
Pulsed welding	2 Pulses/sec	Sample 1	295.121	159.892	10.580
		Sample 2	303.198	152.948	15.400
	4 Pulses/sec	Sample 1	286.385	164.588	8.920
		Sample 2	277.142	161.178	11.720
	6 Pulses/sec	Sample 1	296.936	162.365	12.680
		Sample 2	253.54	151.392	7.260

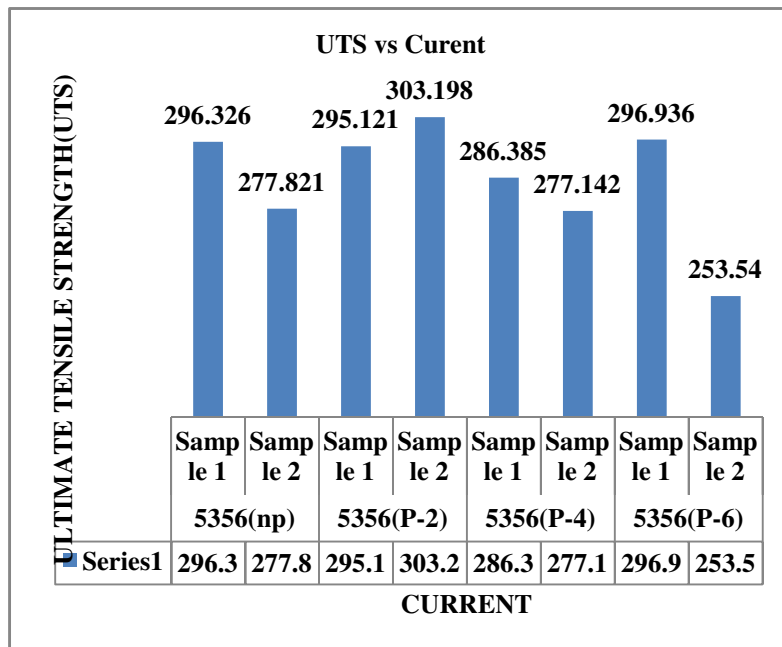


Figure 6: comparison between UTS and Current

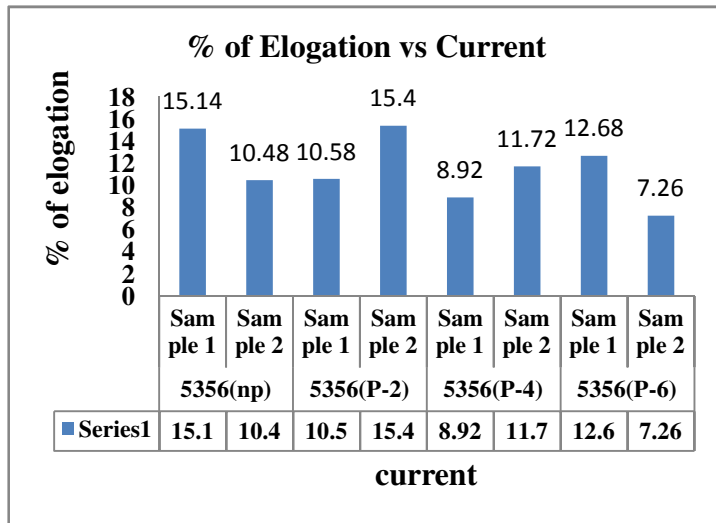


Figure 7: Comparison between % of Elongation

3.3 Weld Joint Efficiency

The weld joint efficiency of material is shown in figure.8. The efficiency is calculated from ultimate tensile strength (UTS) of weldments in comparison to the base metal UTS. The results presented were best values obtained from two trails. It is observed that the weldments produced at 2pulses/sec has produced more weld joint efficiency i.e., 94.68% .

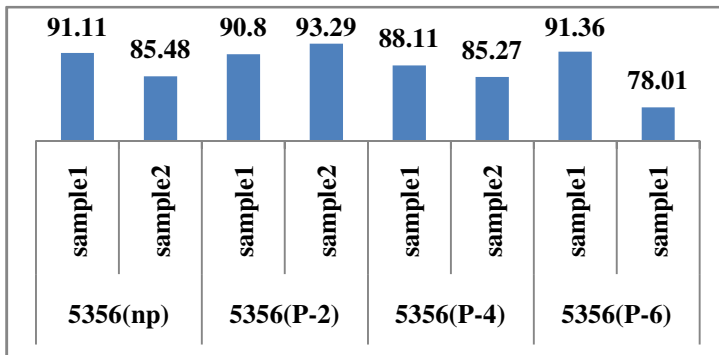


Figure8: Weld joint Efficiency of 5083AA weldments

4. CONCLUSIONS

From the experimental results the following conclusions are drawn

- The increasing of arc welding current in 5083 aluminum alloy will increase the welding heat input. Accordingly, the chance of defect formation such burns, pores, cracks in welded metal also increases. These will effects on the mechanical properties and quality of weld.

- The results shows that at pulsed current welding produces small pores in welding area but these pores are within the acceptable limit of ASTM Standards.
- There is no surface cracks observed in the weld zone.
- The sample 2 (AA5356) produced maximum ultimate tensile strength i.e., 303.198. This may due to fine grain structure and presence of more magnesium (4.5%-5.5%) in filler wire.
- The pulsed current has produced more tensile strength than non-pulsed current
- The sample 2 has maximum % of elongation i.e., 15.40 this is equal to parent material % of elongation.
- presence of magnesium will increases the strength and hardness of the parent material.

5. ACKNOWLEDGEMENT

Authors are very much Thankful to Principal and HOD of Mechanical Engineering-VNRVJIET, to give constant support to carry out the research work. We also grateful to the AICTE & DRDO to provide the financial assistance under RPS & CARS Scheme to the department to purchase of necessary equipments and chemicals to carry out this project work

REFERENCES

1. C.W. MohdNoor, The Effect of Arc Voltage and Welding Current on Mechanical and Microstructure Properties of 5083-Aluminium Alloy Joints used in Marine Applications, Empowering Science, Technology and Innovation towards a Better Tomorrow, UMTAS, 2011.
2. Maamar HAKEM, Welding and characterization of 5083 Aluminum Alloy , Brno, Czech Republic, EU, 2012: 23-25.
3. B. M. PATCHETT, Variable AC Polarity GTAW Fusion Behavior in 5083 Aluminum, professor emeritus of Welding Engineering at the University of Alberta, Edmonton, Alberta, Canada, 196-S, 2007: 86, July.
4. Wajira Mirihanage, Modification of AA 5083 weld joint Characteristics International Symposium of Research Students on Materials Science and Engineering, Department of Metallurgical and Material Engineering, Indian Institute of Technology, Madras, ISRS 2004.
5. ParvinAbachi, Influence of Mechanical treatments on the Mechanical Properties of AA5083 Aluminum Alloy welded joints, Mechanical Engineering Department, Amirkabir University of Technology, Tehran, Iran, METAL 2008, 13-15.5.2008, Hradec nad Morvici.
6. Lakshman Singh, Rohit Kumar, and Nidhi Gupt aand Mayur Goyal, To investigate the effect of Tig welding parameters on 5083 Aluminium Alloy Weldability, International Journal of Mechanical Engineering and Research, 2013: 2(4), June-July.
7. S.Mayur, K.M.Pavan, L.S.Sachin, A.Chandrashekar and B.S.Ajay Kumar, Effect of Welding Current on the Mechanical and Structural Properties of TIG Welded Aluminium Alloy AA-5083, International Journal of Mechanical Engineering and Research, 2013: 3(5), pp. 431-438.
8. B. V. R. RaviKumar and A. Raveendra, Welding Characteristics of Aluminium alloy (6082) and Stainless Steel (304) Weldments, using Pulsed and Non-Pulsed Current GTAW, International Journal of Mechanical Engineering Applications Research, 2011: 2 (2), pp.50-59.

MICRO-HARDNESS AND MECHANICAL PROPERTIES OF 5052 ALUMINIUM ALLOY WELDMENTS USING PULSED AND NON-PULSED CURRENT GAS TUNGSTEN ARC WELDING

A. Raveendra^a and B.V.R. Ravi Kumar^b

^aAssociate Professor, Department of Mechanical Engineering,
Mallareddy Engineering College, Secunderabad, India.,

^bProfessor, Department of Mechanical Engineering, VNR.Vignana Jyothi
Institute of Engineering & Technology, Bachupally, Nizampet,
Hyderabad, India,

Abstract: In this experimental work, micro hardness and mechanical properties of weldments have been carried out on 5052 aluminium alloy using GTAW with pulsed and non-pulsed current at different frequencies 2Hz, 4Hz and 6 Hz. Hardness is the ability of a metal to resist penetration . In order to improve the mechanical integrity of the weldments it would be desirable to study the micro hardness of weldments. The present study was performed to know the difference of micro-hardness and mechanical properties of the weldments made with pulsed and non-pulsed current at different frequencies of GTAW. The hardness measurement can provide information about the metallurgical changes caused by the welding.

Key words: 5052 aluminium alloy, gas tungsten arc welding, micro hardness, ultimate tensile strength, yield strength, % elongation.

Address all correspondence to: ravi.akunuru.a@gmail.com

1. INTRODUCTION

The demand is increasing for aluminium alloy welded products where high quality is required such as aerospace applications. Aluminium alloy can be welded easily by conventional arc welding methods like metal inert gas welding (MIGW) and tungsten inert gas welding (TIGW). Among these two methods, The gas tungsten arc welding (GTAW) process has proved for many years to be suitable for welding aluminium alloy since it gives best quality welds. GTAW process (AC) is used in this experimental work to weld aluminium alloy.

Another development has been pulsed current TIG Welding. Pulsed current welding (PCW) was introduced in the late 1960s as a variant of constant current welding (CCW), PCW process has many specific advances over CCW, including enhanced arc stability, increased weld depth/width ratio, narrower heat affected zone (HAZ) range, reduced

hot cracking sensitivity, refined grain size, produced porosity, low heat input, low distortion, controlled weld bead volume, less absorption of gas by weld pool and better control of the fusion zone[1-8]. Pulsed current welding technology has been widely used in fabrication of high pressure gas storage tanks, rocket motors, structures in aerospace applications such as air crafts, rockets and missiles. Switching between predetermined high and low levels of welding current can be used to produce pulsed current gas tungsten arc welds[9]. Usually, the pulsed waves are rectangular in shape and the parameters used for pulsed GTA welding are shown in figure 1. The main characteristics of PCW are determined by peak current I_p , base current I_B , peak time t_p and base time t_b . Little work has been done on pulsed current GTAW on alloy steels. So far the pulsed current GTAW welding is used to study the effect of pulsed current, shielding gas composition, weld speed, shape, joint strength using alloy sheets of 5083 type[8], angular distortion in stainless steel weldments of 304 and 310 type [9], microstructure [10] and weld bead geometry [11].

Current pulsing has been used by a few investigators [12, 13] to obtain grain refinement in weld fusion zones and improvement in weld mechanical properties. Significant refinement of the solidification structure has been reported in aluminium alloys and titanium alloys. Most of the reported literature is focused on pulsed current welding of medium strength aluminium alloys. Hence, the present investigation has been carried out to know the effect of the pulsed current welding technique on tensile properties and hardness of high strength aluminium alloy.

Pulsed welds show fine grain structure due to thermal disturbances and decrease in heat input. In general, hardness is lower in HAZ region compared to the weld metal and base metal regions irrespective of welding technique which is characterized by the coarse dendritic grains and lack of the strengthener phase. Hardness was higher compared to the continuous welds and this could be due to refinement of grain structure [14].

2. EXPERIMENTAL PROCEDURE

The work pieces were made of 5052 aluminium alloy of various thicknesses i.e. 1.5mm and 2.5mm. The test specimens were machined to the size of 150 mm X 300 mm and welded with pulsed and non-pulsed current GTAW process. Usually, the pulse waves are in rectangular shape and the parameters used for pulsed GTA welding are shown in figure 1. The main characteristics of PCW are determined by peak current I_p , base current I_B , peak time t_p and base time t_B .

Filler wire material of ER4043 was used during the welding which reduced the weld cracks and produced the good strength and ductility than other filler metals [15]. These filler metals melt at a temperature lower than that of the base metal, for this reason it yields during

cooling, since it remains more plastic than the base metal and relieves the concentrated stresses that might cause cracking. The chemical composition and mechanical properties of work material and filler wire as shown in tables 1-3.

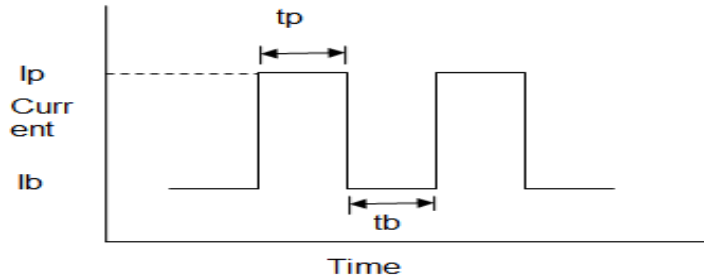


Figure1: Parameters used for pulsed GTAW:

The aluminium alloy work pieces were chemically cleaned with hot Sodium Hydroxide for 10 minutes followed by dipping in Nitric Acid solution for about 15 minutes and then washed with water. Lincoln Electrical square wave TIG 355 GTAW machine with AC was used for welding of 5052 aluminium alloy test specimens. The choice of tungsten electrode depends upon the type of welding current selected for the application. Zirconated tungsten (EWZr) electrodes are best suited for AC wherein they keep hemispherical shape and thoriated tungsten electrodes (EWTh-2) should be ground to taper are suitable for DCSP welding are used for this purpose. This welding process was conducted with 2.5 mm diameter 2% Zirconated tungsten electrode for 5052 aluminium. The welding parameters used in this welding process both in pulsed current and non-pulsed current for two different thicknesses of the above material are given in tables 4 and 5. The edge preparation of the 5052 aluminium alloy specimens and machine are shown in figures 2 and 3. Tensile specimens were made as per ASTM E8 standards. Tensile tested pieces are shown in figure 4.

Table 1: Chemical compositions of work material 5052 aluminum alloy

Material	Chemical Composition % wt								
	Si	Fe	Cu	Mn	Mg	Zn	Ti	Cr	Al
5052 Aluminium Alloy	0.092	0.249	0.015	0.013	2.281	0.012	0.016	0.25	Balance

Table 2: Chemical compositions of filler wire

Material	Chemical Composition % wt							
	Cu	Si	Mn	Mg	Fe	Cr	Ti	Al
ER4043	0.17	4.5 – 6.0	0.24	0.05	0.05	0.05	0.05	Balance

Table 3: Mechanical properties of 5052 Aluminium alloy

Material	UTS(MPa)	0.2% Y.S(MPa)Min	% Elongation
5052 Aluminium Alloy	285	180	10

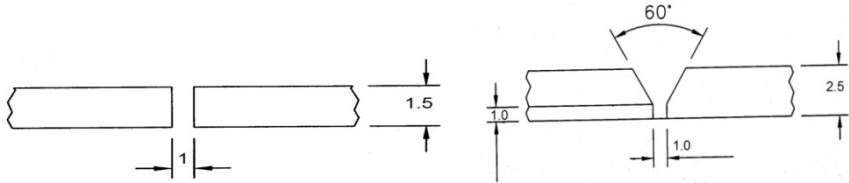


Figure 2: Edge preparation of weld specimens



Figure 3: Lincoln Electrical square wave TIG 355 M/C

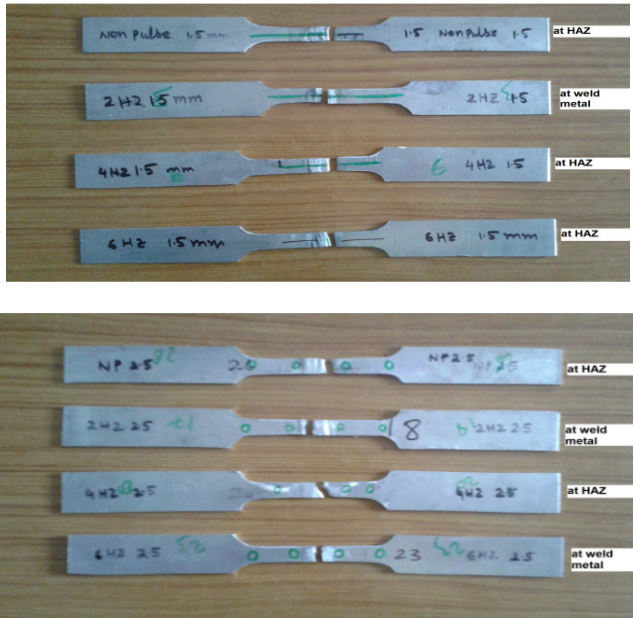


Figure 4: Tensile test specimens after test(1.5&2.5mm thick)

3. RESULTS AND DISCUSSIONS

Weldments are tested for their tensile strength and micro hardness. Results and detailed discussion about variation of tensile strength and micro-hardness values with pulsed current and non-pulsed current welding are given below.

Table 4: Mechanical properties of 1.5 mm thick weldments

S.NO	Sample Description		Trial no	UTS(Mpa)	0.2%S(Mpa)	% of Elongation
1	Base Material		1	286.42	214.32	8.5
			2	272.13	211.66	9.0
			3	274.24	210.72	9.0
2	Non-Pulsed Current GTAW		1	251.59	190.80	4.4
			2	253.64	193.42	6.0
			3	249.32	195.61	4.4
3	Pulsed current GTAW	Pulse=2Hz	1	238.57	189.68	4.0
			2	250.28	189.88	4.5
			3	257.54	199.46	6.4
		Pulse=4Hz	1	244.89	189.76	4.0
			2	254.44	191.75	7.0
			3	220.84	120.65	3.5
		Pulse=6Hz	1	253.55	192.0	8.0
			2	240.54	195.9	4.6
			3	250.58	185.90	9.0

Table 5: Mechanical properties of 2.5 mm thick weldments

S.NO	Sample Description		Trial no	UTS (Mpa)	0.2%Y S(Mpa)	%of Elongation
1	Base Material		1	296.62	228.29	13.0
			2	295.93	227.50	12.0
			3	291.84	226.84	12.0
2	Non-Pulsed Current GTAW		1	288.51	207.3	4.0
			2	282.45	210.8	4.0
			3	298.90	215.3	5.0
3	Pulsed current GTAW	Pulse=2Hz	1	320.35	230.1	4.0
			2	304.15	220.8	6.2
			3	271.32	145.56	3.0
		Pulse=4Hz	1	250.43	182.71	3.0
			2	216.80	168.98	3.0
			3	253.95	182.92	3.0
		Pulse=6Hz	1	282.25	202.42	3.5
			2	258.50	160.84	3.0
			3	262.30	170.35	3.0

3.1 Mechanical Properties

The tensile test specimens were tested using the universal testing machine of 10 ton capacity. Table 4 and table 5 show the tensile test results of each trial specimen of two different thicknesses 1.5mm & 2.5mm. The tensile specimens typically failed through the weld metal

and HAZ in low thickness weldments (1.5 mm) and failed through the parent metal in high thickness weldments (2.5mm).

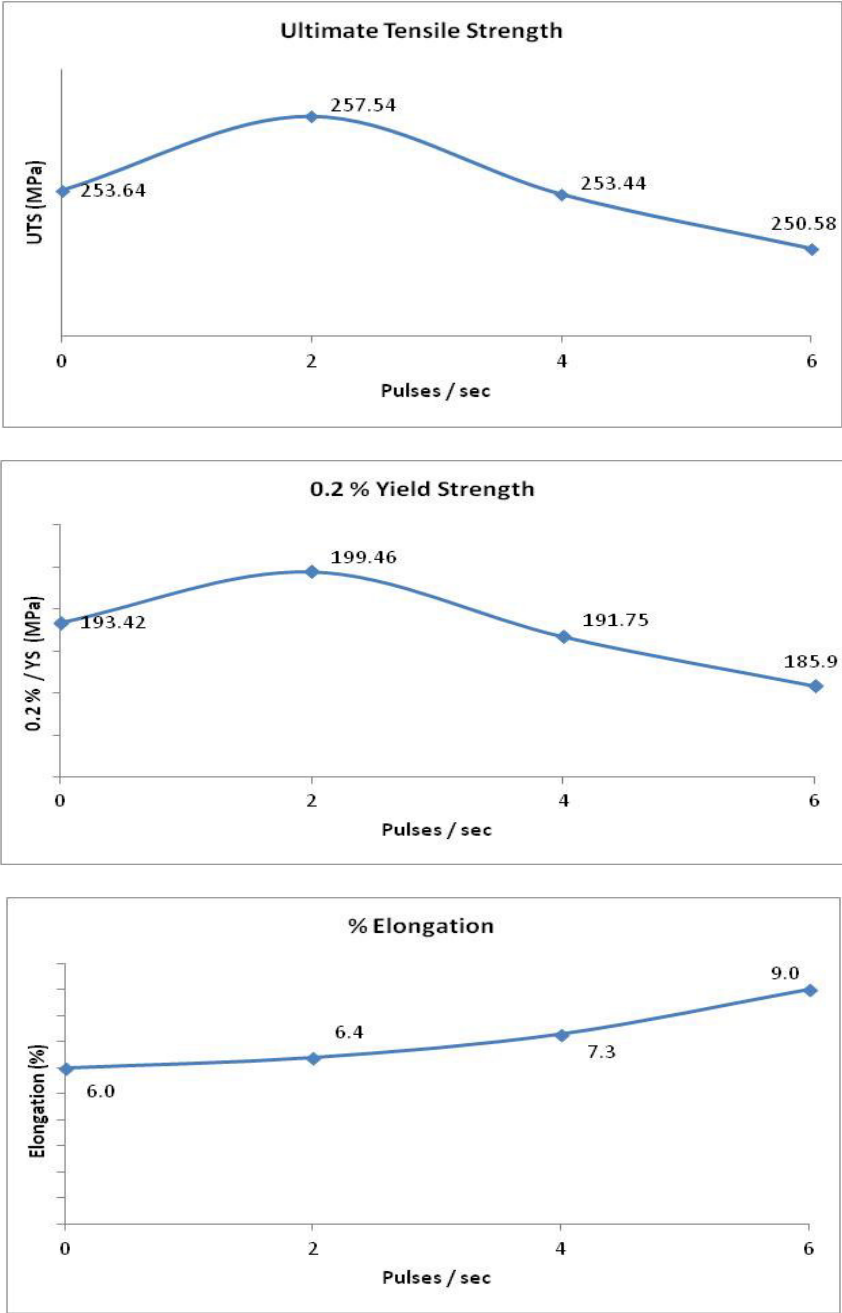


Figure 5: Mechanical properties performance curves of 1.5 mm thick weldments

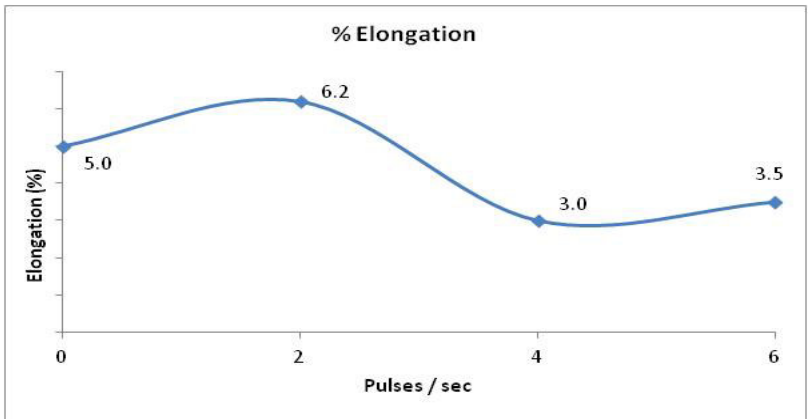
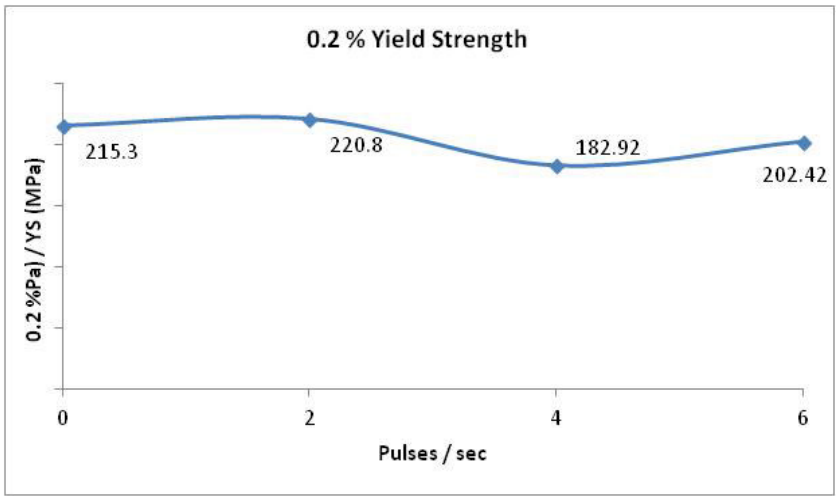
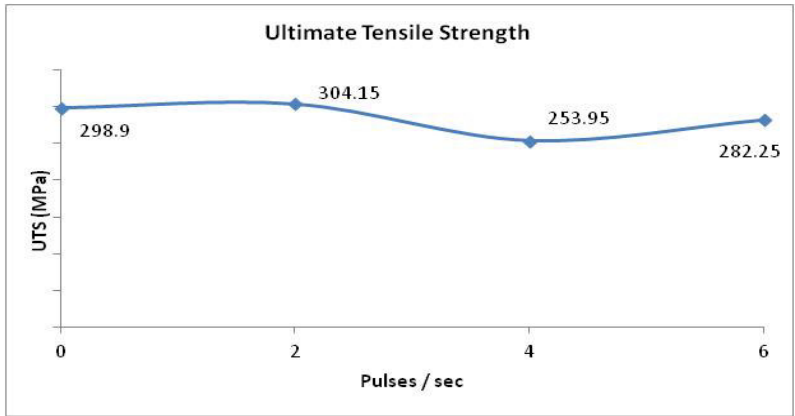


Figure 6: Mechanical properties performance curves of 2.5 mm thick weldments

Low thickness weldments (1.5mm) produced maximum ultimate tensile strength and 0.2% yield strength i.e., 257.54 Mpa and 199.46 Mpa with low frequency(2Hz) than the high frequency (i.e., 4Hz and 6Hz) and non-pulsed current welding, but these weldments produced high % elongation with increase of frequencies. The experimental results show that the low thickness weldments produced more ductility with pulsed current welding than the non-pulsed current welding. The performance curves of the 1.5mm weldments are shown in figure 5.

High thickness weldments (2.5 mm) produced maximum UTS, 0.2 % YS and % elongation at 2Hz i.e., 304.15 Mpa, 220.8 Mpa and 6.2 than the high frequency pulsed and non-pulsed current welding. The performance curves of the high thickness (2.5mm) weldments are shown in figure 6.

3.2 Micro-Hardness

The specimens were tested using Vickers micro hardness machine HV1000 ZDT. In non-pulsed current weldments, the hardness traverse on the welded zone and HAZ, shows little difference, its value gradually reduced and goes towards base metal. These weldments produced maximum hardness value 95HV in weld zone than the HAZ. In pulsed current weldments, the maximum hardness produced was 112HV in the low frequency (2Hz) weldments than the other pulses shown in Figures 7 and 8.

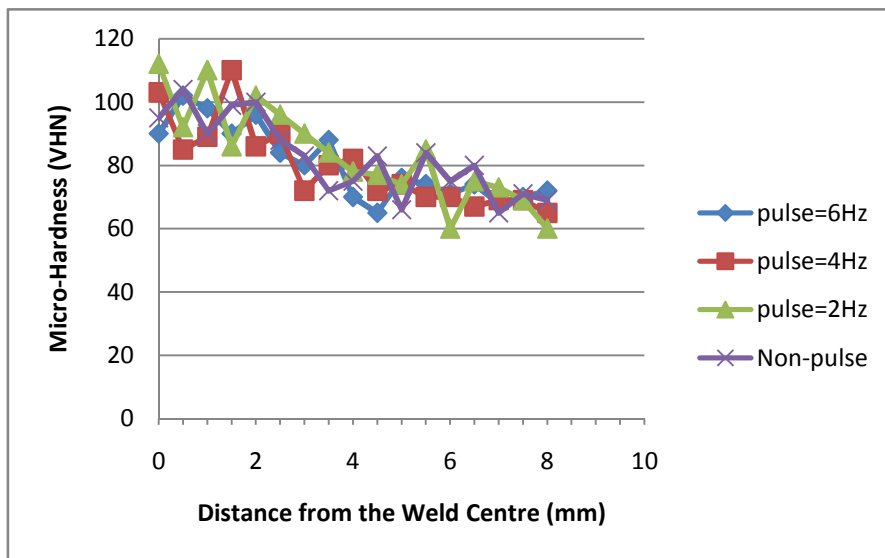


Figure 7: Micro-hardness profiles of 1.5mm Weldments

The use of pulsed current welding improves the strength of the weld observed in the case of continuous welding. The refinement of microstructure due to the pulsed current welding results in a uniform distribution of the fine precipitates more effectively and enhancement

of precipitates in the matrix. In general, hardness in the fusion zone is the lower due to the cast nature of the microstructure, which is characterized by coarse dendritic grains, inter dendritic segregate phases, and the lack of strengthening phases. Hardness is slightly higher in pulsed current weld as compared to continuous current welds and this could be due to the refined microstructure and low segregations of strengthening phases.

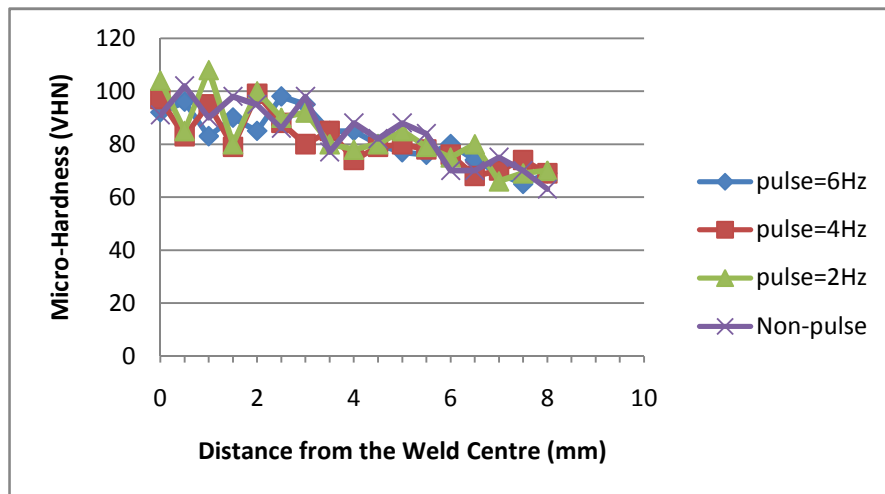


Figure 8: Micro-hardness profiles of 2.5 mm weldments

4. CONCLUSION

From the results it is evident that the pulsed current has great influence on mechanical and metallurgical properties. The weldments produced maximum UTS, 0.2% YS and % elongation with pulse current welding than non-pulsed current welding. The weldments have the better hardness in pulsed current welding than non-pulsed current welding.

The enhancement in mechanical properties such as tensile properties and weld metal hardness are mainly due to the refinement in fusion zone grain size. Hence the basic reason for the improvement in mechanical properties is the refinement produced in fusion zone grain size by pulsed current welding.

REFERENCES

1. W.Troyer, M.Tomsic, and R.Barhotst, Welding characteristics of Aluminium alloy, welding journal, 1977: 56(1), pp.26-32.
2. D.W.Becker, and C.M. Adams, The role of pulsed GTA welding variables in solidification and grain refinement, welding journal, 1979: 58(5), pp.134-152.
3. D.W.Becker, and C.M.Adams, Investigation of Pulsed GTA Welding parameters, Welding Journal, 1978: 57(5), pp.134-138.
4. A.A .Omar, and C.D. Lundin, welding journal, 1970:58(4), pp.97-104.

5. C.F.Tseng, and W.f Savage, The effect of welding oscillation, welding journal, 1971: 50(11), pp.777-786.
6. Y. Sharir, J. Peiieg, and grill, Metallurgical Technology, Spinger, New York: 1978, pp.190-196.
7. C.L.Tsai, and C.A. Hou, Theoretical Analysis of Weld Pool Behavior in the Pulsed Current GTAW Process, Journal of Heat Transfer,1988: 110, pp. 160-165.
8. S.Kate, and S.Tanabe, High speed welding of 0.5mm thickness alloy sheets using pulsed TIG welding, welding International 7, 1988: pp. 602-608.
9. K.H.Tsen, and C.P.Chou, Effect of pulsed gas tungsten arc welding on angular distortion in austenitic stainless steel weldments, science and Technology of welding and joining,2001 :6,(3),pp.149-153.
10. G.M.Reddy, A.A. Gokhale, and K.Prasad Rao, Effect of filler metal composition on weldability of Al-Li alloy 1441, Material Science & Technology, 1998: 14, pp.61-66.
11. P.K.Giridharam ,and N.Muragan, Sensitivity Analysis of pulsed current GTA welding process parameters on weld bead geometry, National conference in advances in joining Technology 2004.
12. T.Mohandas , G.Madhusudhan Reddy, Effect of frequency of pulsing in gas tungsten arc welding on the microstructure and mechanical properties of titanium alloy welds, J Material Science,1996: 15, pp.625-628.
13. DA.Shelwatker , G.Madhusudhan Reddy, Gokhale AA, Gas tungeten arc welding studies on similar and dissimilar combinations of Al-Zn-Mg alloy RDE 40 and Al-Li alloy 1441, Sci Technol weld Join, 2002: pp. 352-361.
14. Vahid Nazarpoor, Abdoreza, Soltanipoor, Khosrow Farmanesh, Effect of current on Mechanical, Metallurgical and Corrosion Properties of AA 5083 Aluminium Alloy Pulse TIG Welding Joints, Journal of Materials Science,2010: vol.2,pp.54-67.
15. M.Ramulu, and M.P.Rubberrt, Gas Tungsten Arc welding of al-li-cu alloy 2090, Welding Journal,1990 Vol. 69, No. 3, pp. 109-114.
16. R.S.Parmar, Welding Engineering and Technology PB(English), p623.

WELDABILITY OF FRICTION WELDING USING H30 ALUMINUM WITH BS970 MILD STEEL

V. Prasanna

Assistant Professor, Department of Mechanical Engineering
Vignana Bharathi Institute of Technology, Hyderabad.

Abstract: Friction welding method is one of the most simple, economical and highly productive method in joining dissimilar materials. It is widely used in the automotive, medical and aerospace industrial applications. The purpose of this present work was to assess the development of solid state juncture of dissimilar materials of H30 aluminum and BS970 mild steel. The joints were obtained by friction welding (FW) process, which combines the heat generated from friction between two surfaces. The results were analyzed by means of tensile, Rockwell hardness test and metallographic tests. Solid state welding processes are characterized by the absence of melting and the formation of narrow heat affected zone (HAZ). The metallurgical properties are usually excellent and most of the processes can be mechanized or automated to be used as high production rate processes. The FW proves to be a great method for obtaining junctures between dissimilar materials which is not possible by fusion welding process.

Key words: friction welding, aluminum, mild steel, dissimilar, tensile test, metallographic test.

Address all correspondence to: vuppula.prasanna@yahoo.com

1. INTRODUCTION

In recent years, the use of joints between dissimilar metals has considerably increased. In the development of new technologies for the aerospace, medical and automotive industries, these junctures are of high importance, because they allows the systems, components manufactured in mild steel and aluminum to be structurally united. Even the fusion welding processes by presenting a heat affected zone (HAZ) well reduced.

Friction welding (FW) is classified by the American welding society (AWS) as a solid state joining process in which bonding is produced at temperatures lower than the melting point of the base materials [1].

Fuji, et.al [2] studied mechanical properties of titanium - 5083 aluminum alloy friction joints. Ylbas, et.al [3] investigated the mechanical and metallurgical properties of friction welded steel-aluminium and aluminium-copper. Fukumoto, et.al [4, 5] studied the

friction welding set up and the strength of the joints and investigated amorphization process between aluminium alloy and stainless steel by friction welding. Furthermore the cleanliness of the parts must be considered as important. Therefore, the ends of the parts were cleaned with acetone prior to the welding process to minimize the effect of organic contamination in the welding zone. Friction welding of aluminium and austenitic stainless steel has been studied experimentally. Elliot and Wallach [6] studied about the reaction of joint strengths and the thickness of intermetallic compound layers.

FW process is solid state joining process that produces a weld under the compressive force contact of one rotating and one stationary work piece, the heat is generated at the weld interface because of the continuous rubbing of contact surfaces, which in turn causes a temperature rise and subsequent softening of metals. In due course, the material at the interface starts to flow physically and forms an upset. When a certain amount of upsetting has occurred, the rotation stops and the compressive force is maintained or slightly increased to consolidate the weld. Friction time, friction pressure, forging time, upset time, forging pressure and rotation speed are the most important operational parameters in the FW process.

Figure 1 shows the phases of the process. (a) One side of the materials to make it join is fixed and the other material is rotated by rotational speed N ; (b) Pressure P_1 and time t_1 – heating phase; (c) Pressure P_2 and time t_2 – forging phase.

Figure 2 shows the basic layout of FW equipment. Usually the structure is fairly rigid to provide stability to the equipment working at high speeds and is driven by high pressure forging. Modern equipment is automatic and allows all the parameters be adjusted and monitored directly on the control panel.

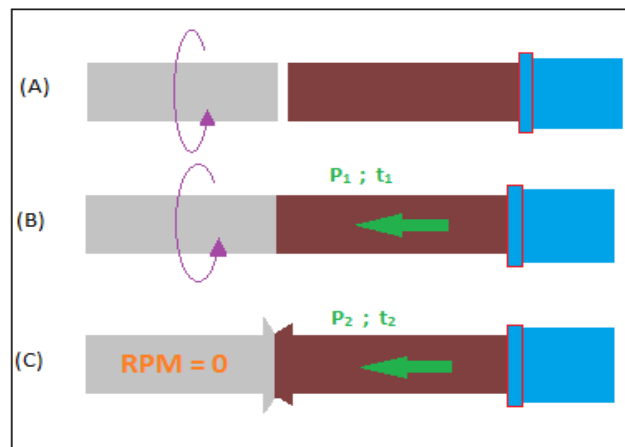


Figure 1: Phases of friction welding process

The difficulties in the welding of aluminum with mild steel by fusion welding processes have been a great challenge for engineering; because they result from hard and brittle inter metallic phases that formed between aluminum and steel at evaluated temperatures. In this study, the materials (H30 aluminum, BS970 mild steel) have been joined by FW and the results were analyzed and presented. Tensile and Rockwell Hardness tests were performed to define welding parameters and analyze the resistance of the weld.

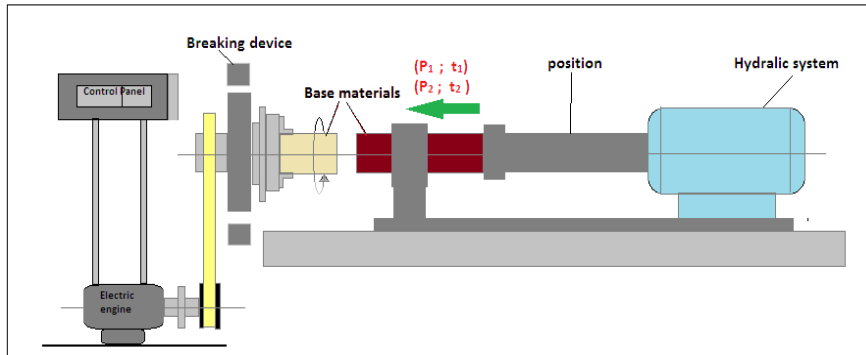


Figure 2: Equipment of friction welding

2. EXPERIMENTAL PROCEDURE

The details of materials used, experimental setup, and tests conducted are discussed under the following subheadings

2.1. Materials

The materials used in this study for dissimilar friction welding H30 aluminum – BS970 mild steel; each material were machined with a diameter of 8mm and length of 200 mm.

2.2. Friction Welding Equipment

A friction welding machine of brand UNITECH configured M250 was used with fixed speed 3000RPM, of H30 aluminum – BS970 mild steel dissimilar materials.

2.3. Tensile Test

After welding was performed, tensile tests were carried out to evaluate the mechanical properties [7] of junctures. The welded specimens were machined subjected to tensile tests on a machine brand UTK-4DE (2005/1281) with a capacity 400kN at room temperature of 25°C.

2.4. Rockwell Hardness Tests

The Rockwell hardness test method measures the permanent depth of indentation produced by a force or load on an indenter. This load represents the zero or reference position that breaks through the surface to reduce the effects of surface finish. A conical diamond

indenter with a round trip is used for hard materials and minor load is 10kgf and major load is 60-150kgf.

2.5 Metallographic Analysis

The junctures were cut in the transverse weld, embedded in an array of Bakelite, polished and examined in the region of the interfaces on aluminum to mild steel under a matascan metallurgical microscope (Jyothi Spectro Analysisn (P) Ltd., Hyderabad, INDIA). The chemical composition of materials used in the present is given in Table 1. The mechanical properties are given in Table 2.

Table 1: Chemical compositions of materials used in present study

Materials	Elements (%)				
	H30 Aluminum	Cu	Mn	Mg	
	0.1	1.0	0.6		
BS970 Mild steel	C	Silicon	Mn	S	P
	0.17	0.3	0.8	≤0.05	≤0.04

Table 2: Mechanical properties of materials

Materials	Young's Modulus (E)		Tensile Strength Mpa	Yield Strength Mpa	Elongation (%)
	Psi	Gpa			
H30 Aluminum	10.0	69	110	95	5.00
BS970 Mild steel	29700ksi	205	440	370	15.0

3. RESULTS

The detailed results of specimen macrostructure, tensile test, hardness test and metallographic analysis are discussed in the following subheading.

3.1 Macrostructure

In macrostructure level, it was observed the formation of flashes with circular symmetry, different formats, and also significant reductions in length of the cylindrical pin H30 aluminium in accordance with the adopted parameters. The BS970 mild steel side was not deformed because this material has higher strength than the aluminium alloy, and it thus provide more resistance to deformation. Hence the formation of flashes was restricted to H30 aluminium alloy. Figure 3 shows the interfaces that were bonded and specimens used for tensile test after machining.

3.2 Mechanical Strength of Junctures Welded by Friction

The results of the tensile tests for different welding parameters (t_1 , t_2 , and P_2) are shown in Table 3. Effects of upset time and upset pressure on the strength of junctures were examined in welding of equal

diameter parts, friction time was kept constant. The strength of junctures was determined by tensile tests, and the results were compared to those of fully machined specimens. Tensile strength of the junctures was estimated dividing the ultimate load by area of 8 mm diameter specimen. The fracture occurred at the interface of the dissimilar metal weld joint, strength of the weld joint was lesser than tensile strength of H30 aluminium 270 Mpa there was an unbounded region around the centre of the fracture surface, although the aluminium alloy was partially bonded to the mild steel. The unbounded region is defined as the region where the adhesion between the materials and inter diffusion of each element are insufficient, and elements are not metallurgically bonded to each other. i.e., insufficient upset pressure and upset time meant that the faying surfaces had not entirely reached up to the certain limit where the amount of axial forging pressure and the time required reaching the bonding temperature therefore, an unbounded region remained at the centre of the weld interface. Only the outer region was bonded because the temperature here was higher than that of the inner region in the forging stage. The obtained results are plotted between tensile strength versus upset pressure and upset time and are shown graphically in Figure 5 and Figure 6. As upset time and upset pressure for the junctures passes through a maximum, when upset time and upset pressure for the junctures are further increased, tensile strength of the joints decreases and finally fails due to high axial upset pressure in which just piercing of mild steel into the aluminium took place with zero mechanical locking or elemental bonding between two dissimilar metals. Thus, it is shown that upset time and upset pressure have a direct effect on joint y time and upset pressure affect cue of the metals the weld reduces the junctures quality, but it was slightly softened. The fracture mechanism of junctures with a shorter time may be different from that of junctures with a longer upset time. The initial step was to examine fracture surfaces for any noticeable difference in fracture mechanism between unsound junctures with lesser and higher upset pressures and upset times. Figure 4 shows the specimens after tensile test.

Table 3: Tensile test values

Number of trails	Friction pressure (P ₁ Mpa)	Friction time (t ₁)	Upset pressure (P ₂ Mpa)	Upset time (t ₂)	Obtained tensile strengths
1	80	4	140	4	134.2
2	80	4	160	5	177.8
3	80	4	200	6	153.6
4	80	4	300	7	0

3.3 Rockwell Hardness Test

Rockwell number was calculated on B-scale of hardness machine values as shown in the Table 4. The variations in the hardness numbers different values of speed and feed rate values of hardness number was increasing and decreasing during testing. The Rockwell

hardness test was conducted for measuring hardness along the weld zone. From results of the hardness testing it is observed that maximum hardness number obtained for Rockwell for sample I, using cylindrical tool at speed 3000 rpm and feed 30 mm/sec.

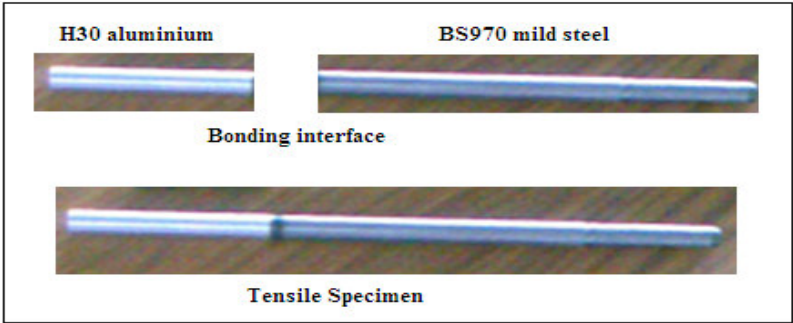


Figure 3: H30 aluminium, BS970 mild steel before and after bonding.



Figure 4: H30 aluminium and BS970 mild steel after tensile test

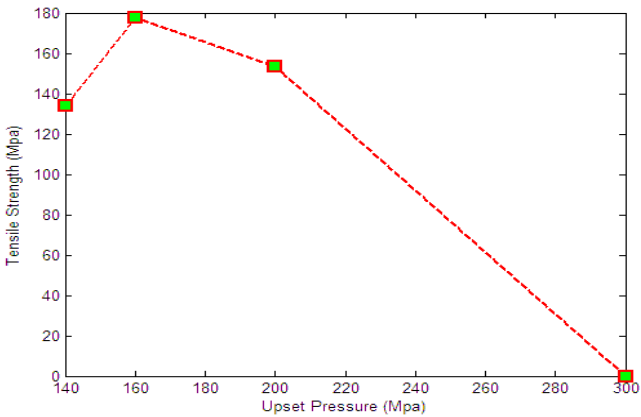


Figure 5: Relation between tensile strength and upset pressure

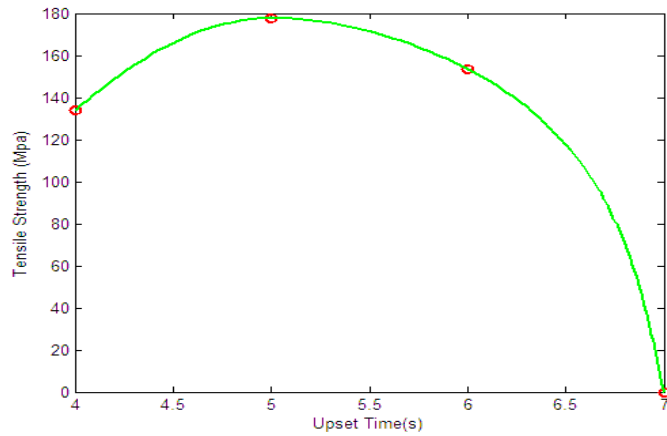


Figure 6: Relation between tensile strength and upset time.

Table 4: Rockwell hardness number

Speed (rpm)	Sample number	Feed (mm/sec)	Rockwell hardness number (B-Scale)
1500	A	20	18
	B	25	35
	C	30	16
2500	D	20	38
	E	25	22
	F	30	36
3000	G	20	25
	H	25	12
	I	30	46

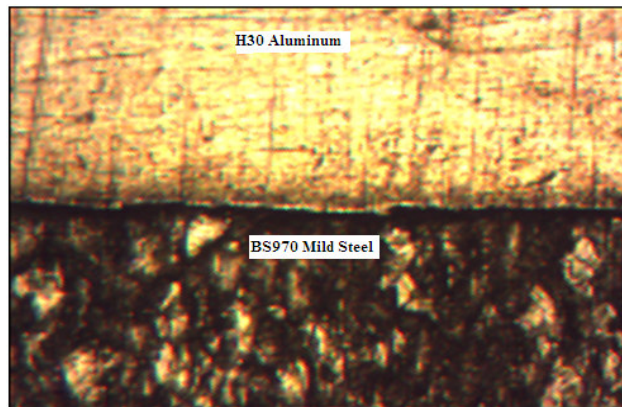


Figure 5: Photomicrograph of the interface bonding between the H30 aluminum and BS970 mild steel with an increase of 100 X.

3.4 Metallographic analysis of the bonding interface

Figure 7 shows a photomicrograph of the junctures between H30 aluminum and BS970 mild steel taken in the central region of the sample with an increase of 100X. The interface region is characterized by a straight line with some imperfections under the friction welding process. Both in the aluminum and mild steel side's microstructural changes are not observed near the interface region as it occurs in fusion welding processes. All plastic deformation resulting from the parameters used in the process occurred in the H30 aluminium, due to the fact that this material has lower strength and lower hot forging temperature.

4. CONCLUSION

The friction welding process was very efficient in the welding of dissimilar metals such as H30 aluminum and BS970 mild steel. It is showed by the results of tension mechanical tests that presented mechanical properties which are not possible to achieve by means of fusion welding processes. Among the parameters used for testing the welding, the one that showed the best results in tensile tests. The HAZ is well fused and free from non metallic defects. Hence we can extend this work to the various residual stresses acting during the process.

5. REFERENCES

1. Cuauhtemoc Maldonado Zepeda, The effect of interlayers on dissimilar friction weld properties, PhD thesis, University of Toronto, Canada, 2001: pp. 35.
2. A.Fuji, M.Kimura, T.H.North, K.Ameyama and M.Aki, Mechanical properties of titanium-5083 aluminium alloy friction joints, *Materials Science and Technology*, 1997:13(8), pp.673-678.
3. B.S.Ylbas, Z.Sahin, N.Kahraman and A.Z.Al-Garni, Friction welding of St-Al and Al-Cu materials, *Journal of Materials Processing Technology*, 1995:49, pp.431-443.
4. S.Fukumoto, T.Inuki, H.Tsubakino, K.Okita, M.Aritoshi and T.Tomita, Evaluation of friction weld interface of aluminium to austenitic stainless steel joint, *Materials Science and Technology*, 1997:13(8), pp.679-686.
5. S.Fukumoto, S.Tsubakino, K.Okita, M.Aritoshi and T.Tomita, Friction welding process of 5052 aluminum alloy to 304stainless steel. *Materials Science and Technology*, 1999:15(8), pp.1080-1086.
6. S.Elliot and E.R.Wallach, Joining aluminum to steel part-1 diffusion bonding, *Metal Construction* 13(3), 1981: pp. 167-171.
7. American Society for Metals, Aluminium properties and physical metallurgy, A book of ASM standards, 1984.

EFFECT OF TOOL SHOULDER DIAMETER TO PIN DIAMETER (D/d) RATIO ON MECHANICAL PROPERTIES OF FRICTION STIR PURE ALUMINIUM WELDMENTS

S. Rajendra Prasad¹, **A. Kumar**²., **Ch. Sridhar Reddy**³.

1. Research Scholar, JNTUH & Assoc.Prof, KITS(S), Huzurabad (TS).

2. Assoc.Prof, NITW, Warangal (TS).

3. Assoc.Prof, JNTUHCEJ, Kondagattu, Karimnagar (TS)

Abstract: The effect of varying tool shoulder diameter to pin diameter (D/d) ratio of a taper cylindrical tool pin profile on mechanical properties of pure aluminium weldments through Friction Stir Welding process was studied. An attempt is being made to understand the effect of tool rotational speed, tool traverse speed and tool pin profile with varying shoulder diameter to pin diameter. The tool with D/d ratio of (3, 2.5, 2) taper cylindrical pin profile were selected to fabricate the joints. Mechanical properties of all the weldments were evaluated. From the results it was observed that at the condition of tool shoulder diameter 24mm, D/d ratio of 3, tool rotational speed of 1400 rpm and tool traverse speed of 40mm/min showed better mechanical properties compared to other conditions. The observed mechanical properties have been correlated with their microstructures.

Keywords: Friction Stir Welding, microstructure, tensile, mechanical properties

Address all correspondence to: rsirumalla@gmail.com

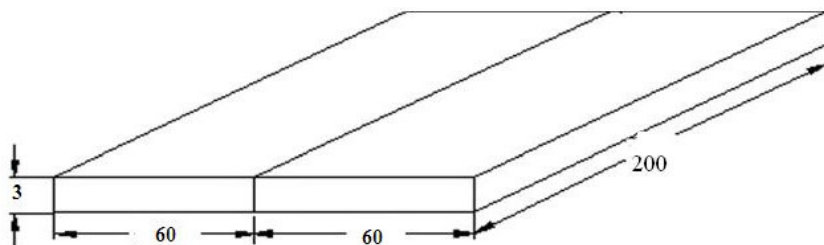
1. INTRODUCTION

Pure aluminium and its alloys are important engineering materials due to their good ductility, corrosion resistance, good conductor of electricity and strength to weight ratio [1]. Commercial pure aluminium has a wide number of applications in transportation, aerospace industry, electrical transmission lines, construction, heat sinks for electronic appliances etc. Welding of aluminium is usually difficult by conventional fusion welding processes because as it often produces defects like porosity, hot cracks in the welded joints which deteriorates the mechanical properties. Hence it will be extreme benefit to go for a solid state joining process which avoids which avoids bulk melting of the base material, hot cracking and porosity. Friction Stir Welding (FSW) is becoming an important solid state joining process invented at The Welding Institute(TWI) of UK in 1991[2] by Wayne Thomas as it makes high quality welds for number of materials as compared to the conventional welding techniques. The convenience of FSW as a joining technique has been demonstrated in a number of studies especially for

commercial pure aluminium [3]. In FSW process, a non-consumable welding tool is used to generate the frictional heat between the tool and the work piece. Due to this frictional heat, the surrounding material softens and allows the tool to be involved along the joint line [4]. The material is plasticized and translated along the welding direction and is transported from the leading edge of the tool to the trailing side. Subsequently, it produces a high quality joint between the two plates by the translation movement of the work piece along with the applied pressure of the tool [5]. FSW is environment friendly , energy efficient, less distortion and faster welding speeds than conventional fusion welding techniques and be able to join materials that are difficult to fusion weld [6]. The shape of the tool pin profiles influence the flow of plasticized material and affects weld properties [7, 8]. The axial force on the work piece material and the flow of material near the tool are affected by the orientation of threads on the pin surface [9]. The material flow behaviour is predominantly influenced by the FSW tool pin profiles, tool dimensions and the process parameters [10]. From the reported literature, it was observed that no work was carried out on FSW of pure aluminium with a taper cylindrical pin profile of varying shoulder diameter(D) to pin diameter(d) i.e. D/d ratio on mechanical and microstructure properties of aluminium weldments. Hence the present study is aimed at investigating the effect of shoulder diameter to pin diameter (D/d ratio) on mechanical properties of friction stir pure aluminium weldments.

2. EXPERIMENTAL PROCEDURE

The experimental study includes the butt joining of 3 mm pure aluminium plates. The welding process is carried out on a vertical milling machine (Make HMT FM-2, 10hp, 3000rpm). Tool is hold in tool arbour and special welding jigs and fixtures are designed to hold two plates of 200 mm X 60 mm X 3 mm thickness as shown in figure 1. Table 1 shows the combinations of the tool rotational speed (RPM), welding speed (mm/min) and tool geometry and diameter of the tool shoulder to the diameter of the tool pin (D/d). These combinations are chosen based on the literature survey and the capability of the milling machine used for the experimental study.



(All the dimensions are in mm)

Figure1: Schematic sketch of weld joint

Table 1: FSW process parameters and tool dimensions

Process Parameters	Values
Tool rotation speed (rpm)	900,1120,1400
Welding speed (mm/min)	40
Axial force	Constant
Pin length (mm)	2.8
Tool shoulder diameter, D (mm)	24,20,16
Pin diameter, d (mm)	8
D/d ratio of tool	3,2.5,2
Tool pin geometry	Taper cylindrical pin profile
Tool material	H-13 tool steel

Non consumable tool made of H-13 tool steel is used to fabricate the joints because of its high strength at elevated temperature, thermal fatigue resistance and low wear resistance and diameters of shoulder 24, 20 &16 mm and pin used were 8mm and the length of the pin is 2.8 mm. The tools used for the present study are taper cylindrical pin profile with varying shoulder diameter to pin diameter are as shown in figure 2. A constant axial force is applied for the entire FSW experiments.



Figure 2: Taper cylindrical pin profiles

The direction of welding is normal to the rolling direction. Single pass welding procedure is used to fabricate the joints. The welding parameters are presented in table 1. Joints were fabricated using different combinations of rotational speed, welding speed and tool profile of varying D/d ratio. Mechanical properties of the base metal are as shown in table 2. Experiments were conducted at different combinations of tool rotational speed 900,1120 and1400 rpm, welding speed of 40mm/min and varying D/d ratio of taper cylindrical tool pin profile 2, 2.5 and 3. Trial experiments were conducted for lower welding speeds and the joints were found to have defects. The FSW joints fabricated using taper cylindrical pin profile with varying shoulder diameter to pin diameter are found to be defect free .The maximum values of tensile strength, impact toughness and hardness is observed

at the condition of tool shoulder diameter of 24mm, D/d ratio 3 and traverse speed 40mm/min when compared to other conditions, this is due to the formation of fine grain microstructure in the stir zone of pure aluminium weldments.

Table 2: Mechanical properties of base metal

Material	UTS (MPa)	YS (MPa)	El (%)	Rockwell Hardness (HR _B)
Pure aluminium	100-112	70	13	30

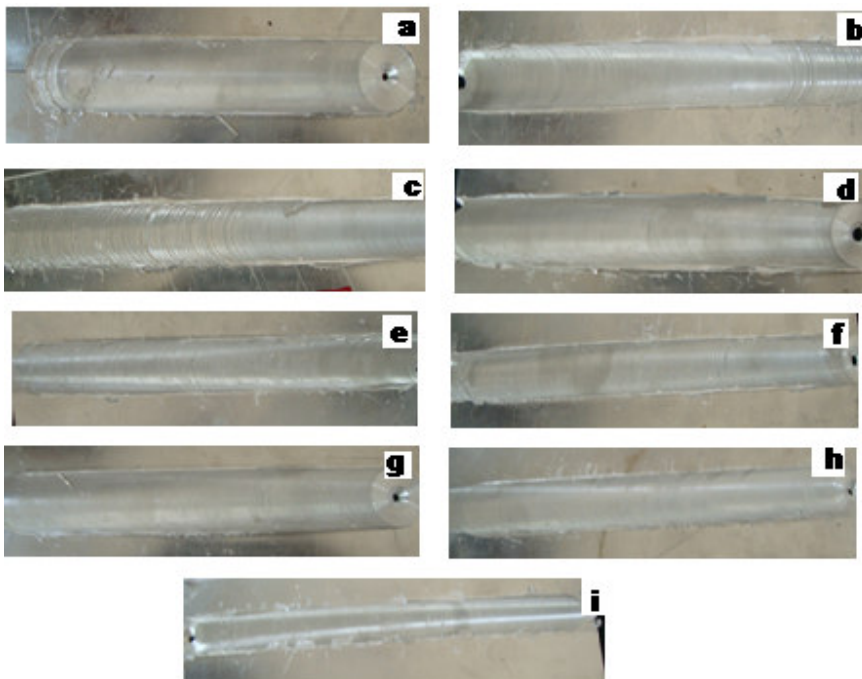


Figure 2.1(a-i): Surface morphologies of the FSW joints made at various conditions: (a) 1120 rpm, 40mm/min, D/d = 3 (b) 900 rpm, 40mm/min, D/d = 3 (c) 1400 rpm, 40 mm/min, D/d = 3 (d) 900 rpm, 40 mm/min, D/d = 2.5 (e) 1120 rpm, 40 mm/min, D/d = 2.5 (f) 1400 rpm, 40 mm/min, D/d = 2.5 (g) 900 rpm, 40 mm/min, D/d = 2 (h) 1120 rpm, 40 mm/min, D/d = 2 (i) 1400 rpm, 40 mm/min, D/d=2

2.1 Metallography

The specimens for metallographic examination were sectioned to the required size from the FSW joints in transverse to the welding direction, polished with different grades of papers, and then etched with a solution of Keller's reagent. The microstructure of the weld zone (WZ) and the unaffected base metal (BM) were examined with optical microscopy (Model: nikon : make: Epiphot 200) and changes in the microstructure of the weld zone were found.

2.2 Mechanical Testing

Specimens for tensile testing were taken in transverse to the weld direction and is taken at the middle of all the joints and machined as per ASTM E8 standards. Tensile test was conducted on computer controlled universal testing machine (Model: Autograph; Make: Shimatzu) with a cross head speed of 0.5mm/min. Specimens for impact testing is taken in transverse to the weld direction and machined as per ASTM A370 standards. The charpy V-notch impact test is conducted at room temperature. Specimens were cut at the middle of the joints in transverse direction for measuring hardness. Rockwell hardness (HR_B) is determined . The surface morphologies of the joints are as shown in figure 2.1(a-i) at different conditions. From the surface morphology it is observed that the amount of flash is low in the joints made.

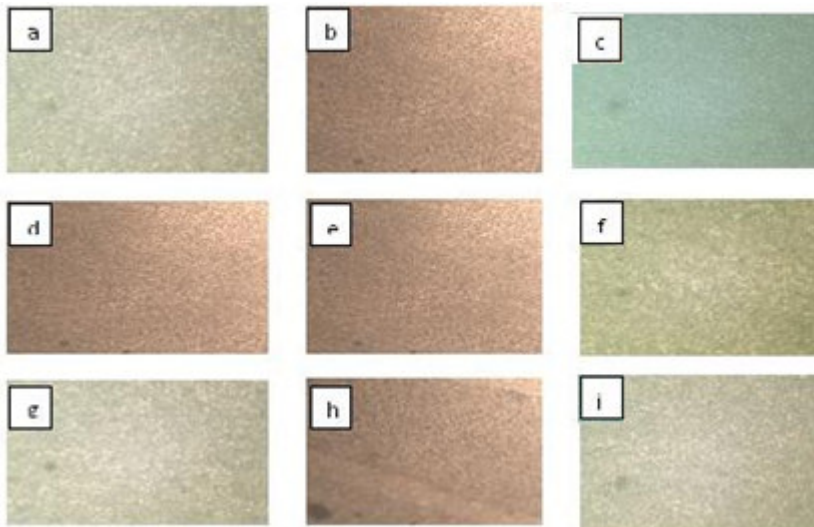


Figure 3(a-i): Stir zone microstructures at different conditions:
(a) 1120 rpm, 40mm/min, $D/d = 3$ (b) 900 rpm, 40mm/min, $D/d = 3$ (c) 1400 rpm, 40 mm/min, $D/d = 3$ (d) 900 rpm, 40 mm/min, $D/d = 2.5$ (e) 1120 rpm, 40 mm/min, $D/d = 2.5$ (f) 1400 rpm, 40 mm/min, $D/d = 2.5$ (g) 900 rpm, 40 mm/min, $D/d = 2$ (h) 1120 rpm, 40 mm/min, $D/d = 2$ (i) 1400 rpm, 40 mm/min, $D/d = 2$

3. RESULTS AND DISCUSSION

The friction stir welded pure aluminium joints were fabricated at various conditions and the results were discussed under the following headings.

3.1 Microstructural Studies

FSW is a well known severe plastic deformation process. The stirring action was observed at the weld center and produced finer grains. The discrepancy reflected significantly in different microstructures in the

stir zone produced by taper cylindrical pin profile with varying D/d ratio as shown in figure 3 (a-i). It is observed that the joints made with D/d ratio= 3 , tool rotational speed= 1400rpm , and weld traverse speed=40mm/min resulted in very much smaller equiaxed grains compared to other conditions. During stirring action of the tool which induces high amount of plastic deformation and frictional heat generation between the tool and the BM. This is due to the mechanism of constant dynamic recrystallization (DRX). The DRX usually occurs in WZ and the microstructure can be refined. Between WZ and BM, small portions of TMAZ and HAZ were observed. The TMAZ consists of a slightly elongated grain structure due to the annealing affect of heat and severe plastic deformation of the material around the pin edge;outside of the TMAZ there is a zone (HAZ) affected only by the heat generation during the welding process in which slightly coarse grains were observed when compared with that of the BM. DRX is of great industrial interest due to the new grains being smaller than the initial grains which improves mechanical properties at room temperature. figure 3(a-i) shows the microstructures of joints made at various conditions using optical microscope under 100X magnification. From the microstructures it is observed that fig c obtained at 1400rpm, 40mm/min and D/d=3 shows finer grains when compared with all other joints made at different conditions.

Table 3: Mechanical properties of welded joints

Traverse speed (mm/min)	Tool rotational speed(rpm)	Condition	D/d ratio	UTS (MPa)	YS (MPa)	% El	Hardness (HR _B)	Impact strength(J)
40	900	b	3	100	72	15	34	10
		d	2.5	98	70	9	31	7
		g	2	95	70	9	31	8
	1120	a	3	105	82	14	35	11
		e	2.5	102	74	11	35	7
		h	2	98	71	10	32	6
	1400	c	3	111	85	18	38	11
		f	2.5	108	82	17	36	8
		i	2	106	81	15	32	6

3.2 Mechanical Properties

Mechanical properties of the joints fabricated by the taper cylindrical tool pin profile with varying D/d ratio are shown in table 3. It is observed that the joint fabricated with tool rotational speed of 1400 rpm, weld speed of 40mm/min and D/d ratio of 3 produced superior tensile properties compared to other joints. This is due to higher rotational speed and more amount of heat generated due to friction due to large contact area and formation of finer grains . Elongation depends on the generated heat input and the heat input depends on the welding parameters and higher the rotational speed more the heat input and %elongation will be higher.Hardness value is also high for the joint

obtained at 1400rpm, weld speed of 40mm/min and D/d ratio of 3 which is due to the formation of fine grain size.

4. CONCLUSIONS

The effect of taper cylindrical pin profile with varying D/d ratio on microstructure and mechanical properties of friction stir welds of pure aluminium was investigated. The main conclusions were drawn as follows:

- The mechanical properties of the pure aluminium weldments were affected by the varying D/d ratio of the tool pin profile.
- The maximum values of tensile strength (111MPa), impact toughness (11J) and Hardness (38HR_B) is observed at tool rotation speed of 1400 rpm, traverse speed of 40 mm/min and D/d ratio of 3 when compared to other conditions. This is due to the formation of fine grain microstructure in the stir zone.
- Finer grains were observed in the stir zone at the condition of D/d=3.

ACKNOWLEDGEMENTS

The authors would like to thank the authorities of Kamala Institute of Technology & Science, Huzurabad and M/S Venkateshwara Enterprises, Balanagar, Hyderabad, India for providing the facilities to carry out this work.

REFERENCES

1. T.Sakthivel, J.Mukhopadhyay, Microstructure and mechanical properties of friction stir welding of copper, *Journal of Material Science*, 2007: 42(19), pp. 8126-8129.
2. H. Fujii, L.Cui, M.Maeda, and K.Nogi, Effect of tool shape on mechanical properties and microstructure of friction stir welded aluminum alloys, *Material Science Engineering. A* 2006: 419 (1-2), pp. 25-31.
3. A.Esmaeili, M.K.B Givi, and H.R.Z Rajani, A metallurgical and mechanical study on dissimilar friction stirs welding of aluminium 1050 to brass (CuZn30)". *Material Science Engineering A*, 2011: 528(22-23), pp.7093-7102.
4. P.C.Sinclair, W.R. Longhurst, C.D. Cox, D.H. L. A. M. Strauss and G. E. Cook, heated friction stir welding: An experimental and theoretical investigation into how preheating influences process forces" *Materials and Manufacturing Processes*, 2010: 25, pp. 1283-1291.
5. Choi and S. B. Jung, "Effect of pin shapes on joint characteristics of friction stir spot welded AA5J32 sheet". *Material Transactions*, 2010: 210(11), pp.1455-1463.
6. Chinese Welding Society, *Welding Handbook*, China machine press: Beijing, 2nd edition, 2001: 2, pp.608-643.

EXPERIMENTAL INVESTIGATION ON ROUNDNESS ERROR IN DRILLING OF GFR/PC THERMOPLASTIC MATRIX COMPOSITES USING BOX-BEHNKEN DESIGN (BBD)

T. Srinivasan ^{1*}, **K. Palanikumar** ² and **K. Rajagopal** ³

¹Research Scholar, Department of Mechanical Engineering, Jawaharlal Nehru Technological University, Hyderabad, Telangana, India.

²Department of Mechanical Engineering, Sri Sai Ram Institute of Technology, Chennai, Tamil Nadu, India.

³Department of Mechanical Engineering, Jawaharlal Nehru Technological University, Hyderabad, Telangana, India.

Abstract: Glass Fiber Reinforced Polycarbonate Composite is used in many automobile, aero space, chemical industry, commercial and industrial products for their good properties such as high strength, stiffness, less weight, corrosion resistance and fatigue resistance. Drilling is the important and the final operation required for joining of two more parts. This study concentrates on the roundness error (diameter error or ovality) on drilling of Glass Fiber Reinforced Polycarbonate matrix composites. The main reason to develop the roundness error is improper cutting parameters such as spindle speed, feed rate and thrust force. The various cutting parameters considered for the experiment for the above listed and the influence of parameters on roundness error is analysed using design of experiments (DOE). Empirical relation developed response surface methodology (RSM) and Box Behnken design is used for analyzing the results. The influence of individual input process parameters on roundness error are analysed with help 3-D response surface graphs and presented in this study.

Keywords: glass fiber, polycarbonate, drilling, roundness error, surface roughness

Address all correspondence to: Tel.: +0-442-251-2111; fax: 91-442-251-2323, e-mail address: seenusreeja@gmail.com

INTRODUCTION

The Composite materials usage is increased due their low cost and availability of materials when compared to the conventional engineering materials. Glass fiber reinforced with thermoplastic matrix composite is used widely in automobile, aircraft, chemical, sports and packaging industry. Benardos et al [1] have studied that the increase the productivity of machine tools and machine components is fully dependent on surface quality. The precision of surface quality is

achieved for smooth function of moving mechanical parts. Chornig et al [2] have studied the short glass fiber with polycarbonate composite laminates and optimized the cutting parameters using neural network and response surface methodology. They suggested that, polycarbonate has high toughness and hardness and can be used to manufacture computer monitors, housings and printers as well as many engineering applications. The variation of a cross section of the actual hole size to ideal hole size indicates the roundness error. The difference is within the prescribed limit, the workpiece is suitable for the assembly, otherwise rejected. Sreenivasulu et al [3] have investigated the influence of drilling parameters on roundness error and surface roughness in drilling of Al6061 alloy material using HSS twist drills. Lin et al [4] have studied the hole quality, roundness error and surface roughness on 6061T6 material. They determined the optimal parameters as feed, speed and drill diameter by using Taguchi – gray relational analysis. Somasundaram and Rajendra Boopathy [5] have provided a comprehensive evaluation on the roundness error value which is always more than the actual hole value, which reduced the percentage of the rejection parts. They considered thickness of work plate, feed, speed and workpiece composition etc.. experiment parameters and predicted the influence of such parameters using response surface methodology. Du et al [6] have investigated the roundness error by Particle swarm optimization (PSO) algorithms and compared the result with two different methods such as particle swarm optimization and Minimum zone circle technique. Palanikumar et al [7] have reported that the feed rate and drill diameter are the important predominant parameters which influence the roundness error in drilling of glass fiber reinforced high impact polystyrene thermoplastic (GFRTTP) composites. Lei Xianqing et al [8] have proposed that the new technique for roundness error damage evaluation such as polar co-ordinate transform algorithm (PCTA) using polar co-ordinate system. Adem et al [9] have predicted the roundness error and surface roughness of the drilled hole and optimized drill parameters using taguchi technique in drilling of AISI 316 stainless steel. Li and Shi [10] have proposed the new concept of curvature technique for calculated the roundness error damage from the data obtained by a co-ordinate measuring machine (CMM) and compared the results. Hussain et al [11] have proposed the parameters obtain the good surface finish through serious experiment conducted based on the Taguchi's design of experiments (DOE) L25 orthogonal array. Palanikumar [12] have developed the model against the delamination factor and surface roughness in drilling Glass Fiber Reinforced Polymer (GFRP) composites using Response surface methodology. The central composite design technique and three factors five levels design was used for carrying out this work. Palanikuamr et al [13] have proposed artificial neural network for the prediction of surface roughness in drilling of GFRP composites. Palanikumar [14] have compared and analysed the An L27 orthogonal array, signal to noise ratio, and pareto ANOVA analysis are used to find the effect of cutting parameters and minimizing the surface

roughness. Prakash and Palanikumar (15) have optimized the drilling parameters used on the prediction of surface roughness during drilling of MDF composites. Box Behnken design has been used to study the influence of the parameters such as feed rate, spindle speed and drill diameter.

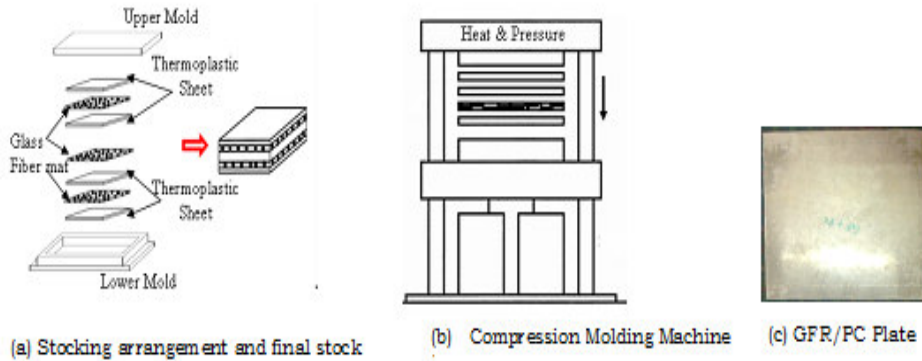


Figure 1: Fabrication Process of GFR/PC composites

MATERIALS AND METHODS

The glass fiber reinforced polycarbonate thermoplastic composite laminates were manufactured by the method of film stacking and hot pressing in a hydraulic compression press molding. The thermoplastic matrix-polycarbonate (PC) in the form of film sheet and the reinforcement as glass fiber (GFR) woven fabric were taken in almost equal to 1:1 ratio. The seven polycarbonate film sheets were stacked between six layers of woven mat type glass fibers. The alternate layers of GF woven and PC films were placed in the mould of 250 mm X 250 mm size between the platens of the press. The mold platens were electrically heated to the glass transition temperature. Silicone spray is applied to the mould surfaces to protect the laminate sticking to the respective mold plate. The composite laminates were fabricated by pressing the material in between hot plates of a compression molding press at 5 bar pressure. The same pressure is maintained for cooling, by placing the laminates for 5 minutes. The temperature and pressure were two important parameter to control the desired processing conditions in the mold. Finally composite laminates were removed from the platens. Fabrication process set-up details are presented in Figure 1.

3. EXPERIMENTAL SETUP

Solid carbide drill bit is used for conducting the drilling experiments and diameter of drill bit is used 6, 9 and 12 mm. The type of the drill bit used is Brad and Spur. The various cutting parameters like spindle speed of 1000, 3000 and 5000 rpm and feed rates of 100, 200 and 300 mm/min used for the experimentation. The parameters and their levels used for the experimentation are given in Table 1. Figure 2 shows the experimental set up used for measuring the roundness error in drilled

holes. The drilling experiment is carried in Computer Numerical Control (CNC) drilling machine using the planned cutting parameters pre fixed. The typical hole drilled in the polycarbonate composites is presented in Figure 3. From the Figure 3, it has observed that the due to roundness error tendency of composite material, perfect circular hole is not achieved and also holes are not very smooth and exactly round. Roundness error is observed by co-ordinate measuring machine (CMM).

Table 1: Experimental condition

Parameters	Levels		
	1	2	3
Spindle speed (N) rpm	1000	3000	5000
Feed (f) mm/min	100	200	300
Drill diameter (d) mm	6	9	12

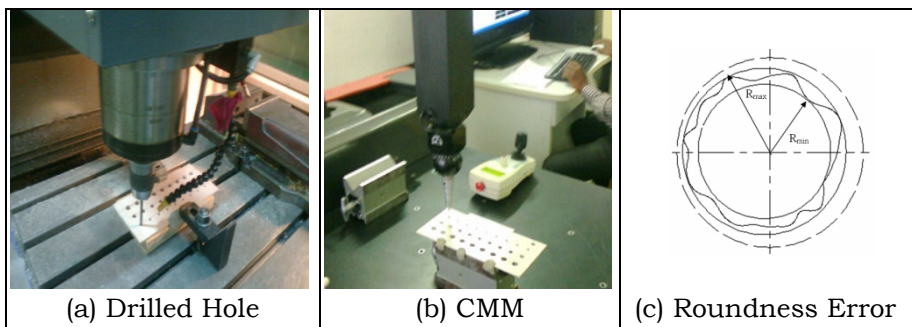


Figure 2: Measurement of roundness error using Co-ordinate Measuring Machine

The result also indicated that the drill diameter is the major influential parameter which affects the roundness error. From the analysis of variance (ANOVA), it has been asserted that the model F-value of 5.10 implies the model is significant. There is only a 2.15% chance that a "Model F-Value" this large could occur due to noise. Values of "Prob > F" less than 0.0500 indicate model terms are significant. The scheme of roundness error and photograph of the drilled hole are presented in Fig. 3. The experimental conditions used, run order and observed roundness error for different conditions are presented in Table 2.

The analysis of response function is carried out by using Analysis of Variance (ANOVA). The result of ANOVA for roundness error is presented in Table 3. Further, Figure 4 shows the correlation graph for roundness error, in which the predicted and actual roundness error fall in a straight line and hence the model has been proved to be adequate in Figure 4.



Figure 3: Typical drilled holes observed at different drilling condition

Table 2: Box Behnken Design for Roundness Error

S. No.	Run order	Drill diameter, mm	Feed rate, mm/min	Spindle speed, rpm	Roundness Error mm
1	2	6	100	3000	0.0469
2	16	12	100	3000	0.066
3	11	6	300	3000	0.059
4	12	12	300	3000	0.089
5	14	6	200	1000	0.053
6	10	12	200	1000	0.079
7	7	6	200	5000	0.055
8	4	12	200	5000	0.076
9	15	9	100	1000	0.051
10	1	9	300	1000	0.067
11	8	9	100	5000	0.064
12	17	9	300	5000	0.075
13	3	9	200	3000	0.066
14	13	9	200	3000	0.068
15	9	9	200	3000	0.065
16	5	9	200	3000	0.070
17	6	9	200	3000	0.069

*Average of 3 results

Table 3: ANOVA for Roundness Error

	Sum of		Mean	F		
Source	Squares	DF	Square	Value	Prob > F	
Model	0.001598	9	0.000178	5.100717	0.0215	significant
A	0.000828	1	0.000828	23.77918	0.0018	
B	6.57E-05	1	6.57E-05	1.885583	0.2121	
C	3.96E-05	1	3.96E-05	1.137722	0.3215	
A2	4.2E-07	1	4.2E-07	0.012055	0.9157	
B2	1.16E-07	1	1.16E-07	0.003335	0.9556	
C2	0.00011	1	0.00011	3.154105	0.1190	
AB	9.1E-05	1	9.1E-05	2.612151	0.1501	
AC	9.21E-05	1	9.21E-05	2.644615	0.1479	
BC	1.96E-05	1	1.96E-05	0.562786	0.4776	
Residual	0.000244	7	3.48E-05			
Lack of Fit	0.000173	2	8.66E-05	6.143459	0.0450	significant
Pure Error	7.05E-05	5	1.41E-05			
Cor Total	0.001842	16				

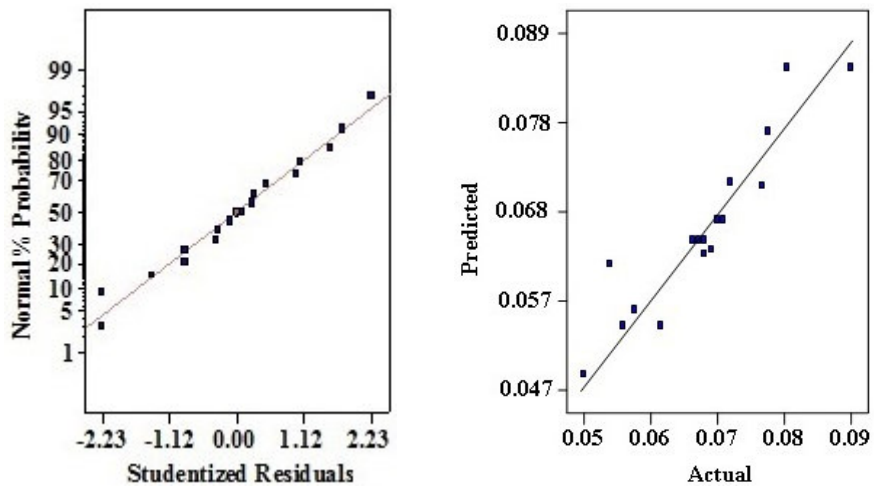


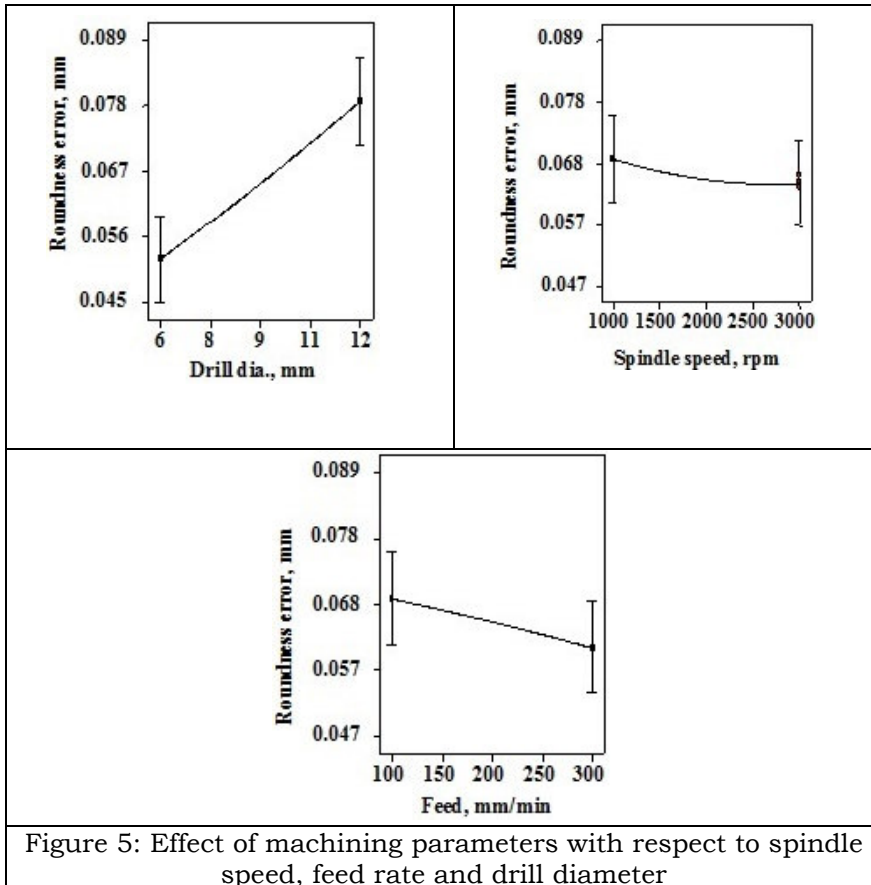
Figure 4: Correlation graph for Roundness Error

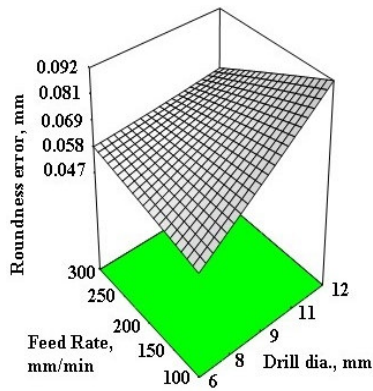
4. RESULT AND DISCUSSION

In Recent Trend, increases the usage of light weight, durable and corrosive resistance material. Glass fiber reinforced thermoplastic

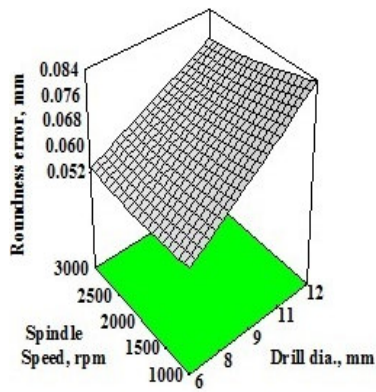
polymer material is well suitable for the same above. Drilling is the most common machining operation in the Assembly section. It is required for the final component shape and quality. Most of the structure failure occurs due to improper hole formation of the plates. Improper selection of cutting parameters leads more stress concentration, which collapse the function of the part and it develops the delamination damage, fiber pullout and roundness error.

The analysis of roundness error in drilling of thermoplastic composite material is carried out through effect graphs. Figure 5(a) shows the influence of drill diameter on drilling of GFR/PC composites. The roundness error increases with the increase in drill diameter due to the increases in contact area between the workpiece and tool. Figure 5 (b) Figure shows the influence of spindle speed on roundness error in drilling of GFR/PC composites. The roundness error decreases slightly with the increase in spindle speed. 5 (c) shows the influence of feed rate on roundness error in drilling of GFR/PC composites. From the figure, it has been asserted that the increase of feed rate reduces the roundness error in drilling of GFR/PC composites.

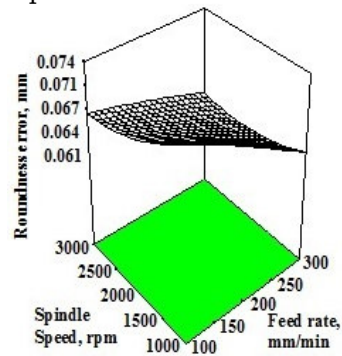




(a) Effect of Feed rate and Drill Diameter on roundness error
(b)



(b) Effect of Spindle Speed and Drill Diameter on roundness error



(c) Effect of Spindle Speed and Feed rate on roundness error

Figure 6: The interaction between the drilling parameters on Roundness Error

The effect of interaction between the parameters are analysed by using three dimensional response graphs. Three dimensional response graphs are the graphs which show the effect of two varying parameters by keeping the third parameter at constant middle level. Figure 6 (a) shows the effect of feed rate and drill diameter on drilling of thermoplastic composite materials. The results indicate that the increase of feed rate and drill diameter increases the roundness error in drilling of GFR/PC composites. Figure 6 (b) shows the effect of drill diameter and spindle speed on drilling of GFR/PC composites with respect to the roundness error. The results indicate the same trends as discussed earlier. Figure 6(c) shows the effect of spindle speed and feed rate on roundness error in drilling of GFR/PC composites. The results indicate that the increase of spindle speed slightly increase the roundness error in drilling of GFR/PC composites as discussed earlier. The experimental result indicates that drill diameter and feed rate are having high influence affecting the roundness error in drilling of thermoplastic composite materials. Drill diameter is the highly influential parameters which affect the roundness. The scanning electron micrograph of the drilled surface is presented in Figure 7, which shows the drilled hole and magnified portion of the hole drilled.

From the above discussion, it has been inferred that the proper usage of cutting parameters may reduce the diameter or roundness error in drilling of GFR/PC composites.

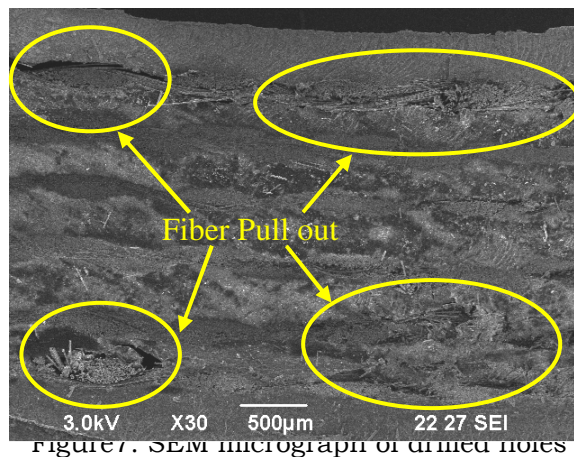


Figure 7. SEM micrograph of drilled holes

5. CONCLUSIONS

Experimental investigation is carried out for study and analysis of the roundness or ovality or diameter error in drilling of Glass Fiber Reinforced Polycarbonate Thermoplastic matrix composite laminates. The influence of various cutting parameters is being considered and listed in detail. The following conclusions are drawn based on the experimental results. Figure 7 shows the scanning electron micrograph image of the cross section of drilled hole surface. The images show clearly in which bundle of the fiber has come out, small pits and improper rough surface

of the workpiece due to the cutting action. It should be avoided by the selection of proper cutting parameters and tools.

1. For Experimentally studying the roundness error in drilling of GFR/PC composites laminates, the drill hole dimensions are measured by using the coordinated measuring machine (CMM) and the relative error is compared by using the nominal diameter of the drill.
2. The results indicated that the increase of drill diameter and feed rate increases the roundness error in drilling of GFR/PC composite laminates.
3. The spindle speed is having only little effect on drilling of GFR/PC composite laminates.

REFERENCES

1. P.Benardos, and G.Vosniakos, Predicting surface roughness in machining: a review, *International Journal of Machine Tools and Manufacture*, 2003: 43, pp.833–844.
2. Chorng-Jyh Tzeng, Yung-Kuang Yang, Yu-Hsin Lin, and Chih-Hung Tsai, A study of optimization of injection molding process parameters for SGF and PTFE reinforced PC composites using neural network and response surface methodology, *International Journal of Advanced Manufacturing Technology*. 2012: 63, pp.691–704,
3. Sreenivasulu Reddy, and Ch. Srinivasa Rao, Application of Gray Relational Analysis for Surface Roughness and Roundness Error in Drilling of Al6061 Alloy, *International Journal of Lean Thinking*, 2012: 3, pp.67-78.
4. S.Lin, M.Chuang, J.Wen, and Y.Yang, Optimization of 6061T6 CNC Boring Process Using the Taguchi Method and Grey Relational Analysis, *The open Industrial and Manufacturing Engineering Journal*, 2009: 2, pp.308-313.
5. G.Somasundaram, S.Rajendra Boopathy, and K.Palanikumar, Modeling and analysis of roundness error in friction drilling of aluminum silicon carbide metal matrix composite, *Journal of Composite Materials*, 2011: 46(2) pp.169–181.
6. Chang-long Du, Chen-xu Luo, Zheng-tong Han, and Yong-she Zhu, Applying particle swarm optimization algorithm to roundness error evaluation based on minimum zone circle, *Measurement*, 2014: 52, pp.12–21.
7. K.Palanikumar, T.Srinivasan, and K.Rajagopal, Investigation on Roundness Error in Drilling of Glass fiber reinforced/High Impact Polystyrene Composites, *Proceedings of the Second International Conference on Smart Technologies for Materials, Communication, Controls, Computing & Energy (ICST-2013)*, Vel Tech Dr. RR & Dr. SR Technical University, Chennai, T.N., India. 2013: pp.64-68.

8. Lei Xianqing, Zhang Chunyang, Xue Yujun, and Li Jishun, Roundness error evaluation algorithm based on polar coordinate transform, *Measurement*, 2011: 44, pp.345–350.
9. Adem Çiçek, Turgay Kivak, and Gürcan Samtaş, Application of Taguchi Method for Surface Roughness and Roundness Error in Drilling of AISI 316 Stainless Steel, *Journal of Mechanical Engineering*, 2012: 58-3, pp.165-174.
10. Li Xiuming, and Shi Zhaoyao, Evaluation of roundness error from coordinate data using curvature technique, *Measurement*, 2010: 43, pp.164–168.
11. S.A.Hussain, V.Pandurangadu, and K.Palanikumar, Surface roughness analysis in Machining of GFRP composite by carbide tool (K20), *European journal of scientific research*, 2010: 5(5), pp.233-438.
12. K.Palanikumar, Modeling and analysis of delamination factor and surface roughness in drilling GFRP composites, *Materials and Manufacturing Processes*, 2010: 25(10), pp.1059-1067.
13. K.Palanikumar, B.Latha, V.S.Senthilkumar, and J.P. Davim, Application of Artificial Neural Network for the prediction of surface Roughness in Drilling GFRP composites, *Materials Science Forum*, 2013: 766, pp.21-36.
14. K.Palanikumar, Cutting Parameters Optimization for Surface Roughness in Machining of GFRP Composites using Taguchi's Method, *Journal of Reinforced Plastics and Composites*, 2006: 25, pp.1739-1751.
15. K.Prakash, K.Palanikumar, J.L.Mercy, and S.Nithyalakshmi, Evaluation of surface roughness parameters (Ra, Rz) in drilling of MDF composite panel using Box-Behnken experimental design (BBD), *International Journal of Design and Manufacturing Technology*, 2011: 5(1), pp.52-62.

SELECTION OF OPTIMAL PROCESS PARAMETERS IN WIRE-ELECTRICAL DISCHARGE TURNING WHILE MACHINING TI-6AL-4V ALLOY

Naresh Baki^{1*}, A. Chennakesava Reddy², Thella Babu Rao¹

¹Assistant, Department of Mechanical Engineering, GITAM University, Hyderabad - 502329, India.

²Professor, Department of Mechanical Engineering, JNTU, Hyderabad – 500085, India.

Abstract: Wire electrical discharge turning (WEDT) is one of the novel configurations of wire electrical discharge machining (WEDM) process developed to produce cylindrical components. A precise rotary spindle is designed and added to the WEDM configuration to enable the generation of free-form cylindrical geometries. In WEDT, the turning process parameters such as spindle rotational speed, feed, depth of cut and the usual WEDM parameters play a significant role on the process performance. Therefore, this further increased complexity of understanding the process variables against the process performance. However, the right selection of WEDT conditions become the most important aspect while producing the precise turned components. This investigation presents an experimental study on the effects of machining parameters on material removal rate (MRR) and surface roughness (R_a) in WEDT process. The machining experiments were conducted on Ti-6Al-4V super alloy by using statistical design of experiment (DOE) method. The experimentally measured responses were analyzed for individual and interaction effects by adopting analysis of variance (ANOVA). Since the machining responses are found with correlation between them, the problem was formulated as a multi-objective optimization problem and is solved to obtain the solutions. An integrated statistical multi-response optimization approach, gray relational analysis was implemented on the experimental results to derive the optimal WEDT conditions. Consequently, the derived optimal process responses are confirmed by the validation experiments and the results are found with good correlation.

Keywords: Wire electrical discharge turning, Ti-6Al-4V alloy, ANOVA, modeling, multi-response optimization.

Address all correspondence to: flytonaresh@gmail.com

1. INTRODUCTION

Wire electric discharge machining (WEDM) is considered as one of the configurations of conventional EDM process. WEDM is evidenced as one of the most extensively used non-traditional thermoelectric process

used to manufacture components with intricate shapes. WEDM utilizes a continuously traveling wire electrode of diameter 0.05-0.3 mm for attaining very small corner radii [1]. During the WEDM process, the material is eroded ahead of the wire due to the thermoelectric sparks generated between the work piece and the electrode. In this process the work piece experiences no mechanical stresses due to no direct contact between the work piece and the wire makes the process widely employed to cut the electrically conductive hard-to-cut material with irrespective of its hardness and strength [2]. Wire electrical discharge turning (turning with WEDM) is one of the emerging area, developed to generate cylindrical form on hard and difficult to cut super alloys such as Titanium and Nickel. In WEDT process the electrical discharge takes place between the traveling wire and the rotating workpiece (a rotary axis is added to WEDM) to be machined. In this process the desired cylindrical forms can be obtained by controlling the electrically charged wire in X and Y directions to remove the unwanted work material [3,4].

2. LITERATURE REVIEW

Several research works that solely study the characteristics of the WEDT process considering various input and output parameters. The turning of small diameter pins of size 5 mm using WEDM works have been reported by Masuzawa and Tonshoff [5-7]. Qu et al. [3] reported the turned automobile components like diesel injector plungers with WEDM. The results of Liao et al., 1997 [8] showed that the MRR and surface finish are easily influenced by the table feed rate and pulse on time. Mohammadi et al. [9] investigated the WEDT process to evaluate the effects of machining parameters on MRR by using the Taguchi approach in design of experiments (DOE). K. Ponappa et.al [10] investigated the influence of EDM parameters on various aspects of the surface integrity of Ti-6Al-4V with different electrode materials. Farnaz Nourbakhsh et al. [11] experimentally investigated the WEDM performance parameters such as cutting speed, surface roughness and wire rupture of Ti-6Al-4V in relation to process parameters and different wire electrode materials. Shajan Kuriakose et al. [12] investigated the surface characteristics of Ti-6Al-4V during WEDM process by employing the Taguchi method and analysis of variance. They found that time between two pulses, pulse duration, injection pressure, wire speed and wire tension are the most influencing parameters and the formation of layer consisting of mixture of oxides is influenced by the time between two pulses.

Recently Aravind Krishnan and Samuel [13] has attempted to optimize the process parameters by considering the MRR and surface roughness as output parameters of wire electrical discharge turning process. Lin et al. [14] reported the use of the grey relational analysis based on an orthogonal array and fuzzy-based Taguchi method for optimizing the multi-response EDM process. Experimental results showed that both approaches can optimize the machining parameters effectively. Grey relational analysis can be recommended as a method for optimizing

[15, 16] the complicated conflicting multiple performance parameters. Moreover, Lin et al. Showed grey relational analysis is more straightforward than the fuzzy-based Taguchi method for optimizing the EDM process with multiple process responses [12]. From the above Literature it is found that several researchers have attempted previously to improve the performance of the WEDT process such as surface roughness, cutting speed, dimensional accuracy and material removal rate (MRR). However, because of its stochastic nature and several variables are involved in this process, the full potential utilization of this process is not completely solved. In addition to that these performance parameters are conflicting in nature so it is difficult to find the single optimal combination of process parameters for the performance parameters.

The present paper deals with the experimental analysis of measured responses such as MRR and Ra for individual and interaction effects by adopting analysis of variance (ANOVA). Gray relational analysis (GRA) integrated Taguchi's S/N ratio optimization approach has been implemented to maximize the MRR and to minimize the surface roughness.

3. MATERIALS AND METHODS

This section discusses the experimental procedure and design of experiments based on Taguchi method.



Figure 1: The experimental setup of turning with wire EDM

3.1 Experimental Procedure

In this research, the experiments are conducted on ROBOFIL 100 high precision 5-axis CNC WEDM shown in figure 1. The wire EDM machine was equipped with a rotary axis in order to produce cylindrical forms. Ti-6Al-4V work piece of 20mm diameter with 150mm length was used to perform the turning experiments on WEDM. The surface finish was measured using a Talysurf (MITUTOYO) with a 0.8mm cut off length (according to DIN EN ISO 3274:1998). Eq. (1) can be derived to describe the calculation for MRR:

$$MRR = \pi(R^2 - r^2)V_f \quad (1)$$

where, R is the original radius of the work piece, r the final radius of the work piece after machining, and V_f is the machining cutting speed or feed rate.

Table 1: Machining parameters and their levels.

S.No.	Parameter	Units	Notation	-1	0	+1
1.	Spindle speed	Rpm	X_1	14	22	30
2.	Pulse-on time	μs	X_2	110	115	120
3.	Pulse-off time	μs	X_3	50	55	60
4.	Peak current	A	X_4	100	150	200
5.	Wire feed	mm/min	X_5	1	2	3
6.	Servo	V	X_6	30	60	90

Table 2: Experimental analysis using Taguchi method

Exp. No.	X_1 (rpm)	X_2 (μs)	X_3 (μs)	X_4 (A)	X_5 (mm/min)	X_6 (V)	R_a (μm)	MRR (mm ³ /min)
1.	14	110	50	100	1	30	0.80	2.553
2.	14	110	55	150	2	60	1.06	2.355
3.	14	110	60	200	3	90	1.43	1.762
4.	14	115	50	150	2	90	1.79	4.406
5.	14	115	55	200	3	30	1.67	5.812
6.	14	115	60	100	1	60	1.02	4.792
7.	14	120	50	200	3	60	2.57	6.208
8.	14	120	55	100	1	90	1.99	5.253
9.	14	120	60	150	2	30	1.72	9.756
10.	22	110	50	100	3	90	1.84	2.816
11.	22	110	55	150	1	30	1.18	4.077
12.	22	110	60	200	2	60	1.46	4.710
13.	22	115	50	150	1	60	1.88	5.463
14.	22	115	55	150	2	90	2.04	3.742
15.	22	115	60	100	3	30	1.58	5.356
16.	22	120	50	200	2	30	2.64	8.536
17.	22	120	55	100	3	60	2.51	6.070
18.	22	120	60	150	1	90	2.34	5.253
19.	30	110	50	200	2	60	2.49	2.626
20.	30	110	55	100	3	90	2.39	3.959
21.	30	110	60	150	1	30	1.70	5.812
22.	30	115	50	100	3	30	2.61	6.829
23.	30	115	55	150	1	60	2.43	7.805
24.	30	115	60	200	2	90	2.74	4.478
25.	30	120	50	150	1	90	3.37	4.406
26.	30	120	55	200	2	30	3.19	5.938
27.	30	120	60	100	3	60	3.03	4.553

3.2 Design of Experiments Based on Taguchi Method

The WEDM process consists of three operations, a roughing operation, a finishing operation, and a surface finishing operation. Usually, performance of various types of cutting operations is judged by different

measures. In case of finish cutting operation, the surface finish is of primary importance whereas both metal removal rate and surface finish are of primary importance for rough cutting operation. Therefore, the rough cutting phase is investigated in the present approach considering two performance goals such as surface roughness (R_a) and metal removal rate (MRR) while spindle speed, pulse-on time, pulse-offtime, peak current, wire feed and servo are considered as the process control variables. Factors and their levels are shown in table 1. In order to reduce the number of experimental runs, experiments were planned based on design of experiments (DoE). Table 2 represents the matrix of experimental design and experimentally measured responses.

4. RESULTS AND DISCUSSION

The effect of process variables on the surface roughness, material removable rate is discussed.

4.1 Analysis of Surface Roughness

Equation 2 presents the linear relationship between factors, factors effects and surface roughness (response) which is the result of regression analysis.

$$R_a = -10.274 + 0.068X_1 + 0.101X_2 - 0.033X_3 + 0.003X_4 + 0.162X_5 + 0.006X_6 \quad (2)$$

The R-Sq (R^2) value in the table 3 indicates that the predictors explain 98.19% of the variance in R_a . The R-Sq (adj) (R^2_{adj}) is 97.65%, which accounts for the number of predictors in the model. Both values indicate that the model fits the data well. Table indicates that the model estimated by regression procedure is significant at an α -level of 0.05. This implies that at least one coefficient is different from zero. The predicted machining parameters performance was compared with the actual machining performance and a good agreement was obtained between these performances. The above mathematical model for surface roughness of WEDT is of great importance to the proper selection of machining parameters during the machining of the cylindrical parts.

4.2 Analysis of Metal Removal Rate

Eq. 3 presents the linear relationship between factors, factors effects and MRR (response) which is the result of regression analysis.

$$MRR = -27.508 + 0.024X_1 + 0.281X_2 + 0.029X_3 + 0.002X_4 - 0.113X_5 - 0.034X_6 \quad (3)$$

The R-Sq (R^2) value in the Table 4 indicates that the predictors explain 78.23% of the variance in MRR. The R-Sq (adj) (R^2_{adj}) is 77.56%, which accounts for the number of predictors in the model. Both values indicate that the model fits the data well. Table 4 indicates that the model estimated by regression procedure is significant at an α -level of 0.05. This implies that at least one coefficient is different from zero. The predicted machining parameters performance was compared with the actual machining performance and a good agreement was obtained between these performances. The mathematical model for metal removal

rate of WEDT is of great importance to the proper selection of machining parameters during the machining of the cylindrical parts. Figure 2 & 3 shows that spindle speed, pulse-on time, pulse-off time, peak current, wire feed and servo have the most significant effect on MRR. Pulse-on time has direct proportion to the R_a ; that is, by increasing this factor, MRR increases significantly. Also it is indicated from this figure that servo has a significant effect on MRR, because at decreasing servo MRR increases strongly.

Table 3: ANOVA Table for regression model for R_a

Source	DF	Seq SS	Adj SS	Adj MS	F	P
X ₁	1	5.4450	5.4450	5.44500	502.684	0
X ₂	1	4.5100	4.5100	4.51001	416.365	0
X ₃	1	0.4900	0.4900	0.49005	45.2420	0.0000015
X ₄	1	0.3610	0.4098	0.40980	37.8330	0.0000052
X ₅	1	0.4737	0.4737	0.47369	43.7310	0.0000019
X ₆	1	0.4969	0.4969	0.49693	45.8770	0.0000014
Error	20	0.2166	0.2166	0.01083		
Total	26	11.9933				
R-Sq : 98.19%		R ² (adj): 97.65%		R ² (pred): 96.75%		

Table 4: ANOVA Table for regression model for MRR

Source	DF	Seq SS	Adj SS	Adj MS	F	P
X ₁	1	0.6841	0.6841	0.6841	0.4022	0.533152
X ₂	1	35.569	35.569	35.569	20.912 2	0.000185
X ₃	1	0.384	0.384	0.384	0.2258	0.639837
X ₄	1	0.4962	0.2064	0.2064	0.1214	0.731215
X ₅	1	0.2332	0.2332	0.2332	0.1371	0.715041
X ₆	1	18.9178	18.917 8	18.9178	11.122 4	0.0033
Error	20	34.0174	34.017 4	1.7009		
Total	26	90.3017				
R-Sq : 78.23%		R ² (adj): 77.56%		R ² (pred): 76.25%		

5. Implementation of Gray Relational Analysis

In the procedure of GRA, the responses are normalized as the first step using the equations 4 and 5 as shown in Table 5. As a part of the estimation of grey relational coefficients, the quality loss estimates of each individual has been calculated and listed in Table 5. Then the individual gray relational grades and the overall gray relational grade have been calculated by using Eq. 6 and are shown in Table 5. Here, the value of distinguishing coefficient is assumed as 0.5. The overall gray relational grade represents the quality index of multiple responses of the process; hence, the multi-objective optimization problem has been converted in to single-objective optimization problem.

Lower-the-better (LB) is the criterion: $x_i(k) = \frac{\max y_i(k) - y_i(k)}{\max y_i(k) - \min y_i(k)}$ (4)

Higher-the-better (HB) is the criterion: $x_i(k) = \frac{y_i(k) - \min y_i(k)}{\max y_i(k) - \min y_i(k)}$ (5)

where, $x_i(k)$ is the normalised value of k^{th} response, $\min y_i(k)$ is the smallest value of $y_i(k)$ for k^{th} response and $\max y_i(k)$ is the largest value of $y_i(k)$ for k^{th} response. x is the normalised array.

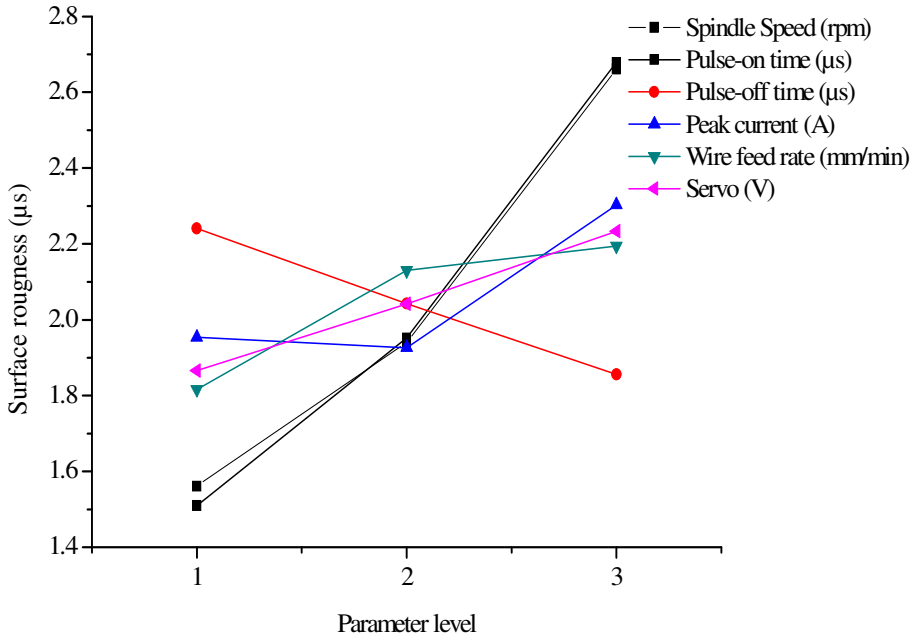


Figure 2: Effects of factors on R_a

Grey relational coefficient calculated from the normalised matrix.

$$\xi_i(k) = \frac{\Delta_{\min} + \zeta \Delta_{\max}}{\Delta_{0i}(k) + \zeta \Delta_{\max}} \quad (6)$$

Where, $\Delta_{0i} = \|x_0(k) - x_i(k)\|$: is the deviation of absolute value $x_0(k)$ and $x_i(k)$.

ζ is the distinguishing coefficient $0 \leq \zeta \leq 1$.

$$\Delta_{\min} = \min_{\forall j \in i} \min_{\forall k} \|x_0(k) - x_j(k)\| \quad (7)$$

$$\Delta_{\max} = \max_{\forall j \in i} \max_{\forall k} \|x_0(k) - x_j(k)\| \quad (8)$$

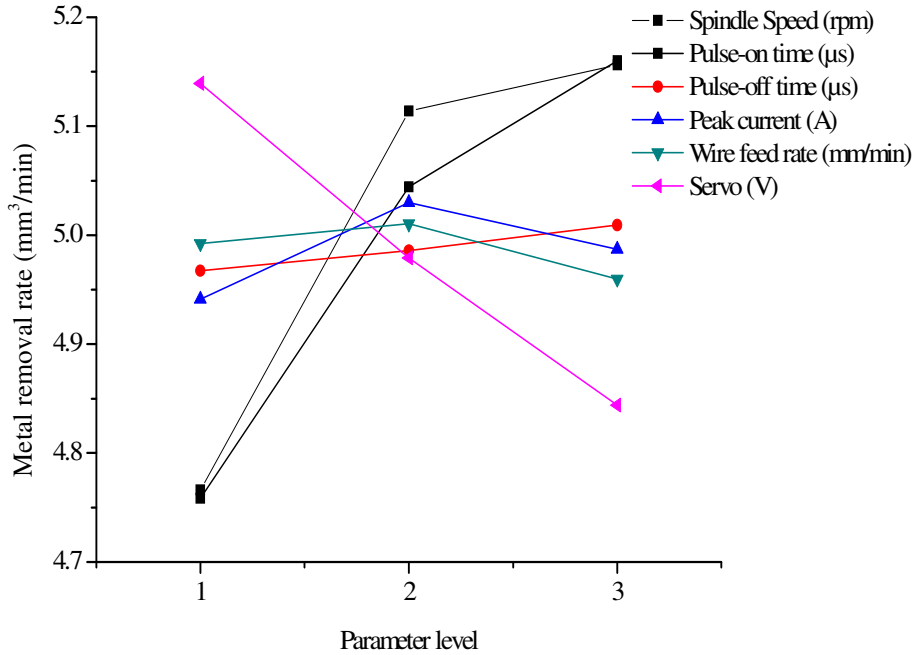


Figure 3: Effects of factors on MRR

The calculated gray relational grade values in the Table 5 serve as an overall quality index for each individual run which represents all the measures multiple responses of the WEDT process. The S/N ratios corresponding to the values of the GRG are then calculated and are tabulated Table 5. Hence, the problem with multi-response optimization has been converted in to single-response optimization with the aim of maximization of GRG. On the basis of maximization of S/N ratio of GRG, the optimal set of WEDT process parameter has been calculated using the Taguchi's maximization criterion which is:

$$\frac{S}{N} = -10 \log \left(\frac{1}{n} \sum_{i=1}^n \frac{1}{y_i^2} \right) \quad (9)$$

These optimal process parameters are depicted in Figure 3. This figure reveals the set of optimal parameter levels as: Spindle speed: 30 rpm, Pulse-on Time: 110µs, Pulse-off Time: 50 µs, Peak Current: 150 A, wire Feed: 3 mm/min and Servo: 90 V. Consequently, the conformation experimental runs have been conducted at the obtained levels of process variables and the comparisons have been made between the predicted and experimental runs at the optimum levels of process parameters and are presented in Table 6. The results in the Table 6 reflect the reasonable result of confirmatory experiment.

Table 5: Procedure of GRA

Normalized values					GRG			S/N ratios of GRG	
Exp. No	Experimentally measured values		Normalized values		$\xi_i(k)$		γ_i		
	Ra(μm)	MRR (mm^3/min)	R _a	MRR	R _a	MRR		GRG	S/N ratio (HB)
1	0.80	2.55	1.00	0.00	0.33	0.83	0.58	0.58	-4.67
2	1.06	2.36	0.90	0.03	0.36	0.87	0.61	0.61	-4.24
3	1.43	1.76	0.75	0.18	0.4	1.0	0.7	0.70	-3.11
4	1.79	4.41	0.61	0.19	0.45	0.6	0.53	0.53	-5.60
5	1.67	5.81	0.66	0.26	0.43	0.5	0.46	0.46	-6.67
6	1.02	4.79	0.91	0.41	0.35	0.57	0.46	0.46	-6.73
7	2.57	6.21	0.31	0.59	0.62	0.47	0.54	0.54	-5.27
8	1.99	5.25	0.54	0.69	0.48	0.53	0.51	0.51	-5.88
9	1.72	9.76	0.64	0.88	0.44	0.33	0.39	0.39	-8.27
10	1.84	2.82	0.60	0.09	0.46	0.79	0.62	0.62	-4.10
11	1.18	4.08	0.85	0.15	0.37	0.63	0.5	0.50	-5.99
12	1.46	4.71	0.74	0.28	0.40	0.58	0.49	0.49	-6.21
13	1.88	5.46	0.58	0.25	0.46	0.52	0.49	0.49	-6.18
14	2.04	3.74	0.52	0.33	0.49	0.67	0.58	0.58	-4.73
15	1.58	5.36	0.70	0.48	0.42	0.53	0.47	0.47	-6.52
16	2.64	8.54	0.28	0.63	0.64	0.37	0.5	0.50	-5.95
17	2.51	6.07	0.33	0.73	0.6	0.48	0.54	0.54	-5.35
18	2.34	5.25	0.40	0.92	0.56	0.53	0.54	0.54	-5.29
19	2.49	2.63	0.34	0.26	0.59	0.82	0.71	0.71	-3.00
20	2.39	3.96	0.38	0.31	0.57	0.65	0.61	0.61	-4.35
21	1.70	5.81	0.65	0.44	0.43	0.5	0.47	0.47	-6.63
22	2.61	6.83	0.30	0.39	0.63	0.44	0.53	0.53	-5.43
23	2.43	7.81	0.37	0.46	0.58	0.4	0.49	0.49	-6.23
24	2.74	4.48	0.25	0.62	0.67	0.6	0.63	0.63	-3.97
25	3.37	4.41	0.00	0.74	1	0.6	0.8	0.80	-1.93
26	3.19	5.94	0.07	1.00	0.88	0.49	0.68	0.68	-3.31
27	3.03	4.55	0.13	0.97	0.79	0.59	0.69	0.69	-3.22

6. CONCLUSIONS

Gray relational analysis integrated with Taguchi method implemented on the experimental values of WEDT to find the optimal levels of process parameters. Results of confirmatory experiment. The results are summarized as follows:

- 1.The performance of the integrated approach is effective while handling with the multiple responses and while converting in to single – response problem with minimum effort.
- 2.The optimal combination process variable obtained from the proposed methods is the set with Spindle speed: 30 rpm, Pulse-on time: 10 μs , Pulse-off time: 50 μs , Peak current: 150 A, wire feed: 3 mm/min and servo: 90 V.
- 3.Ther results of ANOVA reveals the major controllable parameters significantly affecting the process responses are spindle speed, pulse-on time and servo.

4. The proposed methodology can effectively deal with the multi-response optimization problems to determine the optimal WEDT process variables while cutting Ti-6Al-4V.
5. The present work provides the optimal WEDT conditions to produce Ti-6Al-4V based cylindrical component and also helps to automate the process.

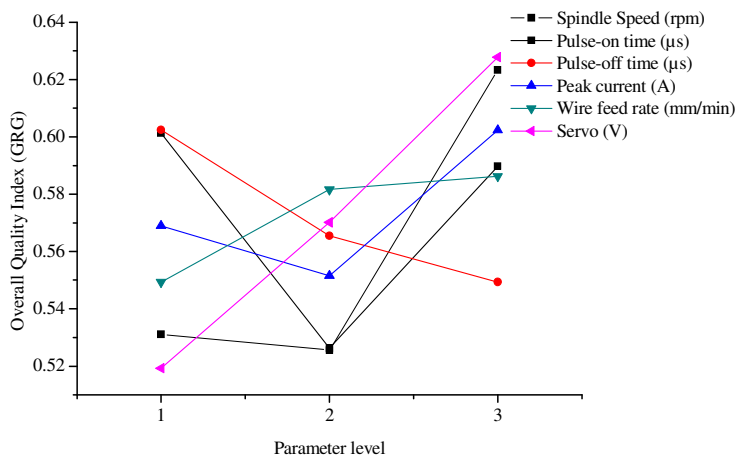


Figure 3: Effects of factors on GRG

Table 6: Results of confirmatory experiment

	Optimal Settings	
	Prediction	Experimental
Level of variables	Spindle speed :30 rpm Pulse-on time :110µs Pulse-off time :50 µs Peak current :150 A Wire feed :3 mm/min Servo :90 V	Spindle speed :30 rpm Pulse-on time :110µs Pulse-off time :50 µs Peak current :150 A Wire feed :3 mm/min Servo :90 V
S/N of GRG	-4.79442	-4.8104
GRG	0.7367	0.6910

REFERENCES

1. K. H. Ho, S. T. Newman, S. Rahimifard and R. D. Allen, State of the art in wire electrical discharge machining (WEDM), International Journal of Machine Tools and Manufacture, volume 44, pp. 247-1259, year 2004.
2. K. T Chiang and FP Chang, Optimization of the WEDM process of particle-reinforced material with multiple performance characteristics using grey relational analysis. Journal of Materials Processing Technology, 2006: 180, pp. 96-101.
3. J Qu, AJ Shih and RO Scattergood, Development of the cylindrical wire electrical discharge machining process, part1: concept, design, and material removal rate, Journal of Manufacturing Science and Engineering, 2002a: 124(3), pp. 702-707.
4. J Qu, AJ Shih and RO Scattergood, Development of the cylindrical wire electrical discharge machining process, part2: Surface Integrity and

- Roundness, *Journal of Manufacturing Science and Engineering*, 2002b: 124(3), pp. 708-714.
5. T. Masuzawa and HK Tonshoff, Three-dimensional micro-machining by machine tools, in *CIRP Annals-Manufacturing Technology*, 1997: pp. 621-628.
 6. B. Anjeneya Prasad, and A. Chennakesava Reddy, Regression analysis approach for predicting process output variables in WEDM, *National Conference on Computer Applications in mechanical Engineering*, 21st December 2005, Anantapur, pp.92-96.
 7. P. Arivazhagan, Moses Raja Cecil, A. Chennakesava Reddy, A. Rajadurai, Surface characteristics behaviour of the EDM eroded surface of al-sic metal matrix composite, *National Conference on Computer Applications in mechanical Engineering*, 21st December 2005, Anantapur, pp. 165-171.
 8. Y. S Liao, JT Huang and Hu Su, A study on the machining parameters optimization of wire electrical discharge machining, *Journal of Materials Processing Technology*, 1997: 71(3), pp. 487-493.
 9. Mohammadi, A. Fadaie Tehrani, E. Emanian, D. Karimi and H. Jafarpisheh, A new approach in turning by wire electrical discharge machining to evaluate the effects of machining parameters on MRR, in *Tehran International Congress on Manufacturing Engineering*, Tehran, Iran, December 12-15.
 10. K Ponappa, S. Aravindan, P. V. Rao, J. Ramkumar and M. Gupta, The effect of process parameters on machining of magnesium nano alumina composites through EDM, *International Journal of Advanced Manufacturing Technology*, 2010: 46, pp. 1035-1042.
 11. Farnaz Nourbakhsh, K. P. Rajurkar, A.P. Malshe and Jian Cao, Wire electrical discharge machining of titanium alloy, *Procedia CIRP*, 2013: 5, pp. 13-18.
 12. M. S. Shajan Kuriakose, Characteristics of wire-electro discharge machined Ti-6Al-4V surface, *Materials Letters*, 2004: 58, pp. 2231-2237.
 13. S. Aravind Krishnan and G. L. Samuel, Multi-objective optimization of material removal rate and surface roughness in wire electrical discharge turning, *International Journal of Advanced Manufacturing Technology*, 2013: 67, pp. 2021-2032.
 14. C. L. Lin, J. L. Lin and T. C. Ko, Optimisation of the EDM process based on the orthogonal array with fuzzy logic and grey relational analysis method, *International Journal of Advanced Manufacturing Technology*, 2002: 19, pp. 271-277.
 15. Shih-Hsing Chang, Jiun-ren Hwang and Ji-Liang Doong, Optimization of the injection molding process of short glass fiber reinforced polycarbonate composites using grey relational analysis, *Journal of Materials Processing Technology*, 2000: 97, pp. 186-193.
 16. J. L. Lin and C. L. Lin, The use of the orthogonal array with grey relational analysis to optimize the electrical discharge machining process with multiple performance characteristics, *International Journal of Machine Tools and Manufacture*, 2002:42(2), pp. 237.

OPTIMIZATION OF MOLD COOLING TIME IN THE INJECTION MOLDING PROCESS

L.Sivakumar¹, Bhramara Panitapu²

¹PTPG (Thermal Engineering),

JNTUH College of Engineering, Hyderabad

²Associate Professor, JNTUH College of Engineering, Hyderabad

Abstract: Injection Molding is the most important process used in the manufacturing of plastic products. Injection molding gains its importance due to its advantage in mass manufacturing systems of intricate components with high dimensional accuracy with no secondary operation. In the Injection molding process, cycle time is an important parameter which consists of the various internal phases, viz., mold open /close, injection, holding, refilling, cooling and ejection. Among the above cooling time plays major part. Sufficient cooling with optimized cooling time increases the productivity and also reduces the power consumption. The objective of the experiment "Optimization mold cooling time" is to reduce the overall cycle time by optimizing the typical molding parameters such as Polymer melt temperature, Coolant temperature, and Cooling time to achieve the part temperature which is less than heat distortion temperature of the plastic material and also capable to handle manually. Experiments are conducted as per the Taguchi's [1] Design of Experiment (DOE), L9 orthogonal array selected based on the three input factors such as Coolant temperature, Cooling time and Melt temperature with three levels of low, medium and high. Two replications are conducted for better accuracy. Output parameter i.e., part temperature is measured at the end of each trial. Analysis of variance is done using ANOVA to find the Optimum parameters value and Optimum mean Ejection temperature. The experiments were conducted again at the optimum conditions. It is observed that the experiment so conducted for optimum conditions resulted in to optimum cooling time, thus verifying the results of Design of Experiment (DOE).

Keywords: injection molding, mold cooling, cycle time, cooling time, design of experiments, anova

1. INTRODUCTION

In the injection molding process plastic melt is injected or forced into a mold where it is held until removed in a solid state, duplicating the cavity of the mold. Several quality related problems like warpage, difference in homogeneous and crystal formation during solidification, can be avoided if desired cooling is maintained in the mold. In the injection molding cyclic process, mold cooling time is a major contribution where the liquid plastic material undergoes solidification process and to ensure the ejection temperature to be within the Heat

Distortion temperature (HDT) of the particular polymer material (< 95°C).Molds with uneven cooling profiles may produce parts with unacceptable mechanical properties, resulting in premature mechanical failure of the molded product. The Second major benefit of the effective cooling system is on productivity. Molding with optimum cooling will produce parts in the shortest possible cycle time, thus resulting into energy saving, reduction in production and operating costs and increasing productivity. Rapid cooling improves process economics whereas uniform cooling improves product quality and ensures shorter molding cycle [2].

In the present project, optimization of mold cooling time of the mold which consist 32 numbers of cavities each connected to flow channels or runners that direct the flow of the plastic melt to the individual cavities is performed.

2. LITERATURE REVIEW

Thermal parameters such as melt temperature, injection Pressure, injection Speed, frictional heat generation, mould cooling are important parameters that govern the injection moulding process. Mould cooling has the major contribution in an Injection moulding cycle time, which is almost more than 50 % of an entire cycle time. Optimizing the cooling time to reduce the cycle time will increases the productivity and also contribute in the energy saving.

Shen Chengyu, et al [3] performed the optimization of injection moulding process parameters using a combination of artificial neural network(ANN) and Genetic Algorithm(GA) methodfor an industrial part in order to improve the quality index of the volumetric shrinkage variation in the part. The volumetric shrinkage variation is influenced by many process variables and they are selected by the Taguchi's DOE Technique. The process conditions are optimized by using GA method.Ng Chin Fei, et al [4] reviewed the research of the practical use of Taguchi's method in the optimization of processing parameters for injection moulding and reported that Taguchi's method has been employed with great success in the experimental design for problems with multiple parameters due to its practical approach, often with integration of ANN and GA.Irene Ferreira, et al [5] studied on the Multidisciplinary optimization of injection moulding systems of an Injection Mould by integrating the structural, feeding, ejection and heat exchange sub systems to achieve improvement in cycle time.

The literature review suggests the scope in the optimization of cooling time as well as use of Design of experiment in the cooling process of the injection mold by using Taguchi method. In the present study, design of experiments are proposed to conduct using Taguchi's Orthogonal array formation with input parameters set as per the orthogonal array (OA) design and recording output parameters along with further analysis by using ANOVA techniques.

In addition, a through survey of industries employing the injection molding process to produce three different products is also conducted and it is found that the cooling time is 49% of a total cycle time in two of the cases, thus revealing the scope for the optimization of cooling time, which forms the objective of the present study.

Proper optimization of the molding process helps the molder to increase the production capacity with the available power. Most of the packaging components are made in plastic material, with an average output capacity of 50 kg /hour/per machine. The average power consumption of per kg of plastic material, viz., Poly propylene is from 0.6 to 0.8 kwh/kg. In the injection molding manufacturing sector, most of the injection molding machines are hydraulically operated, which consume required power even during the cooling time. Hence optimizing the cooling time reduces the power consumption considerably. It also reduces the load on chillers which are used to cool the mold.

3. METHODOLOGY

To achieve the objective of the present study, firstly experiments were performed on the entire cooling cycle for producing the Shoulder component as shown in Figure 1. Experiments are conducted as per Design of Experiment procedure and the output values are recorded. Experimental analysis is conducted using ANOVA to obtain the optimum ejection temperature of the product. Based on the DOE and ANOVA analysis, confirmation experiment is conducted with the optimum input parameters to evaluate the mean output value.



Figure 1: Shoulder, the Product Considered

4. EXPERIMENTAL ANALYSIS

In order to achieve the objectives of the present study, experiments are conducted in the molding plant for producing a plastic component (Shoulder) as shown in Figure 1. The experimental setup with 32 cavities of Mold in the Injection Molding Machine is shown in Figure 2.



Figure 2: Experimental Setup

The typical mold cycle time taken for molding the shoulder component is shown in Table 1, which shows that the cooling time is about 49 % of the overall cycle time of 22.53 seconds as shown in the Figure 3.

Table 1: Cycle time (seconds) Break up

Mold open	Mold close	Injection	Hold on	Ejection	Cooling time	Pause time	Cycle time
2	2.4	0.36	2.5	2	10	1.2	22.53

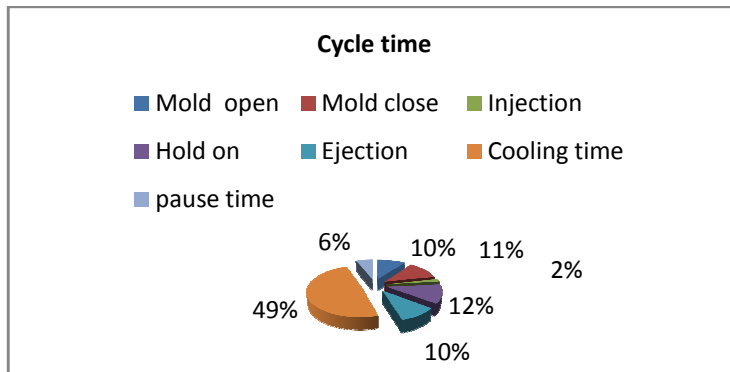


Figure 3: Cycle time before optimization

5. IMPLEMENTATION OF TAGUCHI'S DESIGN OF EXPERIMENTS

The Taguchi's design of an experiment (DOE) is a series of steps to yield an improved understanding of product or process performance. To perform the optimization of mold cooling time, the design of experiment (DOE) method is used in this project. For this, the input factors that affect the performance of the output (ejection temperature) of the process are selected as Coolant Flow which is considered as Turbulent for better heat transfer, Cooling time, Coolant Temperature and lastly Polymer Melt temperature and the same are presented in Table 2. In the above Coolant flow is set as turbulent flow at 12 LPM throughout the experiment.

Table 2: Input factors and Levels

Factors	Units	Allocated code	Level 1	Level 2	Level 3
Cooling time	Sec	A	6	8	10
Coolant Temperature	°C	B	16	17	18
Polymer melt temperature	°C	C	207	215	220

In the above, factors are set as level 1 to 3 for conducting the experiments as per the DOE , Orthogonal Arrays L9 model is selected based on the above input factors and levels [6]. The output parameter, ejection temperature is measured at the end of the each experiment during the trial process as mentioned and the calculation done and tabulated as in the Table 3.

Table 3: Design of experiment matrix

EXP NO	FACTORS			REPLICATIONS (OUTPUT)		
	A	B	C	Rep1	Rep2	Avg
1	6	16	207	50	51	50.5
2	6	17	215	55	54	54.5
3	6	18	220	58	59	58.5
4	8	16	215	47	49	48
5	8	17	220	49	52	50.5
6	8	18	207	50	53	51.5
7	10	16	220	45	46	45.5
8	10	17	207	47	49	48
9	10	18	215	47	48	47.5
Level Total	327	288	300			
Level 2 Total	300	306	300			
Level 3 Total	282	315	309			
Sum of Squares	171	63	9			

6. ANOVA CALCULATIONS TO FIND THE FACTORS OF SIGNIFICANCE

Anova calculations are made to find out the significant factors which are more influence on the process. The inputs for the calculations are made as mentioned in Anova Calculation and tabulated in the Table 4.

Table 4: Summary of Anova on mold cooling time

Source of variation	Sum of squares	DOF	Mean sum of squares	F calculated	F table at $\alpha=0.05$	Remarks
A) Cooling Time	171	2	85.5	34.2	3.98	S
B)Coolant Tempt	63	2	31.5	12.6	3.98	S
C) Barrel Tempt	9	2	4.5	1.8	3.98	NS
Error (N-a-b-c+2)	27.5	11	2.5			
Total	270.5	17				

6.1 Mean Value Calculation

The mean of ejection temperature at different combinations of process parameters and their levels are shown in the Table 5.

Table 5: Mean value of ejection temperature

Level	Process parameters		
	A	B	C
1	54.5	48	50
2	50	51	50
3	47	52.5	51.5

6.2 Optimum Value Calculation

The optimum value of the ejection temperature is at minimum cooling time. In this analysis , the recorded ejection temperatures are all well below within the Heat distortion temperature of the Poly Propylene material , and also the component can be handled by the humans as soon as the component collected in the bin,because of the lower ejection temperature i.e.. 54.5°C. Hence in each column maximum temperature is selected, to find out the optimum thermal parameters as shown in Table 6. Optimum setting of injection molding thermal parameters to reduce the cooling time with the required de molding temperature as given below.

Table 6: Optimum settings of parameters

Level	A Cooling time	B Coolant tempt	C Barrel Tempt
1	6	16	207
2	8	17	215
3	10	18	220

The optimal combination of the levels of the process parameters is A1 B3 C3, which has a cooling time of 6 seconds, Coolant temperature of 18°C. and Barrel temperature of 220°C.

6.3 Confirmation Experiment

The confirmation experiment was carried out by setting the parameters at their optimal values as given in Table 7 and the output results are recorded therein.

Table 7: Confirmation experiment

Experiment No	Factors			Output Ejection tempt (°C)
	Cooling time (seconds)	Coolant tempt (°C)	Melt tempt (°C)	
1	6	18	220	58
2	6	18	220	60
3	6	18	220	59

Experimental confirmation mean value = 59°C.

6.4 Estimation of Predicted Mean Value

Estimation of predicted mean and confidence interval for predicted mean based on the data of the orthogonal array experiment the predicted mean and the confidence interval for the predicted mean are calculated as follows.

Predicted mean, $\mu =$ Best average response out of three levels of A + Best average response out of the three levels of B + Best average of response out of three levels of C-2T (1)

For factor A, A1 is the best, for factor B, B3 is the best and for factor C, C3 is the best.

The predicted mean is given by, $\mu = (A1 + B3 + C3) - 2 * T$ (2)
 where, T= Grand total of observations / Total number of observations,
 thus $T = 909 / 18 = 50.5$

Predicted mean, $\mu = (54.5 + 52.5 + 51.5 - (2 * 50.5))$, which gives Predicted mean $\mu = 57.5^\circ\text{C}$.

6.5 Half Width of Confidence Interval

Half width of confidence interval is the tolerance level of minimum and maximum of the predicted mean value which is calculated as follows.

$$\text{Half width of confidence interval } d = \left[F_{a(1, df \text{ of error}), \frac{MSS_{\text{error}}}{n_{\text{eff}}}} \right]^{1/2} \quad (3)$$

where $F_{a(1, df \text{ of error})}$ is F value at given significance level for degrees of freedom of 1 and n_{eff} is effective sample size

Half width of confidence interval, $d = 2.169$

Confidence interval of the predicted mean $\mu = [A1 + B3 + C3 - 2 * T] \pm d(4)$

Confidence interval of the predicted mean $\mu = [54.5 + 52.5 + 51.5 - 2 * 50.5] \pm 2.169$

Confidence interval of the predicted mean $\mu = 57.5 \pm 2.1^{\circ}\text{C}$.

7. CONCLUSIONS

Among the input factors selected, cooling time and coolant temperature are observed to be significant factors, which contributes more on heat extraction from the mold.

Cooling time reduction from 10 seconds to 6 seconds reduces the overall cycle time from 22.53 seconds to 18.53 seconds which increases the overall productivity by 20%.

Confidence interval of predicted mean is from 55.33°C to 59.66°C , which is well below the Heat Distortion Temperature of PP material. (HDT of PP is 95°C) and also suitable for component ejection.

REFERENCES

1. Philip J. Ross, Taguchi Techniques for Quality Engineering, Tata McGraw-Hill, 2005.
2. Dominick V. Rosato and Donald V. Rosato, Injection Molding Handbook, University of Lowell, MA, USA.
3. Shen Changyu, Wang Lixia, and Li Quin, Optimization of injection molding parameters using artificial neural network and genetic algorithm method, Journal of Material Processing Technology, 2007: 183, pp. 412-418
4. N.G. Chin Fei, Nik Mizamzul Mehat, and Shahrulkamaruddin, Practical Applications of Taguchi Method for Optimization of Processing Parameters for Plastic Injection Mouldings, ISRN Industrial Engineering Volume 2013: Article ID462174.
5. Irene Ferreira, Oliver de Weck, Pedro Saraiva, and Jose Cabral, Multi-disciplinary optimization of injection molding systems, Structural and Multidisciplinary Optimization, Springer, 2010: 41, pp. 621 – 635.
6. R. Pannerselvam, Design and Analysis of Experiments, PHI Learning Pvt. Ltd., 2012.

THERMO-MECHANICAL PROPERTIES OF SILICON NITRATE CERAMIC COMPOSITES FOR FUSED DEPOSITION MODELING

S.Sreenivasulu^a and A chennakeshava Reddy^b

^a Asst.professor in Department of Mechanical Engineering,RGMCET,Nandyal- 518501,

^bProfessor in Department of Mechanical Engineering, JNTUCE, Hyderabad

Abstract: This paper presents an investigation of thermal and mechanical properties of new metal-particle filled silicon nitrate composites for applications in Fused Deposition Modeling rapid prototyping process. Test samples of Iron/ silicon nitrate and Copper/ silicon nitrate composites involving metal content up to 40% by volume have been made by controlled centrifugal mixing, thermally compounded through a single-screw extruder and compression moulding. Dynamic Mechanical Analysis (DMA) techniques were used in order to characterize viscoelastic properties of these newly developed composites materials for use in Fused Deposition Modeling process. It has been shown that significant improvements of Si₃N₄ thermal and mechanical properties due to incorporation of metallic fillers can potentially promote processing of high performance and functional prototypes on the existing FDM platform for a wide range of applications. Sample prototypes from the new composite materials have been successfully made and tested.

KEYWORDS: Fusion deposition modeling, composite materials, thermal properties, filaments

Corresponding author: e-mail:srinivas019@gmail.com

1. INTRODUCTION

The fused deposition modeling (FDM), developed by Stratasys Inc., has been a leading rapid prototyping process where fabricated parts are mainly used for design verification, functional testing, medical applications and patterns for casting processes [1]. Traditionally the FDM systems have been able to fabricate parts only in thermoplastics and waxes and the current FDM systems can process parts in a range of engineering plastics such as silicanitrate, polycarbonate (PC) and blends of Si₃N₄ and PC. The process involves layer-by layer deposition of extruded material through a nozzle using feedstock filaments from a spool.

The basic principle of operation of the FDM process, as shown in figure 1 offers great potential for a range of other materials including metals

and composites to be developed and used in the FDM process as long as the new material can be produced in feedstock filament form of required size, strength and properties. New materials for FDM process are needed to increase its application areas especially in rapid tooling and rapid manufacturing. There has been very limited amount of research conducted over the years to develop new materials for the FDM process. Researchers at Rutgers University were the first to develop some new metallic and ceramic based materials for the FDM process for rapid fabrication of functional components with improved mechanical properties [2, 3]. They have used the process to fabricate functional parts in a variety of materials such as silicon nitride, aluminum oxide, hydroxyapatite, lead-zirconium-titanate (PZT) and lead-magnesium niobate (PMN) as well as stainless steel for structural and bioceramic applications.

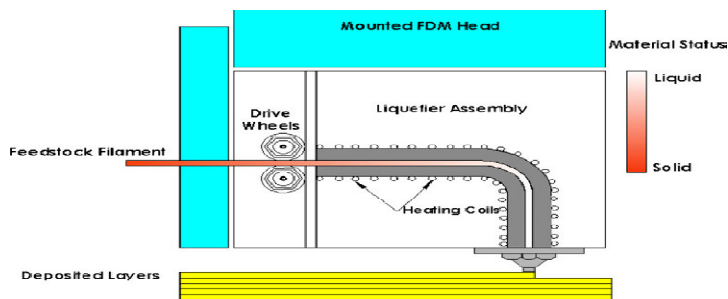


Figure 1: Schematic of Stratasys FDM process.

They created such components on the FDM system using metal/ceramics powders mixed with organic binder system. The properties of the mixed feedstock filament meet the flexibility, stiffness, and viscosity required for successful FDM processing. But the fabricated green parts need to undergo further processing to remove the organic binder and are subjected to sintering to achieve densification. Sintered part may be infiltrated with other type of metal materials. Based on the FDM principle, researchers at Rutgers have also developed a separate process of fused deposition of multi-materials, where up to four different materials can be deposited for applications in multi-material actuators [4]. Work has also been done to develop new thermoplastic composites or to improve the properties of the existing thermoplastics for the FDM process. Gray et al. [5] developed composites of thermotropic liquid crystalline ceramics (TLCP) in polypropylene (PP) matrix for the FDM process with the aim of enhancing the tensile properties and the functionality of the FDM made prototypes.

They used dual extrusion process to develop the filaments and investigated the effects of various factors on the tensile properties and morphology of the prototypes. Zhong et al. [6] have investigated the development of short fiber reinforced ABS composites to improve the strength of the ABS filament for FDM processing. They also studied the

effects of plasticizer and compatibilizer to further enhance other properties. Shofner et al. [7] have developed nanofibre-reinforced based composites for Fused Deposition Modeling process combining single-walled carbon nanotubes with ABS materials. They used nanofibres up to 10% by weight and achieved an average of around 40% increase in tensile strength in the composites. A major focus of research in material development for FDM has been in the area of tissue engineering scaffolds. Attempts have been made to develop biocompatible materials for processing in DM for fabrication of scaffolds for tissue engineering applications.

Table 1: Metal/ceramic composites constituents

Type of matrix	Type of filler material	Size of Filler (μ m)	Filler loading (%)	Designation of composite
silicon nitrate	Cu	10	5	A1
silicon nitrate	Cu	10	10	A2
silicon nitrate	Cu	10	20	A3
silicon nitrate	Cu	10	30	A4
silicon nitrate	Cu	10	40	A5
silicon nitrate	Cu	45	5	B1
silicon nitrate	Cu	45	10	B2
silicon nitrate	Cu	45	20	B3
silicon nitrate	Cu	45	30	B4
silicon nitrate	Cu	45	40	B5
silicon nitrate	Fe	45	5	C1
silicon nitrate	Fe	45	10	C2
silicon nitrate	Fe	45	20	C3
silicon nitrate	Fe	45	30	C4
silicon nitrate	Fe	45	40	C5

Researchers at the University of Singapore have processed PCL and several composites (PCL/HA, PCL/TCP etc.) on the FDM systems [8]. Endres et al. [9] and Rai et al. [10] have used PCL and CaP composite scaffolds developed by FDM for bone tissue engineering. Woodfield et al. [11] have used FDM process for making scaffolds made of PEGT/PBT composites with a range of mechanical properties for articular cartilage application. Kalita et al. [12] have developed particulate-reinforced ceramic-ceramic composites using polypropylene (PP) ceramic and tricalcium phosphate (TCP) ceramic for scaffolds fabrication on the FDM system. From published literature, it is noted that, while some efforts have been made to improve the existing FDM ceramics or to develop new materials for tissue engineering applications using the FDM process, very little research has been directed to develop materials for other engineering applications such as tooling and functional parts with enhanced properties. For tooling and functional applications, strong metal based composites are needed to be processed by the FDM process

with desirable, mechanical and thermal properties. This paper presents the development and characterization of metal-filled FDM-grade composite materials for direct FDM processing without the need of binder removal or infiltration process.

The aim is to develop the new composites with desirable thermo-mechanical properties with direct rapid tooling for injection moulding applications. This research focuses on developing a proper formulation and mixture of constituent materials for obtaining certain properties of the composite material so that they can be produced in filament form for use in the Fused Deposition Modeling process. The success of this unique work depends upon careful selection of proportion of constituent materials and fillers to result in the desired properties of the composite material. The main outcome of this major breakthrough is the manufacture of a strong, flexible and spoolable feed stock filaments made by extrusion from the composite materials for use in the existing FDM system without any hardware or software modification.

In this investigation, three main types of constituent materials are used to develop the new composite materials. The first material, used as the matrix, is the silica nitrate (Si_3N_4) thermoplastic, which is the most commonly used material used in the FDM systems. The Si_3N_4 has good mechanical properties and fluidity, desirable flexibility and stiffness, which are required for successful FDM processing. The other constituent materials are the commercial grade iron powder, and copper powder, which have properties of high strength, toughness and conductivity. Two separate composites are prepared, one with iron powder mixed in Si_3N_4 matrix and the other with copper powder mixed in Si_3N_4 matrix, which are then used to make the feedstock material. The required properties for the matrix material are appropriate stiffness, flow, flexibility, strength and modulus. In addition to forming the part with the layers deposited, the filament also acts as a piston at the entrance of the liquefier head in FDM machine, forcing the molten material out of the nozzle.

In addition to forming the part with the layers deposited, the filament also acts as a piston at the entrance of liquefier head, forcing the molten metal out of the nozzle. Filaments require a high stiffness and lower melt viscosity to a useable level. Due to the high metal powder loading in the ceramic matrix, the viscosity of the composite is increased and dispersion gets worse. Therefore additives, such as surfactants and plasticisers are necessary to this composite material formulation

2. MATERIALS AND METHODS

In this experiment the silicon nitrate is used as a matrix material, the metal used for filler material is copper powder and iron powder of size $10\mu\text{m}$ & $45\mu\text{m}$. Table 1 represent the Metal/ceramic composites

constituents, The filler material is loaded in 5%, 10%, 20%, 30% and 40%. Figure 2 shows the representation of Si_3N_4 and metal particles.



Figure 2: Representing silica nitrate and copper and iron particles

2.1. Preparation of Metal/ Si_3N_4 Composites

To develop the new metal–ceramic composites, mixtures of iron powder with Si_3N_4 powder and copper powder with Si_3N_4 powder, as representative metal–ceramic elements, were chosen with varying volume fractions of metal powder with the aim of producing appropriate feed stock filament for FDM processing. The main reasons for selection of iron and copper powders as short fiber fillers were their reasonably good mechanical and thermal properties as well as their capabilities of mixing and surface bonding with ceramics. The metal powders were purchased from Sigma–Aldrich in Australia.

The purity of both metal powders was 99.7% with one particle size, 45 μm , was used for iron and two particle sizes, 10 μm and 45 μm , were used for copper for this investigation. The specific gravity of iron powder was 7.88 gr/cm^3 and the shape of the powder particles was irregular for iron and spherical for copper. composite designations and the constituents used for each composite investigated in this study.

The Si_3N_4 is prepared by heating powdered silicon between 1300 $^\circ\text{C}$ and 1400 $^\circ\text{C}$ in an atmosphere of nitrogen. The specific gravity of Si_3N_4 was 3.2 gr/cm^3 . To produce Si_3N_4 micro particles, sufficient amount of P400 filament was first pelletized on a mechanical chopper. Then the Si_3N_4 pellets were ground to fine powders using the cryogenic grinding technique.

The machine used for this purpose was a SORVALL OMNI high speed grinder operating at temperatures well below glass-transition temperature of the ceramic. During this process, the Si_3N_4 pellets were frozen by the surrounding liquid nitrogen which resulted in lower molecular energy of the pellets. Simultaneously, high speed rotation of stainless steel blades within the chamber containing the Si_3N_4 pellets could easily break them below the glass-transition temperature. This process does not damage or alter chemical composition of material making it a very efficient ceramic powder production technique. In order to achieve a homogeneous mixture with higher packing factor when mixed with metal particles an Si_3N_4 /metal particle size ratio of approximately 10–1 or over was required [13]. Therefore, the Si_3N_4 pellets were ground to a particle size of approximately 450–500 μm . To

get the same size for Si₃N₄ particles, grinding process was done in three time-interval of 5 min between which the particles were sieved to the appropriate size. This helped to screen the particles of different size range than 450–500 μm.

The composite mixtures were then loaded in a multi-variable speed homogenizer to achieve maximum possible homogeneous-distribution of metal powder in Si₃N₄ matrix. Scanning electron microscopy (SEM) images of the prepared samples were analyzed to make sure a homogeneous matrix of metal–ceramic composite is achieved. At the end, a very small percentage by volume of a surfactant was added to the mixtures. According to the previous studies carried out at Swinburne regarding composition of metal and plastic particulates [14], the addition of surfactant increased homogeneous dispersion of metal particles in ceramic matrix. The surfactant powder is coated on the metal particles, which reduces the high free energy surfaces of the metal fillers, and that in turn results in much lower interfacial tension between composite particles in melt stage. The coated metal particles give good link to lower free energy surfaces of ceramic particles.

2.2. Fabrication of FDM filaments

In order to create a part on the FDM system using the new composite material, a certain amount of this composite is required to create the filaments for FDM machine. This amount of required composite material must have exact amount of its constituent elements, which include Si₃N₄, iron, and surfactant. The amount of each of these elements will depend upon the volume of the filaments required for FDM processing. In this experiment, the exact amount of constituents was determined by considering the CAD model volume. For example, the weight of the Iron/ Si₃N₄ composite was calculated by the following relationship:

$$W_C = \frac{W_{Fe} + W_{Si_3N_4}}{(1 - W_s \%)} \quad (1)$$

where W_C , W_{Fe} , $W_{Si_3N_4}$ are the weight of composite, iron, silica nitrate respectively, and W_s is the weight percentage of surfactant used. A single-screw extruder was selected to fabricate the filaments from the composite materials. The filament used in FDM process needs to be of a specific size, strength and the properties. The composite mixture powder is fed into the feed hopper. The mixture of powder material flows by gravity from the feed hopper down into the extruder barrel. As the material flows, it fills the annular space between the extruder screw and barrel. Since the barrel is stationary and the screw is rotating, the frictional forces will act on the material, both on the barrel as well as on the screw surface.

As the material moves forward, it will heat up as result of frictional heat generated and conducted from the barrel heaters. During extrusion process, a phenomenon referred to as die swell occurs, in

which the ceramic swells while coming out of the die. Figure 3 shows the schematic diagram of the die swell phenomenon. The elastic behavior of the ceramic melt is largely responsible for the swelling of the extrudate upon leaving the die. This is primarily due to the elastic recovery of the deformation of the metal–ceramic composite in the die and the intrinsic elastic property of the ceramic melts [15]. To minimize this effect and achieve a consistent diameter on the extrudate in such a way that the produced filament could be fed into the FDM machine smoothly, different operational variables including screw speed, pressure and temperature as well as optimization of wall shear stresses during extrusion process were considered.

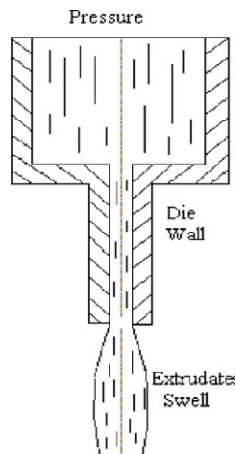


Figure 3: Schematic of ceramic melt swell.

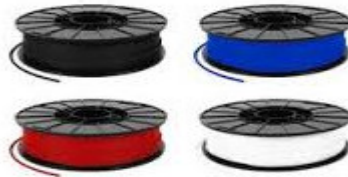


Figure 4: FDM filaments produced from iron/ Si_3N_4 composite material

A die with a short land length will cause a large amount of swelling, while a die with long land length will reduce the amount of swelling. Therefore, the land length of die was increased from 5 mm to 10 mm, which leads to decrease the extrudate swelling. Because of swelling, the diameter of die used was taken to be smaller than the required diameter of the filament. The die diameter was 1.65 mm and the resulting diameter of filament formed was in the range of 1.78–1.85 mm due to the extrudate swelling. Therefore, the geometry of exit flow channel is generally different from the required product geometry. Thus using the proper geometry of the die and appropriate volume of flow parameters, flexible winding filaments of desired diameter and tolerance were

produced. Figure 4 shows the final filament of Iron/ Si_3N_4 composite produced by this process, ready for use in the FDM machine. Figure 5 shows the SEM diagram of the Iron/ Si_3N_4 composite, which indicates uniform distribution of iron particles in the Si_3N_4 matrix.

3. DETERMINATION OF THERMO-MECHANICAL PROPERTIES

After the preparation of composite material the varies tests are performed on the apparatus to determine the thermal conductivity, heat capacity and dynamic mechanical properties.

3.1. Thermal Conductivity

The thermal conductivity of the metal–ceramic composite is one of the very important properties of the material and it is determined for different volumetric percentage of metal and ceramic material. This property is especially useful for proper functioning of injection moulding dies and inserts. The life of injection moulding dies depends greatly on the value of thermal conductivity of the die material and hence on the thermal conductivity of the feedstock material of composites. Thermal conductivity tests for the composites were conducted, in an apparatus made in-house by Autodesk Moldflow Plastic Labs, Melbourne according to ASTM D5930 [16] test method. In this method, thermal conductivity is measured using a transient linesource heating as shown in the schematic diagram of Figure 6. A probe is inserted into the centre of a molten composite sample, and held at its processing temperature.

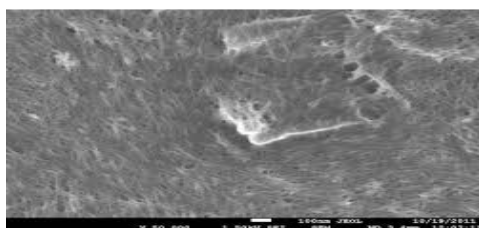


Figure 5: SEM image of iron/ Si_3N_4 composite (1000X)

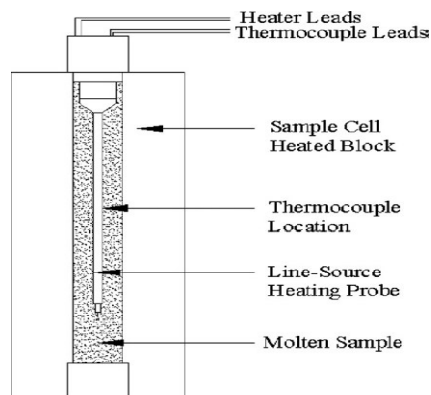


Figure 6: Schematic of thermal conductivity apparatus

A line-source heater runs through the length of the probe with a temperature sensor placed in the middle of the probe. A known amount of heat (Q) is supplied to the line-source heater. Once the thermal equilibrium is achieved, the temperature rise in the sensor is recorded over a period of time. The thermal conductivity (k) is then calculated from the following equation:

$$k = \frac{QC \ln(t_2/t_1)}{4\pi(T_2 - T_1)} \quad (2)$$

where T_1 and T_2 are temperatures of the samples at times t_1 and t_2 respectively, and C is the probe constant. Cooling scans were produced automatically by programming a range of temperatures.

For each type of composite sample, thermal conductivity was calculated at different temperatures. Figure 7 shows the variation of thermal conductivity of copper filled Si_3N_4 composites of various metal content of larger particle sizes at different temperatures. It is seen that for lower concentration of fillers, increase of temperature has a negligible effect whereas in high concentration of copper particles (30 vol. %-sample B4) above glass transition temperature of the matrix, there is a significant increase in the thermal conductivity of copper- Si_3N_4 composite. This is believed to be the result of increase in the mobility of particles in a semi-molten matrix at temperatures beyond its glass-transition temperature. Moreover, it is observed that addition of even up to 10 vol. % of copper particles (samples B1 and B2) cannot break the thermal resistance of the Si_3N_4 matrix, and it is only at about 20 vol. % concentration of particles that conductive chains begin to form and therefore heat conductivity is improved by an order of magnitude.

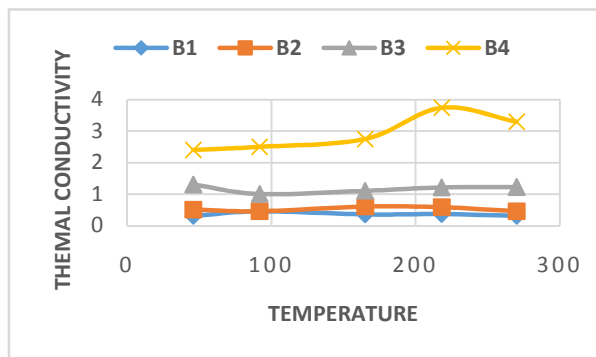


Figure 7: Thermal conductivity of copper-filled Si_3N_4 composites at various temperatures.

This effect is significant for copper contents of 30 vol.% where particle chains are completely formed and their mobilization is facilitated due to phase change in the Si_3N_4 matrix from solid state to liquid state above its glass-transition temperature. Figure 8 shows the thermal conductivity of iron-filled Si_3N_4 composites of varying metal contents of

larger particle sizes at different temperatures. As can be seen in comparison to Figure 7, the influence of iron particles on the thermal conductivity of Si_3N_4 is lower than that of copper particles. This follows the rule of mixture as thermal conductivity of iron is less than that of copper. Thermal resistance of the Si_3N_4 matrix is only overcome considerably when iron particle concentration reaches 30 vol% (sample C4). At concentrations above 30 vol%, the chain formation of metal particles begins to appear in the matrix, and therefore the thermal conductivity of the Si_3N_4 composite is improved noticeably. It should be noted that the thermal conductivity is achieved through the molecular vibrations and free electron movement. Moreover, since the thermal conductivity of iron is only about 380 times that of Si_3N_4 ceramic, heat flows not only through conductive iron chains but also substantially through the ceramic matrix itself. With further increase of the volume fraction of iron, the space between filler particles becomes very small. It has a high probability of making 'effective' contact with neighboring particles to form the contacting chains.

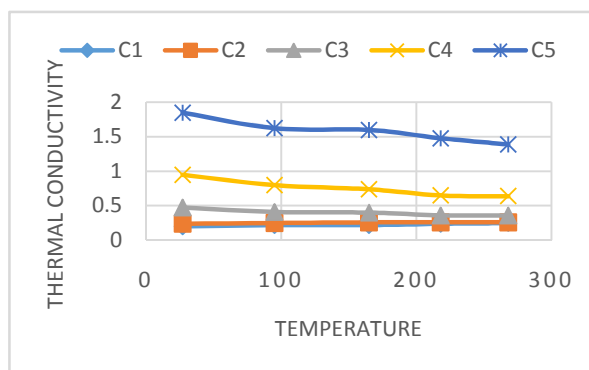


Figure 8: Thermal conductivity of iron-filled Si_3N_4 composite for various temperatures

The free electrons are hopping across the gap between points of close contact. The rate of hopping increases as the distance to be spanned decreases. As more particles are loaded, the more easily the particles are gathered to form conductive chains called a touching system. The thermal conductivity of particles thus contributes to change in the thermal conductivity of the composite. If volume fraction of filler particles approaches the maximum packing fraction, it may lead to the particle becoming very difficult to achieve a well-dispersed homogeneous mixture. The existence of agglomerates at high volume loading may introduce voids into the composite, which reduces the thermal conductivity of the material [17].

3.2. Heat Capacity

Heat capacity and heat flow were measured using standard Differential Scanning Calorimetry modulated at $\pm 5^\circ\text{C}$ at every 40 s with temperature range of $30^\circ\text{C}/\text{min}$ up to 150°C . Figure 9 demonstrate the

graphs of heat capacity variation with temperature for virgin Si_3N_4 and composite materials with 10% iron and 20% iron powder. It shows that 10% Fe decreases heat capacity of the unfilled Si_3N_4 . Further addition of iron powder confirms the same trend of reduction in heat capacity which on the other hand means the thermal conductivity increases by approximately the same percentage.

Increase of thermal conductivity is another advantage of the new material by which much more thermally stable prototypes can be produced on FDM machine making them dimensionally more accurate and reliable for reducing the cooling cycle time when employed as material for injection moulding tools.

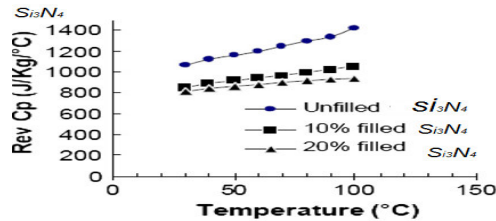


Figure 9: Rev Cp of the iron-filled Si_3N_4 composites.

3.3. Dynamic Mechanical Properties

Dynamic mechanical analysis was conducted on a Multi-Frequency-Dual Cantilever DMA Instrument which is an ideal experiment for rapidly screening and comparing the mechanical properties of the materials such as storage modulus and loss modulus as well as glass-transition temperature. In this method, the material is heated at a constant rate and deformed (oscillated) at a constant amplitude (strain) and frequency. The test mode applied was single frequency one with amplitude of $15\ \mu\text{m}$ with a temperature ramp of $5^\circ\text{C}/\text{min}$ up to 150°C . Data sampling interval was 2 s/pt. Dynamic storage modulus of ceramic composites represents the elastic contribution of ceramic matrix to an external excitation, and defines the ability of composite to store energy when deformed. Figure 10 shows the variation of solid state dynamic mechanical response of various Copper/ Si_3N_4 composites under wide temperature range. Below glass-transition temperature, while in a solid state, there is a dramatic increase in storage modulus of composites as the volume fraction of filler increases.

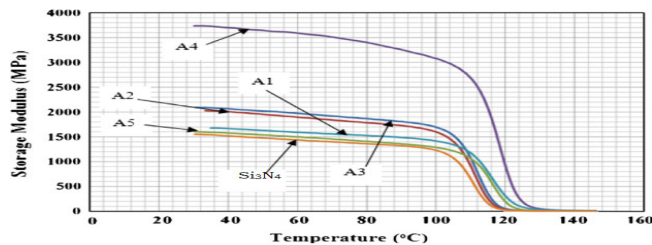


Figure 10: Storage modulus of various Copper/ Si_3N_4 composites with copper particle size of $10\ \mu\text{m}$ at temperature scan.

A maximum value of approximately 3.5–4GPa at room temperature is achieved for storage modulus of Copper/ Si_3N_4 composite containing 30vol% of copper (sample A4). This demonstrates a strong interlocking of copper particle into Si_3N_4 matrix which increases the stiffness of the composite. However, the trend reverses for filler content of more than 30vol%. At very high loading of copper (40vol %), due to significant agglomeration of filler particles (sample A5), and accumulation of inter-particular voids results in the weakening of the matrix rather reinforcing it.

Figure 11 shows the dynamic mechanical response of Copper/ Si_3N_4 composites containing large copper particles (45 μm) under temperature variation. It is observed that the storage modulus of the composite increases with the increase of copper content up to 10 vol%, but significantly drops by further increase of filler. The trend presents less reinforcement in composites contain large particles which could be due to weaker interlocking, and poor distribution of the fillers in the matrix. It worth noting that during preparation of these composites there have been no coupling agent involved. It is usually recommended that a coupling agent be used to provide better bonding between the metallic fillers and the ceramic matrix.

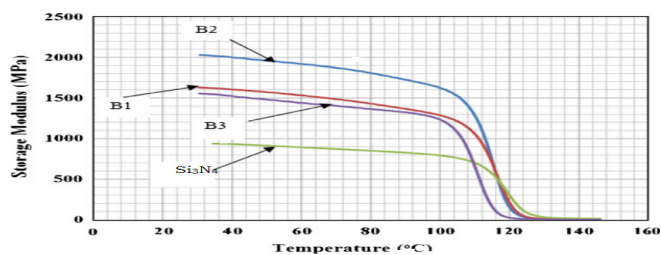


Figure 11: Storage modulus of various Copper/ Si_3N_4 composites with copper particle size of 45 μm at temperature scan.

The maximum storage modulus of approximately 2GPa could be achieved in the case of using large copper particles. It should be noted that composites containing higher volume content (30% and 40%) of large copper particles could not be tested due to adverse bonding between the particles and the ceramic matrix. Figure 12 shows the variation of storage modulus of Iron/ Si_3N_4 composites for varying temperature. Similar to the graphs in Fig. 10 for Copper/ Si_3N_4 composites, reinforcement effect of addition of iron filler particle is evident up to 30vol% by which storage modulus (stiffness) of Iron/ Si_3N_4 composite reaches a range of 2.5–3GPa at room temperature, and subsequently drops back to the storage modulus of the Si_3N_4 matrix. Compared to the Copper/ Si_3N_4 composites of the same particle size, the stiffness values are much higher for Iron/ Si_3N_4 composites with 10–20% volume fraction.

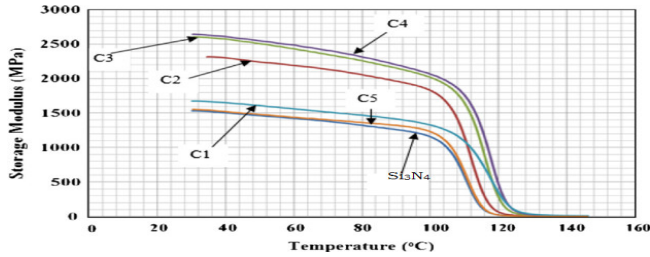


Figure 12: Storage modulus of various Iron/ Si_3N_4 composites with iron particle size of $45 \mu\text{m}$ at Temperature scan.

Stiffness of all three types of composites dramatically drops as the temperature approaches the glass-transition temperature where matrix ceramic transforms from solid state into semi-liquid or glassy state, and therefore due to larger free volume available, it suppresses any potential for interlocking of ceramic and filler particles. In order to see the effect of particle loading on glass-transition temperature, figure 13 shows the comparison of dynamic mechanical properties of 10% iron-powder filled Si_3N_4 composite (shown by solid line) and virgin Si_3N_4 (shown by dotted line). As it can be seen from the graphs, the glass-transition temperature represented on Tan Delta curve has shifted by 7°C for the composite material. By further increase of glass-transition temperature, softening point of the new composite material will be higher, which gives the promise of using the new material as die or insert material for injection moulding of ceramics and plastics with lower softening point.

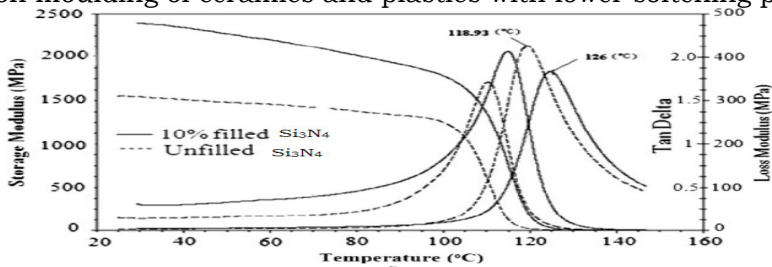


Figure 13: Comparison of dynamic mechanical properties of virgin Si_3N_4 and 10% iron-powder filled Si_3N_4

3.4. Stress-Strain Behavior of Composites

To measure maximum load and elongation at break point, standard tensile test was conducted on a Zwick/Z010 Instrument at a speed of 50 mm/min . At least three samples were prepared for each test and the average values have been considered. Figure 14 shows the effect of iron powder on the tensile strength and elongation. As it can be seen the behavior of iron-filled Si_3N_4 is of characteristics of a brittle and hard material with much lower elongation. Table 2 shows the comparison of actual values of maximum elongation at maximum load and at break point along with the values of maximum load and load at break for the unfilled Si_3N_4 and the iron-filled Si_3N_4 . Although there is only slight difference on elongation at maximum load, it becomes significant at

break point. Tensile strength drops significantly as a result of addition of 10% volume percent of iron powder. It should be noted that the current composition of the new material does not contain any additive which could possibly promote better bonding between iron particles and ceramic matrix.

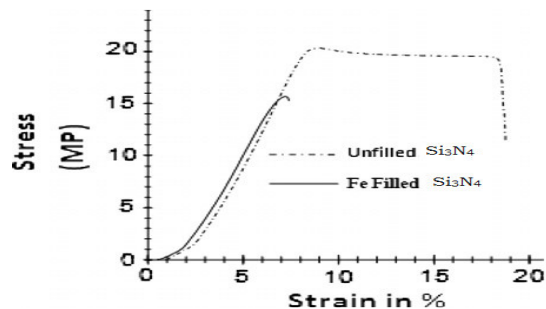


Figure 14: The effect of Iron (Fe) particle on tensile strength of Si_3N_4 matrix.

Table 2: Comparison of elongation test values at maximum load and at break

Sample	Fmax(N)	FBreak(N)	εBreak(mm)	ε Fmax(mm)
Unfilled Si_3N_4	705.8	682.7	2.16	2.12
10%Fe filled Si_3N_4	602.9	341.9	5.34	2.47

4. Fabrication and application of the composites

The Iron/ Si_3N_4 feedstock filaments made from the new composite material were loaded into the FDM3000 rapid prototyping machine and were fed into the liquefier head for part fabrication. The FDM liquefier head and the FDM Quick slice software were used without any modification. In the initial stages of FDM processing, there were a few problems related to filament size variation, over filling with material, clogging of the nozzle and delamination of a few layers due to presence of plasticiser. All of these problems were overcome by making more uniform filaments, regulating the amount of plasticiser, and selecting appropriate values of FDM parameters such as slice thickness, road width, fill patterns and nozzle diameter.

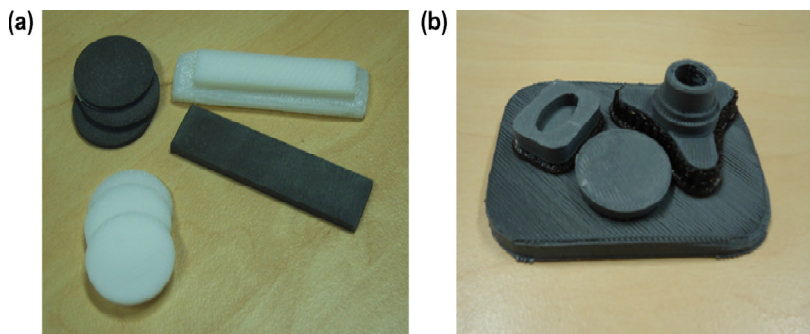


Figure 15: Parts produced on FDM3000 using the new Iron/ Si_3N_4 composites (a) test samples of composite and Si_3N_4 (b) prototype parts of composite

In the initial trials, the build time of a part built with this new composite was almost twice the time taken in building the same part with the Si_3N_4 material used in the FDM3000 machine. But with improved filament characteristics and optimized process parameters, the build time was down to almost the same as that taken to build an equivalent part in Si_3N_4 material. Figure 15 shows a few test parts and prototype parts built directly on the FDM3000 machine using the Iron/ Si_3N_4 filament, along with the some test parts produced using the white Si_3N_4 material only.

One of the major objectives of the work presented here is to develop new metal/ceramic composite materials for direct use in the current Fused Deposition Modeling rapid prototyping platform with long term aim of developing functional parts as well as direct rapid tooling on the FDM system. Using such composites, the direct rapid tooling will allow fabrication of injection moulding dies and inserts with desired thermal and mechanical properties suitable for using directly in injection moulding machines for short term or long term production runs. As the new metal/ceramic composite materials developed in this research work involves use of iron particles and copper particles in a ceramic matrix of Si_3N_4 material, they offer much improved thermal, electrical and mechanical properties enabling current Fused Deposition Modeling technique to produce rapid functional parts and tooling. Higher thermal conductivity of the new metal/ceramic composite material coupled with implementation of conformal cooling channels enabled by layer-by layer fabrication technology of the Fused Deposition Modeling will result in tremendously improved injection cycles times, and thereby reducing the cost and lead time of injection moulding tooling.

5. CONCLUSIONS

New composite materials with iron filled particles in Si_3N_4 and copper filled particles in Si_3N_4 have been successfully developed for direct application in Fused Deposition Modeling rapid prototyping process. The flexible filaments of the new composite material have been successfully produced and processed in the existing FDM3000 machine to fabricate sample parts. Due to highly metal particulate filled matrix of the new composite material, injection tools and inserts are made using this material on Fused Deposition Modeling, will demonstrate a higher stiffness comparing to those made out of pure ceramic material resulting in withstanding higher injection moulding pressures. Moreover, comparison of thermal conductivity and dynamic mechanical test values of the new composites with varying metal filler content show great promise for application of the new materials in functional parts and direct rapid tooling on the FDM systems.

REFERENCES

1. S.H.Masood, Intelligent rapid prototyping with fused deposition modelling. Rapid Prototype Journal, 1996:2(1), pp.24–33.

2. G.Wu, Solid freeform fabrication of metal components using fused deposition of metals. *Mater Design journal*, 2002:23(1), pp.97–105.
3. M. Allahverdi, Processing of advanced electroceramic components by fused deposition technique, *Journal of European Ceramic Society*, 2001:21(10–11), pp.1485–90.
4. J.Mal, A novel system for fused deposition of advanced multiple ceramics. *Rapid Prototype Journal*, 2000:6(3), pp.161–74.
5. R.W. Gray IV, D.G.Baird, J.H. Böhn, Effects of processing conditions on short TLCP fiber reinforced FDM parts, *Rapid Prototype Journal*, 1998:4(1), pp.14–25.
6. W.Zhong, Short fiber reinforced composites for fused deposition modeling, *Journal of Material Science and Engineering- A*, 2001:301(2), pp.125–30.
7. M.L.Shofner, Nanofiber-reinforced ceramics prepared by fused deposition modeling, *Journal of Applied Ceramic Science*, 2003:89(11), pp.3081–90.
8. I. Zein, Fused deposition modeling of novel scaffold architectures for tissue engineering applications, *Journal of Biomaterials*, 2002:23(4), pp.1169–85.
9. M.Endres, D.W.Hutmacher, Osteogenic induction of human bone marrow-derived mesenchymal progenitor cells in novel synthetic ceramic-hydrogel matrices, *Journal of Tissue Eng* 2003:9(4), pp.689–702.
10. B. Rai, The effect of rhBMP-2 on canine osteoblasts seeded onto 3D bioactive polycaprolactone scaffolds, *International Journal of Biomaterials* 2004:25(24), pp.5499–506.
11. T.B.F. Woodfield, Design of porous scaffolds for cartilage tissue engineering using a three-dimensional fiber-deposition technique, *International Journal of Biomaterials*, 2004:25(18), pp.4149–61.
12. S.J.Kalita, Development of controlled porosity ceramic–ceramic composite scaffolds via fused deposition modeling, *Journal of Material Science and Engineering-C*, 2003:23(5), pp.611–20.
13. S.C.Tsai, D.Botts, and J.Plouff, Effects of particle properties on the rheology of concentrated noncolloidal suspensions, *Journal of Rheology*, 1992:36(7), pp.1291–305.
14. S.H.Masood, W.Q.Song, Thermal characteristics of a new metal/ceramic material for FDM rapid prototyping process. *Assembly Automation*, 2005: 25(4), pp. 309–15.
15. C. Rauwendaal, *Ceramic extrusion*. Munich: Hanser Publishers 2001: pp.460–61
16. American society for testing of material-D5930. Standard test method for thermal conductivity of plastics by means of a transient line-source technique. ASTM International: West Conshohocken, PA: 2009.
17. D.M.Biggs, Mechanical, thermal, and electrical properties of metal fiber-filled ceramic composites, *Journal of Ceramic Engineering science* 1979:19(16), pp.1188–92.

INFLUENCE OF HEAT TREATMENT ON MECHANICAL BEHAVIOR OF ALUMINIUM-7075/SILICON CARBIDE COMPOSITES MANUFACTURED BY SQUEEZE CASTING PROCESS

P. Laxminarayana^a and A. Chennakesava Reddy^b

^aProfessor, Department of Mechanical Engineering, OU
College of Engineering, Hyderabad

^bProfessor, Department of Mechanical Engineering, JNTUH
College of Engineering, Hyderabad

Abstract: The effect of heat treatment on mechanical behavior of silicon carbide reinforced aluminum matrix composites has been investigated. Hardness values increased with the increase of silicon carbide addition in both as-cast and heat treated composites. Peak hardness values are about 20-25% higher than as-cast hardness values. The flexural strength increased with increasing reinforcement content up to 10wt% silicon carbide in both as-cast and heat treated composites. The difference between maximum tensile strength and flexural strength is 228 MPa in as-cast and 245 MPa in heat treated aluminum composites. Silicon carbide particulates have even distribution through the as-cast matrix. Agglomeration of silicon carbide particulates was observed in some of the tensile test specimens.

Keywords: 7075, heat treatment, silicon carbide, squeeze casting process

Address all correspondence to: dr_acreddy@yahoo.com

1. INTRODUCTION

Composite materials are composed of a matrix phase and a reinforcement phase. Matrix and reinforcement phase work together to produce combination of material properties that cannot be met by the conventional materials [1-21]. In most of the composites, reinforcement is added to matrix to increase the strength and stiffness of the matrix. Reductions in material density, or increases in stiffness, yield strength, ultimate tensile strength can be directly translated to reductions in structural weight. This led the aerospace industry to develop new materials with combinations of low density, improved stiffness and high strength as attractive alternatives to existing high-strength aluminum alloys and titanium alloys. These high-strength metal matrix composites combine the high strength and hardness of reinforcing phase with ductility and toughness of light metals.

The most common particulate composite system is aluminum reinforced with silicon carbide. So far most of the alloys that have been employed as matrices in aluminum have been focused on the A356, 2xxx and 6xxx series alloys. Although very few studies have been reported on the 7xxx series alloys reinforced with silicon carbide particles, much less attention has been paid to the 7xxx Al alloy matrix composites, which show the highest strength of all commercial Al alloys and widely used for structural applications. Stronger matrix alloys tend to produce stronger composites, but within these composite systems there are many variables such as ageing conditions, weight/volume fraction of particulate, particulate size, which can affect mechanical properties.

Hence, the objective of this paper is to investigate the effect of heat treatment on mechanical behavior of silicon carbide reinforced aluminum matrix composites.

2. MATERIALS

The selection of materials for matrix and reinforcement is discussed to prepare metal matrix composite.

2.1. Matrix Material

Al 7075 was used as matrix material. The main alloying element is zinc. The second is magnesium, which is predominantly added to increase the wetting between matrix and reinforcement. Table 1 gives the chemical composition of 7075 alloy. Al-Ti-B (Al-5wt% Ti-1wt%B) was used to refine and decrease grain size of the matrix.

Table 1: Chemical composition of Aluminium-7075 ally

Alloying element	Cu	Mg	Zn	Cr	Al-Ti-B	Si	Al
Wt%	1.49	2.75	5.91	0.27	0.41	0.02	89.15

2.2. Reinforcement Material

Silicon carbide particulates were used as reinforcement material. Density of silicon carbide is between 3.20 g/cm³ and the mesh size is 30 ± 1 µm.

3. CASTING OF METAL MATRIX COMPOSITE

The squeeze casting process was used to manufacture metal matrix composite. Die material is tool steel. Induction furnace was used to melt the aluminum 7075 alloy. The casting process was carried out through the following steps:

1. Chemical composition was calculated according to the composition of 7075.
2. Elements of aluminum alloy (except magnesium) were added into the induction furnace and temperature of the furnace was adjusted to about 800°C and waited until obtaining a liquid

phase. Magnesium was added after the liquid phase was obtained.

3. After obtaining the melt, silicon carbide powder was added into the molten metal.
4. Then furnace was turned off, and mechanical agitation was started. While making the mechanical agitation, the mould was heated by a torch.
5. After 5 minutes of agitation, the furnace was turned on again to melt the alloy to maintain the loss of heat during agitation.
6. Silicon carbide reinforced aluminum 7075 was processed by squeeze casting process applying 80 MPa pressure. At each casting operation three specimens were prepared. The remaining part was re-melted and recycled.

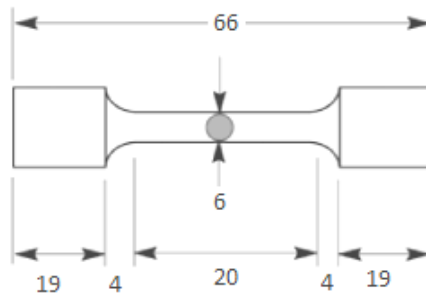


Figure 1: Tensile specimen, all dimensions are in mm.

4. EXPERIMENTAL TESTING

Five types (0-10-15-20-30 wt% SiC) of three point bending test and tensile testing specimens were obtained. The specimens were prepared for tensile testing and three point bending tests after casting. Only the burrs were cleaned before starting the tests. Dimensions and shape of tensile testing specimens are given in figure 1. Dimensions and shape of three point bending test specimens are given in figure 2.

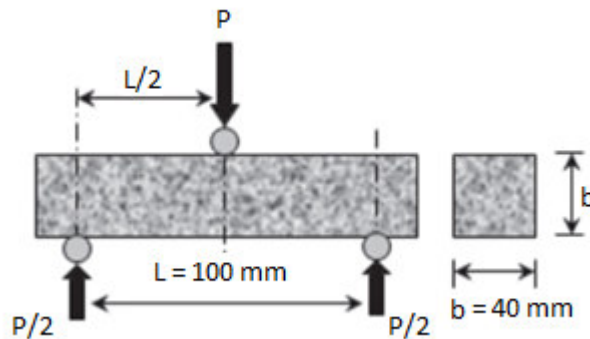


Figure 2: Three point bending specimen, all dimensions are in mm.

Two specimens of three point bending for each composition, as-cast and heat treated were tested. Also two specimens of tensile testing for each composition, as cast and heat treated were tested. Vickers 10 kg

hardness values were acquired. Both sides of the specimens were tested for hardness.

Load (P) versus deflection (δ) data were recorded during tensile testing. Also the ultimate tensile strengths was evaluated. Recorded maximum loads are in kilograms and they were converted to maximum stress values (MPa). Cross-sectional areas of tensile testing samples were measured and lengths are compared before and after fracture. All of the burrs were grinded in order to prevent notch effect. In three-point bending tests, the maximum fracture loads were evaluated. The load values were converted into flexural stress (MPa) values. The flexural stress formula is given as follows:

$$\sigma = \frac{M \times y}{I} \quad (1)$$

where σ flexural stress, M the bending moment, y the distance from the natural axis and I the moment of inertia respectively. The maximum flexural surface stress occurs in the mid-point of the specimen. Therefore:

$$M = \frac{P \times L}{4} \quad (2)$$

$$y = \frac{t}{2} \quad (3)$$

$$I = \frac{b \times t^3}{12} \quad (4)$$

$$\sigma_{\max} = \frac{3 \times P \times L}{2 \times b \times t^2} \quad (5)$$

$$\text{Since } b = t; \sigma_{\max} = \frac{3 \times P \times L}{2 \times b^3} \quad (6)$$

where p load applied, t thickness of the specimen, b width of the specimen, and L span length respectively.

4.1. Heat Treatment

All of the specimens were heat treated according to ASM T6 heat treatment procedures. All of the heat treated samples were also solution treated at 480°C for 60 minutes. Then they were quenched into water. Finally precipitation heat treatment was carried out for 24 hours at 120°C.

4.2. Metallographic Analysis

Microstructures of as-cast and heat treated aluminum composite samples were examined metallographically. Samples were firstly cut

and mounted. Then they were grinded, polished and etched with Keller solution which contains 1.5% HCl , 2.5% HNO_3 , 1% HF , 95% H_2O . At the end, representative photographs were taken by a digital camera. To find the volume fraction of SiC reinforced aluminum 7075 alloy composites, image analyzer study was performed. With the help of Clemex software, area percentages of SiC and aluminum matrix were calculated and this would give an approximate value about the volume percentages of reinforcement and the matrix.

4.3. SEM Study

In order to get interior structures of aluminum samples SEM studies were performed. In particular the precipitates that should form after heat treatment were examined. The percentages of alloying elements were analyzed and their graphs were obtained. SEM studies were done with JSM-6400 Electron Microscope (JEOL).

5. RESULTS AND DISCUSSION

Effects of silicon carbide addition on the fracture behavior of aluminum matrix alloy composites (both as-cast and heat treated) were examined. Hardness tests were also evaluated in order to find out the optimum heat treatment procedure.

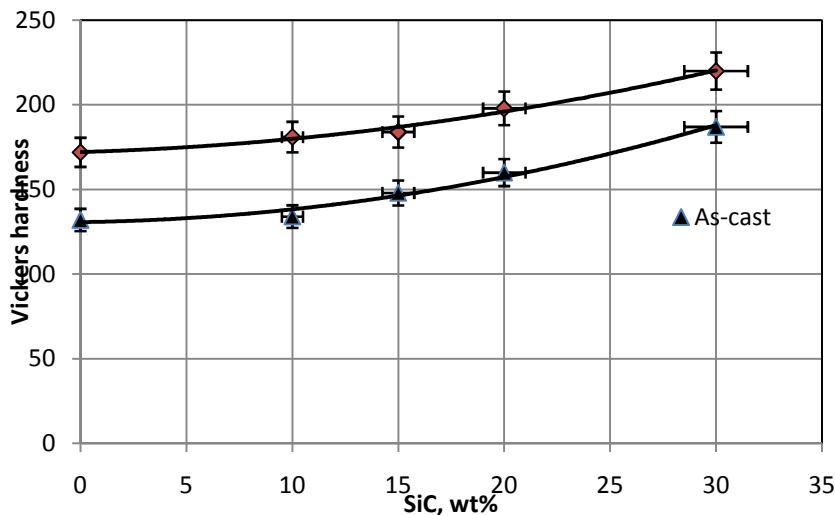


Figure 3: Variation of hardness with silicon carbide reinforcement

5.1. Effect of Silicon Carbide on Hardness

Hardness tests were carried out to observe the effects of heat treatment and effects of wt% addition of silicon carbide on aluminum alloy matrix since hardness is an indicator of a materials resistance to plastic deformation. Figure 3 shows the variation of hardness values with wt% silicon carbide. It is observed that the hardness values increase with the addition of silicon carbide. Silicon carbide particulates are ceramic materials that are harder than the aluminum matrix alloy. They fasten

the dislocation motion and therefore an increase in strain hardening achieved. Heat treatment also has effects on the hardness values of aluminum matrix alloy. By precipitation heat treatment extra hardening was obtained. Precipitates act like silicon carbide particles and they form barricades to dislocation motion. The aluminum matrix composites were solution heat treated at 480°C for 60 minutes and precipitation heat treated at 120°C for twenty-four hours. In figure 3, a comparison between hardness values of as-cast and heat treated silicon carbide reinforced aluminum matrix composites can also be observed. It is seen that heat treatment increases the hardness values.

5.2. Effect of Heat Treatment Time on Hardness

Variation of Vickers hardness values with precipitation heat treatment time is shown figure 4. Peak hardness values are obtained after 24 hours precipitation heat treatment at 120 °C. From 4 hours to 24 hours usually hardness values increased gradually. Only in 15 wt% and 30 wt% SiC composite, a small decrease in hardness observed from 20 hours to 24 hours treatment. This decrease arises from the variation of hardness values in different regions of specimens. If the values were taken from the region where silicon carbide particles existed intensively, hardness values were measured higher than original values.

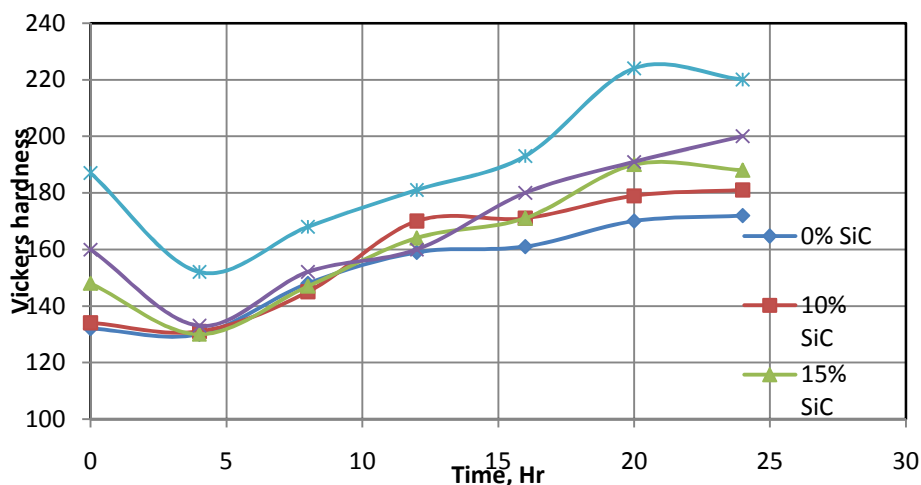


Figure 4: Variation of hardness with precipitation heat treatment time

5.3. Effect of Silicon Carbide on Flexural Strength

Three point bending tests were performed to observe the fracture behavior of aluminum matrix composite with different percentage additions of silicon carbide. Results are given graphically in figure 5. The flexural strength increased with increasing reinforcement content up to 10wt% silicon carbide. After 10 wt% SiC more additions of silicon carbide decreased the strength. In the 30wt% silicon carbide aluminum matrix composite the strength fell down to 302 MPa. Strength began to decrease as content approaches 15wt% silicon carbide. Composites failed at small strain values during the three point bending test for

composites reinforced with 30wt% SiC. The matrixes probably did not have enough internal ductility and cannot overcome the localized internal stresses. All specimens showed brittle fracture at macro scale fracture surface examinations. The 10wt% SiC reinforced aluminum matrix composites have the maximum strength among the other composites. Silicon carbide particulates having particle size in the range of 10-30 μm form barricades and hinder dislocation motion. This supplies an increase in strain hardening and flexural strength. As in the as-cast composites the 10wt% silicon carbide reinforced aluminum matrix composites have maximum flexural strength. Small MgZn_2 , $\text{Mg}_{32}(\text{Al,Zn})_{49}$ precipitates increased strength after T6 heat treatment. They acted as barriers to dislocation motion. Size of precipitates is very small when compared with SiC particulates. Their sizes are between 0.5-1.5 μm . With the effect of precipitates and silicon carbide particulates, the 10%wt SiC reinforced composite reached to 579 MPa of maximum strength.

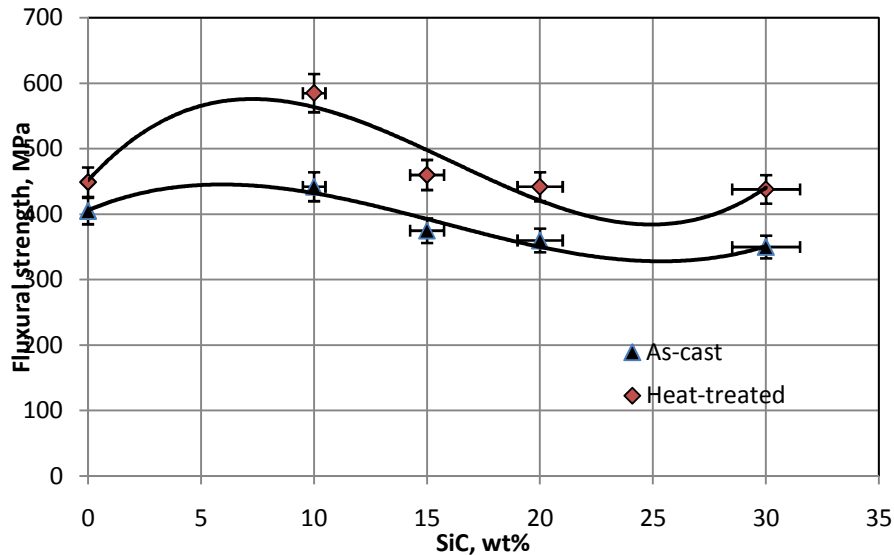


Figure 5: Variation of flexural strength with silicon carbide reinforcement

5.4. Effect of Silicon Carbide Reinforcement on Ultimate Tensile Strength

Variation of Vickers ultimate tensile strength with silicon carbide content and precipitation heat treatment time is shown figure 6. Almost all specimens were broken from the curved parts. Agglomeration of silicon carbide particulates was observed in some of the tensile test specimens. The ultimate tensile strength is found to be maximum for 10% silicon carbide reinforcement in the composite.

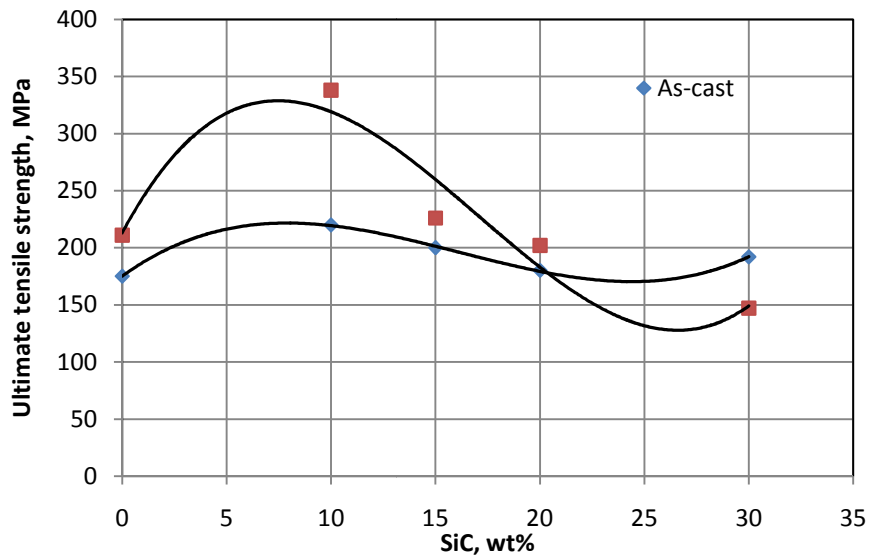


Figure 6: Variation of ultimate tensile strength with silicon carbide reinforcement

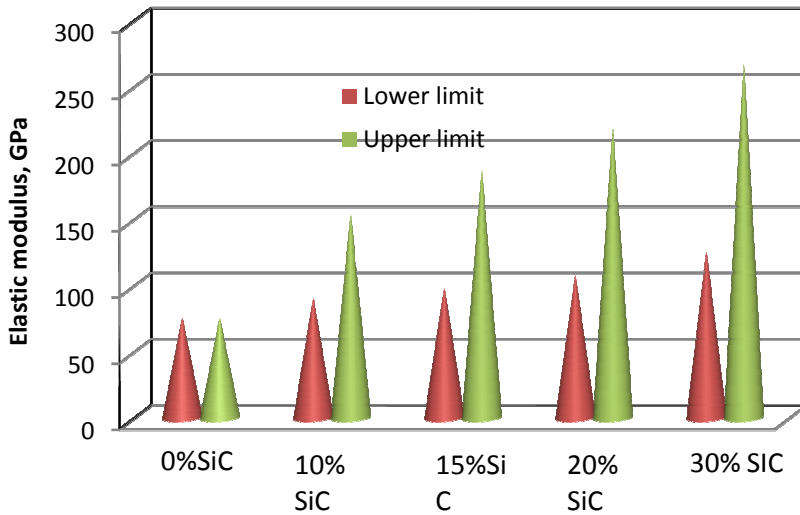


Figure 7: Variation of elastic modulus with silicon carbide reinforcement

5.5. Effect of Silicon Carbide Reinforcement on Elastic Modulus

Elastic modulus values were calculated theoretically with the **rule of mixtures** formula since proper strength-strain values could not be obtained. According to the formula, range of elastic modulus of composites can be found with the following formulae.

For upper limit: $E_{\text{comp}} = E_p \times V_p + E_m \times V_m$ (7)

For lower limit:
$$E_{\text{comp}} = \frac{E_p \times E_m}{E_p \times V_m + E_m \times V_p} \quad (8)$$

where V_p and V_m are volume percentages of silicon carbide particulate and matrix respectively. From the literature, elastic modulus of aluminum 7075 alloy was found between 70-80 GPa and the manufacturer firm states the elastic modulus of SiC as 480 GPa. So, with the calculation according to the rule of mixtures the upper and lower limits of elastic modulus are shown in figure 7. The elastic modulus of the matrix was taken as 75 GPa, which is the average value. Theoretically the elastic modulus increases with increasing vol% of silicon carbide. This increase is valid up to 10 vol% silicon carbide addition where a uniform composite can be produced.

5.6. Microstructural Analysis

Metallographic examinations were carried out to see the distribution of silicon carbide particulates in aluminum matrix and investigate condition of grains. Both as-cast and heat treated aluminum composites were investigated. In figure 8, optical microscopy photographs of as-cast aluminum composites are shown. Silicon carbide reinforced aluminum composites have even distribution of reinforcement and this distribution can be seen in X200 magnified optical microscopy photographs. Aluminum matrices have grains with different sizes. This is due to the result of fast cooling during casting process.

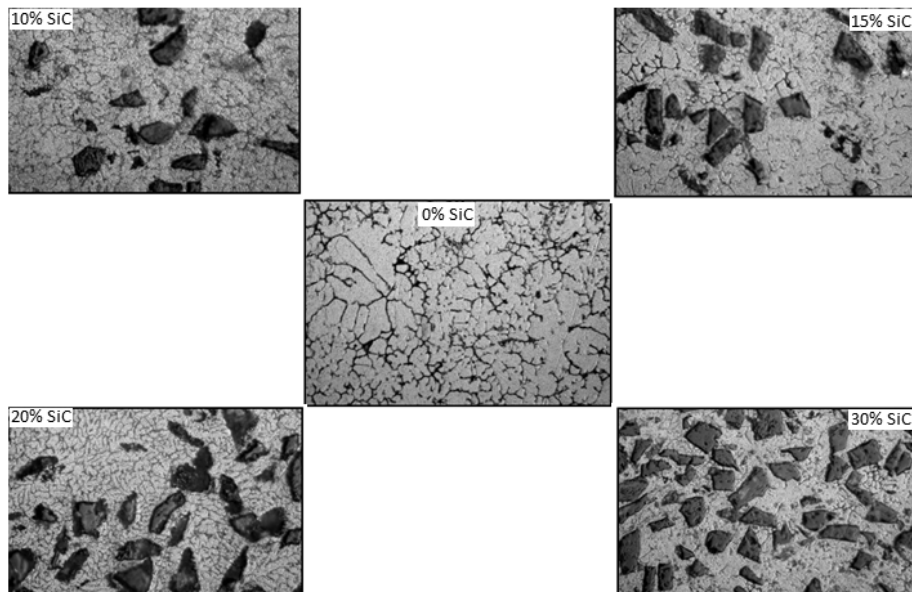


Figure 8: Micrographs of as-cast SiC reinforced 7075 composites, X500

Since the precipitates are very small and it is very hard to observe with optical microscopy, the only reliable way to observe them is scanning electron microscopy. Their size can be predicted from SEM photographs and their sizes are between 0.5-1.5 μm . Figure 9 show SEM photographs of heat treated silicon carbide reinforced aluminum composites. Silicon carbide particulates and precipitates can be observed. Precipitates formed during heat treatment are also observed within each grain. Grain boundaries and precipitates of heat treated aluminum matrix can be observed in matrix alloy (0% SiC). Small black points seen in each grain are the precipitates formed during heat treatment.

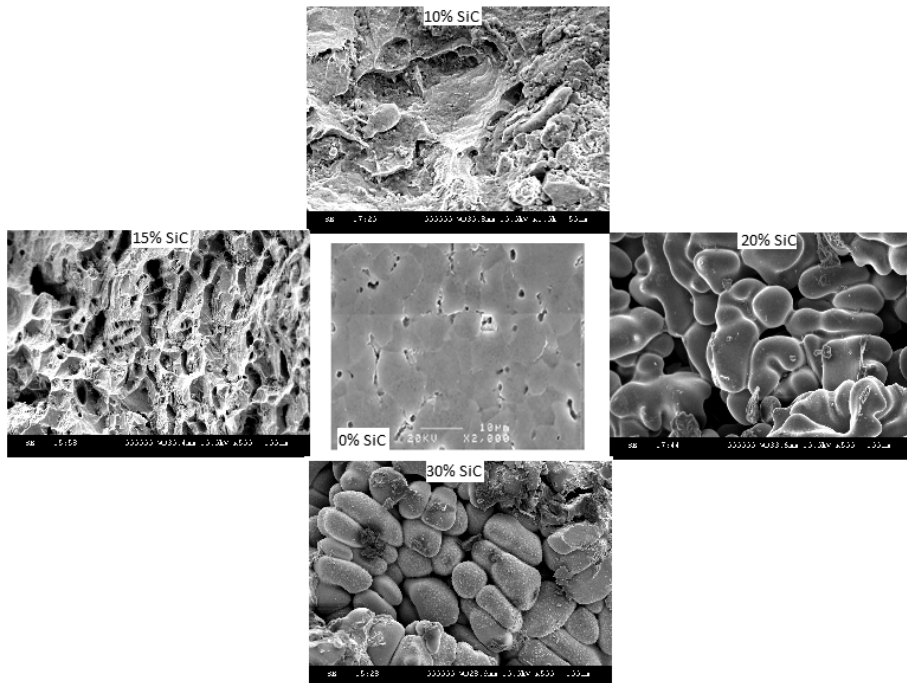


Figure 9: SEM photographs of heat treated SiC reinforced 7075 composites, X5000

CONCLUSIONS

The following results were concluded form the study presented in this paper:

1. Hardness values increased with the increase of silicon carbide addition in both as-cast and heat treated composites.
2. During heat treatment from 4 to 24 hours hardness values increased gradually. Peak hardness values are about 20-25% higher than as-cast hardness values. By precipitation heat treatment extra hardening was obtained.
3. The flexural strength increased with increasing reinforcement content up to 10wt% silicon carbide in both as-cast and heat treated composites.

4. The maximum flexural strength increased about 40 MPa in as-cast, 180 MPa in heat treated composites.
5. Tensile strength values of all as-cast and heat treated samples were lower than flexural strength as expected. The difference between maximum tensile strength and flexural strength is 232 MPa in as-cast and 240 MPa in heat treated aluminum composites.
6. Silicon carbide particulates have even distribution through the as-cast matrix. As-cast aluminum matrices have grains with different sizes as a result of fast cooling during casting and the efficiency of grain refiner addition, Al-Ti-B.
7. Agglomeration of silicon carbide particulates was observed in some of the tensile test specimens.

REFERENCES

1. B. Kotiveerachari, A. Chennakesava Reddy, Interfacial effect on the fracture mechanism in GFRP composites, CEMILAC Conference, Ministry of Defence, India, 20-21st August, 1999: B85-87.
2. A. Chennakesava Reddy, Fracture behavior of brittle matrix and alumina trihydrate particulate composites, Indian Journal of Engineering & Materials Sciences, 2002:5, pp.365-368.
3. A. Chennakesava Reddy, B. Kotiveerachari, Effect of matrix microstructure and reinforcement fracture on the properties of tempered SiC/Al-alloy composites, National conference on advances in materials and their processing, Bagalkot, 28-29th November 2003, pp.121-124.
4. A. Chennakesava Reddy, Finite element analysis of elastic-plastic and tensile damage response in carbon-carbon composites under vehicular crush conditions, National Conference on Emerging Trends in Mechanical Engineering, Nagpur, 05-06th February, 2004: IIA-6.
5. A. Chennakesava Reddy, Experimental evaluation of elastic lattice strains in the discontinuously SiC reinforced Al-alloy composites, National Conference on Emerging Trends in Mechanical Engineering, Nagapur, 05-06th February 2004: VC-12.
6. A. Chennakesava Reddy, Analysis of the relationship between the interface structure and the strength of carbon-aluminum composites, NATCON-ME, Bangalore, 13-14th March 2004, pp.61-62.
7. B. Ramana, A. Chennakesava Reddy, S. Somi Reddy, Fracture analysis of mg-alloy metal matrix composites, National Conference on Computer Applications in mechanical Engineering, Anantapur, 21st December 2005, pp.57-61.
8. A. Chennakesava Reddy, Strength and fracture mechanisms in carbon-carbon composites, International symposium on Advanced Materials and Processing, Bagalkot, 29-30, October 2007, pp.138-145.
9. A. Chennakesava Reddy, Mechanical properties and fracture behavior of 6061/SiCp Metal Matrix Composites Fabricated by Low Pressure Die Casting Process, Journal of Manufacturing Technology Research, 2009:1, pp.273-286.
10. A. Chennakesava Reddy, Essa Zitoun, Matrix al-alloys for alumina particle reinforced metal matrix composites, Indian Foundry Journal, 2009:55(1), pp.12.
10. A. Chennakesava Reddy, B. Kotiveerachari, Effect of aging condition on structure and the properties of Al-alloy / SiC composite, International Journal of Engineering and Technology, 2010:2(6), pp.462-465.
11. A. Chennakesava Reddy, Tensile properties and fracture behavior of 6063/SiCp metal matrix composites fabricated by investment casting process, International Journal of Mechanical Engineering and Materials Sciences, 2010:3(1), pp.73-78.

12. A. Chennakesava Reddy, M. Vidya Sagar, Two-dimensional theoretical modeling of anisotropic wear in carbon/epoxy FRP composites: comparison with experimental data, *International Journal of Theoretical and Applied Mechanics*, 2010:6(1), pp.47-57.
13. A. Chennakesava Reddy, Essa Zitoun, Tensile behavior Of 6063/Al₂O₃ particulate metal matrix composites fabricated by investment casting process, *International Journal of Applied Engineering Research*, 2010:1(3), pp.542-552.
14. A. Chennakesava Reddy , Essa Zitoun , Matrix al-alloys for silicon carbide particle reinforced metal matrix composites, *Indian journal of Science and Technology*, 2010:3(12), pp.1184-1187.
15. A. Chennakesava Reddy, Essa Zitoun, Tensile properties and fracture behavior of 6061/Al₂O₃ metal matrix composites fabricated by low pressure die casting process, *International Journal of Materials Sciences*, 2011:6(2), pp.147.
15. A. Chennakesava Reddy, Influence of strain rate and temperature on superplastic behavior of sinter forged Al6061/SiC metal matrix composites, *International Journal of Engineering Research & Technology*, 2011:4(2), pp.189.
16. A. Chennakesava Reddy, Strengthening mechanisms and fracture behavior of 7072Al/Al₂O₃ metal matrix composites, *International Journal of Engineering Science and Technology*, 2011:3(7), pp.6090-6100.
17. A. Chennakesava Reddy, Evaluation of mechanical behavior of Al-alloy/Al₂O₃ metal matrix composites with respect to their constituents using Taguchi , *International Journal of Emerging Technologies and Applications in Engineering Technology and Sciences*, 2011:4(2), pp.26-30.
18. A. Chennakesava Reddy, Tensile fracture behavior of 7072/SiCp metal matrix composites fabricated by gravity die casting process, *Materials Technology: Advanced Performance Materials*, 2011:26(5), pp.257-262.
19. A. Chennakesava Reddy , Evaluation of mechanical behavior of Al-alloy/SiC metal matrix composites with respect to their constituents using Taguchi techniques, *i-manager's Journal of Mechanical Engineering*, 2011:1(2), pp.31.
20. A. Chennakesava Reddy, B. Kotiveerachari, Influence of microstructural changes caused by ageing on wear behavior of Al6061/SiC composites, *Journal of Metallurgy & Materials Science*, 2011:53(1), pp.31-39.
21. S. Sreenivasulu, A. Chennakesava Reddy, Mechanical Properties Evaluation of Bamboo Fiber Reinforced Composite , *International Journal of Engineering Research*, 2014:3(1), pp.187-194.

MECHANICAL DESIGN OF TRAILER SYSTEM FOR NON CONVENTIONAL POWER DEVICES

B. Sandhya Rani^a, P.H.V.Sesha Talpa Sai^b, Y. Vijay Kumar^a, C.Udayakiran¹

^a Department of Mechanical Engineering, J. B. Institute of Engineering and Technology, Hyderabad, India-500072.

^b Department of Mechanical Engineering, Centre for Innovation, Incubation & Entrepreneurship(CIIE), Malla Reddy College of Engineering & Technology, Dhulapally, Secunderabad-500 100.

Abstract: Generation of electrical power from non-conventional sources energy is the state of art as non conventional sources energy is abundantly available. The non conventional power device installed on roof top should always face the sun to generate maximum power. But presently non conventional power devices will be installed in a fixed position and in a day, position of sun keeps changes from morning till evening. Because of this practical difficulty most of the time very minimal power that emits from the sun will be utilized by the device for generating electricity. To overcome this limitation this work aims at design of trailer system which enables the non conventional power device to change its orientation (Rotates) continuously such that it always remains normal to the sun which increases the device output. The intended system makes use of simple mechanical elements like gear which makes it economical for realization.

Keywords: trailer system, worm gear, non conventional power devices, photo voltaic module, roof top system.

Address all correspondence to: Mobile: +91- 9441365792; e-mail: sandhyasanju@gmail.com

1. INTRODUCTION

Non conventional power device viz. photo voltaic module are not seeing much of light due to a practical draw back that sun should be normal to the plane of the device all the times. Sun should be normal to the plane of the device all the times as the heat transfer occurs by radiation and the condition imposed by radiation heat transfer is heat source should be normal to the absorber in order to achieve effective heat transfer. But presently non conventional power devices are being installed in a fixed position and in a day position of sun keeps changes from morning till evening with relative to the non conventional power device. Because of this practical difficulty most of the time very minimal power that emits from the sun will be utilized for generating electricity.

To overcome this limitation a trailer system is needed which enables the non conventional power device to change its orientation (Rotates) continuously such that it always remains normal to the sun with which effectiveness of the non conventional power devices can be increased tremendously. Typical trailer system is shown in figure 1.

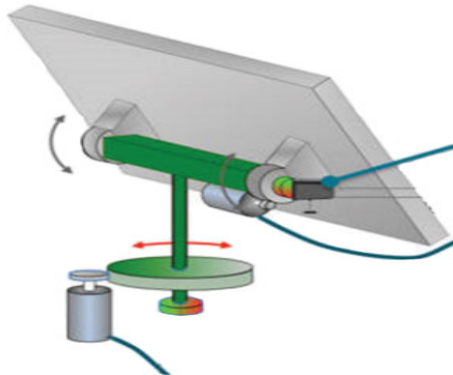


Figure 1: Trailer system

Design and construction of a prototype for trailer system for non conventional power applications with two degrees of freedom, which detects the sunlight using photocells is presented [1]. Design and execution of a trailer system dedicated to the PV conversion panels is discussed. The proposed single axis trailer system device ensures the optimization of the conversion of solar energy into electricity by properly orienting the PV panel in accordance with the real position of the sun [2]. Design of a low cost, 0.9kW solar tracking photo-voltaic (PV) array system took up as part of an undergraduate senior project. The trailer system for non conventional power applications is interfaced with a 1kW wind turbine, a deep cycle battery storage system, a charge controller and an inverter. Solar tracking is realized through complex digital circuit [3]. LDR light detector is used to trace the coordinate of the Sun. While to rotate the appropriate position of the panel, a DC geared motor is used. The system is controlled by two relays as a driver and a microcontroller as a main processor. This project is covered for a single axis and is designed for residential usage [4]. The tracker uses two Nema 23 bipolar stepper motors to rotate two photovoltaic panels around the altitude and azimuth axes. Three tracking algorithms are implemented to track the sun. The first moves the PV panel in little squares in spherical coordinates, finds the point on the square with the best voltage, and moves there, then starts over. The second moves in a little square, finds the voltage gradient, and uses that to decide where to move. The third uses the second strategy to find 5 or 6 good points spread 1hour apart [5]. An innovative system for tracking the sun which is based on the use of a commercial web cam as the sensor element is proposed. An experimental electro-mechanism was designed and developed to evaluate its accuracy and efficacy in tracking the sun under different weather conditions [6]. As can be seen, all the research

focus on design of most complicated systems. Further it is also noticed that all the systems are having electronic controllers and hence costlier. Moreover they demand more power for their own controller and also their maintenance is tedious.

Based on the limitations brought out as an outcome of literature review it is observed that a great need exists for development of trailer system built with all mechanical systems for non conventional power applications.

2. DESIGN PHILOSOPHY

Objective of the present work is to design a trailer system for non conventional power applications. Electronic controller in the existing systems is replaced by mechanical elements in the proposed design. The advantages are as follows:

- Cost will be very less
- Reliability will be very high
- Easy to maintain
- Demands less power for its operation

Taking total time between sun rise and sun set rpm of motor needed to cover is estimated which is very less and hence gear motor (Which is basically a low speed motor) is considered for the proposed design with two stage speed reduction which is very high. It is planned to incorporate worm as driver and worm gear as follower so as to meet the desired high speed reduction. Typical rotation orientation of worm and worm gears is shown in figure 2.

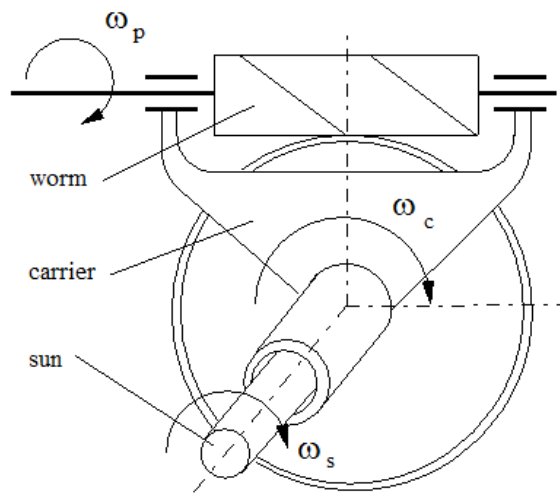


Figure 2: Typical orientation of worm and worm gear

From the design philosophy the following components are identified for which detailed design is carried out.

- Worm (Stage 1 and 2)

- Motor
- Worm gear (Stage 1 and 2)
- Shaft
- Bearing

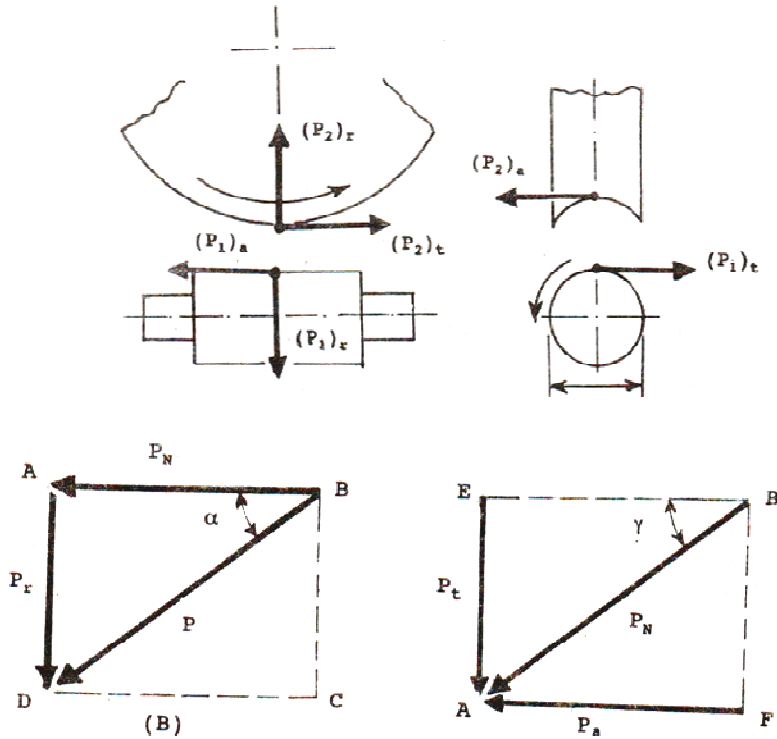


Figure 3: Forces acting in worm and worm gear

2.1 Design of Worm

The power required is calculated as follows:

$$P = \frac{2 \pi N_{\text{worm}} T}{60} \quad (1)$$

Torque can be expressed as follows:

$$T = \frac{\pi}{16} \times f_s \times d^3 \quad (2)$$

From which diameter of worm shaft (d) is calculated.

$$\text{Pitch Circle Diameter (PCD) of worm} = m \times q \quad (3)$$

Outside diameter of worm,

$$d_{\text{al}} = m(q + 2) \quad (4)$$

Velocity of worm can be expressed as follows

$$v_w = \frac{\pi \times \text{PCD of worm} \times \text{Speed of worm}}{60} \quad (5)$$

Rubbing velocity can be expressed as follows

$$v_{\text{rub}} = \frac{v_w}{\cos(\lambda)} \quad (6)$$

In which the helix angle is given by

$$\lambda = \tan^{-1} \left(\frac{1}{q} \right) \quad (7)$$

While serving the function various forces gets developed in worm and worm gear as shown in figure 3.

The components of the resultant force acting on the worm are as follows:

P_{1t} = tangential component on worm

P_{1a} = axial component on the worm

P_{1r} = radial component on the worm

In practice, the tangential component P_{1t} on the worm is determined from the torque, which is transmitted from the worm to the worm gear.

$$P_{1t} = \frac{2T}{\text{PCD of worm}} \quad (8)$$

Axial force is calculated using the following expression:

$$P_{1a} = P_{1t} \times \frac{(\cos\alpha \cos\gamma - \mu \sin\gamma)}{(\cos\alpha \sin\gamma + \mu \cos\gamma)} \quad (9)$$

Radial force is given by

$$P_{1r} = P_{1t} \times \frac{(\sin\alpha)}{(\cos\alpha \sin\gamma + \mu \cos\gamma)} \quad (10)$$

2.2 Design of Worm Gear

The speed of gear is given by

$$\frac{N_{\text{worm}}}{\text{Speed ratio}} \quad (11)$$

$$\text{Number of teeth on the gear, } z_2 = i \times z_1 \quad (12)$$

$$\text{PCD of gear} = m \times z_2 \quad (13)$$

The force acting on the worm gear is equal and opposite reaction of the force acting on the worm.

$$\text{Tangential force in gear, } P_{2t} = \text{Axial force in worm} \quad (14)$$

$$\text{Axial force in gear, } P_{2a} = \text{Tangential force in worm} \quad (15)$$

Radial force in gear = P_{2r}
 Radial force in worm = P_{1r}

Efficiency of the system is given by

$$\eta = \frac{\text{Power output}}{\text{Power input}} = \left(\frac{\cos \alpha - \mu \tan \gamma}{\cos \alpha + \mu \cot \gamma} \right) \quad (16)$$

2.3 Design of Shaft

The load diagram of shaft is shown in figure 4.

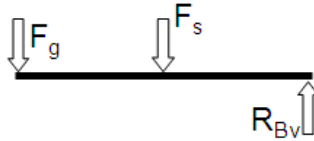


Figure 4: Load diagram of shaft

where, F_g = Tangential tooth load of gear

F_s = Load due to non conventional system

R_{BV} = Reaction at bearing = $F_g + F_s$

Maximum bending moment,

$$M = F_g \times L + F_s \times \frac{L}{2} \quad (17)$$

where, L = Total length of shaft

Then from torque and the total moment effective twisting moment is calculated as follows

$$T_e = \sqrt{(T)^2 + (M)^2} \quad (18)$$

Equivalent twisting moment can also be expressed as

$$T_e = \frac{\pi}{16} f_s d_s^3 \quad (19)$$

where, f_s = Shear stress of shaft material

From which diameter of shaft (d_s) is calculated

2.4 Design of Bearing

Type of bearing plays vital role in any dynamic system, which has bearings. Sliding contact bearings will have large starting friction and they are suitable for huge installations. Whereas for the proposed design, rolling contact bearings will be suitable because, they are of high precision type and will have very low starting friction. Again in rolling contact bearings ball bearings are suitable for low and medium radial loads where as roller bearings are suitable for heavy loads and large shaft diameters. Hence for the proposed design single row deep

groove ball bearings are chosen as they are best suitable for taking both radial and thrust loads.

Bearing reactions are in radial direction. There is no axial thrust on bearing

$$F_a = 0 \quad (20)$$

$$\text{Equivalent dynamic load, } P = XF_r + Y F_a \quad (21)$$

where, X = Radial Factor
Y = Thrust Factor

When no axial load and purely radial, X=1, Y=0
Relationship between life in million revolutions and life in working hours is given by

$$L = \frac{60NL_h}{10^6} \quad (22)$$

where, L_h = Bearing life in hours

From standards load factor is taken as 1.4

Relationship between dynamic load carrying capacity, Equivalent dynamic load & bearing life

$$L = \left(\frac{C}{P \times \text{Load factor}} \right) \quad (23)$$

where, C = Dynamic load capacity

For the diameter shaft (calculated earlier) the selection of bearing is made from the standards pertaining to bearings.

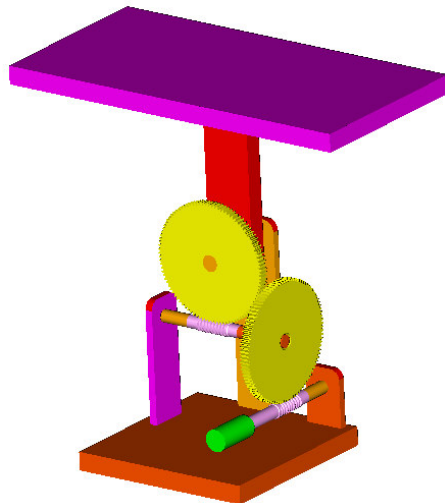


Figure 5: Solid model of the assembly

3. DESIGN CONFIGURATION

All the solid models pertaining to the components designed are assembled to get the assembly of the system. Solid model of the assembly is shown in figure 5.

4. ACKNOWLEDGMENT

The authors sincerely acknowledge the valuable support extended by Dr. Devarayapalli Kamakshaiah Charyulu, Professor & Head of the Science and Humanities Department, Bhaskar Engineering College, Hyderabad, India. The authors thank Dr. Niraj Upadhaya, Principal, J B Institute of Engineering and Technology, Hyderabad, India for the support.

REFERENCES

1. N. Barsoum, and P. Vasant, Simplified Solar Tracking Prototype, Transaction in Controllers and Energy, 2010: 1, pp. 39-45.
2. T. Tudorache, and L. Kreindler, Design of A Solar Tracker System For PV Power Plants, Acta Polytechnica Hungarica, 2010: 7, No. 1, pp. 23-39.
3. S. Lakeou, E. Ososanya, B.O. Latigo, and W. Mahmoud, Design of a Low-cost Solar Tracking Photo-Voltaic (PV) Module and Wind Turbine Combination System, International Conference on Renewable Energy for Developing Countries, ICREDC-06, 2006.
4. A. Ponniran, A. Hashim, and H. Ali Munir, A Design of Single Axis Sun Tracking System, The 5th International Power Engineering and Optimization Conference (PEOCO2011), Malaysia, 2011: pp. 107-110.
5. T. Peterson, J. Rice, and J. Valane, Solar Tracker, I ECE 476, Spring 2005.
6. M. Minor. Arturo, and G. P. Alejandro, High precision solar tracking system, Proceedings of The World Congress on Engineering, 2010: pp. 844-846.

DESIGN OF CAM-FOLLOWER MECHANISMS USING RATIONAL B-SPLINES

N. Sateesh¹, C.S.P. Rao², K. Prashanth Reddy³, R. Raman Goud⁴

¹ Professor, Department of Mechanical Engineering, GRIET, Hyderabad, India.

² Professor, Department of Mechanical Engineering, NIT, Warangal, India.

³ Assistant Professor, Department of Mechanical Engineering, GRIET,
Hyderabad, India

⁴ Associate Professor, Department of Mechanical Engineering, GRIET,
Hyderabad, India

Abstract: This paper proposes an integrated system for improving the cam-follower performance. The design method is to improve the motion characteristics of a cam follower-system. Improvement of the motion characteristics is to achieve low maximum velocity and acceleration for each follower motion curve so that jerk is minimum. Representing basic follower motion curves with non-uniform rational B-splines (NURBS) can do this. Conventional methods in designing and manufacturing of cam are tedious and time consuming. Even programming them on a computer numerical control (CNC) machine can be a difficult job because of the complexity of the cam profiles. A CAD/CAM system is developed, which provides useful design information such as graphical and numerical representation of displacement, velocity, acceleration, jerk, pressure angle and cam profiles for both basic curves and NURBS. An analysis can be carried out based on maximum velocities and accelerations to select the best cam follower motion. It also provides cam profile coordinates for basic curves and NURBS to manufacture a cam on CNC machines.

Keywords: plate-cams, disc-cams, cam profile, NURBS, B-Spline, computer numerical control, rise-dwell-return-dwell.

Address all correspondence to: email: nagarisateesh007@gmail.com

1. INTRODUCTION

A plate-cam is a disc-cam, which is cut out of a piece of flat metal or plate and used to transform a rotary motion into a translating or oscillating motion to its follower [1]. Applications of these cams found in packaging machines, wire-forming machines, internal combustion engines, mechanical and electronic computers. Requirements for high performance of such machinery demand efficient methods for the design and manufacture of cams. The purpose of this paper is to develop a seamless integration of design and manufacturing of plate cams. NURBS have been used to design and optimization of cam profiles. The design parameters will be used in the manufacturing module that generates the NC program required for the machining of the designed cam.

2. BASIC FOLLOWER MOTIONS

To analyze the action of a cam, it is necessary to study its displacement–time diagram and its associated velocity and acceleration curves. Some of the most common types of follower motion curves selected by cam designers for a typical cam follower system shown in the Figure1 are [3]:

Simple harmonic motion (S.H.M.), Cycloidal motion, Parabolic motion, 3-4-5 polynomial, 4-5-6-7 polynomial, and Modified harmonic motion. Simple harmonic motion has smoothness in velocity and acceleration during the stroke is advantage inherent in the curve. However, the instantaneous changes in the acceleration at the beginning and end of the stroke tend to cause vibration, noise, and wear. It is, therefore, suitable only for cams at medium or low speed. Cycloidal motion is obtained by rolling a circle on a straight line. It has the smoothest motion among all of the basic curves. The maximum value of the acceleration of the follower for a given rise is somewhat higher than that of the simple harmonic motion. Cycloidal curve is used often as a basis for designing cams for high-speed machinery because it results in low noise, vibration, and wear. Parabolic motion has constant acceleration and retardation following a parabolic equation. The 4-5-6-7 polynomial curve is worked out from a 7th degree polynomial. It has good acceleration characteristics and is used for high-speed cams.

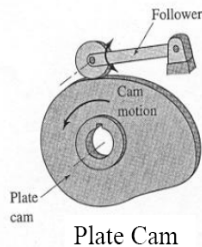


Figure1: Plate cam

2.1 Follower Motion Equations

Displacement (S) equations for different follower motions against cam rotation angle θ have been presented as follows:

$$\text{Cycloidal, } S = h/2[\theta/\beta - \cos(2\pi\theta/\beta)] \quad (1)$$

$$\text{Parabolic motion, } S = 2h [\theta/\beta]^2 \quad (2)$$

$$\text{3-4-5 polynomial, } S = h [10((\theta/\beta)^3 - 15((\theta/\beta)^4 + 6(\theta/\beta)^5)] \quad (3)$$

$$\text{4-5-6-7 polynomial, } S = h [35(\theta/\beta)^4 - 84((\theta/\beta)^5 + 70(\theta/\beta)^6 - 20(\theta/\beta)^7] \quad (4)$$

$$\text{Modified harmonic: } S = h/2 [(1 - \cos(\theta/\beta) - 0.25(1 - \cos(2\theta/\beta))] \quad (5)$$

where h is lift of the follower, β is the angle of rise or return.

2.2. Cam profiles

The workout of a cam profile requires the drawing of many positions of the cam with the follower in each case in its related location. Depends up on the kind of follower, cams used with radial translating follower, an offset roller follower, flat face follower and oscillating followers. In radial translating follower centerline of the follower-stem passes through the center of the camshaft. In offset translating roller follower, the follower is offset from the camshaft center. Generally flat face follower perpendicular to the follower stem. Sometimes centerline of the flat face is offset from the centerline of the camshaft. In oscillating roller follower, follower oscillates about a pivot point depend upon the rotation of cam.

2.3 Cam profile Calculations

The following equations give points on the pitch curve of the cam and points on the cam profile itself in rectangular coordinates for roller follower which is in contact with the cam. The rectangular coordinates (X , Y) about cam center for each angle of cam rotation (θ) as follows.

Radial translating follower,

$$X = (Rp+S)\sin\theta; \quad Y = (Rp+S) \cos\theta \quad (6)$$

3. NON-UNIFORM RATIONAL B-SPLINES (NURBS)

One of the most versatile tools for modeling curves is the Non-Uniform Rational B-splines (NURBS). It has been widely used in modeling of curves and surfaces in CAD/CAM as a standard. It is a smooth spline and it is a ratio of two non-rational B-spline basis functions, making it a vector-valued piecewise rational polynomial. NURBS offer a common mathematical form for representation and used for designing standard curves (conic and quadrics, etc), free form curves and surfaces. NURBS are invariant under translation, rotation, scaling, shear, and parallel and perspective projection. They have ability to interpolate or approximate a set of given data points. They provide local control of the curve shape as opposed to global control by using a special set of blending functions that provide local influence. Another advantage of NURBS is that they provide the ability to add control points without increasing degree of the curve. NURBS are free form curves having C^0 (points continuity), C^1 (slope continuity) and C^2 (curvature continuity).

3.1. Optimization of follower motion curves using NURBS

The motion characteristics of the cam follower mechanisms can be improved by reducing the jerk. The jerk causes vibration, more contact stresses, wear and tear in the cam. This is predominant at the transition points i.e. points where follower motion changes from dwell to rise, rise to dwell, dwell to fall and fall to dwell etc. One method of improving the follower motion characteristics would be to represent the basic curves by Non Uniform Rational B-Splines (NURBS).

3.2 NURBS

Mathematically NURBS can be defined by $n+1$ control points [4]

$$p(u) = \frac{\sum_{i=0}^n N_{i,k}(u) p_i h_i}{\sum_{i=0}^n N_{i,k}(u) h_i} \quad 0 \leq u < u_{\max} \quad (7)$$

Where p_i is a control point, $N_{i,k}(u)$ is a blending function, which is recursive in nature and polynomial of degree $k-1$, h_i is weight at each control point and varies from 0 to 1. If weights are equal at all control points than NURBS becomes non-rational B-splines. $p(u)$ is the position on the curve at parameter u . The range of parameter u depends on the number of control points $n+1$ and the choice for k , so that u varies from 0 to $n-k+2$.

The Blending function has the property of recursion, which is defined as

$$N_{i,k}(u) = \frac{[u-u_i]N_{i,k-1}(u)}{[u_{i+k-1}-u_i]} + \frac{[u_{i+k}-u]N_{i+1,k-1}(u)}{[u_{i+k} - u_{i+1}]} \quad (8)$$

$$N_{i,1}(u) = 1 \text{ if } u_i < u < u_{i+1}, \quad N_{i,1}(u) = 0 \text{ otherwise} \quad (9)$$

where k controls the degree ($k-1$) of the resulting polynomial in u and also controls the continuity of the curve. The values u_i are called knot values. They relate the parametric variable u and control points (p_i). The knot values u_i are given by

$$u_j = 0 \text{ if } j < k, \quad u_j = j-k+1 \text{ if } k \leq j \leq n, \quad u_j = n-k+2 \text{ if } j > n \text{ with } 0 \leq j \leq n+k.$$

$$\begin{aligned} \text{Number of knot values (m)} &= n+k+1, \quad \text{i.e. } u_i \\ &= [u_0, u_1, u_2, u_3, \dots, u_{n+k}] \end{aligned} \quad (10)$$

There are three ways to modify the shape of NURBS. Change the knot vector, move the control points or change the weights. It is relatively difficult to determine how a curve will respond to changes in the knot vector, this is not the best way to change curve shape. On the other hand, effect of changing a control point is predictable and intuitive. If a weight h_i is increased or decreased in value, then the curve is pulled towards or pushed away from the respective control point p_i . This is the best way to modify the shape of the NURBS.

3.3. Applying a NURBS approximation to a basic curve

In cam design, once the basic follower motion curve has been specified, it can then be approximated by NURBS. In the design of NURBS, the curve with degree ($k-1$) three and the six control points ($n+1$) of the basic curve are considered. The following steps illustrate the procedure by a simple example.

1. Create the basic curve of the selected follower motion (simple harmonic, cycloidal, etc).

2. Divide the angle of interval (rise or return) of the curve into 5 parts. Each part has the same angle of interval. This will create 6 control points, $p_0, p_1, p_2, p_3, p_4,$ and p_5 lying on the curve.
3. These 6 control points are interpolated by considering the constraints of $n+1=5$ and $k=4$ in to the equations 1, 2, 3 and 4. The parametric equations obtained are [12]:

$$p_{x,y} = \left\{ \begin{aligned} & (1-u)^3 p_0 h_0 + [u(1-u)^2 + 1/2(2-u)(-3/2u^2 + 2u)] p_1 h_1 + \\ & [u/2(-3/2u^2 + 2u) + u^2/6(3-u)] p_2 h_2 + u^3/6 p_3 h_3 \} / \\ & \{(1-u)^3 h_0 + [u(1-u)^2 + 1/2(2-u)(-3/2u^2 + 2u)] h_1 + \\ & [u/2(-3/2u^2 + 2u) + u^2/6(3-u)] h_2 + u^3/6 h_3 \} \\ & \text{if } 0 \leq u < 1 \end{aligned} \right. \quad (11)$$

$$p_{x,y} = \left\{ \begin{aligned} & 1/4(2-u)^3 p_1 h_1 + [u/4(2-u)^2 + (3-u)/3(-u^2 + \\ & 3u - 3/2)] p_2 h_2 + [u/3(-u^2 + 3u - 3/2) + \\ & 1/4(3-u)(u-1)^2] p_3 h_3 + 1/4(u-1)^3 p_4 h_4 \} / \{ 1/4(2-u)^3 h_1 + \\ & [u/4(2-u)^2 + (3-u)/3(-u^2 + 3u - 3/2)] h_2 + \\ & [u/3(-u^2 + 3u - 3/2) + 1/4(3-u)(u-1)^2] h_3 + 1/4(u-1)^3 h_4 \} \\ & \text{if } 1 \leq u < 2 \end{aligned} \right. \quad (12)$$

$$p_{x,y} = \left\{ \begin{aligned} & 1/6(3-u)^3 p_2 h_2 + [u/6(3-u)^2 + (3-u)/2(-3/2u^2 + \\ & 7u - 15/2)] p_3 h_3 + [(u-1)/2(-3/2u^2 + 7u - 15/2) + \\ & (3-u)(u-2)^2] p_4 h_4 + (u-2)^3 p_5 h_5 \} / \{ 1/6(3-u)^3 h_2 + \\ & [u/6(3-u)^2 + (3-u)/2(-3/2u^2 + 7u - 15/2)] h_3 + \\ & [(u-1)/2(-3/2u^2 + 7u - 15/2) + (3-u)(u-2)^2] h_4 + (u-2)^3 h_5 \} \\ & \text{if } 2 \leq u < 3 \end{aligned} \right. \quad (13)$$

where p_x is the x-coordinate point and p_y is the y-coordinate point on the curve. Using the above procedure, each motion curve is converted into an equivalent NURBS. The new curve may look approximately the same as the former basic curve but it will have differences in the smoothness and maximum velocity and acceleration. These are the factors that affect the kinematics performance of the cam.

4. Integrated system

An integrated system for a disc-cam presented in this paper is an interactive computer program written in Visual Basic language. It is an user interactive system where user can design and manufacture the cam of his choice by providing necessary data such as type of basic follower motion, speed of cam (r.p.m.), lift of the follower (h) in mm, and angle of rise, return, dwell (degrees).

Then the system computes the cam profile for the specified follower motion and generates the following information:

1. Graphical and numerical display of displacement, velocity, acceleration and jerk diagrams for each follower motion basic curves and approximated NURBS against cam rotation θ .
2. Graphical and numerical display of cam profiles and cutter location data points of each follower motion basic curves and approximated NURBS against cam rotation θ .

3. Numerical values of maximum acceleration and maximum velocity for each follower motion basic curves and approximated NURBS.
4. CNC machining of basic curves and approximated NURBS against cam rotation angle (θ) for a typical input data.

4.1 Numerical illustration

The integrated system for design and manufacturing of cams has been thoroughly tested for a typical input to the program, which is given in Figure 2. Lift = 30 mm, Rise angle = 60 degrees, Dwell1 = 120 Degrees, Return = 60 Degrees, Dwell 2 = 120 degrees, Cam speed = 20 Rpm. Weights for NURBS $h_0=0.1$, $h_1=0.2$, $h_2=0.3$, $h_3=0.4$, $h_4=0.5$ and $h_5=0.6$.

The figure consists of two screenshots of a software interface. The top screenshot, titled "PROFILE", shows a window with four radio buttons for follower types: "TRANSLATING ROLLER FOLLOWER" (selected), "OFFSET FOLLOWER", "FLAT FACE FOLLOWER", and "OSCILLATING FOLLOWER". Input fields include "PRIME RADIUS" (35), "LIFT" (30), "RISE" (60), "DWELL1" (120), "RETURN" (60), and "DWELL2" (120). The bottom screenshot, titled "CAM", shows radio buttons for motion types: "SIMPLE HARMONIC MOTION", "CYCLOIDAL MOTION" (selected), "PARABOLIC", "CONSTANT VELOCITY", "POLY 3-4-5", "POLY 4-5-6-7", and "MODIFIED HARAMONIC MOTION". Input fields include "LIFT" (30), "RISE" (60), "DWELL1" (120), "RETURN" (60), "DWELL2" (120), "SPEED" (20), and "WEIGHTS FOR NURBS (BETWEEN 0 TO 1)" with values h0=1, h1=2, h2=3, h3=4, h4=5, and h5=6. Both windows have "PLOT", "CLEAR ALL", and "END" buttons.

Figure 2: Input data: follower motion is cycloidal

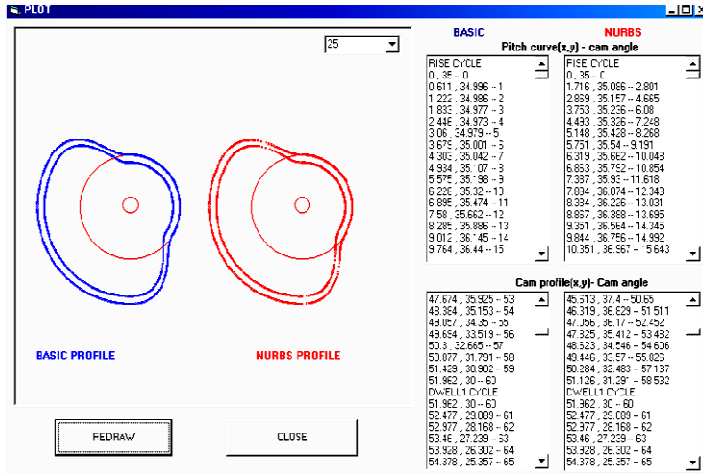


Figure 3: Graphical and numerical displacement(s)

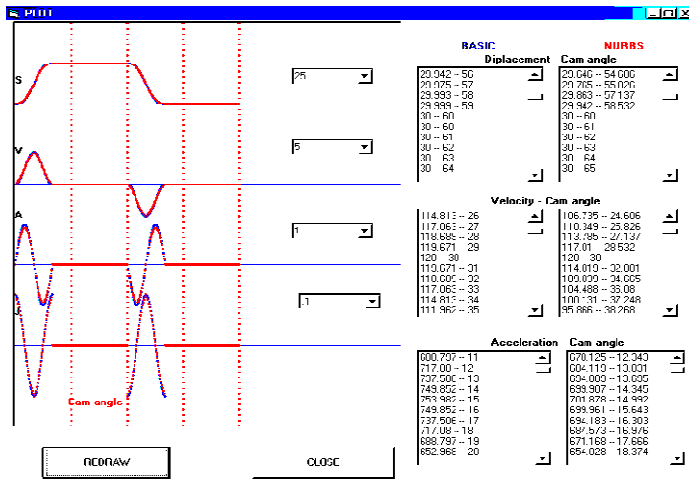


Figure 4: cam profiles and cutter location data points for velocity (v), acceleration, jerk (j).

5. Analysis of motion curves:

Using the integrated system, an analysis was performed to determine the maximum acceleration achieved by a disc-cam designed for different types of follower motions for basic curves and approximated NURBS (as shown in table 1). Lower maximum acceleration provide low jerk, which is useful for selection of best cam profile. Using a follower displacement height of 30 mm, the integrated system was used to compute the maximum acceleration for disc cam in which the rise and return had equal angle intervals of 60° and with the rise and return having the same type of motion curve and dwell of 120° each. This was done for all six types of motions (SHM, Cycloidal etc) for basic curves and approximated NURBS. Three cam speeds 20 rpm and 100 rpm were

used. The results in table 1 shows maximum acceleration (mm/sec²) for each follower motion basic curves and approximated NURBS.

From the above analysis (Table 1) it clear that 4-5-6-7 polynomial curve has maximum acceleration and parabolic has minimum acceleration for the same cam speed among all the motion curves. Approximated NURBS have low maximum acceleration compared to basic curves for cycloidal, 3-4-5 polynomial, 4-5-6-7 polynomial, and modified harmonic motions. So whenever minimum jerk motion (i.e. optimum motion) is required, designer can select approximated NURBS instead of basic curves for cycloidal, 3-4-5 polynomial and modified harmonic motions. This is also shown in the Figure 3 &4 (for cycloidal motion).

Table 1: Maximum accelerations (mm/sec²) for different cam speeds

Type of follower motion	Type of Curve	Cam speed(rpm)	
		20	100
		Max Acceleration (mm/sec ²)	
SMH	Basic	592.17	14804.40
	NURBS	592.17	14804.40
Cycloidal	Basic	753.90	18849.50
	NURBS	701.87	17456.95
Parabolic	Basic	480.00	12000.00
	NURBS	480.00	12000.00
3-4-5 Poly	Basic	692.40	17311.66
	NURBS	645.23	16130.91
4-5-6-7 Poly	Basic	900.50	22512.43
	NURBS	821.96	20549.02
Modified harmonic	Basic	666.10	16652.65
	NURBS	622.71	15567.84

When high acceleration and minimum jerk required than designer can select approximated NURBS for 4-5-6-7 polynomial. When low acceleration is required designer can select either basic or approximated NURBS for parabolic motion. When low velocity is required designer can use either basic or approximated NURBS for SHM.

6. CONCLUSION

This paper proposes the improvement of motion characteristics of a cam-follower system by approximation of NURBS to basic curves. An integrated system is developed which provides useful design information (graphically and numerically) such as displacement, velocity, acceleration and jerk against each cam rotation for basic curves and approximated NURBS.

The analysis can be carried out to select best cam profile (minimum jerk) based low maximum acceleration. The system also provides disc-cam profile coordinates to manufacture the cam on CNC machine. These numerical values are directly copied from the system to any CAM (computer aided manufacturing) software, which generates NC code automatically. So it avoids the writing NC code manually and saving in the time of manufacturing. The NC code fed to the CNC milling machine, which produces required cam profile.

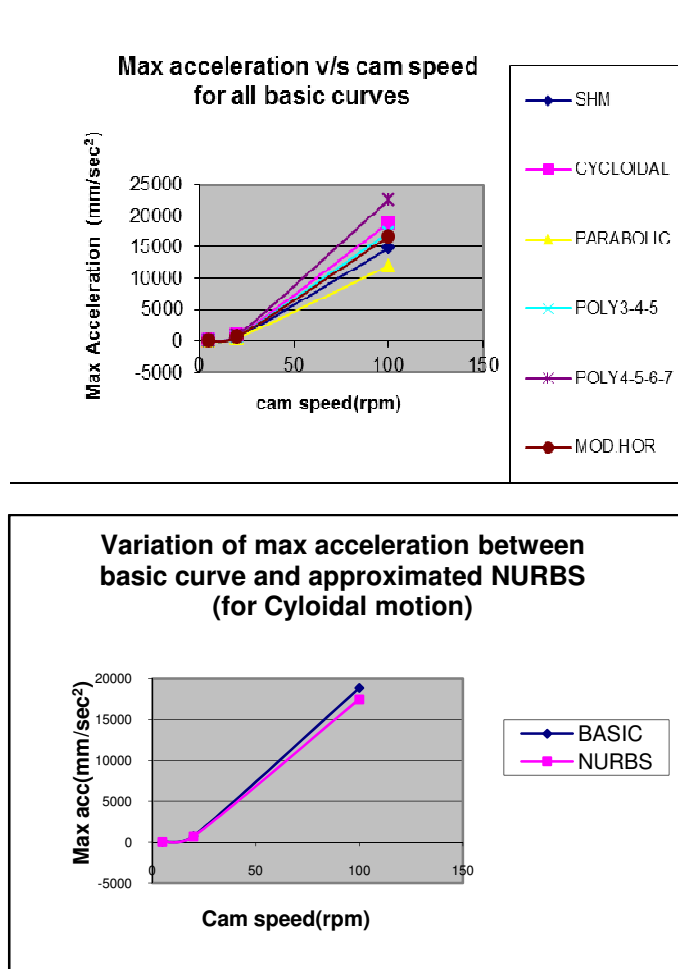


Figure 5: Graphs showing variation maximum acceleration between basic and approximated NURBS (for cycloidal motion) against cam speed.

REFERENCES

1. P. W. Jensen, Cam Design and Manufacture, 2nd Edition, Marcel Dekker Inc, New York: 1987, pp. 35-45.
2. M.E. Mortenson, Geometric Modeling, John Wiley & Sons, New York: 1985, pp.77-85.

3. H.A. Rothbart, *Cams- Design, Dynamics, and Accuracy*, John Wiley & Sons, New York: 1956, pp. 37-45.
4. F.Y. Chen, A Refined Algorithm for Finite Difference Synthesis of Cam Profiles, *Journal of Mechanism and Machine Theory*, 1972: Vol. 7, pp. 453-460.
5. F.Y. Chen, Analysis and Design of Cam-Driven Mechanisms with Nonlinearities, *ADME Journal of Engineering for Industry*, 1973: Vol. 95, pp. 685-694.
6. S.G. Dhande, B.S. Bhadoria, and J. Chakraborty, A Unified Approach to the Analytical Design of Three Dimensional Cam Mechanisms, *ASME Journal of Engineering for Industry*, 1975: 97B (1), pp. 327-333.
7. D.M. Tsay, and C.O. Huey Jr., Synthesis and Analysis of Cam-follower systems with two degrees of freedom, *Journal of ASME advances in Design Automation*, 1989: Vol. 3, pp 281-288.
8. K Sadek, and A. Daadbin, Improved Cam Profiles for High-Speed Machinery Using Polynomial Curve Fitting, *Journal of Process Mechanical Engineering*, 1990: 204, pp. 127-132.
9. M. Yang, and C. Kim, A CAD/CAM System for Precision Cams with Three CNC Interpolation Methods, *International Journal of Advanced Manufacturing Technology*, 1994: Vol. 9, pp. 87-92.
10. Chan, and S. Sim, Optimum Cam Design, *International Journal of Computer Applications in Technology*, 1996: pp. 34-47.
11. W.H. Wang, and C.H. Tseng, and C.B. Tsay, Surface Contact Analysis for a Spatial Cam Mechanism, *ASME Journal of Mechanical Design*, 1997: Vol. 119, pp. 169-177.
12. S.H. Masood, and A. Lau, A CAD/CAM System for the Machining of Precision Cams using A Half Angle Search Algorithm, *International Journal of Advanced Manufacturing Technology*, 1998: 14(3), pp. 180-184.
13. H.S. Masood, A CAD/CAM System for High Performance Precision Drum Cams, *International Journal of Advanced Manufacturing Technology*, 1999: pp. 32-37.
14. J.H. Kim, K.Y Ahn, and S.H. Kim, Optimal Synthesis of a Spring-Actuated Cam Mechanism using a Cubic Spline”, *Journal of Mechanical Engineering Science*, 2002:Vol. 216, pp. 875-883.
15. N. Sateesh, C.S.P. Rao, and T.A. Janardhan Reddy, Optimization of cam-follower motions using B-Splines, *International Journal for Computer Integrated Manufacturing (IJCIM)*, Publisher: Taylor & Francis, England, 2009: Vol. 22, No. 6, pp. 515-523.
16. Chennakesava R. Alavala, *CAD/CAM: Concepts and Applications*, Prentice hall of India, 2009.
17. Chennakesava R. Alavala, *Computer graphics*, Prentice hall of India, 2009.

HONEYCOMB MECHANICS AND A GENERIC APPROACH FOR ITS MODELING AND ANALYSES

Suvir Kumar^{a,*}, MSY Sivaprasad^a, Manzoor Hussain^b and Praveen Garg^a

^a Research Center Imarat, DRDO , Hyderabad-69

^b Principal, JNTUH College of Engineering Sultanpur

Abstract: Honeycomb sandwich is a major part of spacecraft structures and due to its good stiffness to weight ratio, it can be a good replacements for conventional materials in ground applications. The objective of using a sandwich is to minimize weight without compromising the stiffness or strength. And for that the core material has to be light in weight. One can use either a lighter material like wood as core material or a cellular porous core of heavy materials like plastics and metals. Due to advances in material and manufacturing sector, it is possible to produce cellular metallic cores to be used in sandwiches. Out of many cellular cores, aluminium honeycomb core (hexagonal cells) has been used extensively in space industry. This is a promising material for ground applications also with increasing need of high speed vehicles etc. This study is focused to facilitate the design process by understanding the behaviour of honeycomb under certain load conditions. Honeycomb mechanics is guided by the core mechanics which has orthotropic behaviour. Hence, it is important to understand the honeycomb mechanics before designing honeycomb structure. The complete modelling and analysis approach of a honeycomb structure is presented in this paper.

Keywords: honeycomb, mechanics, equivalent models, analysis

Address all correspondence to: suvir.kumar@rcilab.in

1. INTRODUCTION

The concept of using a weak light core with strong face layers to make sandwich is as old as 1820, then introduced by Delau. The Sandwich structures found its first extensive applications during World War 2. The objective of using a sandwich is to minimize weight without compromising the stiffness or strength. And for that the core material has to be light in weight. One can use either a lighter material like wood as core material or a cellular porous core of heavy materials like plastics and metals. Due to advances in material and manufacturing sector, it is possible to produce cellular metallic cores to be used in sandwiches. Out of many cellular cores, aluminium honeycomb core (hexagonal cells) has been used extensively in space industry. This is a promising material for ground applications also with increasing need of high speed vehicles etc.

This paper discusses the deformation process of honeycomb cells for in & out of plane loads. Then the equivalent properties, also referred as theoretical properties based on mechanics of honeycomb cells are estimated. There are other theories or models available in literature for estimating these properties, namely, sandwich theory, honeycomb plate theory and the equivalent plate theory. These theories are also presented in brief. Two case studies with different geometries (beam and plate) are done considering honeycomb sandwich properties based on different theories for modal analyses.

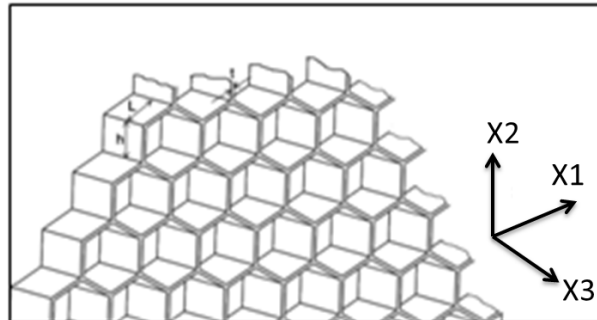


Figure 1: Honeycomb cell structure with axes system

2. HONEYCOMB MECHANICS

To use honeycomb it is necessary to understand the mechanics of core in different loading conditions. Honeycomb core displays different behaviour when loaded in-plane and out of plane. For example, when an elastic-plastic honeycomb (metal) is loaded in X_1X_2 (in-plane) plane in compression, it bends the cell walls. This bending is elastic in nature for small loads. However as the load increases, this bending (strains) tends towards plastic limit. Then at a critical load, plastic yield of walls takes place and further increase in strain causes the cell walls to touch each other. This is also referred as densification of honeycomb cells as the gap between walls is reducing. Now if further load is applied then the resistance to deform will be more due to densification of cells.

In real applications, honeycomb cells are not supposed to deform beyond elastic limit of material. So it is important to have a suitable resistance to bending of cell walls. This resistance can be increased by increasing the relative density or wall thickness of honeycomb.

Now if the loading is in out of plane direction, then honeycomb has better resistance than the in-plane loads. This is because in this case load will try to either compress or extend the cell walls which offer more resistance than bending.

3. HONEYCOMB THEORETICAL MODELING

Honeycomb material properties are calculated in this section using theoretical equations.

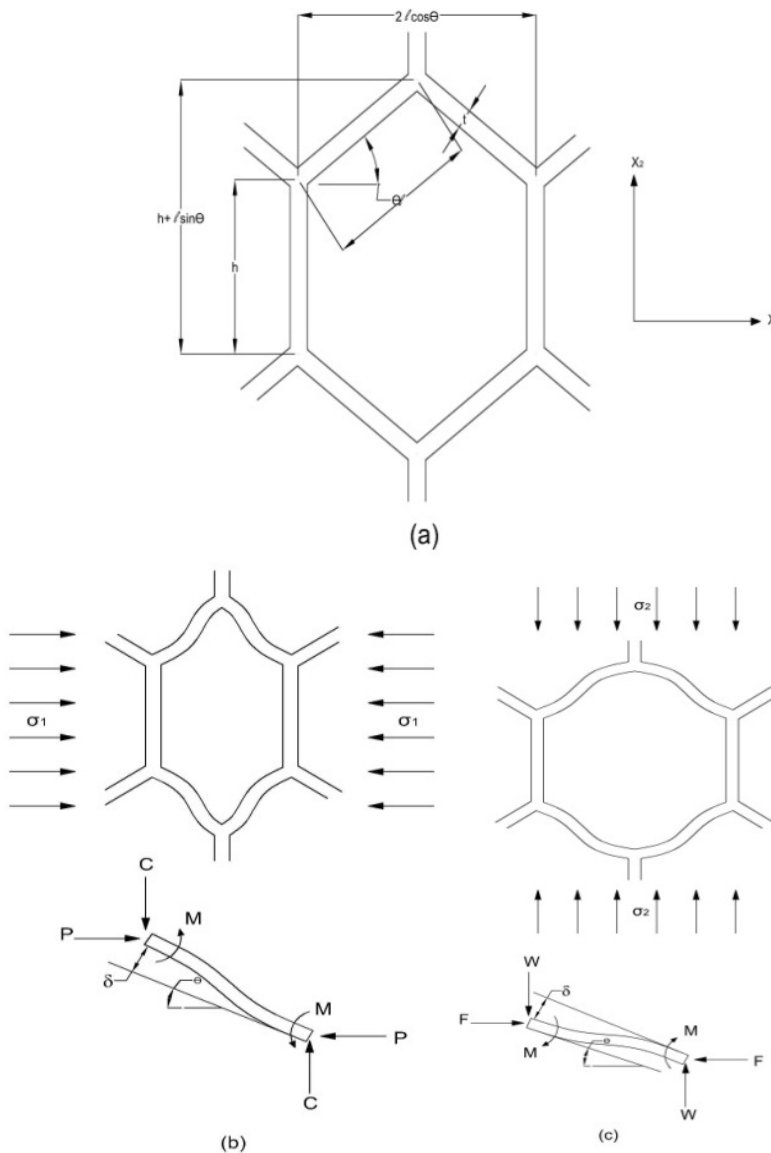


Figure 2: Cell deformation by uniaxial loading

3.1 In-plane Properties of Honeycomb

The in plane properties of honeycomb namely linear elastic constants and Poisson's ratio are to be evaluated. Uniaxial loading is considered for a typical honeycomb model and is shown in Figure 2. The figure shows how the cell walls bend with this load [1].

(a) Linear elastic constants

When a honeycomb is loaded in X_1 and X_2 direction uniaxially, it deforms in a linear elastic way causing the cell walls to bend. A stress σ_1 parallel to X_1 causes one set of cell walls of length l to bend.

The moment bending the cell wall is given by,

$$M = \frac{Pl \sin \theta}{2} \quad (1)$$

Where load, $P = \sigma_1(h + l \sin \theta)b$

From standard beam theory, the wall deflections are given by

$$\delta = \frac{Pl^3 \sin \theta}{12 E_s I} \quad (2)$$

$$\text{Second moment of inertia, } I = \frac{bt^3}{12} \quad (3)$$

$\delta \sin \theta$ is parallel to X_1 , the strain is given by

$$\varepsilon_1 = \frac{\delta \sin \theta}{l \cos \theta} = \frac{\sigma_1(h + l \sin \theta)bl^2 \sin^2 \theta}{12 E_s l \cos \theta} \quad (4)$$

Young's moduli parallel to X_1 , $E_1^* = \frac{\sigma_1}{\varepsilon_1}$

$$E_1^* = \left(\frac{t}{l}\right)^3 \times \frac{\cos \theta}{\left[\frac{h}{l} + \sin \theta\right] \sin^2 \theta} E_s \quad (5)$$

Considering loading in the X_2 direction and by equilibrium law, we get,

$$\text{Load } W = \sigma_2 b l \cos \theta \quad (6)$$

$$M = \frac{W l \cos \theta}{2} \quad (7)$$

$$\text{Deflection, } \delta = \frac{W l^3 \cos \theta}{12 E_s I} \quad (8)$$

$$\text{Strain, } \varepsilon_2 = \frac{\delta \cos \theta}{h + l \sin \theta} = \frac{\sigma_2 b l^4 \cos^3 \theta}{12 E_s l (h + l \sin \theta)} \quad (9)$$

Young's module parallel to X_2 , is given by

$$\begin{aligned} E_2^* &= \frac{\sigma_2}{\varepsilon_2} \\ &= \left(\frac{t}{l}\right)^3 \times \frac{\left[\frac{h}{l} + \sin \theta\right]}{\cos^3 \theta} \end{aligned} \quad (10)$$

For a regular hexagon with uniform cell wall thickness, the following relation holds good.

$$\frac{E_1^*}{E_s} = \frac{E_2^*}{E_s} = 2.3$$

$$\left(\frac{t}{l}\right)^3 \quad (11)$$

(b) Poisson's ratio

$$\text{For loading in } X_1 \text{ direction, } \nu_{12}^* = -\frac{\varepsilon_2}{\varepsilon_1} = \frac{\cos^2 \theta}{\left[\frac{h}{l} + \sin \theta\right] \sin \theta} \quad (12)$$

$$\text{For regular hexagon, } \nu_{12}^* = 1 \quad (13)$$

$$\text{For loading in } X_2 \text{ direction, } \nu_{21}^* = -\frac{\varepsilon_1}{\varepsilon_2} = \frac{\left[\frac{h}{l} + \sin \theta\right] \sin \theta}{\cos^2 \theta} \quad (14)$$

$$\text{For regular hexagon, } \nu_{12}^* = 1$$

(b) Shear modulus

The shear modulus is given by

$$\frac{G_{12}^*}{E_s} = \left(\frac{t}{l}\right)^3 \times \frac{\left[\frac{h}{7} + \sin\theta\right]}{\left(\frac{h}{l}\right)^2 \left[1 + \frac{2h}{l}\right] \cos\theta} \quad (15)$$

For a regular hexagon, $G_{12}^* = 0.57 \left(\frac{t}{l}\right)^2 E_s = \frac{1}{4} E^*$

3.2 Out of Plane Properties of Honeycomb

When the honeycomb is loaded along the X_3 direction as shown in Figure 3, the cell walls are extended or compressed and the modulus in this direction is much higher than the in plane module.

The expressions for properties are as given by

$$E_3^* = \frac{\rho^*}{\rho_s} E_s ; \nu_{31} = \nu_{32} = \nu_s ; G_{13} = G_{23} = 0.577 \left(\frac{t}{l}\right) G_s \quad (16)$$

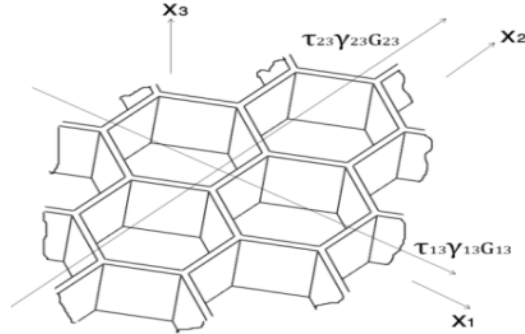


Figure 3: Honeycomb carrying load along X_3

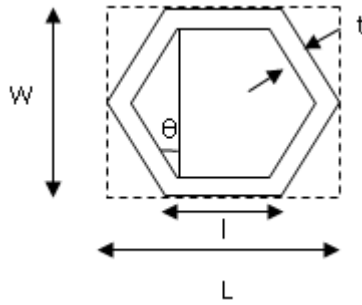


Figure 4: Cell geometry

3.3 Equivalent core density calculation

Equivalent core density is calculated by replacing unit hexagonal cell by rectangle of dimension $L \times W$ as shown in Figure 4. From above figure for a unit depth of hexagonal cell the actual area of unit cell is given by

$$(A_c) = 6lt \quad (17)$$

$$\text{And } L = l(1 + 2\sin\theta) ; W = 2l\cos\theta \quad (18)$$

$$\text{So, area of equivalent rectangle } (A) = L.W = 2l^2 \cos\theta(1 + 2\sin\theta) \quad (19)$$

$$\text{Now, relative density } (\rho^*/\rho_c) = A_c / A = \frac{6tt}{2l^2 \cos\theta(1+2\sin\theta)} \quad (20)$$

For a regular hexagonal cell, $\theta = 30^\circ$,

$$\text{so, } \rho^*/\rho_c = \sqrt{3} \frac{t}{l} \quad (21)$$

Generally datasheets provides cell size (W) and foil thickness (t)

$$\text{So, } \rho^*/\rho_c = 3 \frac{t}{W} \quad (22)$$

4. HONEYCOMB EQUIVALENT MODELS

Modelling of honeycomb requires estimation of various properties in different directions. There are number of equivalent models used for this purpose namely sandwich theory, Honeycomb plate theory and equivalent plate theory [2]. These models are discussed in this section.

4.1 The sandwich theory

This theory models the honeycomb sandwich as 3 layered plate with top and bottom isotropic face sheets and an orthotropic honeycomb core in the middle. To simplify the mathematical model, HC core is modelled as a continuous material but orthotropic in nature which actually is a cellular porous material. For a regular hexagonal honeycomb core, equivalent elastic parameters are given below.

$$E_x = E_y = \frac{4}{\sqrt{3}} \left(\frac{t}{l}\right)^3 E \quad (23)$$

$$G_{xy} = \frac{\sqrt{3}}{2} \gamma \left(\frac{t}{l}\right)^3 E \quad (24)$$

$$G_{xz} = \frac{\gamma}{\sqrt{3}} \frac{t}{l} G G_{yz} = \frac{\sqrt{3}}{2} \gamma \frac{t}{l} E \quad (25)$$

$$\nu_{xy} = 1/3 \quad (26)$$

Where E, G are the engineering constants of core material. γ is an engineering constant whose value is between 0.4 and 0.6.

4.2 The honeycomb plate theory

This theory models the sandwich plate as a single layer homogeneous plate with orthotropic properties. The equivalent properties based on stiffness and inertial equalization are given below.

$$E_x^* = (e_{11} e_{22} - e_{12}^2)/e_{22} \quad (27)$$

$$E_y^* = (e_{11} e_{22} - e_{12}^2)/e_{11} \quad (28)$$

$$G_{xz}^* = e_{44}$$

$$G_{yz}^* = e_{55} G_{xy}^* = e_{66} \nu_{xy}^* = e_{12}/e_{22} \quad (29)$$

where,

$$\begin{aligned}
e_{11} &= \frac{[(h+d)^3-h^3]e_{f11}+h^3e_{c11}}{(h+d)^3} & e_{22} &= \frac{[(h+d)^3-h^3]e_{f22}+h^3e_{c22}}{(h+d)^3} \\
e_{12} &= \frac{[(h+d)^3-h^3]e_{f12}+h^3e_{c12}}{(h+d)^3} & e_{44} &= \frac{d}{h+d}e_{f44} + \frac{h}{h+d}e_{c44} \\
e_{55} &= \frac{d}{h+d}e_{f55} + \frac{h}{h+d}e_{c55} & e_{66} &= \frac{[(h+d)^3-h^3]e_{f66}+h^3e_{c66}}{(h+d)^3} \\
\rho &= \frac{d\rho_f+h\rho_c}{h+d} \\
e_{c11} &= e_{c22} = \frac{1}{1-\vartheta_{xy}^2}E_x e_{c12} = \frac{\vartheta_{xy}}{1-\vartheta_{xy}^2}E_x \\
e_{c44} &= e_{c55} = G_{xz} = G_{yz}e_{c66} = G_{xy} \\
e_{f11} &= e_{f22} = \frac{1}{1-\vartheta^2}E e_{f12} = \frac{\vartheta}{1-\vartheta^2}E & e_{f44} &= e_{f55} = KGe_{f66} = G
\end{aligned}$$

Where ϑ is Poisson ratio of the facesheets, d is thickness of facesheets, h is one half of core thickness.

4.3 Equivalent Plate Theory

This theory models the HC sandwich plate as an equivalent homogeneous isotropic plate. Let total thickness of HC sandwich plate be $2H$, and facesheet thickness be t , elastic modulus of facesheet be E and Poisson ratio be ν .

$$\text{Bending stiffness of equivalent plate} = \frac{E_{eq}t_{eq}^3}{12(1-\vartheta^2)} \quad (30)$$

$$\text{Bending stiffness of HC sandwich plate} = \frac{2E}{(1-\vartheta^2)} \left(\frac{t^2}{12} + \left(H - \frac{t}{2} \right)^2 t \right) \quad (31)$$

It can be deduced from equivalence of axial stiffness between the HC sandwich plate and equivalent plate to get the following relation

$$E_{eq}t_{eq} = 2Et \quad (32)$$

Equating (30) and (31) and solving with (32):

$$t_{eq} = \sqrt{(t^2 + 12h^2)}E_{eq} = \frac{2Et}{t_{eq}} \quad (33)$$

Where $h = H - t/2$

$$\text{From mass equivalence } \rho_{eq}t_{eq} = 2\rho_f t + 2\rho_c(H - t) \quad (34)$$

Here ρ_f is facesheet density and ρ_c is core density. Therefore

$$\rho_{eq} = \frac{2\rho_f t + 2\rho_c(H - t)}{t_{eq}} \quad (35)$$

5. EQUIVALENT PROPERTY CALCULATION

3/16-.0007-Al5056 is considered as the material for this study. Core and face sheet thickness are 40 mm and 0.25 mm respectively. All the Properties of Honeycomb are estimated using different theories mentioned above. The properties are calculated and presented in Table 1.

Table 1: Physical Properties for different theories

Properties	Theoretical equations	Sandwich theory	Honeycomb plate theory	Equivalent Plate theory
E_x (MPa)	4.29 E-2	4.29 E-2	2524	$E_{eq} = 495$
E_y (MPa)	4.29 E-2	4.29 E-2	2524	
E_z (MPa)	772			
G_{xy} (MPa)	1.07E-2	8.08E-3	948	
G_{yz} (MPa)	99	74.3	258	
G_{xz} (MPa)	99	49.5	258	
ν_{xy}	1	0.33	0.33	$\nu = 0.33$
ν_{yz}	0.33			
ν_{xz}	0.33			
density	32		64.94	36.71
Thickness	40			69.70

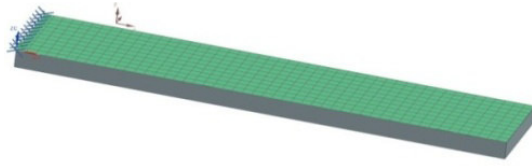
6. CASE STUDIES

A comparative study of honeycomb beam and plate for a given configuration is carried out using various theories as discussed in the previous sections. The analysis results are discussed and compared in this section.

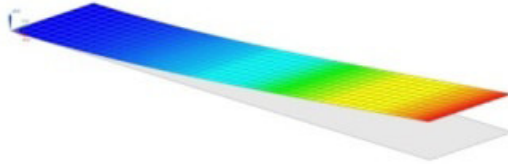
6.1 Case Study with Honeycomb Beam

A honeycomb beam of 1000 mm x 200 mm x 40.5 mm is considered for this case study. The top and bottom facesheet thickness is 0.25mm and core thickness is taken as 40 mm. NX NASTRAN FEA package is used for modal analyses. This beam is modelled as 2-D thin shell with CQUAD4 elements. As earlier discussed there are two types of equivalent approaches, in one it is modelled as 3 layers and in other it is modelled as an equivalent single layer material. Multilayer properties are assigned with help of laminate module in the software and single layer properties are given as PSHELL with appropriate thickness. The beam is fixed at one end. The model is created as per standard FE guidelines. The element size is taken as 20mm after mesh convergence study. Rigid body checks are performed and Modal analysis is carried out to find the different modes of the beam. FE model of HC beam with one end clamped along with the representative mode shapes are shown in Figure 5.

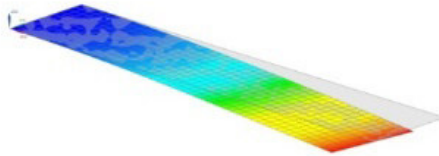
This analyses is performed with all four equivalent models and the results are given in Table 2. As we can see from the table above, the modal frequencies are almost same for the first three modes and it starts varying from the fourth mode except the second modal frequency using honeycomb plate model.



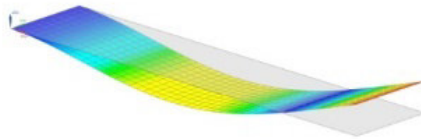
(a). FE model with one end clamped



(b). First mode shape (bending)



(c). Second mode shape (in-plane)

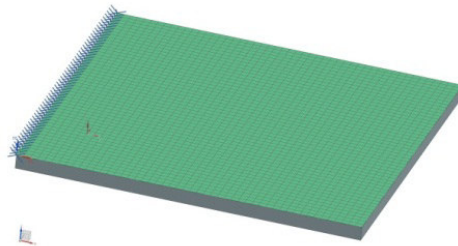


(d). Third mode shape (bending)

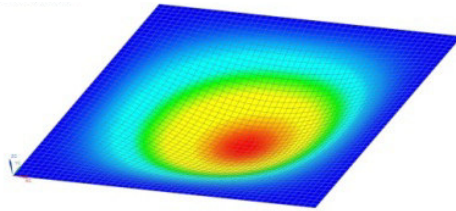
Figure 5: FE model and results for beam

Table 2: Modal frequencies of beam for different equivalent models

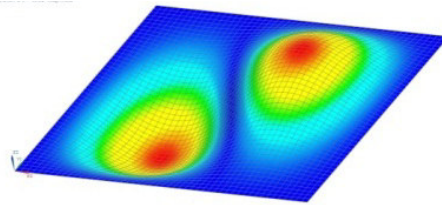
Modes	Theoretical	Sandwich theory	HC plate theory	Equivalent plate theory
1	40.3	40.0	40.9	41.6
2	112.7	112.7	195.9	115.4
3	241.4	229.6	251.1	255.9
4	308.9	271.8	343.6	355.5
5	607.6	574.2	680.5	622



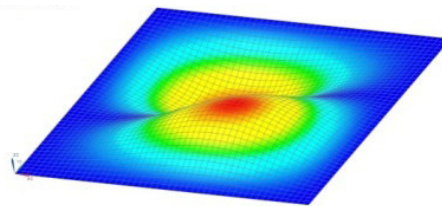
(a). FE model with all ends clamped



(b). First mode shape



(c). Second mode shape



(d). Third mode shape

Figure 6: FE model and results for plate

6.2 Case Study with Honeycomb Plate

A honeycomb plate of 1000 mm x 1000 mm x 40.5 mm is considered for this case study. The top and bottom facesheet thickness is 0.25mm and core thickness is taken as 40 mm. FE model is prepared as similar to beam. The plate is considered to be clamped on all 4 sides. Figure 6

below shows the FE model and representative mode shapes of considered plate.

This analysis is also performed with all four equivalent properties and the results are given in Table 3.

Table 3: Modal frequencies of plate for different equivalent models

Modes	Equivalent models			
	Theoretical	Sandwich theory	HC plate theory	Equivalent plate theory
1	386.8	362.8	415.2	425.7
2	730.9	647.3	812.4	838.6
3	730.9	683.9	812.4	838.6
4	1018	913.1	1157	1200
5	1195	1016	1380	1437

The modal frequencies variation for different models is more than the case of beam. It is seen that three layered models predict lesser values than the single layered plate models. Experimental data shall be generated for validating the above results.

7. CONCLUSION

This article discussed the mechanics and behavior of honeycomb core in different loadings and estimated the equivalent physical properties of core based on its mechanics (also referred as theoretical properties). These properties are used to analyze complex behavior of honeycomb core by taking an equivalent solid block of same volume roughly. As presented earlier, there are different theories available in literature which also gives these equivalent properties, namely, sandwich theory, Honeycomb plate theory and the equivalent plate theory. In this study, two case studies are performed with equivalent properties estimated from these four theories. It is observed that modal analyses results were in better agreement in case of beam than the plate for different theories. In case of plate, 3-layered theories predicted lower values of natural frequency than the single layer theories. One shall be cautious while selecting the appropriate theory for design. Properties based on mechanics as discussed earlier can be used to model a three layered sandwich panel. However, honeycomb plate theory can be preferred in case of limited computational and FEA resources. Although it is suggested to perform experiments or use existing data to validate these theories.

REFERENCES

1. L.J. Gibson, Michael F. Ashby, Cellular Solids, 2nd edition, pp. 101-105, 148-151.
2. LuoHao, Liu Genget all. Dynamic Analysis of the spacecraft structure on orbit made up of Honeycomb sandwich plates. Computer science and Automation engineering (CSAE), 2011 IEEE.

MESH INDEPENDENCE AND CONVERGENCE TEST IN THE OIL FILM CHARACTERISTICS OF A TILTING PAD THRUST BEARING

D.V.Srikanth^a, K.K.Chaturvedi^b and A.Chenna Keshav Reddy^c
^a Associate Professor, Department of Mechanical Engineering, MLRIT,
Hyderabad

^b Retd. Sr. Deputy General Manager, BHEL(R&D), Adhoiwala, Dehradun

^c Professor, Department of Mechanical Engineering, JNTUH CEH,
Hyderabad

Abstract: The objective of this paper is to carry out a mesh independence study and ensure the validity of the load and centre of pressure location for a Tilting Pad Thrust Bearing. The computation is done by numerically solving the two dimensional Reynolds' equation at different nodes of the oil film using a finite difference procedure. It is ensured that the solution satisfies: (a) load obtained by integrating pressure values is within $\pm 5\%$. (b) radial and angular coordinates of centre of pressure viz. R_{cp} and θ_{cp} lie within $\pm 3\%$, and (c) convergence satisfies the $\pm 1\%$ criteria. The aim is to have simulated output values of integrated load, R_{cp} and θ_{cp} converge to steady specified values corresponding to a pressure distribution with maximum nodal pressure of 4.5 MPa. Finally it is to be ensured that overall domain imbalance is less than 1% for all variables. The approach outlined above results in a unique solution for the given mesh that we have used. Although the solution satisfies the convergence based on load and centre of pressure location values, it has to be made sure that the solution is also independent of the mesh resolution. This check is carried out once to determine right sizing & eliminates erroneous results. This analysis improves the validity of the results.

Keywords: Load, pressure, convergence, mesh independence

Address all correspondence to: dvsrikanth1@hotmail.com

1. INTRODUCTION

A thrust bearing is the main component of a hydroelectric installation. The weight of the hydraulic turbine, generator components and the thrust load are all borne by the thrust bearing. The hydroelectric generator rotor moves with low friction and negligible wear. A large sector pad thrust bearing with an outer diameter of over 1 m, provides an important feature. Continuous fluid films are developed over the pad surface. The bearing pads are supported by a pivot or a distributed spring mattress. The support arrangements allow the bearing pad to tilt and produce a favorable geometry for the fluid film formation. Tilting-

pad thrust bearings unlike fixed geometry bearings have the ability to self-adjust the tilt to accommodate varying operating conditions. In equalizing tilting pad thrust bearings the thrust-load distribution over the pads is permitted. In this paper the importance of using numerical methods and digital computers in developing mathematical methods for any practical problem are discussed. Numerical methods are powerful and versatile because they use algebraic equations in the place of differential equations. In this chapter, the finite difference method used for solving the formulated two dimensional Reynolds' equation for the pressure is described. Integration of the nodal pressure values help in the computation of load.

Hydrodynamic principles were used in the design of tilting pad bearings utilized in mechanisms carrying shaft thrust or radial loads. Optimized pivot positions in the radial and circumferential directions of tilting pad thrust and radial bearings were derived by Ni et al [1]. Hsia- Ming Chu [2] used an inverse method to develop an algorithm for designing the optimum shape and pressure distribution of a slider bearing. The algorithm was developed from the Reynolds' integral, force and moment equations. The load and moment conditions were obtained by the algorithm in order to simultaneously estimate the slider bearing shape and pressure distribution.

2. REYNOLDS' EQUATION

The analysis of hydrodynamic thrust bearings for pressure distribution is based on the Reynolds' equation [3]. With the increasing capacity of computers, numerical models including the pad deformation and influences of viscosity variations along and across the lubricant film have been developed. This is derived through an order of dimension analysis from the Navier-Stokes equations. The lowest order terms are retained and introduced in the continuity equation which is then integrated across the fluid film to give the Reynolds' equation. This was first shown by Reynolds' for a fluid with constant properties. Various researchers have since extended the equation along or across the fluid film to include compressibility and variations in fluid properties. Dowson [4] introduced a general extension of the equation to include varying fluid properties both along and across the fluid film [7-10]. The two dimensional equation Reynolds equation is obtained as follows.

$$\begin{aligned} \frac{\partial^2}{\partial R^2} \left[\frac{RH^3 P}{\bar{\mu}} \right] + \frac{RH^3}{\bar{\mu}} \frac{\partial^2 P}{\partial R^2} - P \frac{\partial^2}{\partial R^2} \left[\frac{RH^3}{\bar{\mu}} \right] + \frac{1}{R\beta^2} \frac{\partial^2}{\partial \theta^2} \left[\frac{H^3 P}{\bar{\mu}} \right] \\ + \frac{1}{R\beta^2} \frac{H^3}{\bar{\mu}} \frac{\partial^2 p}{\partial \theta^2} - \frac{P}{R\beta^2} \frac{\partial^2}{\partial \theta^2} \left[\frac{H^3}{\bar{\mu}} \right] = 12R \frac{\partial H}{\partial \theta} + 24R\beta \frac{\partial H}{\partial t} \end{aligned} \quad (1)$$

3. COMPUTATIONAL PROCEDURE

Solution of Reynold's equation using FDM discretization of thrust pad is done by considering a total of 81 nodes in the form of a grid. The Reynold's equation is a non-homogeneous partial differential equation

of two variables for which closed form analytical solutions are not available. The use of finite difference methods for a numerical approximation of this type of partial differential equation was discussed in Capitao [5].

The Finite difference equation is derived by approximating the derivatives in the differential equation via the truncated Taylor series expansion for three successive grid points. The central difference form where in the values of the function at adjacent nodes on either side are required to evaluate the derivatives is used. Writing the Reynold's equation in the above finite difference form results in a set of linear algebraic equations which can be transformed into matrix form and solved simultaneously by available subroutines. This yields the non-dimensional pressure at each node. The computational procedure uses these calculated pressures along with numerical methods for integration to obtain the load capacity, radial and angular location of centre of pressure. To ensure numerical accuracy the pressure distribution satisfied the 0.1 percent convergence limit.

4. RESULTS AND DISCUSSIONS

The mesh independence and convergence test is done taking into consideration the values of load, R_{cp} and θ_{cp} for three different mesh models. The mesh independence study is straight forward and done as follows:

1. The initial simulation is run with 11×11 nodal mesh as in figure 1 and the load, R_{cp} and θ_{cp} values are found to be $2.037e^6$, 1.0571 m and 0.2625 radians. The corresponding pressure distribution is given in figure 2.
2. As the above values in step 1 have not converged to required ones, we refine the mesh taking a 10×10 nodal matrix as in figure 3. The values obtained for load, R_{cp} and θ_{cp} are $2.0957e6$, 1.0565m and 0.2603 radians. The corresponding pressure distribution is shown in figure 4.
3. These are not the same as obtained for the 11×11 mesh and have also not converged to our prescribed values. This shows that the solution is changing because of the mesh resolution and hence it is not yet independent of the mesh. The mesh is refined further to a 9×9 nodal matrix as in figure 5. which yields values of load, R_{cp} and θ_{cp} of $2.1663e^6$, 1.0557 m and 0.2575 radians. These converge within $\pm 1\%$ of our earlier prescribed values for 4.5 MPa maximum nodal pressure distribution shown in figure 6. This gives the mesh independent solution and is obtained by using the smallest mesh that reduces the simulation time.

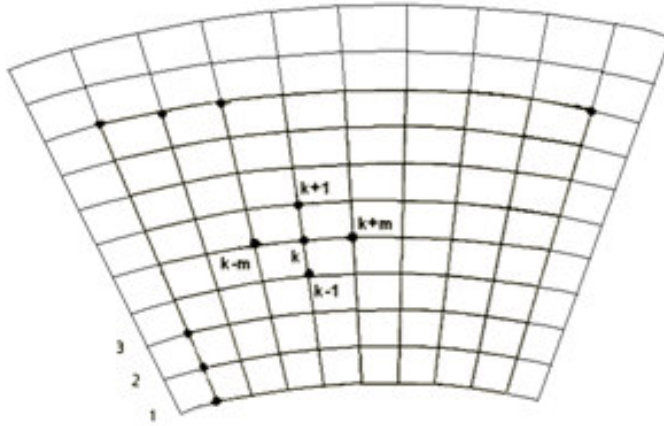


Figure 1: Discretization of pad for Reynold's equation 11×11 matrix

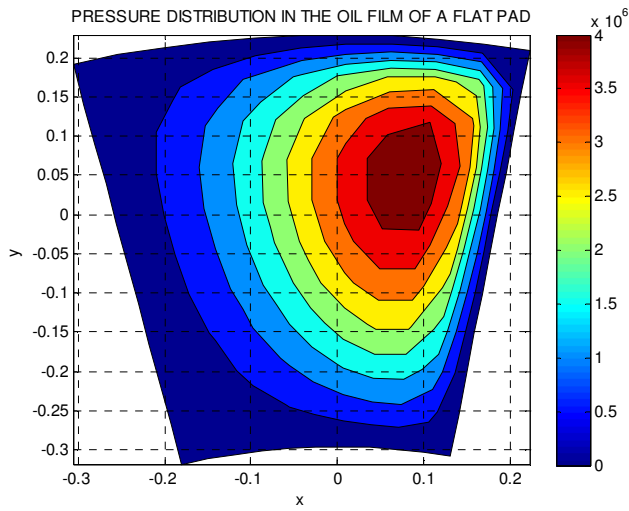


Figure 2: Pressure distribution for 11×11 nodal matrix mesh

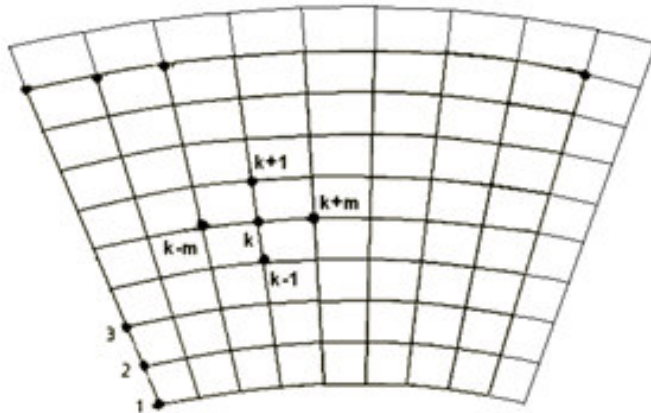


Figure 3: Discretization of pad for Reynold's equation 10×10 matrix

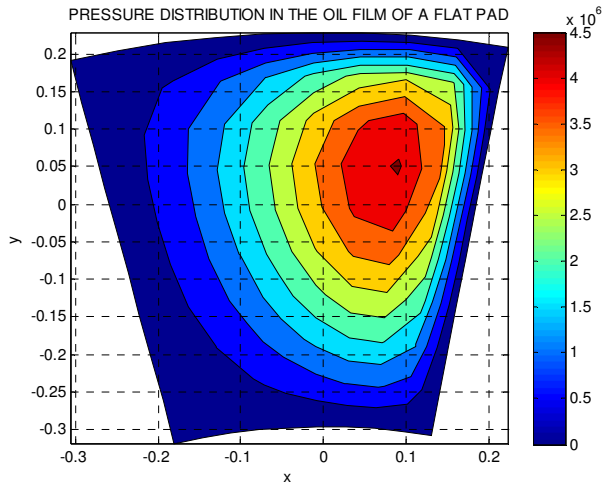


Figure 4: Pressure distribution for 10×10 nodal matrix mesh

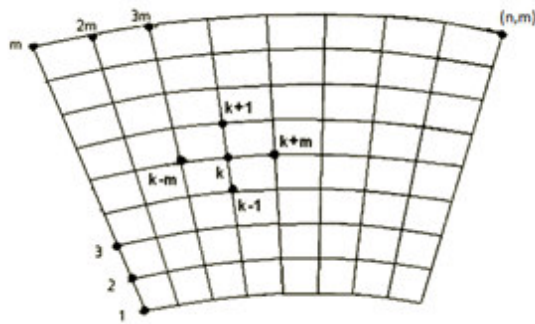


Figure 5: Discretization of pad for Reynolds' equation 9×9 matrix

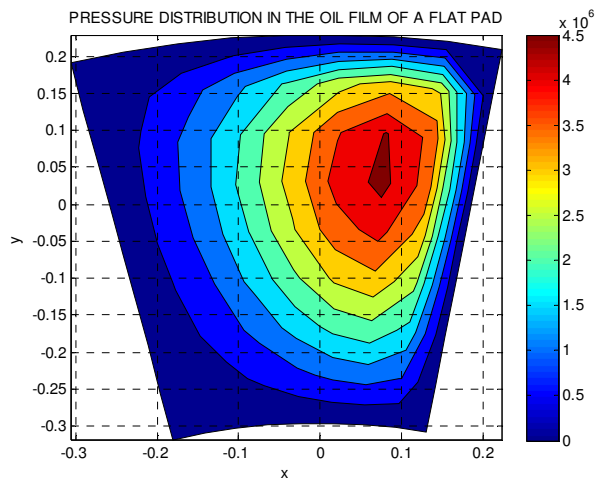


Figure 6: Pressure distribution for 9×9 nodal matrix mesh.

5. CONCLUSION

For a given mesh the convergence ensured that the simulation values of interest viz. steady pressure that were monitored matched the values that were set prior to starting the simulation. In addition the mesh independence test ensured that the results obtained are due to the boundary conditions and physics used and not the mesh resolution. The mesh independent solution corresponds to the smallest mesh size with 81 nodes and that which reduces simulation run time. This confidently proves the validity of our results and theoretical model.

REFERENCES

1. W. Ni, C. Griffiths, D. Bartholme, and R. Hergert, Two Dimensional Analytical Analysis of Fluid Film Thickness on Pivoted Tilting Pad Bearings, Conference and Exhibition, Powertran and Fluid systems, Chicago, IL , USA, October, 2007.
2. H. M., Chu, Shape Optimum Design of Slider Bearings using Inverse Methods, Tribology International , 2007: 40, pp. 906-914.
3. O. Reynolds, On the Theory of Lubrication and its application to Mr. Beauchamp Tower's Experiments including an Experimental Determination of the Viscosity of Olive oil, Philosophical Transactions Royal Society, 1886: 177, pp. 155-234.
4. D. Dowson, A Generalised Reynolds' Equation for Fluid Film Lubrication, International Journal of Mechanical Science, 1962: 4, pp.159-170.
5. J. W. Capitaio, Influence of Turbulence on Performance Characteristics of the Tilting Pad Thrust Bearing, Transactions of the ASME, Journal of Lubrication Technology, 1974: January, pp.110-117.
6. Chennakesava R Alavala, Finite Element Methods: Basic Concepts and Applications, PHI Learning Private Limited, New Delhi, 2009.
7. D.V. Srikanth, K.K. Chaturvedi, A. Chennakesava Reddy, Predictions of Performance Characteristics in a large Tilting Pad Thrust Bearing, Journal of Tribology and Surface Engineering, 2010: 1(1&2), pp. 21-28.
8. D.V. Srikanth, K.K. Chaturvedi, A. Chennakesava Reddy, Determination of a large tilting pad thrust bearing angular stiffness, Tribology International, 2012: 47(1), pp. 69-76.
9. D.V. Srikanth, K.K. Chaturvedi, A. Chennakesava Reddy, Determination of Pad Thickness in a Large Thrust Bearing , Journal of Tribology and Surface Engineering, 2012: 3(1&2), pp.67-86.
10. D.V. Srikanth, K.K. Chaturvedi, A. Chennakesava Reddy, Variation of tilting stiffness with pad deformation in a large thrust bearing, Journal of Tribology Research, 2011 2(1), pp. 21-38.

FINITE VOLUME ANALYSIS OF TWO-STAGE FORGING PROCESS FOR ALUMINIUM 7075 ALLOY

M. Vidya Sagar^a and A. Chennakesava Reddy^b

^aAssociate Professor, Department of Mechanical Engineering, JNTUH College of Engineering, Hyderabad - 50085

^bProfessor, Department of Mechanical Engineering, JNTUH College of Engineering, Hyderabad - 50085

Abstract: Two-stage (upsetting and finish operations) forging has been carried out using finite volume process. It was observed that the maximum stresses are greater in finish operation than those in upsetting operation. It was also concluded that the maximum die force increases as the initial temperature of the billet decreases.

Keywords: forging, upsetting, aluminium 7075 alloy, finite volume analysis.

Address all correspondence to:

1. INTRODUCTION

Forging is a plastic deformation process. In forging, simple billet geometry is transformed into a complex geometry by applying required pressure on material with the aid of forging machines such as hammers and presses.

In open die forging, at least one of the workpiece surfaces deforms freely. Open die forgings can be made with repeated blows in an open die, where the operator controls the workpiece in the die. During the forming process, as the height of the workpiece is decreased, cross-section area is increased by the rule of material volume conservation [1]. In closed die forging operations, flash, the excess material to the outside of the dies may occur and high tool stresses are generated [2].

In hot forging process, billet is heated above its recrystallization temperature. Greater deformation is attained, die wear is reduced and dimensional accuracy is low in hot forging process. In warm forging process, billet is heated to a temperature which is between its recrystallization temperature and work hardening temperatures. Warm forging process provides products with better dimensional tolerances than hot forging process although forging loads and die wear is greater. On the other hand, in cold forging process, billet is forged usually at the room temperature. Cold forging improves mechanical properties and greater dimensional accuracy is achieved. However, higher force is necessary in cold forging process [3].

The usage of process simulation programs is common for research and development of forging processes. By using this type of programs, forging tool designer could decrease costs by improving achievable tolerances, increasing tool life, predicting and preventing flow defects, and predicting part properties [4].

2. GEOMETRIC MODELING

Finite volume method is a simulation method in which the grid points are fixed in space and the elements are simply partitions of the space defined by connected grid points. The finite volume mesh is a fixed frame of reference. The material of a billet under analysis moves through the finite-volume mesh; the mass, momentum, and energy of the material are transported from element to element. The finite-volume solver, therefore, calculates the motion of material through elements of constant volume, and therefore no remeshing is required. The most common finite volume software used in forging is MSC SuperForge to predict to forging variables [5].

3-D modeling of the part and dies has been realized by using PRO/ENGINEER Wildfire 3.0 [6]. In the simulation process, aluminum forging in different temperatures for the modeled part has been investigated and proper forging stages have been defined to fill the forging dies without any defects by using finite volume method (FVM) with sfForming 8.0 module of Simufact 3.0 [7]. The technical drawing of forging die is given in figure 1 and its 3-D model is given in figure 2.

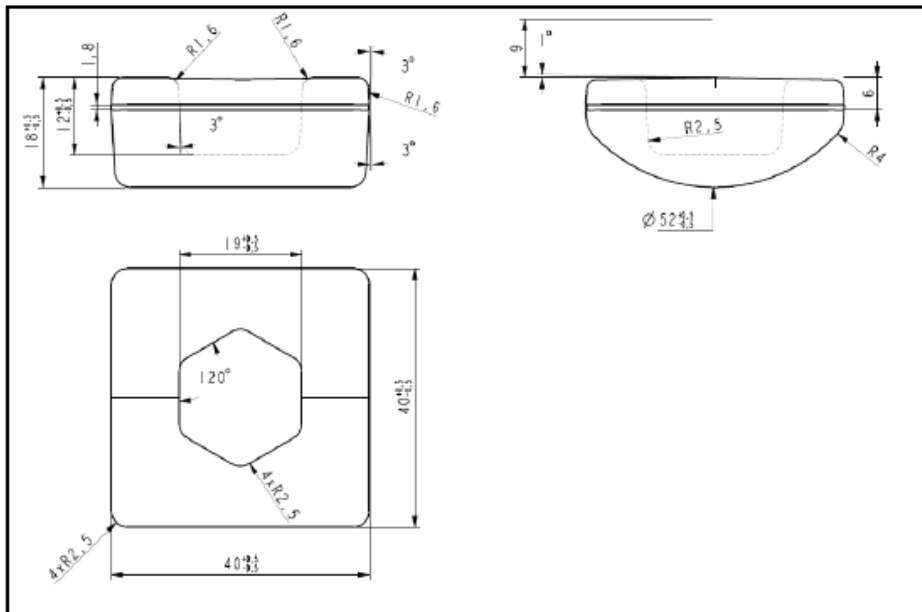


Figure 1: Part drawing

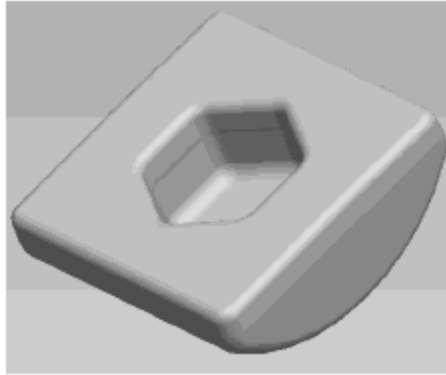


Figure 2: Solid modeling of the forging

The parting line is located at the 5.1 mm from the top of the forging part as shown in figure 3 since parting line is always located along the largest cross-section.

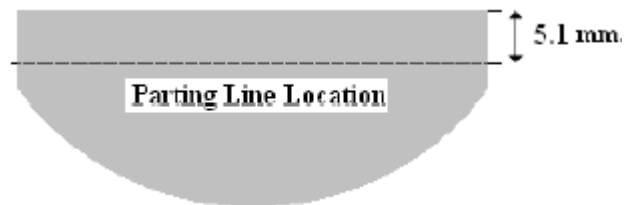


Figure 3: Parting line location on the forged part

The flash thickness is defined for the plan area of the forging. Plan area, at square cross-section of the part along the parting line, is calculated as 1600 mm^2 since one edge of the square is 40 mm. The minimum recommended flash thickness for the plan area less than 6500 mm^2 is given as 0.8 mm for aluminum forging alloys. However, the flash thickness, i.e. the face clearance between upper and lower die, is taken as 1.8 mm by considering an additional 1 mm for the safety of the forging operation to avoid any clash of the upper and lower dies as can be shown in Figure 4.

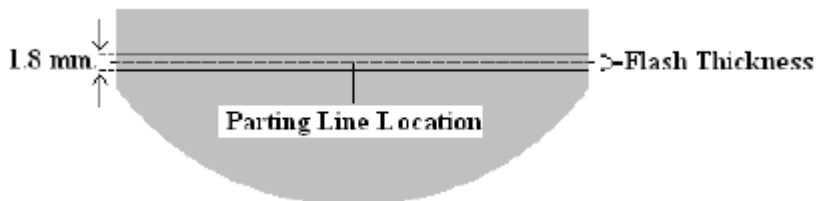


Figure 4: Flash thickness on the forged part

After defining location of the parting line and value of the flash thickness, the draft angles of 3° are applied to the outer surface of the part and to hexagonal hole on the part. A bottom draft of 1° is provided for the upper surface of the part to prevent the sticking the part to the

upper die at the bottom of stroke and to remove the part easily. The application of draft is shown in figure 5.

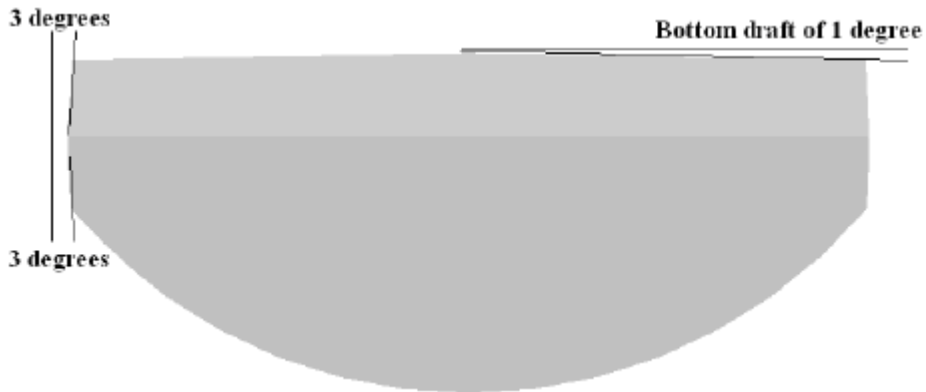


Figure 5: Draft angle on the forged part

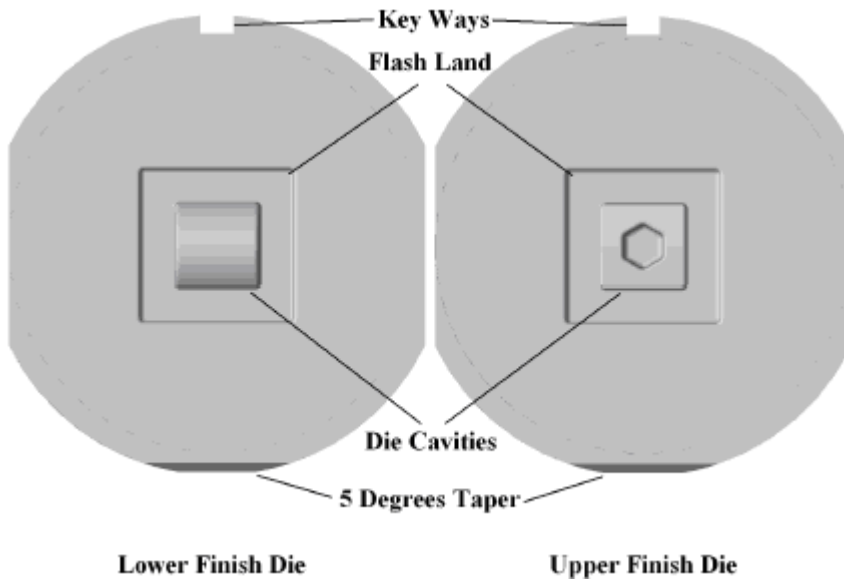


Figure 6: Lower and upper finish dies

According to the constraints of the die holder, the upper and the lower dies in the finish stage are designed based on the designed part geometry. In design of the upper and lower dies, a shrinkage allowance of 1.5 % is taken since some shrinkage occurs after the forged part cools. Total height of the upper and lower die is 200 mm by considering the flash thickness when the press is at the bottom dead center. The dies are designed by considering 99.1 mm in height and by adding flash thicknesses of 1.8 mm, the total height of the dies becomes 200 mm. As seen in figure 6, the flash land is provided at the circumference of the die cavity. Since the die housing at the middle is going to be used for

the finish stage, the upper and lower finish dies will have an external diameter of 222 mm. The key ways are also modeled with 16 mm in width and 9 mm in depth to prevent the rotational motion of the dies relative to the die holder. The gutter is not designed since it is not used in the finish die.

2.1 Definition of Process

Process type may be selected as "open die" or "closed die" forging. After selecting process type, it should be noted that forging process is "hot forging", simulation is 3-D and the used solver is finite volume. The models of upper and lower die geometries from CAD program are imported to the finite volume program in "stl" (i.e. stereo lithography) format after the process type is defined. The billet dimension is selected according to part volume with considering flash volume as given in table 1. By using the mass properties module of CAD program, the part volume is found as 20657 mm³.

Table 1: Geometry and dimensions of billet

Geometry of billet	Dimensions of billet
Cylindrical	30 mm in diameter 32 mm in height

2.2 Assignment of Material Properties

The dies are considered as rigid die with heat conduction. 7075 aluminum alloy is chosen because this material is extensively used in aerospace, automotive and defense industry with its high strength, low density, and low cost. The flow stress-strain relation for hot forging temperatures is given by

$$\text{Flow stress, } \sigma_f = C(\dot{\epsilon})^m \quad (1)$$

where, C is the yield constant

$\dot{\epsilon}$ is the strain rate

m is the strain rate hardening component.

Tensile yield strength 7075 aluminium alloy is $\sigma_t = 103$ MPa and Ultimate tensile strength is $\sigma_{uts} = 228$ MPa at room temperature. Poisson's ratio is 0.33. Density is 2800 kg per m³. Thermal conductivity is 172 Watt/ m-°K. Specific heat is 960 Joule/ kg-°K. Coefficient of thermal expansion is 2.50x10⁻⁵. Solidus temperature is 476 °C and melting temperature is 635 °C.

2.3 Initial Temperature of Billet and Dies

Initial temperatures of the billet are taken as 375 °C, 400 °C, 425 °C and simulation is made for these temperature values. Initial temperature of the dies is assumed as 200 °C. other parameters used in this work are given below:

Room temperature = 25 °C,

Emissivity = 0.25,
 Ambient heat transfer coefficient = 50 Wt/ m²-⁰K, and
 Workpiece heat transfer coefficient = 600 Wt/ m²-⁰K

2.4 Coefficient of Friction

Friction between die and billet is an important consideration in a metal forming process. Such friction produces a tangential (shear) force at the interface between die and billet which restricts movement of the material and results in increased energy and press forces. The magnitude of the shear friction stress influences the deformation pattern, temperature rise, the tool deflection and total force in metal forming. In this study, plastic shear friction is used with a coefficient of 0.2 since high loads are applied in forging operations.

2.5 Definition of Press

Schematic illustration of the crank press is shown in figure 7. Crank radius of the press is 110 mm; rod length is 750 mm; and speed of revolution is 100 rpm.

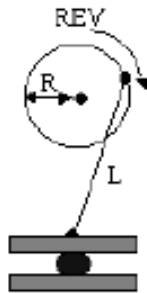


Figure 7: Schematic representation of crank press.

4.4.6 Finite Volume Meshing

Element size in finite volume program should be assigned for the billet. Billet element size is 1 mm. number of output divisions are 21. The finite volume ratio is 0.2. The stroke length depends on billet dimension.

5. FORGING PROCESS BY FINITE VOLUME METHOD

Different finite volume simulations are made to ensure to proper forging operation without any defects. Forging operation is firstly thought as single operation and analysis are made for the single operation.

The billet is placed on the upsetting die at the horizontal position and the upsetting operation is applied and then the finish forging operation is performed in the finish die. Position of the billet on the upsetting die and the finish die are shown in figure 8. In this orientation, the billet is upset to 18.5 mm in height and width of the part in x-direction becomes 37.4 mm and width of the part in y-direction becomes 38.5 mm as shown in Figure 9.

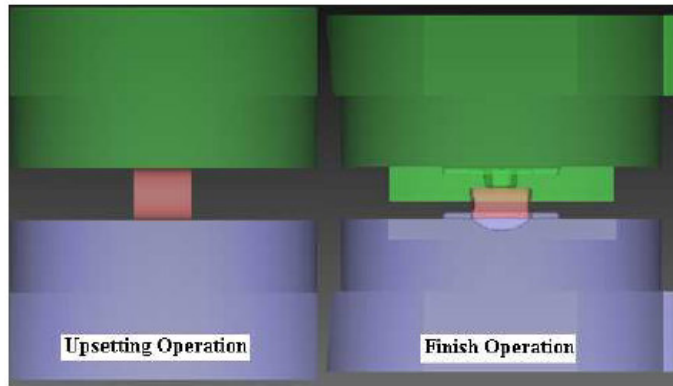


Figure 8: Position of billet on the upsetting die and finish die.

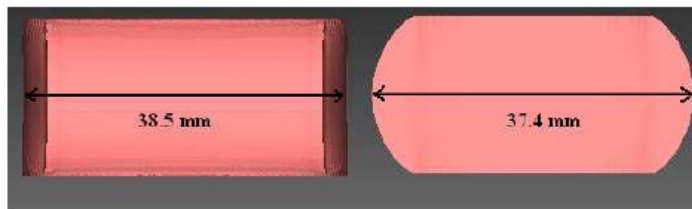


Figure 9: Dimensions of billet after forging operation.

The die is completely filled in the finish operation as seen in figure 10 and the flash distribution is more uniform. No fold is observed during the forging operation.

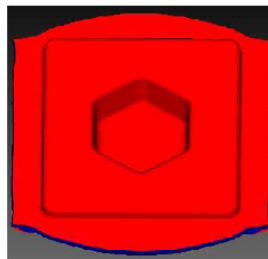


Figure 10: Die filling during forging operation.

6. RESULTS AND DISCUSSION

In the finite volume analysis, 25512 finite volume elements are created for the upsetting operation while 24997 finite volume elements are created for the finish operation and the simulation time is measured nearly 3 hours 15 minutes for the upsetting operation while the simulation time is nearly 2 hours for the finish operations for a workstation with 10 GHz processor and 100 GB RAM.

After finite volume simulation of the forging operation, the force requirement, stress values and part temperature after the upsetting and the finish forging operations can be obtained by the finite volume

program. As stated previously, the simulations have been made for the forging temperatures of 375 °C, 400 °C and 425 °C and simulation results are given in Table 2.

Table 2: Maximum die force and stress for forging of 7075 Al-alloy

Temperature of billet (°C)	Die force for upsetting (Ton)	Die force for finish (Ton)	Maximum stress for upsetting (MPa)	Maximum stress for finish (MPa)
375	7.5	32.0	101.2	110.0
400	7.4	29.1	99.8	108.4
425	6.3	26.2	87.6	95.2

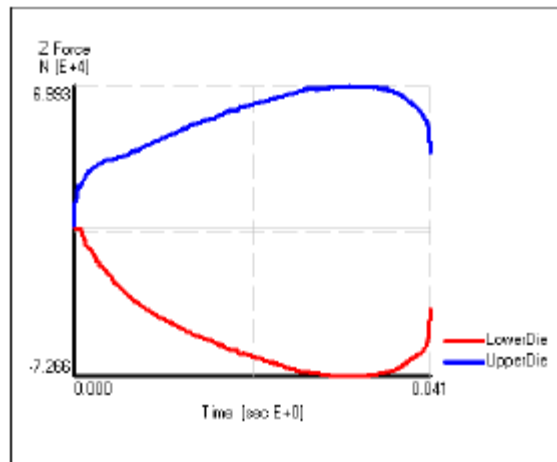


Figure 11: Die force for upsetting operation.

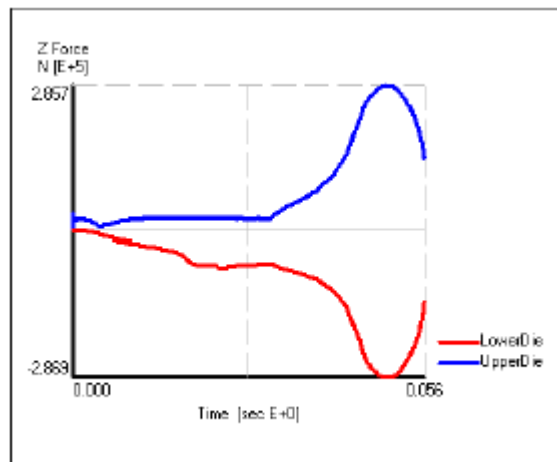


Figure 12: Die force for finish operation.

In the die force diagrams, the force is given as a function of time as shown in figure 11. The force increases almost linearly for the upsetting

operation. The force slightly increases initially for the finish operation as revealed in figure 12. At the beginning of the finish operation upsetting occurs and later the force increases dramatically and reaches the maximum value to complete the forming.

The maximum stress distributions are shown in figures 13 and 14 for upsetting and finish operations. The red color represents the highest stress value and the blue the lowest value. The maximum stress occurs in the loading regions where the lower and the upper die contact with the workpiece at first time. The maximum stress values are relatively higher in finish operation since deformation is much more in finish operation.

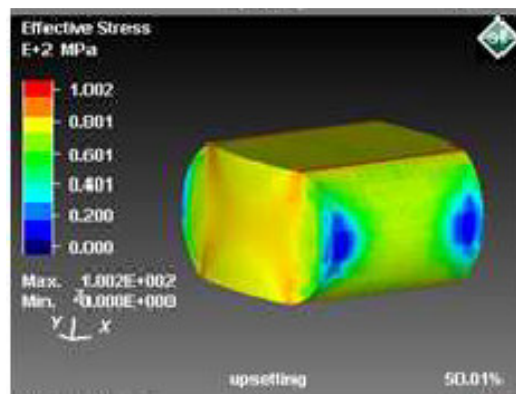


Figure 13: Maximum stress distribution for the upsetting operation at 400 °C

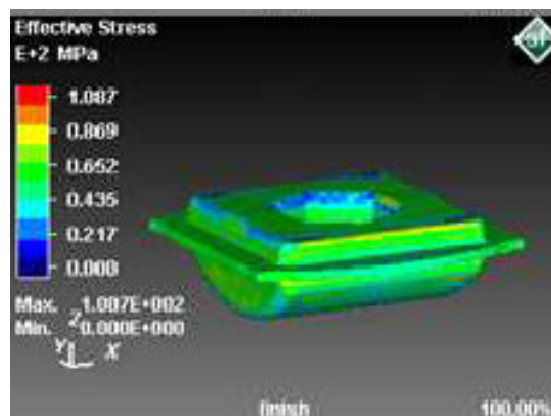


Figure 14: Maximum stress distribution for the finish operation at 400 °C

The temperature distributions are shown figures 15 and 16 for upsetting and finish operations. It is seen that the maximum temperature occurs at the zones where the maximum deformation happens throughout the forging operation. The temperature values at

the end of the upsetting process are directly transferred to the finish operation.

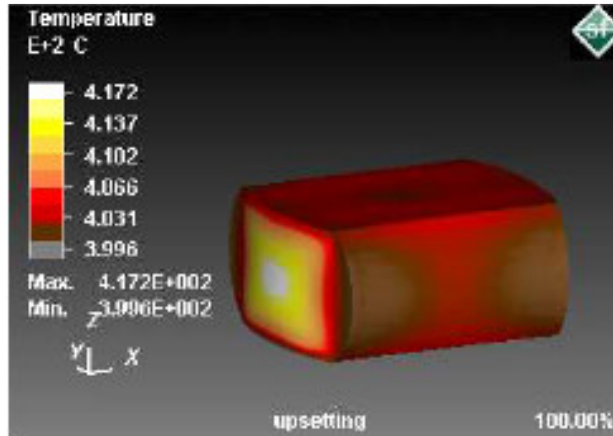


Figure 15: Temperature distribution for upsetting operation at 400 °C

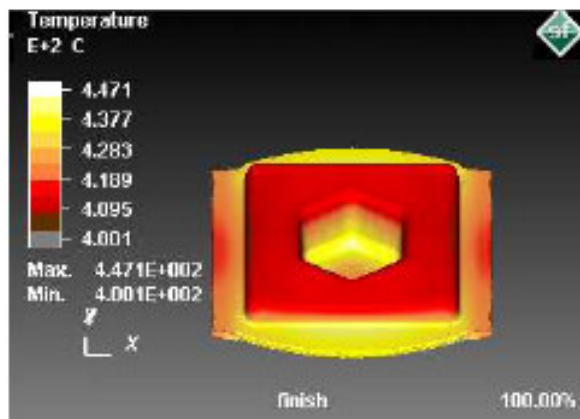


Figure 16: Temperature distribution for finish operation of at 400 °C

The stress on the workpiece decreases as the initial temperature of the billet increases. The maximum stress occurs during the initial contact of the lower and the upper die with the workpiece. The maximum die force increases as the initial temperature of the billet decreases. The die forces slightly increase at the beginning of the finish forging and then the die forces increases rapidly to fill the die cavity completely.

The workpiece temperatures increase during the upsetting and finish forging operations and the maximum temperatures occur at the zones where the deformation on the part is high. The temperature rise is much higher in low forging temperatures which can be attributed to close die and billet temperatures at the low forging temperatures. As a result of this, there is less heat loss to the dies from the part.

7. CONCLUSION

The following conclusions are drawn from the forging operations of 7075 Al-alloy:

1. The force increases almost linearly for the upsetting operation.
2. The maximum stress occurs in the loading regions where the lower and the upper die contact with the workpiece.
3. Maximum stresses are greater in finish operation than those in upsetting operation.
4. The maximum temperature occurs at the zones where the maximum deformation happens.
5. The stress on the workpiece decreases as the initial temperature of the billet increases.
6. The maximum die force increases as the initial temperature of the billet decreases.

8. ACKNOWLEDGEMENTS

The authors are thankful to UGC, New Delhi for sponsoring this project.

REFERENCES

1. P.H. Kim, M.S. Chun, J.J. Yi, and Y.H. Moon, Pass schedule algorithms for hot open die forging, *Journal of Materials Processing Technology*, 2002: 130–131, pp.516–523.
2. E. Korner, and R. Knodler, Possibility of warm extrusion in combination with cold extrusion, *Journal of Materials Processing Technology*, 1992: 35, pp.451–465.
3. Y.H. Kim, T.K. Ryou, H.J. Choi, and B.B. Hwang, An analysis of the forging processes for 6061 aluminum-alloy wheels, *Journal of Materials Processing Technology*, 2002: 123, pp. 270–276.
4. V.Victor, and A.Taylan, New concepts in die design-physical and computer modelling applications, *Journal of Materials Processing Technology*,2000: 98, pp.212-223.
5. V. Bhavin Mehta, I. Al-Zkeri, and J.S.Gunasekera, Evaluation of super forge for 3D simulation of streamlined and shear extrusion dies”, MSC.Software Corporation, Ohio University, Athens, Ohio, USA, 2000.
6. PRO/ENGINEER Wildfire 3.0.
7. Simufact 3.0.

GEOMETRICAL AND MATERIAL OPTIMIZATION OF ALLOY WHEEL FOR FOUR WHEELER

M.Indira Rania, Racha Venub

aDepartment of Mechanical Engineering, Jawaharlal Nehru Technological University Hyderabad College of Engineering, Kukatpally, Hyderabad – 500 085, India

bM.Tech Student Department of Mechanical Engineering, JNTUHCEH, Hyderabad

Abstract: Automobile wheels are made from an alloy of magnesium or aluminum metals or sometimes a alloy consisting mixture of both is used. The alloy wheels are of lighter weight and differ from normal steel wheels. Due to the lighter weight the steering and the speed of the car improves. Alloy wheels will reduce the unstrung weight of a vehicle compared to one fitted with standard steel wheels. The benefit of reduced unstrung weight is more precise steering as well as a nominal reduction in fuel consumption. At present four wheeler wheels are made of Aluminum Alloys or steel. In this work a parametric model is made to design for Alloy wheel used in a four wheeler by collecting data from reverse engineering process from existing model. Design is evaluated by analyzing the model by considering the constraints as ultimate stresses and variables as different materials. The main aim of the paper is to suggest best geometric shape along with material, for geometrical optimization three different shapes of straight, inclined and Y-shape are analyzed with above described materials by applying load. Structural analysis is done at maximum load conditions to determine structural characteristics. Model analysis is done on all above models to compare vibration range.

Keywords: Alloy wheels, parametric model, structural analysis, geometrical optimization

Address all correspondence to: marpuindira@jntuh.ac.in

1. INTRODUCTION

A wheel, together with an axle overcomes friction by facilitating motion by rolling. A moment needs to be applied to the wheel about its axis to rotate, either by way of gravity, or by application of another external force. The steel wheel is the first type and the most-used wheel. This kind of wheel is heavy and strong as several sheets of steel are stamped into shape and typically welded together. The second type of wheel to be mentioned is the rally wheel. These are essentially steel wheels but they are made somewhat differently, and tend to consist of a heavier gauge of steel. While the inner portion of a steel wheel is generally welded to the rim along its entire circumference, a steel wheel's inner portion is

cut to resemble the spokes of a magnesium wheel, and is welded accordingly. Presently four wheeler wheels are made of Aluminum Alloys. In this paper Aluminum alloy wheel is replaced with different alloys like magnesium.

Previously steel wheels are used to manufacture wheels for the higher strength, but these alloy wheels are heavily due to its density and also giving trouble to manufacture because of its higher melting point and hard to forge it. Weight is also playing crucial role in mileage. The aluminum and magnesium wheels are getting yield (bends) at the larger run and also these types of materials are not permitting heavy loads. New type of alloy wheels are not permitting heavy loads and also getting yield (bend) during bumps and pits in long run.

2. OBJECTIVES

The selection of suitable material for alloy wheel is one of the major tasks and the following are the objectives attempted to study

- To design the wheel with best geometric shape for cross members.
- Increasing the life time of product, increasing the mechanical efficiency by decreasing the component weight.
- To suggest the best material for alloy wheel.

3. LITERATURE SURVEY

Liangmo Wang et al. [1], studied to improve the quality of aluminum wheels. The author proposed a new method for evaluating the fatigue life of aluminum wheels. For simulating the rotary fatigue test the ABAQUS software is used to build the static load finite element model of aluminum wheels. The equivalent stress amplitude is calculated based on the nominal stress method by considering the effects of mean load, size, fatigue notch, surface finish and scatter factors. The fatigue life of aluminum wheels is predicted by using the equivalent stress amplitude and aluminum alloy wheel S-N curve. The results from aluminum wheels rotary fatigue bench test showed that the base line wheel failed the test and its crack initiation is around the hub bolt whole area that agreed with the simulation. Using the method proposed in this work, the wheel life cycle is improved to over 1.0×10^5 and satisfied the design requirement. The results indicated that the proposed method of integrating finite element analysis and nominal stress method is a good and efficient method of predict the fatigue life of aluminum wheels.

WANG Qiang, ZHANG Zhi-min, ZHANG Xing [2], studied the development of forged magnesium road wheel are reviewed. Methods of flow-forming, spin forging of manufacturing a forged magnesium alloy wheel are introduced. A new extrusion method is investigated especially. Extrusion from hollow billet was proposed in order to enhance the strength of spoke portion and reduce the maximum forming load. By means of the developed technique, the one-piece Mg wheels are produced successfully by extrusion from AZ80+ alloy. At the

same time, the existing problems on the research and development of forged magnesium road wheel are analyzed. The impact testing, radial fatigue testing and bending fatigue testing results show that AZ80+ wheel can meet application requirement in automobile industry.

J.Stearns, T.S.Srivatsan, X.Gao, and P.C.Lam [2006], studied the use of the finite element technique for analyzing stress and displacement distributions in wheels of automotive vehicles when subject to the conjoint influence of inflation pressure and radial load. A potentially viable technique for finite element modeling of radial wheel, subjected to loading, is analysed. The extrinsic influence of inflation pressure on performance of the rotating body, that is, the wheel, is rationalized.

Amalia ana Dascal [4], studied the tensions that arise when a wheel is subjected to aerodynamic loading conditions, trying to play the best areas in which attention must be enhanced in order to prevent premature destruction. The question always arises buying rims "steel or alloy wheels?" In addition to the rims look more appealing than those of alloy steel, there are technical reasons why it tends to use them: reduced weight, starting and braking, rigidity, rapid cooling. Although it can produce sheet steel or cast alloy wheels profile is adopted depending on the specifics of the construction vehicles and the stress faced by their wheels. Using 3D modeling software designed a concept of light and has undergone a finite element method using different forces and accelerations restrictions in areas where problems occur during use. Calculating the diagrams thus playing rim is observed when the material behavior is tensed and so can be correct the areas that present a danger of destruction. At the end of the method could draw the conclusion which shows the success of the concept, but also design new technologies for observation and verification of parts or assemblies.

4. DESIGN OF ALLOY WHEEL

The economics and metallurgy of the extrusion process permit to economically create unique shapes, even multi-hallow shapes, for unique applications, perhaps combining what would otherwise be several separate parts that would have to be joined, into one specially shaped piece. Extrusion is one of the aluminum's "aces in the hole", as the expression goes. A 3D model is designed for straight and inclined shape cross members and is as shown in figure 1.

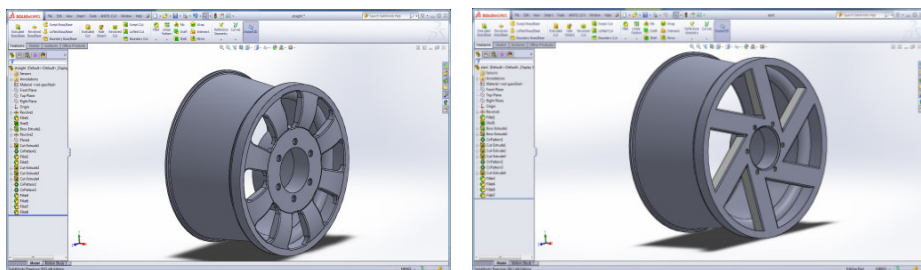


Figure1: 3D model for straight and inclined cross members

4.1 Load Calculations

The Mercedes Benz c250 type of car is selected for study This model car has 201 HP, at 2000rpm engine and the car weight (w_c) is approximately 944 kgf. The weight of passengers and luggage is considered as 500 kgf. The Area (A) is 128738.66 mm²

$$\begin{aligned} \text{Pressure} &= \frac{w_c + w_p}{A \times 4} & (1) \\ &= \frac{(1944+500) \times 9.81}{128738.66 \times 4} \\ &= 0.04578 \text{N/mm}^2 = 45.78 \text{KPa} \end{aligned}$$

5. RESULTS AND DISCUSSION

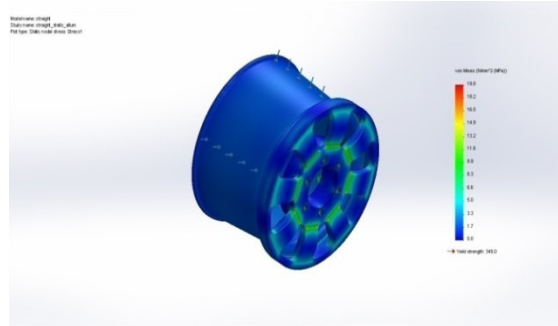
Structural and frequency analysis is conducted on different types of geometric types of alloy wheel cross-members by varying material. Aluminum and Magnesium made alloy wheels are designed and considered for study. The analysis for providing optimum shape along with material is studied. Figure 2 shows that meshed component for straight cross member for aluminum material using solid element. Meshing is used to separate as complex problems into no. of small problems by FEM based study [5].



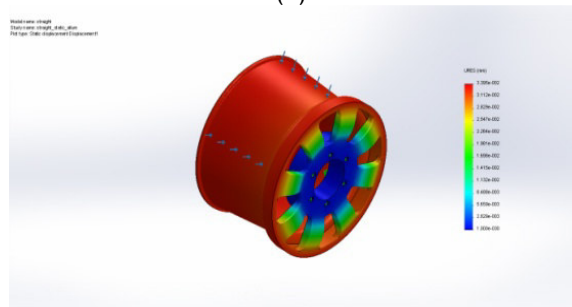
Figure 2: meshed component for straight cross member

5.1 Structural Analysis of Straight Cross Member Type Wheel

The distribution of Von-mises stress and displacement for straight cross Aluminum and Magnesium members is as shown in figure 3 and 4. Figure 3 (a) shows that stress distribution diagram for straight cross member for aluminum material. The von-mises stress is depends on von-mises theories of failure. The maximum von-mises stress is 19.819 MPa which is within the safe limit. Figure 3 (b) shows that displacement distribution diagram for straight cross member for aluminum material. The deformation is mainly occurred on cross members caused by loads. The maximum displacement is 0.0339539 mm which is within the safe limit.

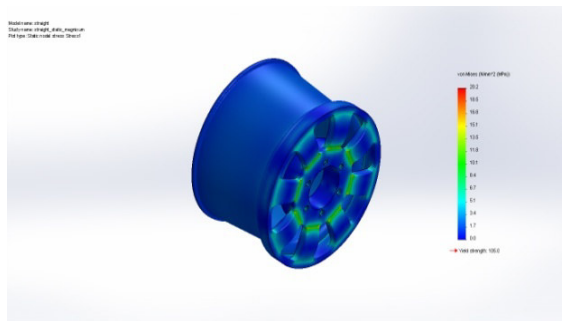


(a)

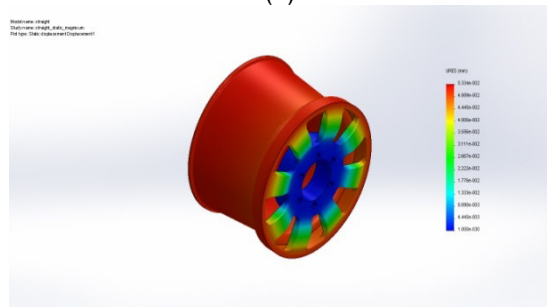


(b)

Figure 3 a & b: Distribution of Von-mises stress and displacement for straight cross Aluminum member



(a)



(b)

Figure 4 a & b: Distribution of Von-mises stress and displacement for straight cross Magnesium member

Similarly Figure 4 (a) shows that stress distribution diagram for straight cross member for Magnesium material. The maximum von-mises stress is 20.1763 MPa. Figure 4 (b) shows that displacement distribution diagram for Magnesium material. The maximum displacement is 0.0533379 mm which is within the safe limit.

5.2 Structural Analysis of Inclined Cross Member Type Wheel

The Structural and frequency analysis for inclined cross member for aluminum and magnesium material is conducted. The figure 5 (a) and 6 (a) shows the stress distribution diagram for inclined cross member for Aluminum and Magnesium material respectively. The maximum von-mises stress of Aluminum and Magnesium material is 30.4378 MPa and 30.3679 MPa. Figure 5 (b) and 6 (b) shows the displacement distribution diagram for inclined cross member for Aluminum and Magnesium material respectively. The maximum displacement for aluminum and magnesium members is observed as 0.0343769 mm and 0.0541355 mm respectively which is within the safe limits.

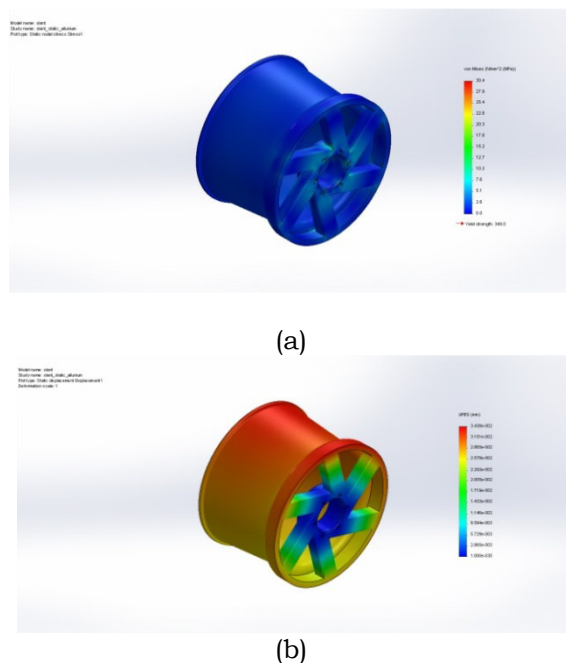
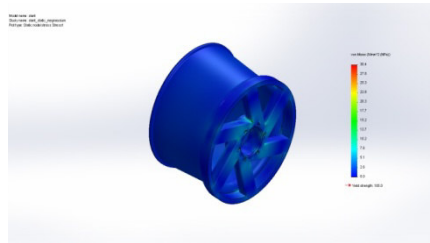
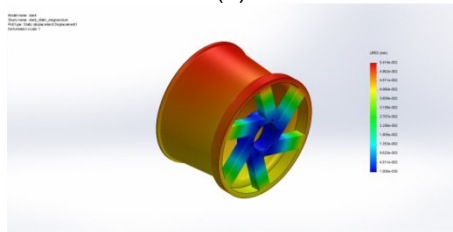


Figure 5 a & b: Distribution of Von-mises stress and displacement for inclined cross Aluminum member

The frequency analysis of straight and inclined cross member type wheel for two different materials is conducted at different modes. The materials selected for study are Aluminum and Magnesium. The figure 7 a, b and c represents the distribution of frequency at mode 1, 2 and 3 for straight cross Aluminum member and figure 8 a, b c for the distribution of frequency at mode 1, 2 and 3 for straight cross Magnesium member.

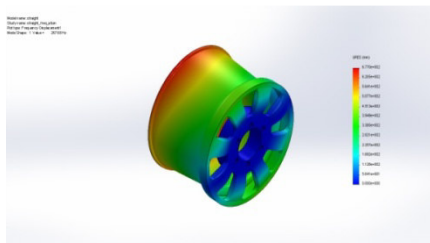


(a)

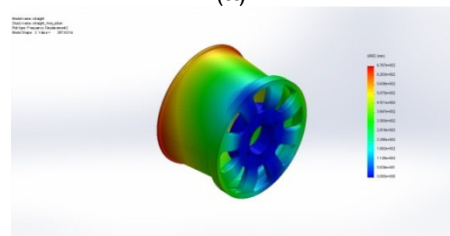


(b)

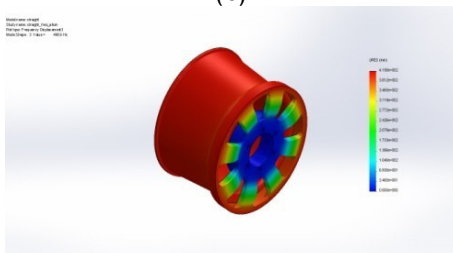
Figure 6 a & b: Distribution of Von-mises stress and displacement for inclined cross Magnesium member



(a)



(b)



(c)

Figure 7 a, b & c: Distribution of frequency at mode 1,2 & 3 for straight cross Aluminum member

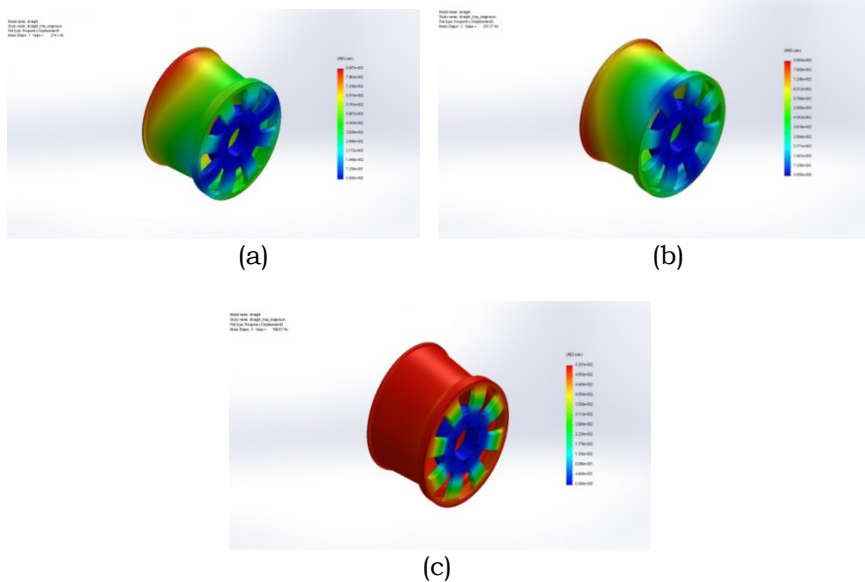


Figure 8 a, b & c: Distribution of frequency at mode 1, 2 & 3 for straight cross Magnesium member

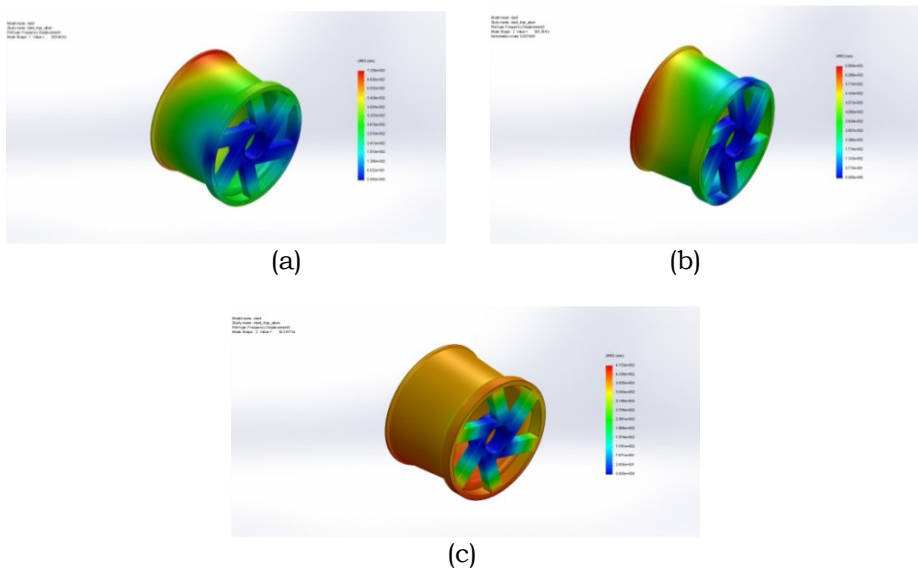
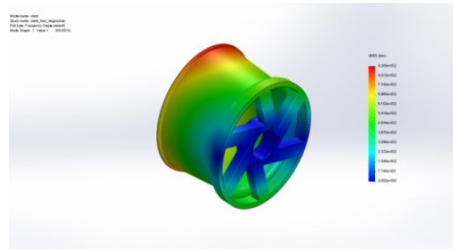


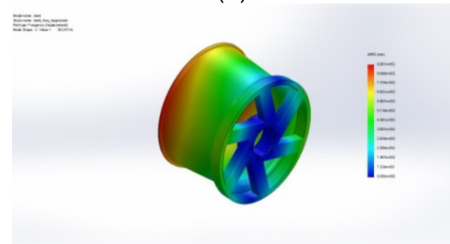
Figure 9 a, b & c: Distribution of frequency at mode 1, 2 & 3 for inclined cross Aluminum member

5.3 Frequency Analysis of Inclined Cross Member Type Wheel

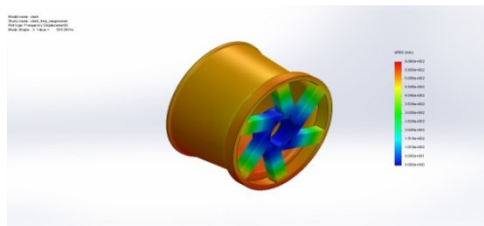
The frequency analysis of inclined cross member type wheel for two different materials is conducted at different modes 1, 2 and 3 as represented in figure 9 a, b and c for Aluminum member and figure 10 a, b c for Magnesium member.



(a)



(b)



(c)

Figure 10 a, b & c: Distribution of frequency at modes 1,2 & 3 for inclined cross Magnesium member

The table 1 & 2 are the stress levels and displacement levels are attained for two different geometric shapes straight and inclined cross members for two materials i.e Aluminum and Magnesium. It describes structural characteristics of the wheel.

Table 1: Stress and Displacement values for Aluminum material

Model	Stress in N/mm ²	Displacement in mm
Straight	19.819	0.0339539
Inclined	30.4378	0.0343769

Table 2: Stress and Displacement values for Magnesium material

Model	Stress in N/mm ²	Displacement in mm
Straight	20.1763	0.0533379
Inclined	30.3679	0.0541355

The table 3 shows are the frequency values attained for two different geometric shapes along with two materials at three modes. Frequency analyses of all type wheels, it shows amplitudes due to natural frequency, it should be maintain in low level than previous model to reduce amplitude errors.

Table 3: Model frequencies at three different modes

Models	mode	Frequency in Hz	
		Aluminum	Magnesium
Straight	1	267.68	274.10
	2	267.90	274.37
	3	496.90	509.69
Inclined	1	329.46	336.65
	2	345.36	352.87
	3	523.67	535.58

6. CONCLUSIONS

- In this paper optimized alloy wheel for car by simulating alloy wheel on different geometric shapes with different materials is presented.
- Geometrical shapes are chosen according to the standards of alloy wheel manufacturers. Modeling of alloy wheel is done using solid works on different geometric shapes Straight, inclined and simulation works is done in simulations (COSMOS).
- From results Magnesium material along with inclined cross members is better.

REFERENCES

1. L. W.Chen, C.Wang, andQ.Wang, Fatigue Life Analysis of Aluminum Wheels by Simulation of Rotary Fatigue Test, 2010: 12 (11)
2. W.Qian, Z. Zhimin, and Z.Xing, New extrusion process of Mg alloy automobile wheels, 2010.
3. J. Stearns, T. S. Srivatsan, X. Gao, and P. C. Lam: Understanding the Influence of Pressure and Radial Loads on Stress and Displacement Response of a Rotating Body: The Automobile Wheel, 2006
4. A. A. Dascal, and D.Carauleanu, Wheels auto modeling using finite element method, 2011.
5. Chennakesava R Alavala, Finite Element Methods: Basic Concepts and Applications, PHI Learning Private Limited, 2009.

MODIFICATION OF GATING SYSTEM FOR PROPER MOULD FILLING OF BRACKET CASTING USING PROCAST

G. Devendar, K. Shiva Kumar, and A. Chennakesava Reddy

Department of Mechanical Engineering
JNTUH College of engineering, Hyderabad – 500 085

Abstract: Gating system is an important factor in the production of quality castings. The objective of this paper is the modification of gating system for truck bracket using Procast software. The gating system for simultaneous casting 6 brackets has been optimized by changing choke area.

Keywords: truck bracket, gating system, mould filling, procast.

Address all correspondence to: degantha@gmail.com

1. INTRODUCTION

Mould filling plays a very significant role in casting quality control [1]. Due to the importance of mould filling, extensive research effort has been made in attempt to study the effect of gating design on the flow pattern of melt entering the mould [2]. It has been shown that an optimum gating system design could reduce the turbulent extent of the melt flow, minimize gas and entrap inclusion and dross [3]. The formation of various casting defects could be directly related to fluid flow phenomena involved in the stage of mould filling [4]. The bottom gate was used to study the effect of gate sizes on the entry velocity of molten metal into the vertically-cast plate mould. Their results indicate that a critical entry velocity is present during mould filling, under which oxide entrapment is minimized. The geometry of gating system is another very important factor influencing mould filling patterns [5].

Gating system is an important factor in the production of quality castings, therefore, should be fully considered in the design and construction of pattern. The objective of this paper is the modification of gating system using Procast software. The product is truck bracket. The bracket is to be cast through vertical pouring of the mould. The number of brackets per mould is 6. The material of bracket is ductile cast iron (EN-GIS-500-7).

2. MATERIALS AND METHODS

The material used to make the brackets is ductile cast iron. The chemical composition of ductile cast iron is C: 2.7-3.7, Si: 0.8-2.9, Mn: 0.3-0.7, P: ≤ 0.1 , S: ≤ 0.02 , Fe: remaining.

The mechanical properties of ductile cast iron are given below:

- Tensile strength is minimum 500 Mpa.
- Yield strength is minimum 320 Mpa.
- Elongation is minimum 7%.
- Hardness range is Brinell Hardness 170-230.

The typical casting products using this grade are such as iron brackets for trucks, tractors, other agricultural and construction machinery as shown in figure 1.



Figure 1: Typical applications of ductile cast iron

The solid drawing of bracket used in the present work is shown in figure 2.



Figure 2: Solid drawing of bracket

To get better gating system to produce 6 brackets per mould the following procedure is adapted:

Step-1: Solidification Simulation

Simulation of solidification helps to identify for proper design of the risers (number, location, and size). For every pair of parts 3 risers with 5 cm in diameter by 7.7 cm in height were applied. With solidification simulation any defects related to solidification in cast part can be detected.

Step-2: Mould filling Simulation

In this the gating system is checked for its dimensions. Proper design of an optimized gating system was made easier by application of fluid flow simulation. To design the gating system the following factors were considered:

- Minimizing turbulence
- Rapid mould filling
- Maximizing yield
- Removal slag, dross, and inclusions
- Facilitate gating removal

- Desire thermal gradients

It is important to fill every mould quickly, but turbulent flow needs to be avoided. Figure 5 shows the initial structure of gating system for the bracket.

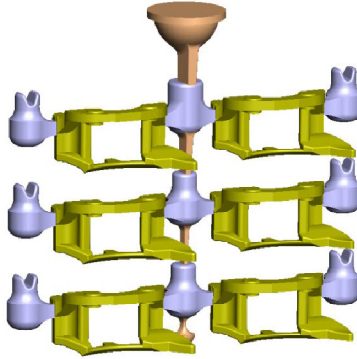


Figure 5: Gating system

To speed up the calculation of gating systems and Design the appropriate choke, equation (1) can be used.

$$\text{Choke area, } A = \frac{1036 \times W}{t \times f \sqrt{h}} \quad (1)$$

where, W is weight of molten metal
 t is filling time (8 seconds)
 h is height (h_1, h_2, h_3)
 f is coefficient of friction ($=0.5$).

3. RESULTS AND DISCUSSION

In figure 3, 4 the simulation results show the shrinkage and Liquid mapping of the process. It is observed from figure 4 that the cast parts are free of shrinkage. The shrinkage is observed only in the risers. Therefore, the location and sizes of riser were selected properly.

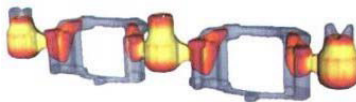


Figure 3: Liquid mapping



Figure 4: Shrinkage

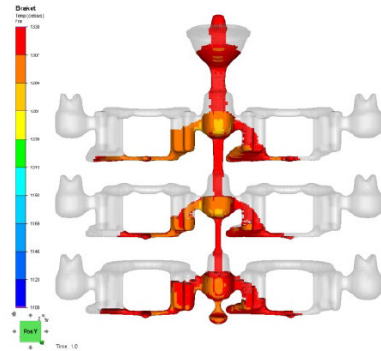


Figure 6: Mould filling time at 3 seconds

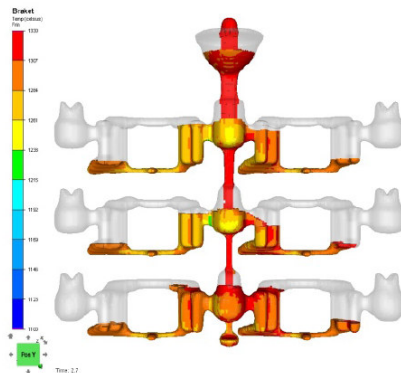


Figure 7: Mould filling time at 5.5 seconds

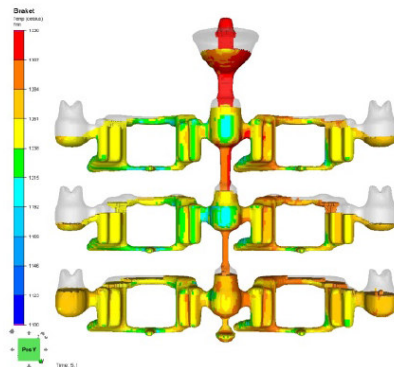


Figure 8: Mould filling time at 3 seconds with recalculate choke area

By mould filling simulations the results at 3 seconds and 5.5 seconds time of filling (figure 6 and 7), confirm that this gating approach is not appropriated, because some cavities are going to fill (vertical parted moulds as a guide) in less than 8 s (bottom) and some after 8s (top). All of cavities should be filled by molten metal at the same time.

To re-sizing chocks area and to set up the filling time in upper and middle and lower cavities, the $A1$, $A2$, $A3$ were recalculated based on 8 seconds. It is important to know that the real coefficient of friction (f) can be determined only after mould filling simulation. Once applied changing, the mould filling simulation was run again to see how all of cavities are filling by molten metal. Figures 8 and 9 show after 3 seconds and 5.5 seconds these confirmed all cavities are filled at the same time.

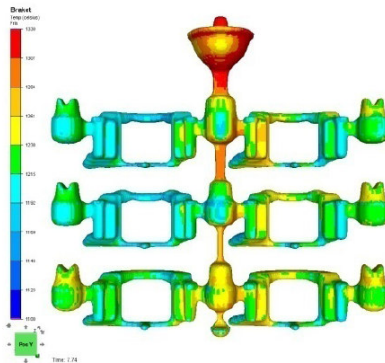


Figure 9: Mould filling time at 5.5 seconds with recalculate choke area

With application of simulation, the design of gating can be optimized in the short period of time and decreasing cost.

4. CONCLUSIONS

The outputs from the present work are as follows:

1. Proper design (location, number, and size) of the risers can be determined from solidification simulation
2. A predicted map of possible macro-shrinkage defects.
3. The appropriate of choke and gating system can be determined quickly through fluid flow simulation.

REFERENCES

1. Ch. Rajanna, and A. Chennakesava Reddy, Solidification behaviour of Al-Si-Mg alloys in the gravity die-casting process, Indian Foundry Journal, 2007:53(10),pp.29-36.
2. S.H.Jong, and W.s.Hwang, Three-dimensional mould filling simulation for casting and its experimental verification, AFS Transactions, 1991: 99, pp. 117-124.
3. V.S.R.Murti, and A. Chennakesava Reddy, Finite difference analysis of gray cast-iron solidification process, National Conference on Computer integrated Design and Manufacturing, Coimbatore, 28-29th November 2003, pp. 103-110.
4. A. Chennakesava Reddy, Pattern of cooling contours in the flyash ceramic shell and Al-Mg alloy casting, National Conference on Investment Casting, Hyderabad, 28-29 December 2006, pp. 142-146.
5. J.Runyoro, S.M.A.Boutorabi, and J.Campbell Critical gate velocity for film forming casting alloys, a basis for process specification, AFS Transactions, 1992:100, pp. 225-234.

INFLUENCE OF PARAMETERS AND OPTIMIZATION OF EDM PERFORMANCE MEASURES ON MDN 300 STEEL USING PCA-TAGUCHI BASED METHOD

P.Raghuram reddy^a, Prasanna^b, G.Shravan^c, K.Raju^d

^{a,d} PG student, ^b Assistant professor, ^c Lecturer
Mechanical Engineering Department
JNTUH college of Engineering, Hyderabad-85

Abstract: Day by day many new materials are coming in to use due to continuous demand from the defense, aerospace and medical fields for machining intricate shapes. The traditional machining process cannot meet the requirement because of the increased hardness and strength of new materials. Non-traditional machining methods are found to be suitable for these conditions. Technologies to improve the material removal rate and reduce the tool wear rate, achieve the good surface finish and dimensional accuracy are very demanding in electrical discharge machining (EDM). Electric discharge machining is suitable for machining die steels, titanium and Nickel based alloys. In the present work, it is proposed to comparing performance of optimum silver coated copper electrode with conventionally used copper electrode using kerosene as dielectric fluid in electrical discharge machining of MDN300 Steel. Principal component analysis- Taguchi methodology (PCA-TM) is adopted in evaluating the optimization of the process with different process parameters for performance measures for maximizing of material removal rate(MRR), while minimizing Tool wear rate (TWR), Surface roughness (Ra) and Relative wear ratio (RWR). The obtained optimal results have compared with experimental results. Further, the Sensitivity analysis is also carried out to compute the relative influence of factors on the performance measures. It is observed that the Current is having more influence on the performance measures.

Keywords: electric discharge machining, principal component analysis, material removal rate, tool wear rate, surface roughness

Address all correspondence to: prajntu@jntuh.ac.in

1. INTRODUCTION

It is essential to understand the past and present status of the EDM process to suggest future areas of work. Extensive literature survey has been carried out to find the state of the art of EDM process. Review of the research work reveals that much work has been done on various aspects of electric discharge machining (EDM) on low carbon steels, carbides and few die-steels with only one or two electrode materials like copper, graphite and brass etc, Research is going on to develop a

composite material which satisfies the basic requirement of tool properties. Few composites tools like Cu-W, Cu-WC, Cu-Cr, etc have been tested as tool material for EDM study. A. Khan et al. [1] discuss the performance about the shape configuration of the electrode. The maximum MRR was found for round electrodes followed by square, triangular and diamond shaped electrodes. However, the highest EWR were found for the diamond shaped electrodes. Boujelbene et al. [2] Carried out experiment on two electrical discharge machines to obtain high surface finish and other machining aspects. Moro et al. [3] Studied application of electrical discharge coating (EDC) to improve cutting tool life instead of Physical Vapor Deposition (PVD) or Chemical Vapour Deposition (CVD). Tool electrode prepared by semi-sintering of TiC powder at 900°C for 1 hour. The experiment were carried out for 16 min with discharge current of 8 amps, Ton time of 8 μ s, and duty factor as 5.9%. The relation between a wear rate of an electrode and maximum thickness has been investigated. Zaw et al.[4] suggested some electrode materials for electrical-discharge machining i.e. graphite, copper, copper alloys, copper-tungsten, brass, silver-tungsten and steel. The performance of this electrode is compared with the conventional electrode materials such as Cu, Graphite, CuW. M.P. Samuel *et al.* [5] has been studied the performance of P/M electrodes on various aspects of EDM operation. Shunmugan et al. [6] used tungsten carbide powder as the compost and experimented on EDM with reverse polarity to evaluate wear resistance by cutting tests and compared it with the deposition obtained when he used bronze P/M electrode. The tool used was of 10mm diameter and 20 mm length prepared with 40%WC and 60% iron at a compaction pressure of 700 MPa.

H.M.Zaw. Tsai et al [7] have working martial of graphite, copper and copper alloys are widely using EDM because these materials have high melting temperature, and excellent electrical and thermal conductivity. S Kumar and Batra [8] investigated the surface modification by EDM method with tungsten powder mixed in the dielectric medium. Peak current, pulse on-time and pulse off time were taken as variable factors and micro-hardness of the machined surface was taken as the response parameter. Dhar and Purohit [9] evaluates the effect of current (c), pulse-on time (p) and air gap voltage (v) on MRR, TWR, ROC of EDM with Al-4Cu-6Si alloy-10 wt. % SiCP composites. Bhaduri et al. [10]studied the effects of EDM process parameters on multiple responses. But instead of simultaneous optimization of multiple responses, they determined the optimal. Lin et al.[11] investigated the effects of six control factors on machining performance of EDM process on conductive ceramics and found that the required optimal settings for the three responses (MRR, EWR and SR) were not the same. But none of these methods take care of the possible correlation between the response variables that may exist, whereas, correlation analysis reveals that some of the responses of EDM process are usually correlated.

So, ideally, a principal component analysis (PCA)-based method that can take into account the possible correlation between the responses should be used for multi-response optimization of EDM processes. Chakravorty et al. [11] analyzed some experimental data on EDM processes using four PCA-based approaches, e.g. PCA-based GRA method, PCA-based proportion of quality loss reduction (PQLR) method, PCA-based technique for order preference by similarity to ideal solution (TOPSIS) method and weighted principal component (WPC) method. The authors found that the PCA-based approaches, in general, would lead to better optimization performance and among the four PCA-based approaches, PCA-based PQLR method would result in the best optimization performance. Panda and Mahapatra [12]. Pradhan et al. [13] have optimized micro-EDM process parameters for machining Ti-6Al-4V super alloy. To verify the optimal micro-EDM process parameters settings, MRR, TWR, OC and T are chosen as observed performance criteria. In this present work the current, pulse on time, pulse off time, thickness of coating on electrode to study their performance measures on MRR, TWR, RWR, using PCA based taguchi method followed by sensitivity analysis.



Figure 1: EDM machine

2. EXPERIMENTAL METHODS

The whole experiment was conducted on Electrical Discharge Machine which is a die sinking type EDM machine of model tool craft systems A15 shown in figure 1. The voltage set as 75V. The polarity of work piece set as positive (anode) and electrode as negative (cathode). Kerosene is taken as dielectric fluid. The choice of the electrode material depends upon the performance criteria required (material, surface finish, wear rate, machining stability) and also upon electrode manufacturing constraints (cost, Block size, ease of machining). The shape of the copper electrode tool can be seen in figure 2. Silver coating is done on copper electrode of diameter 4mm by using electroplating as shown in figure 3 below. The mechanical properties of silver coated

electrode are in the table 1. For the present study Mar aging 300 steel is considered. The Chemical composition and mechanical properties are mentioned in the table 2 & 3. MDN 300 steel as shown in figure 4 is an iron-nickel steel alloy that, as with all mar aging steels, exhibits high levels of strength and hardness. The process input parameters have been used for the conducting experiment on EDM of MDN 300 steel and mentioned in the table 4. The evaluation of performance measures are measured like material removal rate (MRR) tool wear rate (TWR) relative wear rate (RWR), surface roughness (Ra).



Figure 2: Copper electrode



Figure 3: Silver 260electrode

Table 1: Mechanical properties of silver

Property	Quantity
Density (g/cm ³)	8.1
Specific Heat (J/Kg ⁰ K)	831
Melting Point (°C)	1427-1454
Thermal conductivity (W/m ⁰ K)	25.8
Yield Tensile Strength (MPa)	758
Electrical resistivity (Ω cm)	0.174x10 ⁻⁴
Hardness (BHN)	34

Table 2: Chemical Composition of MDN300 Steel

Alloying element	Percentage by weight
Ni	17-19
Co	12
Mo	3-5
Ti	0.2-1.6
Fe	65-68
C	0.01
Al	0.10

Table 3: Mechanical properties of MDN300 Steel

Property	Quantity
Density (g/cm ³)	8.1
Specific Heat (J/Kg ⁰ K)	831
Melting Point (°C)	1427-1454
Thermal conductivity (W/m ⁰ K)	25.8
Yield Tensile Strength (MPa)	758
Electrical resistivity (Ω cm)	0.174x10 ⁻⁴
Hardness (BHN)	34



Figure 4: MDN steel

TABLE 4: Working Range of the Process Parameters

Process parameters	Units	Range
Current	Amps (A)	6-18
Pulse on time (T _{on})	Micro sec(μ s)	15-35
Pulse off time (T _{off})	Micro sec(μ s)	10-30
Thickness	Microns (μ)	5-25

3. PRINCIPAL COMPONENT ANALYSIS BASED TAGUCHI METHOD (PCA-TM)

Principal Component Analysis (PCA) is probably the most well known multivariate statistical technique and is used in almost all scientific disciplines. It is also likely to be the oldest multivariate technique. It was invented in 1901 by Pearson but its modern formulation was due to Hotelling who also coined the term principal component. The PCA is a mathematical procedure that is used to analyse a data set representing observations described by several dependent variables which are, in general, inter-correlated. Its goal is to extract the important information from the data and to express this information as a set of new orthogonal variables called principal components. The steps involved in PCA are given as follows:

Step 1: Getting some data: The data is taken from the source, for which the optimization is to be performed. The multiple responses are tabulated into a matrix form as

$$B = \begin{bmatrix} x_{11} & x_{12} & x_{13} & \dots & x_{1k} \\ x_{21} & x_{22} & x_{23} & \dots & x_{2k} \\ x_{31} & x_{32} & x_{33} & \dots & x_{3k} \\ \cdot & \cdot & \cdot & \cdot & \cdot \\ x_{i1} & x_{i2} & x_{i3} & & x_{ik} \end{bmatrix} \quad (1)$$

Where, i is the number of experimental runs, k the number of the response.

Step 2: Normalization of responses: The responses are normalized using the following formulae:

$$\text{Lower the better (LB): } x_i(k) = \frac{\max y_i(k) - y_i(k)}{\max y_i(k) - \min y_i(k)} \quad (2)$$

$$\text{Higher the better (HB): } x_i(k) = \frac{y_i(k) - \min y_i(k)}{\max y_i(k) - \min y_i(k)} \quad (3)$$

where $z_i(k)$ is the normalized value of k^{th} response, $\min z_i(k)$ the smallest value of $x_i(k)$ for k^{th} response, and $\max x_i(k)$ the largest value of $\min x_i(k)$ for k^{th} response. z is the normalized array.

$$z = \begin{bmatrix} z_{11} & z_{12} & z_{13} & \dots & z_{1k} \\ z_{21} & z_{22} & z_{23} & \dots & z_{2k} \\ z_{31} & z_{32} & z_{33} & \dots & z_{3k} \\ \cdot & \cdot & \cdot & \cdot & \cdot \\ z_{i1} & z_{i2} & z_{i3} & & z_{ik} \end{bmatrix} \quad (4)$$

Step 3: Checking for covariance: The covariance matrix N is formulated from the normalized data as

$$N = \begin{bmatrix} M_{11} & M_{12} & M_{13} & \dots & M_{1k} \\ M_{21} & M_{22} & M_{23} & \dots & M_{2k} \\ M_{31} & M_{32} & M_{33} & \dots & M_{3k} \\ \cdot & \cdot & \cdot & \cdot & \cdot \\ M_{i1} & M_{i2} & M_{i3} & & M_{ik} \end{bmatrix} \quad (5)$$

$$N_{i,k} = \frac{\text{cov}(z_i(k), z_i(l))}{\sqrt{\text{var}(z_i(k)) \times \text{var}(z_i(l))}} \quad (6)$$

where $l = 1, 2, 3, \dots, k$; and $\text{Cov}(z_i(k), z_i(l))$ is the covariance of sequences $z_i(k)$ and $z_i(l)$. Calculate the eigen values and eigen vectors

from the correlation coefficient array and denoted by k_j and V_j respectively.

Step 4: Evaluate the principal components (ϕ_j):The Eigen vector V_j represents the weighting factor of j number quality characteristics of the j^{th} principal component. For example, if Q_j represents the j^{th} quality characteristic, the j^{th} principal component ϕ_j will be treated as a quality indicator with the required quality characteristic.

$$\phi_j = (V_{1v}Q_1 + V_{2v}Q_2 + \dots + V_{jv}Q_j)^{1/j} = \sum_{j=1}^n (V_v \times Q_j)^{1/j} \quad (7)$$

Where, ϕ_1 is the first principal component, ϕ_2 the second principal component, and so on. The principal components are aligned in descending order with respect to variance, and therefore the ϕ_1 account for the most variance in the data. The CPC (ϕ) represents the index of multi-composite quality for multi-quality responses. It is defined as the combination of principal components with their individual Eigen values.

Table 5: Design matrix and estimated performance measures

Std	Current (Amps)	Pulse On time T_{on} (μ s)	Pulse Off Time T_{off} (μ s)	Thickness (t) μ	MRR (mm^3/min)	TWR (mm^3/min)	RWR (%)	Ra (μ m)
1	9	15	10	5	28.98	0.16	1.01	1.13
2	15	15	10	5	30.84	0.24	1.5	1.34
3	9	25	10	5	25.1	0.1	0.91	0.85
4	15	25	10	5	28.32	0.18	1.14	1.22
5	9	15	20	5	27.01	0.36	1.13	0.95
6	15	15	20	5	28.56	0.47	1.39	1.15
7	9	25	20	5	24.95	0.28	0.89	0.81
8	15	25	20	5	26.41	0.39	1.24	0.98
9	9	15	10	15	27.59	0.17	1.21	1.12
10	15	15	10	15	31.32	0.3	1.46	1.46
11	9	25	10	15	25.54	0.13	0.99	0.88
12	15	25	10	15	29.28	0.2	1.27	1.33
13	9	15	20	15	26.48	0.32	0.98	0.94
14	15	15	20	15	27.78	0.43	1.32	1.04
15	9	25	20	15	24.93	0.2	0.81	0.79
16	15	25	20	10	27.09	0.32	1.13	0.97
17	6	20	15	10	25.69	0.14	1.01	0.83
18	18	20	15	10	29.54	0.38	1.59	1.37
19	12	10	15	10	30.85	0.35	1.47	1.36
20	12	30	15	10	26.88	0.2	1.03	1.04
21	12	20	30	20	27.89	0.14	1.12	1.03
22	12	20	25	20	25.42	0.48	0.99	0.8
23	12	20	15	20	29.55	0.15	0.97	1.26
24	12	20	15	20	27.21	0.13	0.79	1.17
25	12	20	15	20	28.19	0.24	1.27	1.22
26	12	20	15	25	27.24	0.34	1.25	1.08
27	12	20	15	25	27.32	0.27	1.2	1.1
28	12	20	15	25	27.18	0.29	1.26	1.13
29	12	20	15	25	28.96	0.3	1.24	1.15
30	12	20	15	25	29.07	0.22	1.29	1.24

Table 6: Normalized experimental data

S.No	MRR, (mm ³ /min)	TWR ,(mm ³ /min)	RWR,(%)	Ra,(μ m)
1	0.633803	0.864865	0.725	0.492537
2	0.924883	0.648649	0.1125	0.179104
3	0.026604	1	0.85	0.910448
4	0.530516	0.810811	0.5625	0.358209
5	0.325509	0.324324	0.575	0.761194
6	0.568075	0.027027	0.25	0.462687
7	0.00313	0.540541	0.875	0.970149
8	0.231612	0.243243	0.4375	0.716418
9	0.416275	0.837838	0.475	0.507463
10	1	0.486486	0.1625	0
11	0.095462	0.945946	0.75	0.865672
12	0.680751	0.756757	0.4	0.19403
13	0.242567	0.432432	0.7625	0.776119
14	0.446009	0.135135	0.3375	0.626866
15	0	0.702703	0.975	1
16	0.338028	0.405405	0.575	0.731343
17	0.118936	0.918919	0.725	0.940299
18	0.72144	0.27027	0	0.134328
19	0.926448	0.351351	0.15	0.149254
20	0.305164	0.567568	0.7	0.626866
21	0.463224	0.918919	0.5875	0.641791
22	0.076682	0	0.75	0.985075
23	0.723005	0.891892	0.775	0.298507
24	0.356808	0.945946	1	0.432836
25	0.510172	0.648649	0.4	0.358209
26	0.361502	0.378378	0.425	0.567164
27	0.374022	0.567568	0.4875	0.537313
28	0.352113	0.513514	0.4125	0.492537
29	0.630673	0.486486	0.4375	0.462687
30	0.647887	0.675676	0.375	0.328358

3.1 Taguchi Method

Taguchi's philosophy, developed by Taguchi, is an efficient tool for the design of high quality manufacturing system. Taguchi method is an efficient problem solving tool, which can upgrade/improve the performance of the product, process, design and system with a significant slash in experimental time and cost. This method combines the experimental design theory and quality loss function concept applied for carrying out robust design of processes and products. Further, this technique determines the most influential parameters in the overall performance. The optimum process parameters obtained from the Taguchi method are insensitive to the variation in environmental condition and other noise factors. Taguchi's Orthogonal Array (OA) provides a set of well-balanced experiments (with less number of experimental runs), and Taguchi's signal-to-noise ratios (S/N), which are logarithmic functions of desired output; serve as objective functions in the optimization process. Taguchi method uses a statistical measure of performance called signal-to-noise ratio. The S/N ratio takes both the mean and the variability into account. The S/N ratio is the ratio of the mean (Signal) to the standard deviation (Noise).The ratio depends on the quality characteristics of the product/process to be optimized. The standard S/N ratios generally

used are as follows: - Nominal-is-Best (NB), lower-the-better (LB) and Higher-the-Better (HB). The optimal setting is the parameter combination, which has the highest S/N ratio. Because, irrespective of the quality criteria may be (NB, LB, HB) S/N ratio should always be maximized. Once experimental data (quality attribute value) is normalized using NB/LB/HB criteria; normalized value lies in between zero to one. Zero represents worst quality to be rejected and one represents most satisfactory quality. Since S/N ratio is expressed as mean (signal) to the noise (deviation from the target); maximizing S/N ratio ensures minimum deviation and hence it is (S/N ratio) to be maximized.

$$\text{Taguchi's S/N Ratio for (NB) Nominal-the-best, } \eta = 10 \ln_{10} \frac{1}{n} \sum_{i=1}^n \frac{\mu^2}{\sigma^2} \quad (8)$$

$$\text{Taguchi's S/N Ratio for (LB) Lower-the-better, } \eta = -10 \ln_{10} \frac{1}{n} \sum_{i=1}^n y_i^2 \quad (9)$$

$$\text{Taguchi's S/N Ratio for (HB) Higher-the-better, } \eta = -10 \ln_{10} \frac{1}{n} \sum_{i=1}^n \frac{1}{y_i^2} \quad (10)$$

η = S / N Ratio, y Value of the quality characteristic at i^{th} setting, n = Total number of trial runs at i^{th} setting, μ = Mean, σ = Standard Deviation

3.2 PCA Integrated with Taguchi Method (PCA-TM)

In PCA, the experimentally measured response data are converted to a set of individual components so that optimal set of variable combination can be found. There are two drawbacks in PCA [15].

1. If the Eigen values exists greater than one, Eigen vector corresponding to principal component is selected to replace the actual responses. In practical manufacturing systems, there exists more than one Eigen value which is greater than 1. In such case, determination of feasible solution corresponding to each of the response is not guaranteed.
2. The derived Composite Principal Component (CPC) based on optimal set of variables cannot guarantee to replace the multi response as chosen principal component.

But PCA integrated with Taguchi method results more practical and efficient methodology for solving multi response optimization problems.

Table7: Eigen vectors, Eigen values

	Ψ_1	Ψ_2	Ψ_3	Ψ_4
Eigen vectors	0.487	-0.707	0.497	0.126
	0.487	0.707	0.497	0.126
	0.517	0.416	-0.305	-0.8
	0.508	0.317	-0.643	0.573
Eigen value	2.2165	0.6338	0.5992	0.5505
proportion	0.554	0.158	0.15	0.138
cumulative	0.554	0.713	0.862	1

4. RESULTS AND DISCUSSIONS

The design matrix with estimated mechanical properties and normalized matrix are shown in table 5 and 6 respectively.

Table 8: principal component analysis for experimental data

S.No	ψ_1	ψ_2	ψ_3	ψ_4
1	1.354885	0.621095	0.207012	-0.10894
2	0.915457	-0.09172	0.632569	0.210892
3	1.401914	1.330403	-0.33445	-0.02896
4	1.126009	0.545721	0.264749	-0.07574
5	1.00043	0.479661	-0.34186	0.058043
6	0.65411	-0.13185	-0.07799	0.140103
7	1.209978	1.051487	-0.62048	-0.0756
8	0.821382	0.417328	-0.35809	0.120339
9	1.114119	0.656511	0.15212	0.068795
10	0.807931	-0.29545	0.689221	0.057297
11	1.334677	1.18771	-0.2678	0.027247
12	1.005434	0.281644	0.46768	-0.02769
13	1.117205	0.697464	-0.39613	-0.08023
14	0.797184	0.132577	-0.24406	0.186366
15	1.354291	1.219411	-0.59113	-0.11846
16	1.030849	0.518671	-0.27614	0.052732
17	1.357932	1.165263	-0.30992	0.089561
18	0.551201	-0.2764	0.406507	0.201925
19	0.775659	-0.29688	0.493346	0.126525
20	1.105368	0.675436	-0.18283	-0.09084
21	1.302871	0.770024	0.095066	0.071896
22	0.925512	0.570055	-0.82404	-0.02589
23	1.338771	0.53643	0.374289	-0.24548
24	1.371322	0.96973	0.064155	-0.38784
25	0.953116	0.377855	0.223606	0.031265
26	0.868166	0.368522	-0.12659	0.07821
27	0.983547	0.509965	-0.02621	0.036521
28	0.885032	0.441845	-0.0123	0.061293
29	1.005289	0.226732	0.124283	0.055882
30	1.005256	0.279736	0.332302	0.054918

Analysis of Covariance matrix of Eigen values, Eigen vectors, Accountability proportion (AP) and Cumulative accountability proportion (CAP) are computed in table7 for the four major quality indicators. From the normalized response matrix, the co variance matrix with Eigen values and Eigen vectors are derived as follows. The principal component analyses for experimental data are present in the table 8.

$$PC_1 = 0.487 MRR_i + 0.487 TWR_i + 0.517 RWR_i + 0.508 Ra_i \quad (11)$$

$$PC_2 = -0.707 MRR_i + 0.707 TWR_i + 0.416 RWR_i + 0.317 Ra_i \quad (12)$$

$$PC_3 = 0.497 MRR_i + 0.497 TWR_i - 0.3052 RWR_i - 0.643 Ra_i \quad (13)$$

$$PC_4 = 0.126 MRR_i + 0.126 TWR_i - 0.8000 RWR_i + 0.573 Ra_i \quad (14)$$

Where MRR, TWR, RWR and R_a are the normalized values of material removal rate, tool wear rate, relative wear ratio and surface roughness.

- After finding ψ_1, ψ_2, ψ_3 and ψ_4 the corresponding values and S/N ratios are found out as follows and the CPC values are given in the table 9.

$$CPC = (PC_1^2 + PC_2^2 + PC_3^2 + PC_4^2)^{0.25} \quad (15)$$

For S/N ratio: Lower -the -Better is the criterion (LB) is taken from equation (9), Higher- the- Better is the criterion (HB) is taken from equation (10).

Table 9: Composite Principal Component and Corresponding S/N Ratio

S.No	CPC	S/N LB	S/N HB
1	1.228294	-1.78605	1.786047
2	1.065956	-0.55479	0.554788
3	1.400586	-2.92619	2.926193
4	1.131912	-1.07625	1.076252
5	1.078146	-0.65355	0.653553
6	0.828409	1.6351	-1.6351
7	1.311707	-2.35674	2.356739
8	1.117252	-0.96302	0.963024
9	1.026841	-0.23006	0.230063
10	1.237732	-1.85253	1.85253
11	1.25668	-1.98449	1.984493
12	1.115244	-0.9474	0.947398
13	1.064761	-0.54505	0.545047
14	1.181094	-1.44569	1.44569
15	1.385465	-2.83191	2.831913
16	1.08983	-0.74718	0.747178
17	1.34841	-2.59644	2.596441
18	0.875022	1.159619	-1.15962
19	0.987046	0.113249	-0.11325
20	1.145157	-1.1773	1.177302
21	1.232111	-1.81299	1.812993
22	1.168021	-1.34901	1.349014
23	1.228863	-1.79007	1.790072
24	1.313372	-2.36775	2.367753
25	1.024621	-0.21127	0.211266
26	0.977144	0.20083	-0.20083
27	1.052998	-0.44855	0.448554
28	0.995575	0.038521	-0.03852
29	1.019849	-0.17072	0.170717
30	1.047081	-0.3996	0.399604

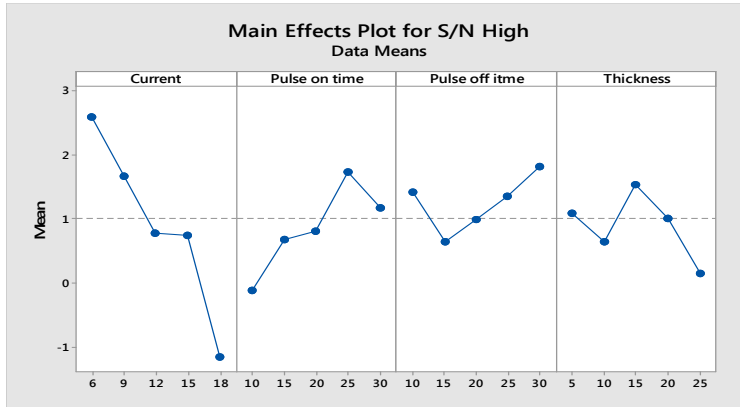


Figure 5: Main effect plot of S/N Ratios

The maximum value in the fig 5 indicates the optimal values of the process parameters. So the optimal values (table 10) are Current 6 Amps, Pulse on time (T_{on}) is 25 micro sec, pulse off time (T_{off}) is 30 micro sec and thickness of coating is 15 microns.

Table 10: Results of confirmation test

Process variable	Level	Optimal	Settings
		Prediction	Experimental
Current(A)	-2	6	6
Pulse on time (T_{on}) (μ s)	1	25	25
Pulse off time (T_{off}) (μ s)	2	30	30
Thickness (t) (μ)	1	15	15
Value of (CPC)		1.2594	1.2631
S/N Low		-2.00298	-2.1837
S/N high		2.00298	2.1837

The following results are made from PCA-TM:

- Principal Component Analysis integrated with Taguchi method proven to be a hygienic optimization method for finding the effect of multi variable input parameters on the multiple output responses.
- The optimized input parameters were derived as $I=6$ Amps, $T_{on}=25\mu$ s, $T_{off}=30\mu$ s, and $t=15\mu$. Corresponding output responses are derived as $MRR= 26.71\text{mm}^3/\text{min}$, $TWR=0.19\text{mm}^3/\text{min}$, $RWR=1.07\%$ and $R_a=0.89\mu\text{m}$.

4.2 Comparison of coated and uncoated electrodes: Further the experiments were conducted on same work piece with uncoated electrode at optimum set of condition values i.e. current of 6 amps, Pulse on time of 25micro sec and pulse off time of 30 micro sec. The

obtained results are shown in table 11.

Table 11: Comparison between coated and uncoated electrodes

	MRR	TWR	RWR	R _a
Current	36.217	-0.326	1.425	0.048
Pulse On Time	35.693	-0.341	1.916	1.032
Pulse Off Time	32.615	-0.331	1.453	1.058
Thickness of coating	35.502	-0.326	0.676	1.005

The results also show that the Performance measures obtained by coated electrode are higher than the uncoated electrode with the variation of 5-10% improved results. By comparing the performance of coated and uncoated electrodes, the coated electrodes give better MRR, TWR and RWR.

5. CONCLUSIONS

From the experiments that were conducted on the EDM, the following conclusions are drawn.

1. When current increases, the MRR increases but at the same time surface finish reduces tremendously.
2. Machining of mar aging steel (MDN 300 steel) at high current results in increased tool wear rate. So for MDN 300 steel at current is 6amps.
3. Optimum parameters are current 6Amps, Pulse on time 25 μ s, Pulse off time 30 μ s and thickness of coating 15 μ by using PCA Taguchi based.
4. From the experimental observations, by increasing the current the MRR increases but at the same time TWR also increases with poor surface finish.
5. From the experiments the RWR is increased from 6 amps to 15 Amps and it is almost constant beyond the current.
6. From the comparison experiment of coated and uncoated electrodes it can be concluded that the coated electrode will give the maximum MRR and minimum TWR.

REFERENCES

1. K. M. Ali, M. Haque, A study of electrode shape configuration on the performance of die sinking EDM, International Journal of Mechanical and Materials Engineering. 4(1) (2009) pp:19-23.
2. M Boujelbene., E Bayraktar., W Tebni., S Ben Salem. – Influence of machining parameters on the surface integrity in electrical discharge machining, Archives of Materials Science and Engineering, volume 37, issue 2, June 2009, pp:110-116.
3. T Moroa, N Mohri, H Otsubo, A Goto A, N Saito, “ Study on the surface modification system with electrical discharge machine in the practical usage,” Journal of Materials Processing Technology, 2004, 149 pp.65-70.
4. H.M.Zaw, J.Y.H. Fuh, A.Y.C Neeb, L. Lub, “Formation of a new EDM electrode material using sintering techniques,” Int J AdvManufTechnol ,1999, 89-90, pp.182-186.

5. M.P. Samuel and P.K. Philip, "Power metallurgy tool electrodes for electrical discharge machining ," Int. J. Mach. Tools Manufact. vol. 37, 1997, pp. 1625-1633.
6. M.S Shunmugam, P.K.Philip, A. Gangadhar, "Improvement of wear resistance by EDM with tungsten carbide P/M electrode," Wear, 1994,171, pp.1-5
7. H.C. Tsai, B.H.Yan, F.Y. Huang, "EDM performance of Cr/Cu-based composite electrodes. International Journal of Machine Tools and Manufacture", 43(3), 2003, pp: 245-252.
8. S. Kumar and U. Batra, "Surface modification of die steel materials by EDM method using tungsten powder-mixed dielectric," Journal of Manufacturing Processes, vol. 14, pp. 35-40, 2012.
9. S.Dhar, R.Purohit, N.Saini, A.Sharma, and G.H.Kumar, "Mathematical modeling of electric discharge machining of cast Al-4Cu-6Si alloy-10 wt.% sicp composites", Journal of Materials Processing Technology, 193(1-3),2007 pp: 24-29.
10. D.Bhaduri, A.S.Kuar, S.Sarkar, S.K.Biswas, and S.Mitra, " Electro discharge machining of titanium nitride-aluminiumoxide composite for optimum process criteria yield.*Materials and Manufacturing Processes*, Vol. 24, pp. 2009,1312-1320.
11. J.L.Lin, K.S.Wang, B.H.Yan, and Y.S.Tarng, "Optimisation of the electrical discharge machining process based on the Taguchi method with fuzzy logics", *Journal of Materials Processing Technology*, Vol. 102, 2009,pp. 48-55.
12. R.Chakravorty, S.K.Gauri, and S.Chakraborty, "Optimization of correlated responses of EDM process. *Materials and Manufacturing Processes*, Vol. 27, 2012, pp. 337-347.
13. S.S.Panda, and S.S. Mahapatra, "Online multi-response assessment using Taguchi and artificial neural network. *International Journal of Manufacturing Research*, Vol. 5, 2010 pp. 305-326.
14. M.K.Pradhan, and C.K. Biswas, "Multi-response optimisation of EDM of ALSI D2 tool steel using response surface methodology. *International Journal of Machining and Machinability of Materials*, Vol. 9,2013 pp. 66-85.
15. R. Jeyapaul ,P. Shahabudeen and K. Krishnaiah ,"Quality management research by considering multi-response problems in the Taguchi method—a review", *Int J Adv Manuf Technol.*, Vol. 26,pp. 2013,pp:1331–1337.

DIFFERENCE BETWEEN DENAVIT - HARTENBERG (D-H) CLASSICAL AND MODIFIED CONVENTIONS FOR FORWARD KINEMATICS OF ROBOTS WITH CASE STUDY

A. Chennakesava Reddy

Professor of Mechanical Engineering
JNTUH College of Engineering
Kukatpally, Hyderabad

Abstract: This paper highlights the difference between the D-H classical convention and D-H modified convention for RR manipulator. The forward kinematics ends at a frame, whose origin lies on the last joint axis z_2 as per modified D-H convention, a_2 does not appear in the link parameters whereas a_2 appears in the link parameters of D-H classical convention.

Keywords: RR manipulator, D-H classical convention, D-H modified convention

Address all correspondence to: e-mail: dr_acreddy@yahoo.com

1. KINEMATIC CHAIN

A robotic manipulator may be considered as set of links connected in a chain called **kinematic chain** by joints (figure 1). The simple joints are prismatic joint (figure 2a) and revolute joint (figure 2b). The prismatic joints permit a linear motion and the revolute joints allow a rotary motion. The revolute and prismatic joints exhibit one degree of freedom (dof).

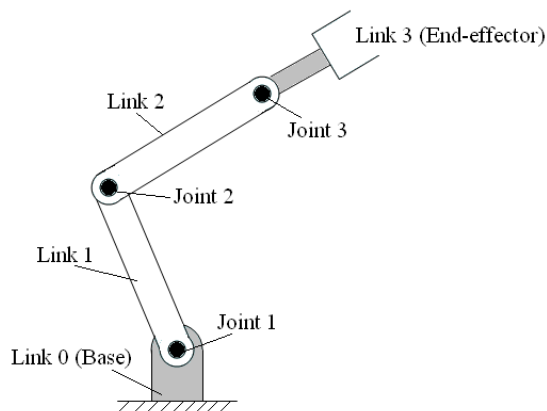


Figure 1: A three-degrees of freedom robotic manipulator

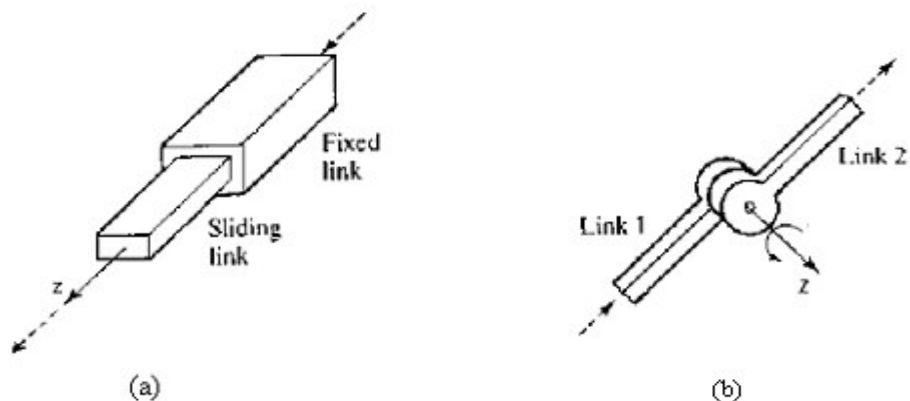


Figure 2: Joints (a) Prismatic joint, and (b) revolute joint

Typical robots are *serial-link manipulators* comprising a set of bodies, called *links*, in a chain, connected by *joints*. In this book, each joint has one degree of freedom, either translational or rotational. Note that the assumption does not involve any real loss of generality, since joints such as a ball and socket joint (two degrees-of-freedom) or a spherical wrist (three degrees-of-freedom) can always be thought of as a succession of single degree-of-freedom joints with links of length zero in between. For a manipulator with n joints numbered from 1 to n , there are $n+1$ links, numbered from 0 to n . Link 0 is the base of the manipulator, generally fixed, and link n carries the end-effector. Joint i connects links i and $i - 1$. when joint i is acutated, link i moves. A link can be specified by two numbers, the *link length* and *link twist*, which define the relative location of the two axes in space. Joints may be described by two parameters. The *offset length* is the distance from one link to the next along the axis of the joint. The *joint angle* is the rotation of one link with respect to the next about the joint axis.

A coordinate frame is attached rigidly to each link. To facilitate describing the location of each link we affix a coordinate frame to it: frame i is attached to link i . When the robotic manipulator executes a motion, the coordinates of each point on the link are constant. Each joint has a joint axis with respect to which the motion of joint is described. By convention, the z -axis of a coordinate frame is aligned with the joint axis.

Description of an end-effector in space requires a minimum of six degrees of freedom. Typical robotic manipulators have five or six degrees of freedom. The objective of forward kinematic analysis is to determine the cumulative effect of the entire set of joint variables.

The displacement of joint is denoted by q_i and is called joint variable. The collection of joint variables

$$q = [q_1, q_2, \dots, q_n]^T \quad (1)$$

is called the joint vector.

The position of the end-effector is denoted by the dimensional vector

$$r = [r_1, r_2, \dots, r_m]^T \quad (2)$$

The relation between r and q determined by the manipulator mechanism is given by

$$r = f(q) \quad (3)$$

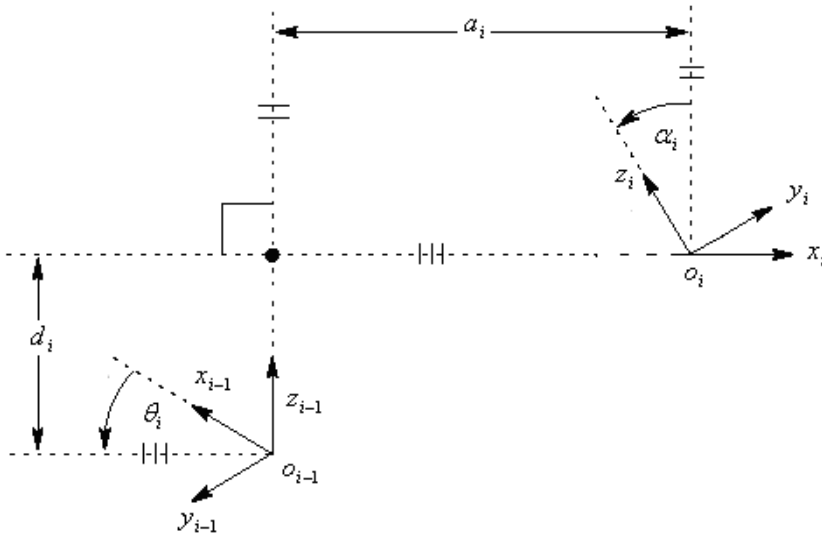


Figure 3: Description of link parameters

2. LINK AND JOINT PARAMETERS

Links are the solid bits between joints. Links have a *proximal* end closest to the base and a *distal* end closest to the tool. The proximal end of the link has the lower joint number. Each type of link has 4 parameters, 2 directions of translation and 2 axes of rotation. These are called the *link parameters*.

Let us consider a binary link of an articulated mechanism as shown in figure 3. It establishes a rigid connection between two successive joints numbered i and $(i+1)$. Its geometry in terms of size and shape can be described very simply in terms of only two parameters:

1. The distance a_i , measured along the common normal to both axes. The variable a_i is called the link length;
2. The twist angle α_i , defined as the angle between both joint axes. The variable α_i is called the twist angle. The twist angle is measured between the orthogonal projections of joint axes i and $(i+1)$ onto a plane normal to the common normal.

If the relative motion is restrained to joints of revolute, and prismatic, the relative displacement occurring at joint i may also be described in terms of two parameters:

1. The rotation θ_i about the joint axis. The variable θ_i is called joint angle;
2. The displacement d_i along the same axis. The variable d_i is called link offset.

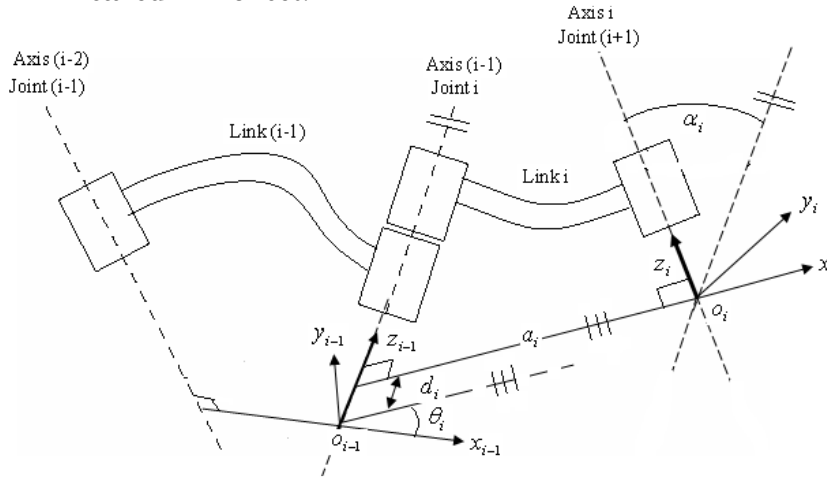


Figure 4: Description of link and joint parameters

2.1 Link Parameters

A link i is connected to two other links (i.e. link $i - 1$ and link $i + 1$). Thus two joint axes are established at both ends of the link as shown in figure 4. Joints $i-1$ and i are connected by link $i-1$. Joints i and $i+1$ are connected by link i . The significance of links is that they maintain a fixed configuration between the joints which can be characterized by two parameters a_i and α_i , which determine the structure of the link.

They are defined as follows:

1. a_i is the shortest distance measured along x_i axis from the point of intersection of x_i axis with z_{i-1} axis to the origin.
2. α_i is the angle between the joint axes z_{i-1} and z_i axes measured about x_i axis in the right hand sense.

2.2 Joint Parameters

A joint axis establishes the connection between two links. This joint axis will have two normals connected to it, one for each link. The relative position of two such connected links $i-1$ and i is given by d_i which is the distance measured along the joint axis z_{i-1} between the

common normals. The joint angle θ_i between the common normals is measured in a plane normal to the joint axis z_{i-1} . Hence, the parameters d_i and θ_i are called distance and angle between adjacent links. They determine the relative position of neighboring links. For revolute joint, θ_i varies and d_i is a fixed length (i.e., zero or constant). For prismatic joint, d_i varies and θ_i is zero or constant.

3. LINK FRAMES

Let us define a coordinate frame $o_i x_i y_i z_i$ attached to link i as follows:

1. z - axis is along the rotation direction for revolute joints, along the translation direction for prismatic joints.
2. The z_{i-1} axis lies along the axis of motion of the i th joint.
3. The origin o_i is located at the intersection of joint axis z_i with the common normal to z_i and z_{i-1} .
4. The x_i axis is taken along the common normal and points from joint i to joint $i+1$.
5. The y_i axis is selected to complete right-hand frame. The y_i axis is defined by the cross product $\mathbf{y}_i = \mathbf{z}_i \times \mathbf{x}_i$.

Showing only z and x axes is sufficient, drawing is made clearer by **NOT** showing y axis.

By the above procedure, the link frames for links 1 through $n-1$ are determined.

4. DENAVIT - HARTENBERG (D-H) CONVENTION

A commonly used convention for selecting frames of reference in robotic application is Denavit-Hartenberg convention. In this convention, the position and orientation of the end-effector is given by

$$H = {}^0T_n = {}^0T_1 {}^1T_2 {}^2T_3 \dots {}^{n-1}T_n \quad (4)$$

where,

$${}^{i-1}T_i = \begin{bmatrix} {}^iR_{i-1} & {}^i d_{i-1} \\ 0 & 1 \end{bmatrix} \quad (5)$$

Many people are not aware that there are two quite different forms of Denavit-Hartenberg representation for the kinematics of serial-link manipulators:

1. Classical convention as per the original paper of Denavit and Hartenberg [1], and used in textbooks such as by Paul [2], Fu et al [3], or Spong et.al [4].

- Modified convention as introduced by John J. Craig in his textbook [5] and Tsuneo Yoshikawa in his textbook [6].

Both notations represent a joint as 2 translations (a and d) and 2 angles (α and θ). However the expressions for the link transform matrices are quite different. In short, you must know which kinematic convention your Denavit-Hartenberg parameters conform to. Unfortunately many sources in the literature do not specify this crucial piece of information, perhaps because the authors assume everybody uses the particular convention that they do.

4.1 Classical Convention

The link and joint parameters in the classical convention as shown in figure 5 are as follows:

- Link length, a_i is the offset distance from o_i to the intersection of the z_{i-1} and x_i axes along the x_i axis;
- Twist angle, α_i is the angle from the z_{i-1} axis to the z_i axis about the x_i axis;
- Offset length, d_i is the distance from the origin of the $(i-1)$ frame to the intersection of the z_{i-1} axis with the x_i axis along the z_{i-1} axis;
- Joint angle, θ_i is the angle between the x_{i-1} and x_i axes about the z_{i-1} axis.

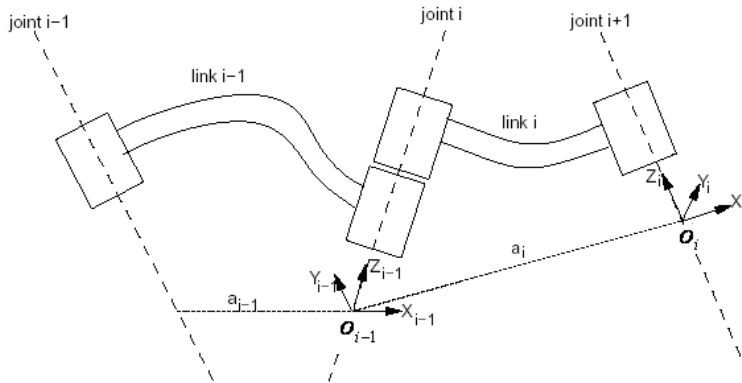


Figure 5: Classical convention

The positive sense of α_i and θ_i is shown in figure 6.

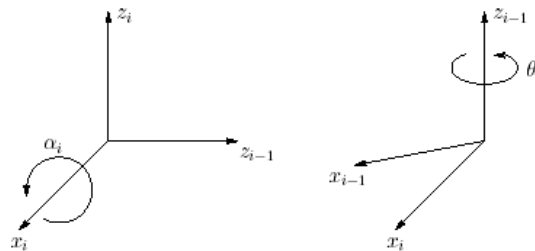


Figure 6: Positive sense of α_i and θ_i

The D-H parameters are tabulated in table 1.

Table 1: D-H parameters for classical convention

Link, i	a_i	α_i	d_i	θ_i
1				
2				

The frame transformation ${}^{i-1}T_i$ describing the finite motion from link $i-1$ to link i may then be expressed as the following sequence of elementary transformations, starting from link $(i-1)$:

1. A rotation θ_i about \mathbf{z}_{i-1} axis;
2. A translation d_i along the \mathbf{z}_{i-1} axis ;
3. A translation a_i along the x_i axis
4. A rotation α_i about x_i axis.

The homogeneous transformation ${}^{i-1}T_i$ is represented as a product of four basic transformations as follows:

$$\begin{aligned}
 {}^{i-1}T_i &= R(z_{i-1}, \theta_i) T(z_{i-1}, d_i) T(x_i, a_i) R(x_i, \alpha_i) \\
 &= \begin{bmatrix} C\theta_i & -S\theta_i & 0 & 0 \\ S\theta_i & C\theta_i & 0 & 0 \\ 0 & 0 & 0 & 0 \\ 0 & 0 & 0 & 1 \end{bmatrix} \begin{bmatrix} 1 & 0 & 0 & 0 \\ 0 & 1 & 0 & 0 \\ 0 & 0 & 1 & d_i \\ 0 & 0 & 0 & 1 \end{bmatrix} \begin{bmatrix} 1 & 0 & 0 & a_i \\ 0 & 1 & 0 & 0 \\ 0 & 0 & 1 & 0 \\ 0 & 0 & 0 & 1 \end{bmatrix} \begin{bmatrix} 1 & 0 & 0 & 0 \\ 0 & C\alpha_i & -S\alpha_i & 0 \\ 0 & S\alpha_i & C\alpha_i & 0 \\ 0 & 0 & 0 & 1 \end{bmatrix} \\
 &= \begin{bmatrix} C\theta_i & -C\alpha_i S\theta_i & S\alpha_i S\theta_i & a_i C\theta_i \\ S\theta_i & C\alpha_i C\theta_i & -S\alpha_i C\theta_i & a_i S\theta_i \\ 0 & S\alpha_i & C\alpha_i & d_i \\ 0 & 0 & 0 & 1 \end{bmatrix} \tag{6}
 \end{aligned}$$

Algorithm for classical D-H Convention:

Step - 1: Identify and number the links starting with base and ending with end-effector. The links are numbered from 0 to n . The base frame is $\{0\}$ and the end-effector frame is $\{n\}$. Locate and label the joint axes z_0, \dots, z_{n-1} .

Step - 2: The location of frame to the base is arbitrary. The x_0 axis, which is perpendicular to z_0 , is chosen to be parallel to x_1 when the first joint angle variable $\theta_1 = 0$ in the home position. The y_0 axis is defined by the cross product $y_0 = z_0 \times x_0$.

For $i = 1, \dots, n$, perform Steps 3 to 5.

Step - 3: Locate the origin o_i where the common normal to z_i and z_{i-1} axes intersect at z_i axis. If z_i axis intersects z_{i-1} axis, locate the origin o_i at this point of intersection. If z_i and z_{i-1} axes are parallel, locate the origin o_i in any convenient position along z_i axis.

Step - 4: Establish x_i along the common normal between z_i and z_{i-1} through o_i . The x_i axis is fixed perpendicular to both z_i and z_{i-1} axes and points away from z_i axis. The origin of frame (i) is at the intersection of z_i and x_i axes.

- If the z -axes of two successive joints are intersecting, there is no common normal between them (or it has zero length). We will assign the x -axis along a line perpendicular to the plane formed by the two axes. If z_i and z_{i-1} axes intersect, choose the origin at the point of intersection. The x_i axis will be perpendicular to the plane containing z_i and z_{i-1} . In this case, the parameter a_i equals 0.
- If two joint z -axes are parallel, there are an infinite number of common normals present. We will pick the common normal that is collinear with the common normal of the previous joint. a common method for choosing o_i is to choose the normal that passes through o_{i-1} as the x_i axis; o_i is then the point at which this normal intersects z_i . In this case, d_i is equal to zero. Since the z_i and z_{i-1} axes are parallel, α_i is equal to zero.
- If z_i and z_{i-1} axes coincide, the origin lies on the common axis. If the joint i is revolute, the origin is located to coincide with origin of frame (i) and x_i axis coincides with x_{i-1} axis. If the joint i is prismatic, x_i axis is chosen parallel to x_{i-1} axis and the origin is located at the distal end of the link i .

Step - 5: The y_i axis is selected to complete right-hand frame. The y_i axis is defined by the cross product $y_i = z_i \times x_i$.

Step - 6: Establish the end-effector frame (o_n) as shown in figure 7. assuming the n th joint is revolute, set $z_n = a$ (approach direction) along the direction z_{n-1} and pointing away from the link n . Establish the origin o_n conveniently along z_n , preferably at the center of the gripper or at the tip of any tool that the manipulator may be carrying. Set $y_n = s$ in the sliding direction along which the fingers the gripper slide to open or close and set $x_n = n$ as $s \times a$. If the tool is not a simple gripper set x_n and y_n conveniently to form a right-hand frame.

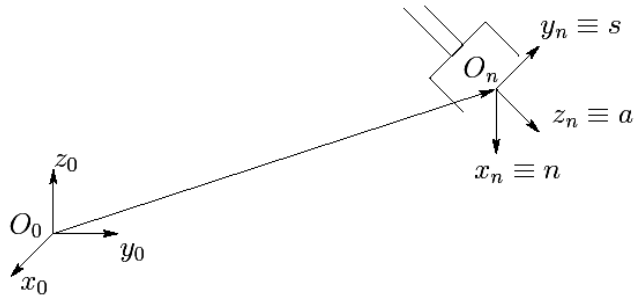


Figure 7: Establishing frame for end-effector

Step - 7: Create a table 2 of link parameters a_i , α_i , d_i , and θ_i .

Table 2: Link parameters

Link, i	a_i	α_i	d_i	θ_i
1				
2				

- The link length a_i is the shortest distance between z_{i-1} and z_i axes. It is measured as the distance along the direction of x_i from the intersection of z_{i-1} and x_i to the origin of the i th coordinate frame. For intersecting joint axes the value of a_i is zero. It has no meaning for prismatic joints and is set to zero in this case.
- The offset angle, α_i , is measured from z_{i-1} axis to z_i about the x_i axis, again using a right-hand rule. For most commercial manipulators the offset angles are multiples of 90° .
- The distance between links, d_i , is the distance from the x_{i-1} to the x_i axis measured along the z_{i-1} axis. If the joint is prismatic, d_i is the joint variable. In the case of a revolute joint, it is a constant or zero.
- θ_i is the angle from the x_{i-1} to the x_i axis measured about z_{i-1} axis. This is defined using a right-hand rule since both x_{i-1} and x_i are perpendicular to z_{i-1} . The direction of rotation is positive if the cross product of x_{i-1} and x_i defines the z_{i-1} axis. θ_i is the joint variable if the joint i is revolute. In the case of a prismatic joint it is a constant or zero.

Step - 8: Form the homogeneous transformation matrices ${}^{i-1}T_i$ by substituting the above parameters into equation (6).

Step - 9: Form ${}^0T_n = {}^0T_1 {}^1T_2 {}^2T_3 \dots {}^{n-1}T_n$. This gives the position and orientation of the end-effector frame expressed in the base coordinates.

Note: The origin of the base frame is coincident with the origin of the joint 1. This assumes that the axis the first joint is normal to the xy plane.

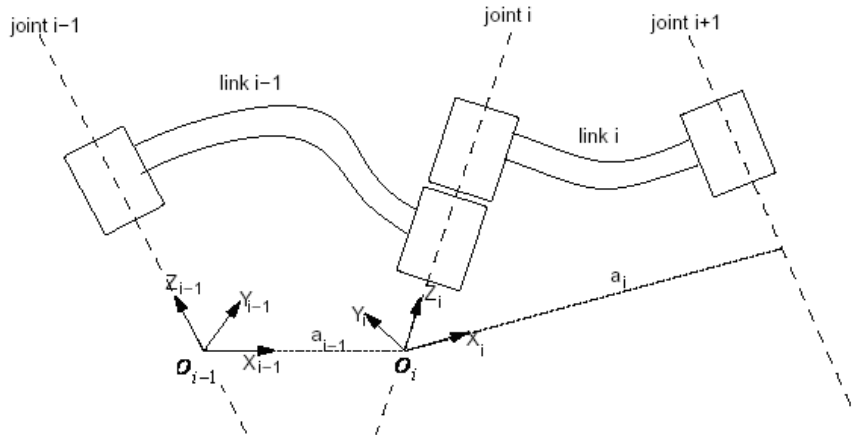


Figure 8: Modified convention

4.2 Modified Convention

The link and joint parameters in the classical convention as shown in figure 8 are as follows:

- Twist angle, α_{i-1} is the angle between z_{i-1} to z_i measured about x_{i-1}
- Link length, a_{i-1} is the distance from z_{i-1} to z_i measured along x_{i-1}
- Offset length, d_i is the distance from x_{i-1} to x_i measured along z_i
- Joint angle, θ_i is the angle between x_{i-1} to x_i measured about z_i

The D-H parameters are determined as per table 3.

Table 3: D-H parameters for modified convention

Link, i	a_{i-1}	α_{i-1}	d_i	θ_i
1				
2				

The frame transformation ${}^{i-1}T_i$ describing the finite motion from link $i-1$ to link i may then be expressed as the following sequence of elementary transformations, starting from link $(i-1)$:

1. A rotation α_{i-1} about x_{i-1} .
2. A translation a_{i-1} along the x_{i-1} axis
3. A rotation θ_i about z_i ;
4. A translation d_i along the same axis z_i ;

The homogeneous transformation ${}^{i-1}T_i$ is represented as a product of four basic transformations as follows:

$$\begin{aligned}
{}^{i-1}T_i &= R(x_{i-1}, \alpha_{i-1})T(x_{i-1}, a_{i-1})R(z_i, \theta_i)T(z_i, d_i) \\
&= \\
&\begin{bmatrix} 1 & 0 & 0 & 0 \\ 0 & C\alpha_{i-1} & -S\alpha_{i-1} & 0 \\ 0 & S\alpha_{i-1} & C\alpha_{i-1} & 0 \\ 0 & 0 & 0 & 1 \end{bmatrix} \begin{bmatrix} 1 & 0 & 0 & a_{i-1} \\ 0 & 1 & 0 & 0 \\ 0 & 0 & 1 & 0 \\ 0 & 0 & 0 & 1 \end{bmatrix} \begin{bmatrix} C\theta_i & -S\theta_i & 0 & 0 \\ S\theta_i & C\theta_i & 0 & 0 \\ 0 & 0 & 0 & 0 \\ 0 & 0 & 0 & 1 \end{bmatrix} \begin{bmatrix} 1 & 0 & 0 & 0 \\ 0 & 1 & 0 & 0 \\ 0 & 0 & 1 & d_i \\ 0 & 0 & 0 & 1 \end{bmatrix} \\
&= \begin{bmatrix} C\theta_i & -S\theta_i & 0 & a_{i-1} \\ S\theta_i C\alpha_{i-1} & C\theta_i C\alpha_{i-1} & -S\alpha_{i-1} & -d_i S\alpha_{i-1} \\ S\theta_i S\alpha_{i-1} & C\theta_i S\alpha_{i-1} & C\alpha_{i-1} & d_i C\alpha_{i-1} \\ 0 & 0 & 0 & 1 \end{bmatrix} \quad (7)
\end{aligned}$$

An alternative representation of ${}^{base}T_{end-effector}$ can be written as

$${}^{base}T_{end-effector} = {}^b T_e = \begin{bmatrix} r_{11} & r_{12} & r_{13} & p_x \\ r_{21} & r_{22} & r_{23} & p_y \\ r_{31} & r_{32} & r_{33} & p_z \\ 0 & 0 & 0 & 1 \end{bmatrix} \quad (8)$$

where r_{kj} 's represent the rotational elements of transformation matrix (k and $j = 1, 2$ and 3). p_x , p_y and p_z denote the elements of the position vector. For a six jointed manipulator, the position and orientation of the end-effector with respect to the base is given by

$${}^0T_6 = {}^0T_1(q_1) {}^1T_2(q_2) {}^2T_3(q_3) {}^3T_4(q_4) {}^4T_5(q_5) {}^5T_6(q_6) \quad (9)$$

where q_i is the joint variable (revolute or prismatic joint) for joint i , ($i = 1, 2, \dots, 6$).

Algorithm for modified D-H Convention:

Step - 1: Assigning of base frame: the base frame $\{0\}$ is assigned to link 0. The base frame $\{0\}$ is arbitrary. For simplicity chose z_0 along z_1 axis when the first joint variable is zero. Using this convention, we have $a_0 = 0$ and $\alpha_0 = 0$. This also ensures that

$d_1 = 0$ if the joint is revolute and $\theta_1 = 0$ if the joint is prismatic.

Step - 2: Identify links. The link frames are named by number according to the link to which they are attached (i.e. frame $\{i\}$ is attached rigidly to link i). For example, the frame $\{2\}$ is attached to link 2.

Identify joints. The z -axis of frame $\{i\}$, called z_i , is coincident with the joint axis i . The link i has two joint axes, z_i and z_{i+1} .

The z_i axis is assigned to joint i and z_{i+1} is assigned to joint $(i+1)$.

For $i = 1, \dots, n$ perform steps 3 to 6.

Step - 3: Identify the common normal between z_i and z_{i+1} axes, or point of intersection. The origin of frame $\{i\}$ is located where the common normal (a_i) meets the z_i axis.

Step - 4: Assign the z_i axis pointing along the i th joint axis.

Step - 5: Assign x_i axis pointing along the common normal (a_i) in the direction from z_i axis to z_{i+1} axis. In the case of $a_i = 0$, x_i is normal to the plane of z_i and z_{i+1} axes.

- As seen from figure 3.7, the joints may not necessarily be parallel or intersecting. As a result, the z -axes are skew lines. There is always one line mutually perpendicular to any two skew lines, called the common normal, which has the shortest distance between them. We always assign the x -axis of the local reference frames in the direction of the common normal. Thus, if a_i represents the common normal between z_i and z_{i+1} , the direction x_i is along a_i .
- If two joint z -axes are parallel, there are an infinite number of common normals present. We will pick the common normal that is collinear with the common normal of the previous joint.
- If the z -axes of two successive joints are intersecting, there is no common normal between them (or it has zero length). We will assign the x -axis along a line perpendicular to the plane formed by the two axes.

Step - 6: The y_i axis is selected to complete right-hand coordinate system.

Step - 7: Assigning of end-effector frame: If the joint n is revolute, the direction of x_n is chosen along the direction of x_{n-1} when $\theta_n = 0$ and the origin of frame $\{n\}$ is chosen so that $d_n = 0$. If the joint n is prismatic, the direction of x_n is chosen so that

$\theta_n = 0$ and the origin of frame $\{n\}$ is chosen at the intersection of x_{n-1} with z_n so that $d_n = 0$.

Step – 8: The link parameters are determined as mentioned in table 4.

Table 4: Link parameters

Link, i	a_{i-1}	α_{i-1}	d_i	θ_i
1				
2				

- a_{i-1} = the distance from z_{i-1} to z_i measured along x_{i-1}
- α_{i-1} = the angle between z_{i-1} to z_i measured about x_{i-1}
- d_i is the distance from x_{i-1} to x_i measured along z_i
- θ_i is the angle between x_{i-1} to x_i measured about z_i

Step - 9: Form ${}^0T_n = {}^0T_1 {}^1T_2 {}^2T_3 \dots {}^{n-1}T_n$. This gives the position and orientation of the end-effector frame expressed in the base coordinates.

5. CASE STUDIES

RR planar manipulator is used to differentiate between D-H classical convention and D-H modified convention.

5.1 Case Study for D-H Classical Convention

Formulate the forward kinematic model of two-degree of freedom RR planar manipulator as shown in figure 9. Find the home position of the manipulator. Use classical D-H convention.

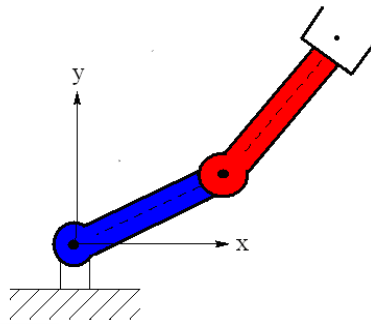


Figure 9: Two-degree of freedom RR Planar manipulator

Solution:

The manipulator consists of two joints. The two joints are revolute joints. The scheme of frame assignment of the manipulator is shown in figure 10. For revolute joint, $d = 0$.

The manipulator consists of two joints (i.e. $n = 2$). The axis of revolute joint is perpendicular to the paper (figure 10).

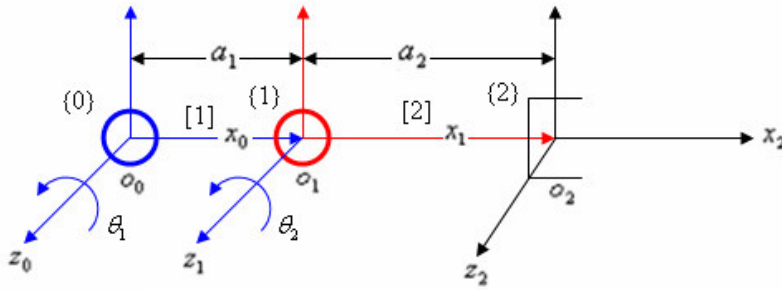


Figure 10: Frame assignment for two-degrees of freedom RR planar manipulator

Step -1: The joints are revolute type. The two links are numbered [1] and [2]. The base frame is {0} and frames for the rest of links are numbered {1} and {2}. The joint axes are labeled as z_0 , z_1 , and z_2 .

Step -2: The location of frame to the base is arbitrary. The x_0 axis, which is perpendicular to z_0 , is chosen to be parallel to x_1 when the first joint angle variable $\theta_1 = 0$ in the home position. The y_0 axis is defined by the cross product $y_0 = z_0 \times x_0$.

For $i = 1$, perform steps 3 to 5.

Step -3: The link 1 has two joint axes, z_0 and z_1 . The z_0 axis is assigned to joint 1. The z_1 axis is assigned to joint 2. There is a common normal between z_0 and z_1 axes. Axis z_1 is parallel to z_0 axis. The origin o_1 is located in any convenient position along z_1 axis as shown in figure 3.12.

Step -4: Axis x_1 is established along the common normal between z_0 and z_1 through o_1 .

Step -5: The y_1 axis is defined by the cross product of $y_1 = z_1 \times x_1$.

For $i = 2$

Step -3: The link 2 has one joint axis, z_1 which is common to link 1 and link 2. The second end of link 2 is rigidly connected to the end-effector. The z_2 axis is set parallel to z_1 axis. Since z_1 and z_2 axes are parallel, the origin o_2 is located in any convenient position along z_2 axis as shown in figure 3.12.

Step -4: The common normal between z_1 and z_2 axes is x_2 . Since the joint 2 is revolute, x_2 axis is chosen in the direction parallel to x_1 axis and passing through the origin o_2 .

Step -5: The y_2 axis is defined by the cross product of $y_2 = z_2 \times x_2$.

Step -6: Establish the end-effector frame {2} as shown in figure 3.12.

Step -7: The joint-link parameters are tabulated in table 5.

Table 5: Joint-link parameters of classical convention

Link, i	a_{i-1}	a_{i-1}	d_i	θ_i
1	a_1	0	0	θ_1
2	a_1	0	0	θ_2

Step -8: Form the homogeneous transformation matrices ${}^{i-1}T_i$ by substituting the above parameters into equation (3.7)

$${}^0T_1 = \begin{bmatrix} c_1 & -s_1 & 0 & a_1c_1 \\ s_1 & c_1 & 0 & a_1s_1 \\ 0 & 0 & 1 & 0 \\ 0 & 0 & 0 & 1 \end{bmatrix}$$

$${}^1T_2 = \begin{bmatrix} c_2 & -s_2 & 0 & a_2c_2 \\ s_2 & c_2 & 0 & a_2s_2 \\ 0 & 0 & 1 & 0 \\ 0 & 0 & 0 & 1 \end{bmatrix}$$

Step- 9: Form ${}^0T_2 = {}^0T_1 {}^1T_2$. This gives the position and orientation of the tool frame expressed in base coordinates.

$${}^0T_2 = \begin{bmatrix} c_1 & -s_1 & 0 & a_1c_1 \\ s_1 & c_1 & 0 & a_1s_1 \\ 0 & 0 & 1 & 0 \\ 0 & 0 & 0 & 1 \end{bmatrix} \times \begin{bmatrix} c_2 & -s_2 & 0 & a_2c_2 \\ s_2 & c_2 & 0 & a_2s_2 \\ 0 & 0 & 1 & 0 \\ 0 & 0 & 0 & 1 \end{bmatrix} = \begin{bmatrix} c_{12} & -s_{12} & 0 & a_1c_1 + a_2c_{12} \\ s_{12} & c_{12} & 0 & a_1s_1 + a_2s_{12} \\ 0 & 0 & 1 & 0 \\ 0 & 0 & 0 & 1 \end{bmatrix}$$

The home position of the manipulator is corresponding $\theta_1 = \theta_2 = 0$. By substituting these values in 0T_2 , we get the home position of the manipulator.

$${}^0T_2 = \begin{bmatrix} 1 & 0 & 0 & a_1 + a_2 \\ 0 & 1 & 0 & 0 \\ 0 & 0 & 1 & 0 \\ 0 & 0 & 0 & 1 \end{bmatrix}$$

5.2 Case Study for D-H Modified Convention

Derive forward kinematics of two-degree of freedom RR planar manipulator as shown in figure 11. Find the home position of the manipulator. Use modified D-H convention.

Solution:

The manipulator consists of two joints. The two joints are revolute joints. The scheme of frame assignment of the manipulator is shown in figure 11. For revolute joint, $d = 0$. The axis of revolute joint is perpendicular to the paper.

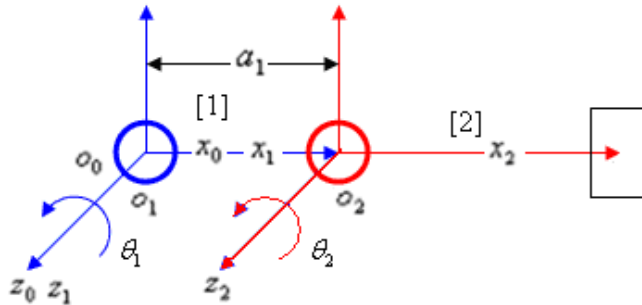


Figure 11: Frame assignment for two-degrees of freedom RR planar manipulator

Step -1: The base frame $\{0\}$ is assigned to link 0. The base frame $\{0\}$ is arbitrary. For simplicity chose z_0 along z_1 axis when the first joint variable is zero. Using this convention, we have $a_0 = 0$ and $\alpha_0 = 0$. This also ensures that $d_1 = 0$ as the joint 1 is revolute.

Step - 2: The manipulator consists of two links. The two links are numbered [1] and [2]. The link frames are numbered as {1} and {2}. The joint 1 is between link 0 and link 1 and its z axis is z_1 . The joint 2 is between link 1 and link 2 and its z axis is z_2 .

For $i = 1$, perform steps 3 to 6.

Step - 3: There is a common normal between z_1 and z_2 axes. The origin o_1 of frame {1} is located where the common normal (a_1) meets the z_1 axis.

Step - 4: Assign the z_1 axis pointing along the 1st joint axis.

- Step – 5: The x_1 axis is pointing along the common normal (a_1) in the direction from z_1 axis to z_2 axis and passing through the origin o_1 .
- Step – 6: The y_1 axis is selected to complete right-hand coordinate system.
For $i = 2$, perform steps 3 to 6.
- Step – 3: The link 2 consists of only one joint that is z_2 axis and the other end of link 2 is rigidly fixed to the end-effector. There is a common normal between z_2 and z_3 axes (here: the z_3 axis is belonging to the end-effector). The origin o_2 of frame {2} is located where the common normal (a_2) meets the z_2 axis.
- Step – 4: Assign the z_2 axis pointing along the 2nd joint axis.
- Step – 5: The x_2 axis is pointing along the common normal (a_2) in the direction from z_2 axis to z_3 axis and passing through the origin o_2 .
- Step – 6: The y_2 axis is selected to complete right-hand coordinate system.
- Step – 7: Assigning of end-effector frame: The direction of x_3 aligns with x_2 when $\theta_3 = 0$ and the origin of frame {3} is chosen so that $d_3 = 0$.
- Step – 8: The link parameters are determined as mentioned in table 6.

Table 6: Link parameters of modified convention

Link, i	a_{i-1}	a_{i-1}	d_i	θ_i
1	0	0	0	θ_1
2	a_1	0	0	θ_2

Step - 9: Form ${}^0T_2 = {}^0T_1 {}^1T_2$. This gives the position and orientation of the end-effector frame expressed in the base coordinates.

$${}^0T_1 = \begin{bmatrix} c_1 & -s_1 & 0 & 0 \\ s_1 & c_1 & 0 & 0 \\ 0 & 0 & 1 & 0 \\ 0 & 0 & 0 & 1 \end{bmatrix}$$

$${}^1T_2 = \begin{bmatrix} c_2 & -s_2 & 0 & a_1c_2 \\ s_2 & c_2 & 0 & a_1s_2 \\ 0 & 0 & 1 & 0 \\ 0 & 0 & 0 & 1 \end{bmatrix}$$

$${}^0T_2 = \begin{bmatrix} c_1 & -s_1 & 0 & 0 \\ s_1 & c_1 & 0 & 0 \\ 0 & 0 & 1 & 0 \\ 0 & 0 & 0 & 1 \end{bmatrix} \times \begin{bmatrix} c_2 & -s_2 & 0 & a_1c_2 \\ s_2 & c_2 & 0 & a_1s_2 \\ 0 & 0 & 1 & 0 \\ 0 & 0 & 0 & 1 \end{bmatrix} = \begin{bmatrix} c_{12} & -s_{12} & 0 & a_1c_{12} \\ s_{12} & c_{12} & 0 & a_1s_{12} \\ 0 & 0 & 1 & 0 \\ 0 & 0 & 0 & 1 \end{bmatrix}$$

Note: The forward kinematics ends at a frame, whose origin lies on the last joint axis z_2 , therefore, a_2 does not appear in the link parameters.

5.3 Difference between Classical and Modified Conventions

The position and orientation of the end-effector frame expressed in the base coordinates obtained by the modified D-H convention are given by:

$${}^0T_2 = \begin{bmatrix} c_1 & -s_1 & 0 & 0 \\ s_1 & c_1 & 0 & 0 \\ 0 & 0 & 1 & 0 \\ 0 & 0 & 0 & 1 \end{bmatrix} \times \begin{bmatrix} c_2 & -s_2 & 0 & a_1c_2 \\ s_2 & c_2 & 0 & a_1s_2 \\ 0 & 0 & 1 & 0 \\ 0 & 0 & 0 & 1 \end{bmatrix} = \begin{bmatrix} c_{12} & -s_{12} & 0 & a_1c_{12} \\ s_{12} & c_{12} & 0 & a_1s_{12} \\ 0 & 0 & 1 & 0 \\ 0 & 0 & 0 & 1 \end{bmatrix}$$

The forward kinematics ends at a frame, whose origin lies on the last joint axis z_2 as per modified D-H convention, therefore, a_2 does not appear in the link parameters as shown in figure 12. The home position of the manipulator is corresponding $\theta_1 = \theta_2 = 0$. By substituting these values in 0T_2 , we get the home position of the manipulator.

$${}^0T_2 = \begin{bmatrix} 1 & 0 & 0 & a_1 \\ 0 & 1 & 0 & 0 \\ 0 & 0 & 1 & 0 \\ 0 & 0 & 0 & 1 \end{bmatrix}$$

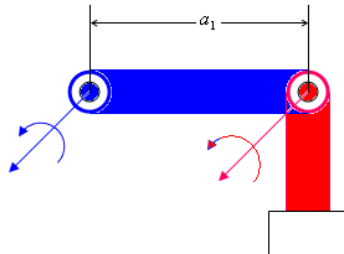


Figure 12: Home position of RR planar manipulator as obtained by modified D-H convention.

The position and orientation of the tool frame derived from the classical D-H convention are given by

$${}^0T_2 = \begin{bmatrix} c_1 & -s_1 & 0 & a_1c_1 \\ s_1 & c_1 & 0 & a_1s_1 \\ 0 & 0 & 1 & 0 \\ 0 & 0 & 0 & 1 \end{bmatrix} \times \begin{bmatrix} c_2 & -s_2 & 0 & a_2c_2 \\ s_2 & c_2 & 0 & a_2s_2 \\ 0 & 0 & 1 & 0 \\ 0 & 0 & 0 & 1 \end{bmatrix} = \begin{bmatrix} c_{12} & -s_{12} & 0 & a_1c_1 + a_2c_{12} \\ s_{12} & c_{12} & 0 & a_1s_1 + a_2s_{12} \\ 0 & 0 & 1 & 0 \\ 0 & 0 & 0 & 1 \end{bmatrix}$$

The home position of the manipulator is corresponding $\theta_1 = \theta_2 = 0$. By substituting these values in 0T_2 , we get the home position of the manipulator as shown in figure 13.

$${}^0T_2 = \begin{bmatrix} 1 & 0 & 0 & a_1 + a_2 \\ 0 & 1 & 0 & 0 \\ 0 & 0 & 1 & 0 \\ 0 & 0 & 0 & 1 \end{bmatrix}$$

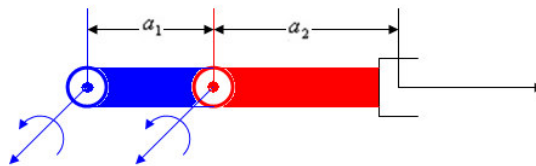


Figure 13: Home position of RR planar manipulator as obtained by classical convention.

6. CONCLUSIONS

Two conventions have been established for assigning coordinate frames, each of which allows some freedom in the actual coordinate frame attachment.

D-H parameter	Classical convention	Modified convention
Joint axis	z_{i-1} is for joint i	z_i is for joint i
Link length (a_i)	The distance from o_i to the intersection of the z_{i-1} and x_i axes along the x_i axis	The distance from z_i to z_{i+1} measured along x_i
Twist angle (α_i)	The angle from the z_{i-1} axis to the z_i axis about the x_i axis	The angle between z_i to z_{i+1} measured about x_i
Offset length (d_i)	The distance from the origin of the $(i-1)$ frame to the intersection of the z_{i-1} axis with the x_i axis along the z_{i-1} axis	The distance from x_{i-1} to x_i measured along z_i
Joint angle (θ_i)	The angle between the x_{i-1} and x_i axes about the z_{i-1} axis	The angle between x_{i-1} to x_i measured about z_i

This paper discusses both the conventions (classical and modified) for the forward kinematics of RR manipulator. One can have choice of using any one method. Most of the universities are having several affiliated technical institutions. In such situations, the question paper is set by the university for the end examinations. It may happen that the answer scripts may consist of either of the conventions. Teachers are requested to correct the answer scripts as per the convention followed by the student but not the convention that he taught in the class room.

REFERENCES

1. J.Denavit, R.S.Hartenberg, A kinematic notation for lower-pair mechanisms based on matrices, Transactions ASME Journal of Applied Mechanics, 1955: 23, 215–221.
2. R.Paul, Robot manipulators: mathematics, programming, and control: the computer control of robot manipulators, Cambridge, MA: MIT Press, 1981: ISBN 978-0-262-16082-7.
3. K.S.Fu, R.C.Gonzalez, and C.S.G.Lee, Robotics: control, sensing, vision and intelligence, McGraw Hill, New York, 1987: ISBN 0-07-022625-3.
4. Spong, W.Mark, M.Vidyasagar, Robot Dynamics and Control, New York: John Wiley & Sons, 1989: ISBN 9780471503521.
5. John J Craig, Introduction to Robotics: mechanics and control, Pearson Education, India, 2001: ISBN 8131718360.
6. T.Yoshikawa, Foundations of Robotics: analysis and control, Cambridge, MA: MIT Press, 1998: ISBN026224028-9.
7. A. Chennakesava Reddy, G. Satish Babu, Dynamic mechanisms of kneecap, compliant ankle and passive swing leg to simulate human walking robot, International Journal of Advanced Mechatronics and Robotics, 2011: 3(1), pp. 1-7.
8. B. Rajasekhara Reddy, A. Chennakesava Reddy, Obstacle avoidance of planar redundant manipulators for pick-and-place operations using real-coded genetic algorithm, National Conference on Advances in Manufacturing Technology, Palghat, 15-16th February 2003, 5-A-2.
9. A. Chennakesava Reddy, B. Kotiveerachari, P. Ram Reddy, Kinematic model of a flexible link using local curvatures as the deformation coordinates, National Conference on Advances in Manufacturing Technology, Palghat, 15-16th February 2003, 1-A-7.
10. B. Rajasekhara Reddy, A. Chennakesava Reddy, Dynamic modeling of two-link robot arm driven by DC motors using linear graph theory and principles of mechanics, National Conference on Trends in Mechanical Engineering, Warangal, 30th August 2003, pp.130-132.
11. A. Chennakesava Reddy, P. Ram Reddy, B. Kotiveerachari, Two methods for computing reduced-form dynamics of closed – chain mechanism, National Conference on Trends in Mechanical Engineering, Warangal, 30th August 2003, pp.133-136.
12. B. Kotiveerachari, A. Chennakesava Reddy, Kinematic and static analysis of gripper fingers using reciprocal screws, National Conference on Computer integrated Design and Manufacturing, Coimbatore, 28-29th November 2003, pp.121-124.
13. A. Chennakesava Reddy, P. Ram Reddy, Hazard detection for multi - agent reactive robotic system using on - line software analysis of safety constraints, National Conference on Computer integrated Design and Manufacturing, Coimbatore , 28-29th November 2003, pp.294-301.

14. B. Kotiveerachari, A. Chennakesava Reddy, Non-linear finite element modeling for dynamic trajectory controlling of robotic manipulators with flexible links, National Conference on Advanced Materials and Manufacturing Techniques, Hyderabad, 08-09th March 2004, pp.265-272.
15. A. Chennakesava Reddy, P. Rami Reddy, Elastic rigid-body dynamic modeling of planar parallel robot actuated by servomotors, National Conference on Advanced Materials and Manufacturing Techniques, Hyderabad , 08-09th March 2004, pp.273-279.
16. A. Chennakesava Reddy, P. Ram Reddy, B. Kotiveerachari, Optimization of path dependent trajectory for an arm - like serial chain robot using genetic algorithm, National Conference on Recent Trends in CAD/CAM, Bidar, 29-30th July 2004, pp.25-33.
17. A. Chennakesava Reddy, P. Ram Reddy, B. Kotiveerachari, Optimum trajectory path planning for 3-dof planar robot with minimum joint disturbances, National Conference on Advances in Manufacturing Technology in the Era of Globalization, Pune, 21-22nd January 2005, pp.08.
18. A. Chennakesava Reddy, P. Ram Reddy, B. Kotiveerachari, Generation of RPR and RRR planar parallel robots using computer program, National Level Technical Symposium Nalgonda , 12th March 2005, P2.
19. A. Chennakesava Reddy, A.C.S Kumar, Proportional and derivative control system to reduce the computations of transformation between different space reference frames of SCARA serial manipulator, National Conference on Computer Applications in mechanical Engineering, Anantapur, 21st December 2005, pp.115-119.
20. A. Chennakesava Reddy, P. Ram Reddy, B. Kotiveerachari, Optimization of robot arm path planning without collision in its workspace using genetic algorithm, International Conference on Emerging Technologies in Intellectual System and Control, Coimbatore, 5-7th January 2005, C06-1-9.
21. A. Chennakesava Reddy, P. Ram Reddy, B. Kotiveerachari, Studies on the effect of vibration of robot links on the end point trajectory path using cad, International Conference on Recent Advances in Material Processing Technology, Kovilpatti, 23-25th February 2005, pp.195-202.
22. A. Chennakesava Reddy, Robot and its engineering field applications, Journal of Engineering Advances, 2002:14(1), pp.33-35.
23. A. Chennakesava Reddy, B. Kotiveerachari, P. Ram Reddy, Dynamic trajectory planning of robot arms, Journal of Manufacturing Technology, 2004:3(3), pp.15-18.
24. A. Chennakesava Reddy, B. Kotiveerachari, P. Ram Reddy, Finite element analysis of flexibility in mobile robotic manipulators, Journal of Institution of Engineers, 2004:85(2), pp.27-31.
25. A. Chennakesava Reddy , B. Kotiveerachari, Different methods of robotic motion planning for assigning and training paralysed person, Journal of Institution of Engineers, 2008:88(2), pp. 37-41.

AWJM PROCESS OPTIMIZATION USING PRINCIPAL COMPONENT ANALYSIS (PCA)

B. SATYANARAYANA^a, G. SRIKAR^b

^aAssociate Professor, Department of Mechanical Engineering, VNR VJIET, Bachupally, Nizampet (SO), Hyderabad-500090,

^bB.Tech Student, Department of Mechanical Engineering, VNR VJIET, Bachupally, Nizampet (SO), Hyderabad-500090.

Abstract: Abrasive water jet machining (AWJM) is a non-conventional machining process that uses high pressure water jet mixed with abrasive particles for cutting various materials such as plastics, insulation, rubber, food, automotive, carpeting, ceramics and super alloys like Inconel 718. Since there is no thermal and electrical energy involved in this process many material defects are avoided. Material Removal Rate (MRR) and Kerf Width (KW) are the two important parameters in AWJM process, which decides the production rate and economics of the machining operation. Therefore, these two are considered as performance characteristics in this paper. Principal Component Analysis (PCA) method is used to optimize the multiple response problems. PCA method combines all principal components in order to form a multi-response performance index (TPCI). Thus, multi-response problem is converted into a single response problem and Taguchi analysis can be applied with TPCI as the response. The objective of this paper is to optimize the machining parameters in AWJM process to get higher MRR and lower Kerf Width simultaneously while machining Inconel 718 work material using Principal Component Analysis (PCA) method. In addition the effect of AWJM parameters on Material Removal Rate (MRR) and Kerf Width (KW) are also discussed.

Keywords: AWJM, Inconel 718, Material Removal Rate (MRR), Kerf Width (KW) and Principal Component Analysis (PCA)

Address all correspondence to: sanbollu@gmail.com

1. INTRODUCTION

Abrasive water jet machining (AWJM) is an unconventional cutting process that was first developed in 1974 to clean metal surface prior to surface treatment. It was found that adding abrasives to the water jet greatly increased its cutting ability by many folds and since then it has found use as a machining process to cut hard materials like ceramics, glass, and tough composites. AWJM employs water jet stream to which abrasive particles are added. The material removal takes place by the erosive action of the abrasives on work, but not the water. The output of the process depends on various process parameters and the ones chosen for this project are abrasive flow rate, pressure, and standoff-distance [1].

2. PRINCIPLE

In this process, a focused stream of high-pressure water at a high velocity is made to enter into a mixing chamber where the abrasive particles are added. Here, gradual entrainment of irregularly shaped, sharp edged abrasive particles with the water jet takes place. Material removal is by erosion of the high velocity abrasive particles on the work material [2, 3]. A schematic layout of AWJM process is shown in figure 1. The characteristics of AWJM Process are presented in table 1.

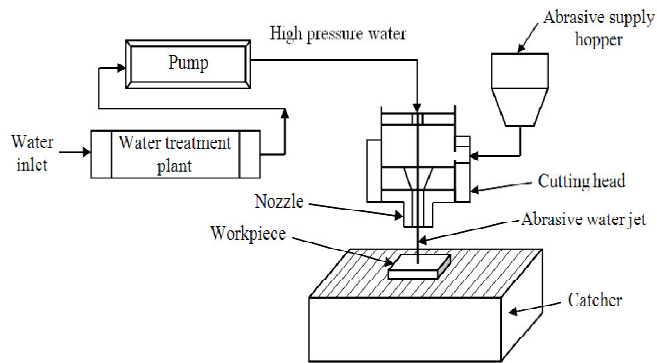


Figure 1: Schematic layout of AWJM process [3]

Table 1: Characteristics of AWJM Process

Medium	Air, Water, CO ₂ , N ₂
Abrasive	SiC, Al ₂ O ₃ (of size 20 μ to 50 μ)
Flow rate of abrasive	1 to 4 lb/min
Velocity	150 to 300 m/min
Pressure	10 to 55 kpsi
Nozzle size	0.07 to 1 (mm)
Material of nozzle	Stainless steel, Sapphire
Nozzle life	12 to 300 hr
Standoff distance	0.25 to 15 mm (8mm generally)
Work material	Non Metals like glass, ceramics, and granites. Metals and alloys of hard materials like germanium, silicon, etc.
Part application	Drilling, cutting, de-burring, and cleaning.

3. LITERATURE SURVEY

The extensive work on various work materials has been carried out in this field of research has given rise to many improvements and optimizations. All work starts by deciding which type of material shall be used for the experiment. Many researchers and scholars have found AWJM to be a viable process for machining of materials like Aluminium,

Steel, Glass, Rubber [4], Inconel, Titanium and Aluminium alloys [5]. Research has also been done on the use of metal cutting for composites like Kevlar [6, 7, 8], glass/epoxy laminates [9], Aramid fiber reinforced composites [10, 11] and ZC63/SiC_p metal matrix composite (MMC) [12].

The important process parameters for AWJM are found as water jet pressure, feed rate, nozzle diameter, standoff distance, material thickness [13, 14, 15], traverse speed, abrasive flow rate, size of orifice, size of mixing tube, drilling time, speed, feed, depth of cut [16, 17], type of abrasive material [18], mass flow rate of water, and standoff distance.

For analyzing and optimizing data, methods like Principal Component Analysis [19, 20] which involves reducing the dimensions of data and forming Eigen vectors, Taguchi's method in which a loss function is developed to find the deviation of a characteristic from its target value, Grey Relational Analysis where all data is normalized to a scale of zero to one to find the correlation between actual and normalized values, or even their combination like Taguchi Grey Relational Analysis [21] can be used. This is done to optimize output parameter like material removal rate (MRR), kerf width, and surface roughness [22].

4. PRINCIPAL COMPONENT ANALYSIS (PCA)

Lindsay I Smith (2002) defines "Principal Component Analysis as a way of identifying patterns in data, and expressing it in such a way as to highlight their similarities and differences" [22].

Sander Magi and Tuan Anh (2009) explains PCA as "A statistical tool used to explore, sort and group data. It takes a large number of correlated (interrelated) variables and transforms this data into smaller number of uncorrelated variables, thus making it easier to operate the data and make predictions".

The advantage of PCA is that once the patterns in the data are found it can be compressed, i.e. by reducing the number of dimensions, without much loss of information. PCA is concerned with explaining the variance-covariance structure of data through a few linear combinations of the original variables.

PCA starts with data procurement. Here the experiment consists of 27 values of MRR and Kerf width. The data is then normalized which is used to calculate the variance-covariance matrix (Eq.1). From here the Eigen values and Eigen vectors are obtained and a feature vector is formed. Total Principle Component Index (TPCI) (Eq.2) is calculated from the data obtained from feature vector. S/N ratios (Eq.3) are calculated using TPCI.

$$\text{Cov}(x, y) = \sum_{i=1}^n \frac{(x_i - \bar{x})(y_i - \bar{y})}{n - 1} \quad (1)$$

$$TPCI = \sqrt[3]{(p_1 + p_2)} \quad (2)$$

$$\frac{S}{N} = -10 \log \left(\frac{1}{k} \sum_{i=1}^k \frac{1}{TPCI^2} \right) \quad (3)$$

5. EXPERIMENTATION

Experiments are conducted on Inconel 718 work piece using Dardi Water Jet flying arm Computer Numeric Control Abrasive Water Jet Cutting Machine equipped with Karoline Machine Tool model of water jet pump. The significant AWJM process parameters, Abrasive flow rate, Water pressure and Standoff distance are chosen as input parameters. The Material Removal Rate and Kerf Width are the performance measures. The details of experimentation are discussed in this section.

5.1 Material

INCONEL 718 is a Nickel-Chromium precipitation hardened alloy which has high creep-rupture strength at high temperatures to about 700°C (1290°F). It has many applications in the field of aerospace, nuclear reactors, and gas turbines.

5.2 Machining

The equipment used for machining the samples is DWJ (Dardi Water Jet) flying arm CNC (Computer Numeric Control) shown in figure 2, abrasive water jet cutting machine equipped with KMT (Karoline Machine Tool) model of water jet pump with the designed pressure of 3800 bar (55000psi) and rated discharge of 2.3l/min. The machine is equipped with a gravity feed type of abrasive hopper, an abrasive feeder system, a pneumatically controlled valve and a work table with dimension of 1600mm×2100mm. For the nozzle assembly shown in figure 3, it has an orifice of 0.25mm diameter of sapphire nozzle.



Figure 2: DWJ flying arm CNC

The abrasives were delivered using compressed air from a hopper to the mixing chamber and were regulated using a metering disc. All the cutting experiments were performed on INCONEL 718 material and are single pass experiments conducted by choosing jet impact angle of 90°. Granite sand abrasives were used as abrasives.



Figure 3: Sapphire tipped nozzle

A total of three machining parameters with three levels were chosen as the factors such that the levels are sufficiently far apart so that they cover wide range. The factors and their alternative levels are listed in table 2. Full factorial design of experiment technique and L_{27} orthogonal array were used to conduct the experiments. Figure 4 shows the INCONEL 718 work piece after the AWJM machining process.

Weight of the work piece was measured before and after iteration of cut and MRR was calculated as weight difference of the work piece before and after machining with respect to time of cutting. The machined work piece was put under a profile projector (figure 5) and a profile (figure 6) was taken and used to measure KW.

Table 2: factors and levels for the experimentation

Factor	Level 1	Level 2	Level 3
Abrasive flow rate (A)	2.7	2.85	3
Water Pressure (B)	30	40	50
Standoff distance (C)	3	4	5



Figure 4: Inconel 718 work piece after machining



Figure 5: Profile projector with work piece to measure kerf width

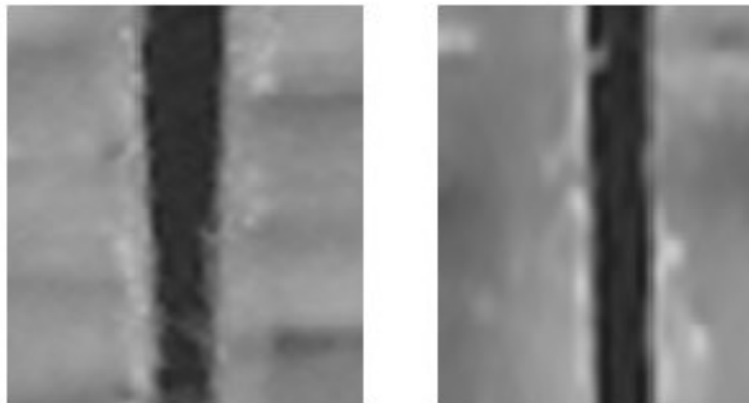


Figure 6: Scanned view of produced Kerf

6. RESULTS AND DISCUSSION

The results obtained from experimentation are presented in table 3. The Table 3 also presents the values of TPCI and its S/N ratios. These values are calculated using the Eq. 1 to 3. The calculation of S/N ratios was extended to factor level and is tabulated in Table 4. MINITAB (version 17) statistical software tool was used to analyze the data. From the main effects plot (figure 7), it can be seen that the best condition for abrasive flow rate factor is level 1 (2.7lb/min), for Pressure is level 3 (50kpsi), for standoff distance is level 1(3mm). Thus, the optimum conditions chosen were: A1-B3-C1 combination.

Table 3: Process parameters in three levels with respective output parameters and S/N ratios

S. No	Abrasive flow rate	Water pressure	Standoff distance	MRR (x)	Kerf Width (y)	TPCI	S/N Ratio (dB)
1	2.7	30	3	799.14	2.04	0.571	-4.865
2	2.7	30	4	810	2.14	0.543	-5.312
3	2.7	30	5	825.42	2.18	0.545	-5.279
4	2.7	40	3	993.6	1.8	0.740	-2.619
5	2.7	40	4	939.6	1.7	0.732	-2.709
6	2.7	40	5	880.2	1.6	0.722	-2.831
7	2.7	50	3	1053.2	1.54	0.790	-2.045
8	2.7	50	4	978.75	1.4	0.782	-2.132
9	2.7	50	5	958.5	1.36	0.780	-2.154
10	2.85	30	3	808.13	2.1	0.558	-5.072
11	2.85	30	4	770.89	2.18	0.439	-7.146
12	2.85	30	5	804.41	2.24	0.473	-6.502
13	2.85	40	3	955.8	1.8	0.724	-2.800
14	2.85	40	4	955.8	1.82	0.722	-2.835
15	2.85	40	5	982.8	1.84	0.730	-2.735
16	2.85	50	3	1012.5	1.6	0.771	-2.259
17	2.85	50	4	985.5	1.58	0.764	-2.334
18	2.85	50	5	985.5	1.52	0.771	-2.256
19	3	30	3	763.44	2.1	0.489	-6.205
20	3	30	4	782.06	2.05	0.547	-5.243
21	3	30	5	782.06	2.06	0.542	-5.315
22	3	40	3	912.6	1.62	0.732	-2.705
23	3	40	4	977.4	1.8	0.733	-2.694
24	3	40	5	972	1.82	0.728	-2.754
25	3	50	3	924.75	1.42	0.763	-2.354
26	3	50	4	951.75	1.46	0.767	-2.304
27	3	50	5	924.75	1.4	0.765	-2.327

Table 4: S/N ratios of input parameters at factor level

Factor	Level 1	Level 2	Level 3
Abrasive flow rate (A)	-3.474	-3.760	-3.516
Pressure (B)	-5.660	-2.742	-2.241
Standoff distance (C)	-3.436	-3.634	-3.573

6.1 Verification

A verification experiment was conducted to ascertain the accuracy of the process whose results are tabulated in table 5. The S/N ratio of predicted value and confirmation test values are compared for validity of the optimum condition. It is found that the S/N ratio value of confirmation test is within the limits of the predicted value and the objective is fulfilled. Hence, these suggested optimum conditions can be adopted.

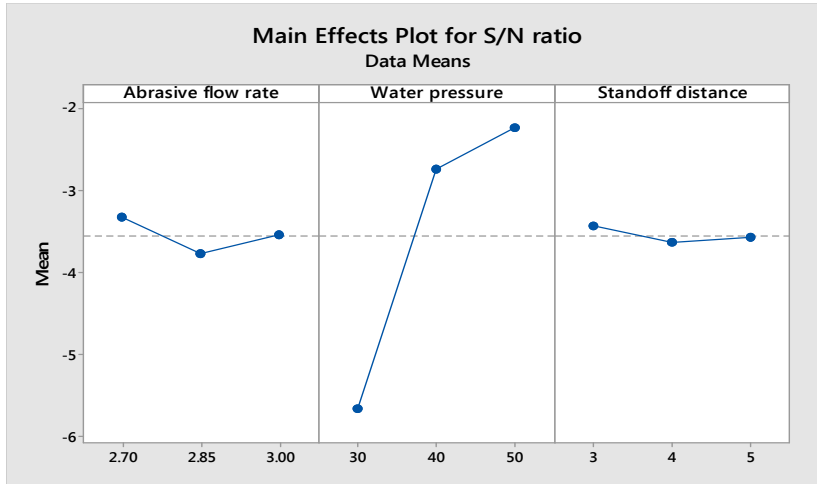


Figure 7: Main effect plot for S/N ratios

Table 5: Verification Experiment

S. No	Abrasive flow rate	Water pressure	Standoff distance	MRR (x)	Kerf Width (y)	TPCI	S/N Ratio (dB)
1	2.7	50	3	1060.5	1.51	0.78	-2.154

$$\eta_{\text{predicted}} = Y + (\overline{A1} - Y) + (\overline{B3} - Y) + (\overline{C1} - Y) \quad (1)$$

$$= \overline{A1} + \overline{B3} + \overline{C1} - 2Y$$

$$\eta_{\text{predicted}} = -2.055 \text{ dB} \quad (2)$$

$$\eta_{\text{confirmation}} = -2.154 \text{ dB} \quad (3)$$

6.2 Analysis of Variance

ANOVA was conducted for the input process parameters to understand their influence on the overall performance of the process. Table 6 shows ANOVA being conducted at 95% statistical confidence level. It shows that the influence of water pressure is more on MRR and KW followed by Abrasive flow rate and standoff distance.

Table 6: ANOVA for the input parameters

Source	DF	Seq SS	Adj SS	Adj MS	F	P
Abrasive flow rate	2	0.885	0.885	0.443	2.32	0.124
Water pressure	2	61.361	61.361	30.680	161.02	0.000
Standoff distance	2	0.185	0.185	0.093	0.49	0.622
Error	20	3.811	3.811	0.191		
Total	26	66.242				

6.3 Effect of Abrasive flow rate on MRR & KW

The influence of abrasive flow rate on MRR is shown in figure 8 (a). As the rate of flow of abrasives increases the material removal rate increases but this also causes a larger cut on the work piece. The influence of abrasive flow rate on KW is shown in figure 8 (b). As the rate of flow of abrasives increases a larger kerf is machined on the work piece.

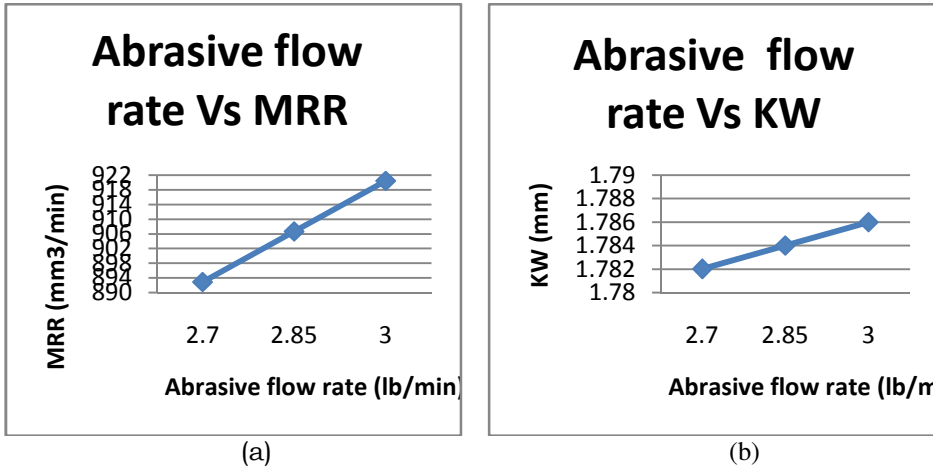


Figure 8: Influence of Abrasive Flow Rate on (a) MRR & (b) KW

6.4 Effect of Water Pressure on MRR & KW

The influence of water pressure on MRR is shown in figure 9 (a). As the jet pressure increases the material is removed faster hence the output of the process is improved. The influence of water pressure on KW is shown in figure 9 (b). This increases the kinetic energy of the abrasive particles and produces a finer Kerf but with larger dimensions.

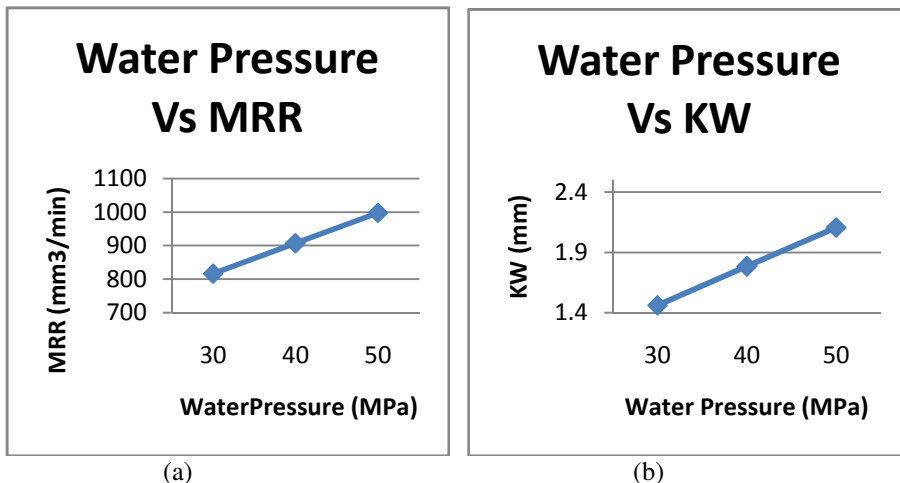


Figure 9: Influence of Water Pressure on (a) MRR & (b) KW

6.5 Effect of Standoff Distance on MRR & KW

The influence of standoff distance on MRR is shown in figures 10 (a). Higher standoff distance means that the kinetic energy of the particles will be lower by the time they come in contact with the work surface and results in lower material removal rate. The influence of standoff distance on is shown in figures 10 (b). From the figure it is evident that the standoff distance influences a little on the KW of work piece.

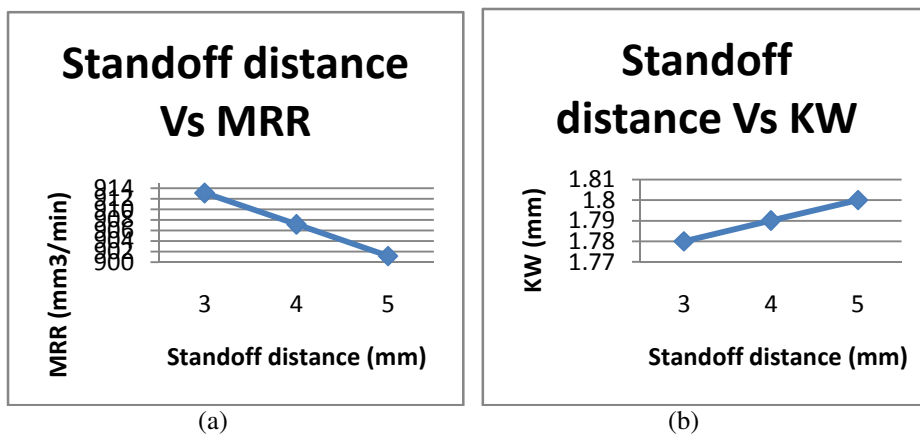


Figure 10: Influence of Standoff Distance on (a) MRR & (b) KW

7. CONCLUSIONS

Experimental investigations have been carried for the MRR & KW in abrasive water jet cutting of Inconel 718. The use of the Taguchi method with PCA to optimize the AWJM process with multiple performance characteristics has been successfully reported in this paper. The effects of different operational parameters such as: water pressure, abrasive mass flow rate and nozzle standoff distance on MRR & KW have been investigated:

- The optimal values of input parameters are abrasive flow rate of 2.71b/min, water pressure of 50 kpsi and standoff distance 3mm to get higher MRR and lower Kw simultaneously within the selected limits.
- Confirmation experiment has been performed and is found to be in good agreement with the actual set of optimal process parameter values.
- From ANOVA it can be concluded that water pressure has the most significant effect on the output parameters MRR and KW followed by Abrasive flow rate and Standoff distance.

REFERENCES

1. T. U. Siddiqui and M. Shukla, Robust parameter design for multi-characteristic optimization of abrasive water jet cutting of aramid composite, Journal of Modern Manufacturing Technology, 2008:1. 2008.

2. M. A. Azmir, A.K. Ahsan, Investigation on glass/epoxy composite surfaces machined by abrasive water jet machining, *Journal of Materials Processing Technology*, March 2008: 198(1-3), pp.122-128.
3. Tauseef Uddin Siddiqui, Mukul Shukla, Pankaj B. Tambe, Optimization of surface finish in abrasive water jet cutting of Kevlar composites using hybrid Taguchi and response surface method, *International Journal of Machining and Machinability of Materials*, 2008: 3(3/4), pp.382 - 402.
4. Conner, I., Hashish, M., Ramulu, M, Abrasive water jet machining of aerospace structural sheet and thin plate materials, *Proceedings of the 12th American Water jet Conference*, Houston, USA, 2003: 1-G, pp.1-19.
5. W. König, Ch. Wulf, P. Gras, H. Willerscheid, Machining of fiber reinforced plastics, *Annals of CIRP*, 1985:34 (2)
6. Neelesh K. Jain, V.K. Jain, Kalyanmoy Debb, Optimization of process parameters of mechanical type advanced machining processes using genetic algorithms, *International Journal of Machine Tools and Manufacture*, 2007: 47(6), pp. 900-919
7. M. A. Azmir, A.K. Ahsan, A. Rahmah, Investigation On Abrasive Waterjet Machining Of Kevlar Reinforced Phenolic Composite Using Taguchi Approach, *Proceedings of the International Conference on Mechanical Engineering 2007 (ICME2007)*, pp.29-31.
8. Ramulu and Arola D, The influence of abrasive water jet cutting conditions on the surface quality of graphite/epoxy laminates, *International Journal of Machine Tools & Manufacture*, 1994: 34 (3).
9. Ersan Aslan, N.Camuscu, B.Birgoren, Optimization of cutting parameters on tool performance measures-flank wear and surface roughness, *Material and Design*, 2007:28(5).
10. Khan A.A. and Haque M.M, Performance of different abrasive materials during abrasive water jet machining of glass, *Journal of Materials Processing Technology*, 2007: 191.
11. Ramulu, M., Posinasetti, P. and Hashish, M, Analysis of abrasive water jet drilling process, *Proceedings of the 13th WJTA American Waterjet Conference*, Houston, Texas, 2005: 5A-2.
12. Thella Babu Rao, Gopal Rao A, Simultaneous Optimization of multiple characteristics of WEDM for machining ZC63/SiCp MMC, *Advanced Manufacturing*, 2013: 1, pp.265-275.
13. B. Satyanarayana, G. Srikar, Optimization of abrasive water jet machining process using Taguchi Grey Relational Analysis (TGRA), *Proceedings of 13th IRF International Conference*, July 20-2014, Pune, India.
14. Lindsay I Smith, A tutorial on Principal Component Analysis, February 26-2002.
15. M. Hashish, An investigation of milling with abrasive-water jets, *ASME Journal Engineering Industires*, 1989:111, pp.158-166.

16. M. A. Azmir, A.K. Ahsan, A. Rahmah, M.M. Noor and A.A. Aziz, Optimization of Abrasive Water jet Machining Process Parameters Using Orthogonal Array With Grey Relational Analysis, Regional Conference on Engineering Mathematics, Mechanics, Manufacturing & Architecture (EM3ARC), 2007: pp 21~30
17. S. Naveen & Aslam A. Hirani, Design & Fabrication of Abrasive Jet Machining, International Journal of Mechanical and Production Engineering Research and Development (IJMPERD), 2014: pp.55-62.
18. M. Hashish, A modeling study of metal cutting with abrasive water jets, ASME Journal of Engineerinr Materials Technology, 1984: 106, pp. 88–100.
19. Tauseef Uddin Siddiqui and Mukul Shukla, Experimental Investigation and Hybrid Multi-Response Robust Parameter Design in Abrasive Water Jet Machining of Aircraft grade Layered Composites, IJAEA, 2008: 1 (5), pp.39-48.
20. Tuan Anh and Sander Mägi, A report on Principal Component Analysis in Financial Pricing, National Cheng Kung University, June 17-2009.
21. Singh, Comprehensive evaluation of abrasive water jet cut surface quality, Proceedings of the 6th American Water Jet Conference, Houston, USA, 1991.
22. M. Joseph Davidson, Surface roughness prediction of flow formed AA6061 alloy by design of experiments, Journal of Material processing Technology, 2008: 202.

Modeling the Dynamic behavior of MR Fluid Damper for Structural Vibration Mitigation

G. Sailaja¹, N. Seetharamaiah², M. Janardhana³

¹Assistant Professor, Dept. of Mech. Engg., MJCET, Road No.3, Banjara hills, Hyderabad-34.

E-mail: sailajasinha@gmail.com, Mobile: +91 9948439301. (Corresponding author)

²Professor, Dept. of Mech. Engg., MJCET, Road No.3, Banjara hills, Hyderabad-34.

E-mail: sitaram1881@gmail.com, Mobile: +91 9849402284.

³Professor, Dept. of Civil Engg., JNTUHCEH (A), Kukatpally, Hyderabad- 85.

E-mail: jmaganti@jntuh.ac.in, Mobile: +91 9441864828.

Abstract: Magnetorheological (MR) fluids are materials that respond to an applied magnetic field with a dramatic change in rheological behavior. An MR fluid is a free-flowing liquid in the absence of magnetic field, but under a strong magnetic field its viscosity can be increased by more than two orders of magnitude in a very short time (milliseconds) and it exhibits solid-like characteristics. The focus of this work is to model the dynamic behavior for designing the MR Fluid Damper in order to suppress the structural vibrations. Because of their mechanical simplicity, high dynamic range, low power requirements, large force capacity and robustness, MR Fluid Dampers have been shown to be semi-active control devices that mesh well with application demands and constraints to offer an attractive means of controlling the intensity of vibrations in structures. Following an overview of the essential features of MR Fluids, this paper discusses the current status of this new technology for structural vibration control.

Keywords: MR Fluids, MR Fluid Damper, Semi-active control

.Introduction:

Magnetorheological(MR) fluids, shown in Fig.1, are the suspensions of micron sized, magnetisable particles (iron, iron oxide, iron nitride, iron carbide, carbonyl iron, chromium dioxide, low-carbon steel, silicon steel, nickel, cobalt, and combinations thereof [1] in an appropriate carrier liquid (non-magnetisable) such as mineral oil, synthetic oil, water or ethylene glycol. The carrier liquid serves as a dispersed medium and ensures the homogeneity of particles in the fluid. A typical MR fluid consists of 20-40 percent by volume of relatively pure, 3-10 micron diameter iron particles, suspended in a carrier liquid. They are field responsive in nature and the magnetorheological response of these fluids lies in the fact that the polarization is induced in the suspended particles by the application of an external magnetic field. This allows the fluid to transform from freely flowing liquid state to solid-like state within milliseconds, because the magnetically dispersed particles attract each other to form fibril/chain-like structures along the direction of magnetic field. The chain-like structures resist the motion of the fluid and increase its viscous characteristics. Such behavior of MR fluid is analogous to Bingham plastics (non-Newtonian fluids) capable of developing a yield stress.



Fig.1: MR Fluid

A favorable arrangement consists of particle chains aligned in the direction of the applied field and this, in turn, gives rise to a strong resistance to applied strains (Fig. 2). The yield stress developed within the MR fluid is a function of the applied magnetic field. However, once this yield stress is exceeded, the behavior of the MR fluid deviates from that of a Bingham plastic. This is attributable to the breakdown of the chains of particles under the forces of the fluid flow, and results in a shear-stress/shear-rate characteristic that is highly non-linear. When used in a damping device, the result is a damper whose force/velocity characteristic is non-linear, but can be changed by the way the magnetic field is applied.

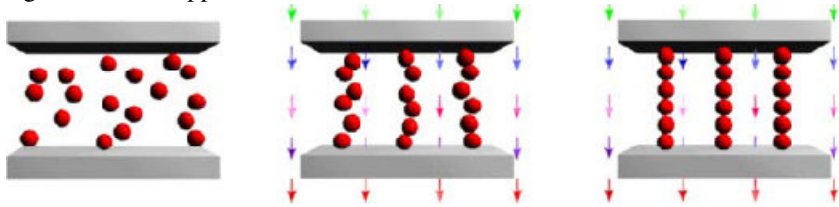


Fig. 2 Activation of MR fluid

2. MR Fluid Flow in an Annular Duct:

The pressure gradient along the flow is resisted by the fluid shear stress which is governed by the Navier- Stokes equation

$$\rho \frac{\partial}{\partial t} u_x(r) + \frac{\partial}{\partial r} \tau_{xr}(r) + \frac{\tau_{xr}(r)}{r} = \frac{\partial p}{\partial x} \quad (1)$$

where $u_x(r)$ = flow velocity; $\tau_{xr}(r)$ = shear stress; r = radial coordinate;

x = longitudinal coordinate; ρ = fluid density; and $\frac{\partial p}{\partial x}$ = pressure gradient.

To analyze the quasi-static motion of the fluid inside the damper, the fluid inertia can be neglected. In this case, Eq. (1) can be reduced to

$$\frac{d}{dr} \tau_{xr}(r) + \frac{\tau_{xr}(r)}{r} = \frac{dp}{dx} \quad (2)$$

Note that for oscillatory or unsteady flow, the fluid inertia must be taken into account. The solution of Eq. (2) is

$$\tau_{rx}(r) = \frac{1}{2} \frac{dp(x)}{dx} r + \frac{D_1}{r} \quad (3)$$

Where D_1 = a constant which can be evaluated with boundary conditions.

A typical shear stress diagram, along with velocity profile, for MR fluid flow through the annular gap is shown in Fig. 3. In regions I and II, the shear stress has exceeded the yield

stress and fluids flow. In region C, because the shear stress is less than the yield stress, there is no shear flow; this is often referred to as the plug flow region.

2.1 Modeling Based on the Herschel-Bulkley Model

To account for the fluid shear thinning or thickening effect, the Herschel-Bulkley viscoplasticity model is employed. In region I, the shear strain rate $\dot{\gamma} = du_x/dr \geq 0$. Therefore, the shear stress given by

$$\tau_{rx}(r) = \tau_o(r) + K \left(\frac{du_x(r)}{dr} \right)^{\frac{1}{m}} \quad (4)$$

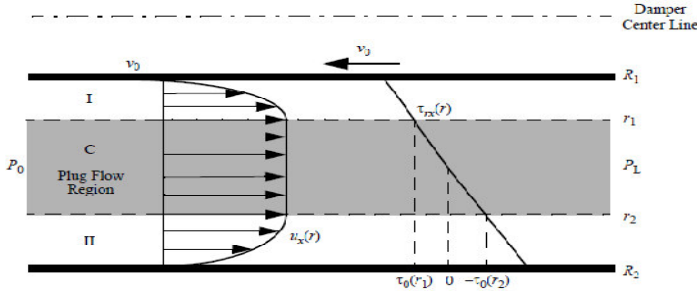


Fig. 3 Stress and velocity profiles of MR fluids through an annular duct.

This is substituted into Eq. (3) and integrated once with respect to r . One obtains

$$u_x(r) = \int_{R_1}^r \left[\frac{1}{K} \left(\frac{1}{2} \frac{dp(x)}{dx} r + \frac{D_1}{r} - \tau_o(r) \right) \right]^m dr - v_p \quad (R_1 \leq r \leq R_1) \quad (5)$$

by imposing the boundary condition that the flow velocity at $r = R_1$ is $u_x(R_1) = -v_p$.

In region II, the shear strain rate $\dot{\gamma} = du_x/dr \leq 0$. Thus, the shear stress is given by

$$\tau_{rx}(r) = -\tau_o(r) - K \left(\frac{-du_x(r)}{dr} \right)^{\frac{1}{m}} \quad (6)$$

Similarly proceeding in region II with the boundary condition $u_x(R_2) = 0$ at $r = R_2$ gives

$$u_x(r) = \int_r^{R_2} \left[-\frac{1}{k} \left(\frac{1}{2} \frac{dp(x)}{dx} r + \frac{D_1}{r} + \tau_o(r) \right) \right]^m dr \quad (r_2 \leq r \leq R_2) \quad (7)$$

Note that the flow velocity is constant in the plug flow region because the shear stress is less than the yield stress. Thus, the flow velocities at the boundaries of the plug flow region satisfy $u_x(r_1) = u_x(r_2)$. Combining Eqs. (5) and (8) yields

$$\int_{R_1}^{r_1} \left[\frac{1}{K} \left(\frac{1}{2} \frac{dp(x)}{dx} r + \frac{D_1}{r} - \tau_0(r) \right) \right]^m dr - \int_{r_2}^{R_2} \left[-\frac{1}{K} \left(\frac{1}{2} \frac{dp(x)}{dx} r + \frac{D_1}{r} + \tau_0(r) \right) \right]^m dr = v_p \quad (8)$$

Also the shear stresses τ_{rx} satisfy $\tau_{rx}(r_1) = \tau_0(r_1)$ and $\tau_{rx}(r_2) = -\tau_0(r_2)$, therefore D_1 can be determined by using Eq. (3) as

$$D_1 = \frac{r_1 r_2 (\tau_0(r_2) r_1 + \tau_0(r_1) r_2)}{r_2^2 - r_1^2} \quad (9)$$

The expression for the volume flow rate Q given by

$$Q = 2\pi \int_{R_1}^{R_2} r u_x(r) dr \quad (10)$$

Because the shear strain rate $du_x(r)/dr$ is zero in the plug flow region $r_1 < r < r_2$, Eq. (10) can also be written as

$$Q = v_p A_p = \pi R_1^2 v_p - \pi \int_{R_1}^{r_1} r^2 \frac{du_x(r)}{dr} dr - \pi \int_{r_2}^{R_2} r^2 \frac{du_x(r)}{dr} dr \quad (11)$$

Where A_p = Cross section area of the piston head, and v_p = piston head velocity. Substitution of Eqs. (5) and (7) into Eq. (11) results in

$$Q = v_p A_p = \pi R_1^2 v_p - \pi \int_{R_1}^{r_1} r^2 \left[\frac{1}{K} \left(\frac{1}{2} \frac{dp(x)}{dx} r + \frac{D_1}{r} - \tau_0(r) \right) \right]^m dr + \pi \int_{r_2}^{R_2} r^2 \left[-\frac{1}{K} \left(\frac{1}{2} \frac{dp(x)}{dx} r + \frac{D_1}{r} + \tau_0(r) \right) \right]^m dr \quad (12)$$

Fig. 4 shows the free body diagram of MR fluids through an annular duct. The equation of motion of fluid materials enclosed by $r = r_1$ and $r = r_2$ is which yields

$$\frac{dp}{dx} \pi (r_2^2 - r_1^2) dx + 2\pi r_2 \tau_0(r_2) dx + 2\pi r_1 \tau_0(r_1) dx = 0 \quad (13)$$

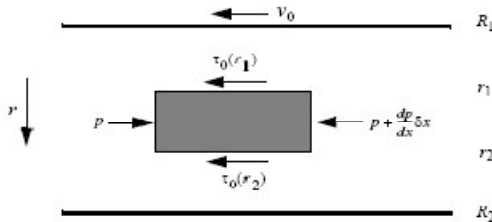


Fig.4 Free body diagram of MR fluids through an annular duct

$$\frac{dp(x)}{dx} (r_2^2 - r_1^2) + 2[\tau_0(r_2) r_2 + \tau_0(r_1) r_1] = 0 \quad (14)$$

In summary, the resulting equations that can be solved numerically to determine r_1, r_2 , and the pressure gradient $\frac{dp}{dx}$ between the two ends of the cylinder using the Herschel-Bulkley model are given by

$$\int_{R_1}^{r_1} \left[\frac{1}{K} \left(\frac{1}{2} \frac{dp(x)}{dx} r + \frac{D_1}{r} - \tau_o(r) \right) \right]^m dr - \int_{r_2}^{R_2} \left[-\frac{1}{K} \left(\frac{1}{2} \frac{dp(x)}{dx} r + \frac{D_1}{r} + \tau_o(r) \right) \right]^m dr = v_p \quad (15)$$

$$Q = v_p A_p = \pi R_1^2 v_p - \pi \int_{R_1}^{r_1} r^2 \left[\frac{1}{K} \left(\frac{1}{2} \frac{dp(x)}{dx} r + \frac{D_1}{r} - \tau_o(r) \right) \right]^m dr + \pi \int_{r_2}^{R_2} r^2 \left[-\frac{1}{K} \left(\frac{1}{2} \frac{dp(x)}{dx} r + \frac{D_1}{r} + \tau_o(r) \right) \right]^m dr \quad (16)$$

$$\frac{dp(x)}{dx} (r_2^2 - r_1^2) + 2[\tau_o(r_2)r_2 + \tau_o(r_1)r_1] = 0 \quad (17)$$

$$\text{Where } D_1 = \frac{r_1 r_2 [\tau_o(r_2)r_1 + \tau_o(r_1)r_2]}{r_2^2 - r_1^2} \quad (18)$$

To solve the resulting algebraic equations numerically, a method based on the constrained nonlinear least-squares algorithm is utilized in conjunction with the cubic polynomial interpolation and extrapolation method. The integrals in Eqs. (15) and (16) are evaluated using the adaptive recursive Newton-Cotes approach. From Eq. (17) the thickness of the plug flow region can be obtained by

$$r_2 - r_1 = -\frac{2[\tau_o(r_1)r_1 + \tau_o(r_2)r_2]}{\frac{dp(x)}{dx} (r_1 + r_2)} \quad (19)$$

which varies with the fluid yield stress τ_o . Note that the flow can only be established when $r_2 - r_1 < R_2 - R_1$, which implies that the plug flow needs to be within the gap otherwise, there is no flow. The damper force is then computed as

$$F = \Delta p A_p \quad (20)$$

where $\Delta P = P_L - P_o = -L(dp(x)/dx)$; and L = effective pole length. The velocity profile can be determined from Eqs. (5) and (7) as follows:

$$u_x(r) = \int_{R_1}^r \left[\frac{1}{k} \left(\frac{1}{2} \frac{dp(x)}{dx} r + \frac{D_1}{r} - \tau_o(r) \right) \right]^m dr - v_p \quad R_1 \leq r \leq r_1$$

$$u_x(r) = \int_{r_2}^{R_2} \left[-\frac{1}{k} \left(\frac{1}{2} \frac{dp(x)}{dx} r + \frac{D_1}{r} + \tau_o(r) \right) \right]^m dr \quad r_1 < r < r_2 \quad (21)$$

$$u_x(r) = \int_r^{R_2} \left[-\frac{1}{k} \left(\frac{1}{2} \frac{dp(x)}{dx} r + \frac{D_1}{r} + \tau_o(r) \right) \right]^m dr \quad r_2 \leq r \leq R_2$$

Further, the shear stress diagram can be obtained from Eq. (3)

Note that when the yield stress $\tau_0=0$, there is no plug flow region which implies that $r_1 = r_2$. Therefore, Eqs. (17) and (18) are no longer valid due to the singularity. However, in this case, the velocity achieves its maximum at $r = r_1$ where the shear stress is zero. By using Eq. (3), the following equations can be employed to obtain pressure gradient where yield stress $\tau_0 = 0$

$$\int_{R_1}^{r_1} \left[\frac{1}{K} \left(\frac{1}{2} \frac{dp(x)}{dx} r + \frac{D_1}{r} \right) \right]^m dr - \int_{r_1}^{R_2} \left[-\frac{1}{K} \left(\frac{1}{2} \frac{dp(x)}{dx} r + \frac{D_1}{r} \right) \right]^m dr = v_p \quad (22)$$

$$Q = v_p A_p = \pi R_1^2 v_p - \pi \int_{R_1}^{r_1} r^2 \left[\frac{1}{K} \left(\frac{1}{2} \frac{dp(x)}{dx} r + \frac{D_1}{r} \right) \right]^m dr \quad (23)$$

$$+ \pi \int_{r_1}^{R_2} r^2 \left[-\frac{1}{K} \left(\frac{1}{2} \frac{dp(x)}{dx} r + \frac{D_1}{r} \right) \right]^m dr$$

$$D_1 = \frac{1}{2} \frac{dp}{dx} r_1^2 \quad (24)$$

Note that the solution of the MR flow in an annular duct does not reduce to that of the pipe flow as $r_1 \rightarrow 0$. This is because the annular duct model has a boundary condition at r_1 ; however, there is no boundary condition at $r = 0$ for the pipe flow.

2.2 Modeling based on the Bingham model

The Herschel-Bulkley model reduces to the Bingham model when the MR fluid parameter $m=1$. Using Eqs. (15) – (17), the resulting equations for the Bingham model are

$$\frac{dp(x)}{dx} (R_2^2 - r_2^2 - R_1^2 + r_1^2) / 4 + D_1 \ln(R_2 r_1 / r_2 R_1) + D_2 - \eta v_p = 0 \quad (25)$$

$$Q = v_p A_p$$

$$= \pi R_1^2 v_p - \frac{\pi}{8\eta} \left[\frac{dp(x)}{dx} (R_2^4 - R_1^4 - r_2^4 + r_1^4) + 4D_1 (R_2^2 - R_1^2 - r_2^2 + r_1^2) + 8D_3 \right] \quad (26)$$

$$\frac{dp(x)}{dx} (r_2^2 - r_1^2) + 2[\tau_0(r_2)r_2 + \tau_0(r_1)r_1] = 0 \quad (27)$$

$$\text{where } D_1 = \frac{r_1 r_2 [\tau_0(r_2)r_1 + \tau_0(r_1)r_2]}{r_2^2 - r_1^2} \quad (28)$$

$$D_2 = \int_{r_2}^{R_2} \tau_0(r) dr + \int_{r_1}^{R_1} \tau_0(r) dr \quad (29)$$

$$D_3 = \int_{r_2}^{R_2} \tau_0(r) r^2 dr + \int_{r_1}^{R_1} \tau_0(r) r^2 dr \quad (30)$$

and the velocity profile is given by

$$\begin{aligned}
u_x(r) &= \frac{-1}{4\eta} \frac{dp}{dx} (R_1^2 - r^2) + \frac{D_1}{\eta} \ln \frac{r}{R_1} - \frac{1}{\eta} \int_{R_1}^r \tau_0(r) dr - v_p & R_1 \leq r \leq r_1 \\
&= \frac{-1}{4\eta} \frac{dp}{dx} (R_2^2 - r_2^2) - \frac{D_1}{\eta} \ln \frac{R_2}{r_2} - \frac{1}{\eta} \int_{r_2}^{R_2} \tau_0(r) dr & r_1 < r < r_2 \\
&= \frac{-1}{4\eta} \frac{dp}{dx} (R_2^2 - r^2) - \frac{D_1}{\eta} \ln \frac{R_2}{r} - \frac{1}{\eta} \int_r^{R_2} \tau_0(r) dr & r_2 \leq r \leq R_2
\end{aligned} \tag{31}$$

In the absence of magnetic field, the yield stress $\tau_0 = 0$. The pressure gradient can be obtained directly from

$$\frac{dp}{dx} = \frac{8\eta v_p}{\pi} \frac{\frac{\pi}{2} (2R_1^2 - \frac{R_2^2 - R_1^2}{\ln(R_2/R_1)}) - A_p}{R_2^4 - R_1^4 - \frac{(R_2^2 - R_1^2)^2}{\ln(R_2/R_1)}} \tag{32}$$

In general, the yield stress τ_0 in the axisymmetric model will be a function of r. But when $R_2 - R_1 \ll R_1$, variation of the yield stress in the gap can be ignored, and Eqs. (28)– (30) can be further simplified substantially as follows:

$$D_1 = \frac{r_1 r_2 \tau_0}{r_2 - r_1} \tag{33}$$

$$D_2 = \tau_0 (R_2 + R_1 - r_1 - r_2) \tag{34}$$

$$D_3 = \frac{1}{3} \tau_0 (R_1^3 + R_2^3 - r_1^3 - r_2^3) \tag{35}$$

Note that in this case, the thickness of the plug flow can be calculated by using Eq. (19)

$$r_2 - r_1 = - \frac{2\tau_0}{\frac{dp(x)}{dx}} \tag{36}$$

which is a constant, and only depends on the yield stress and pressure gradient of the flow.

3. Conclusions:

In this work, a fundamental understanding of the dynamic behavior of Magnetorheological (MR) fluids has been developed through annular duct using Navier- Stokes equation based on the Herschel-Bulkley and Bingham models for Non-Newtonian fluid flows. These models are useful for further designing the MR Fluid Damper for structural vibration mitigation.

References:

1. M. Kciuk, S. Kciuk and R. Turczyn (2009), Magnetorheological characterization of carbonyl iron based suspension, *Journal of Achievements in Materials and Manufacturing Engineering*, Vol. 33, pp.135-141.

1. Shinichi KAMIYAMA, Kazuo KOIKE and Zhi-ShanWANG (1987), Rheological Characteristics of Magnetic Fluids, *JSME International Journal*, Vol. 30, No. 263, pp.761-766.
2. Gheorghe GHITA, Marius GIUCLEA and Tudor SIRETEANU, Modeling of Dynamic Behavior of Magnetorheological Fluid Damper by Genetic Algorithms Based Inverse Method, The 6th International Conference on Hydraulic Machinery and Hydrodynamics, Timisoara, Romania, October 2004, pages 21-22.
3. Xiaojie Wang and Faramarz Gordaninejad, Flow Analysis and Modeling of Field-Controllable, Electro- and Magneto-Rheological Fluid Dampers, *Journal of Applied Mechanics, ASME*, Vol. 74, pp 13-22, 2007.
4. Yukio TOMITA, Flows of Non-Newtonian Fluids, *JSME International Journal*, Vol. 30, No. 270, 1877-1884, 1987.
5. N.Seetharamaiah, Semi-Active Behavior of Magnetorheological (MR) Fluid Damper: Design, Modeling And Testing, Osmania University, 2010.